Title

Novel Quantitative Composite Delamination Injection Repair Procedure and Characterization for Strength Restoration

Author

Massey, Justin Torasuke

Publication Date

2023

Peer reviewed|Thesis/dissertation

UNIVERSITY OF CALIFORNIA SAN DIEGO

Novel Quantitative Composite Delamination Injection Repair Procedure and Characterization for Strength Restoration

A Dissertation submitted in partial satisfaction of the requirements
for the degree Doctor of Philosophy

in

Materials Science and Engineering

by

Justin Torasuke Massey

Committee in charge:

Professor Hyonny Kim, Chair
Professor Shengqiang Cai
Professor Veronica Eliasson
Professor Ken Loh
Professor Yu Qiao

2023

The Dissertation of Justin Torasuke Massey is approved, and it is acceptable in quality and form for publication on microfilm and electronically.

University of California San Diego

2023

DEDICATION

To my wife Dezarae, thank you for your unwavering support in my educational pursuit. To my parents, thank you for giving me the tools in life to succeed. And finally, to my children Kohana and Nikola, may you one day read this and see that Daddy fixes more than toys.

TABLE OF CONTENTS

LIST OF FIGURES

LIST OF TABLES

LIST OF ABBREVIATIONS

2-D	Two Dimensional
3-D	Three Dimensional
ASM	American Society of Materials
AMS	Aerospace Material Specification
ASME	American Society of Mechanical Engineers
ASTM	American Society of Testing and Materials (ASTM)
ATR	Attenuated Total Reflectance
B-K	Benzeggagh and Kenane
C	Compliance
CAI	Compression After Impact
COTS	Commercial Off the Shelf
CT	Computes Tomography
DCB	Dual Cantilever Beam
DIC	Digital Image Correlation
DRIFTS	Diffuse Reflectance Infrared Fourier Transform Spectrometry
ENF	End-Notch Flexure
FEA	Finite Element Analysis
FTIR	Fourier Transform Infrared
GC-MS	Gas Chromatograph Mass Spectrometer
HDR	High Dynamic Range
HF	Hydraulic Fluid
HPLC	High Performance Liquid Chromatography

IR	Infrared
LEFM	Linear Elastic Fracture Mechanics
LO	Lubricating Oil
MIBK	Methylisobutylketone
MEK	Methylethylketone
MMB	Mixed-mode Bending
m/z	Mass to Charge Ratio
NDI	Non-Destructive Inspection
NIST	National Institute of Standards and Technology
PC	Pre-Cracked
PMC	Polymer Matrix Composite
PTFE	Polytetraflouroethylene
QGA	Quantitative Gas Analysis
RMS	Root Mean Square
SEM	Scanning Electron Microscope
TOF	Time of Flight
UCSD	University of California San Diego
U.S.	United States
UT	Ultrasonic Testing
VCCT	Virtual Crack Closure Technique
WCA	Water Contact Angle

LIST OF SYMBOLS

A	Cross-sectional Area, m^2
a	Crack Length, m
B	Specimen Width, m
F	Input Force, N
F^{CAI}	Compression After Impact Ultimate Strength, MPa
G_c	Critical Strain Energy Release Rate, J/m^2
G_{Ic}	Mode I Fracture Toughness, J/m^2
G_{IIc}	Mode II Fracture Toughness, J/m^2
h	Delamination Thickness, m
K	Permeability Constant
L	Delamination Length, m
λ_c	Long Wavelength Cutoff, mm
λ_s	Short Wavelength Cutoff, μm
m	Compliance Calibration Coefficient
η	Viscosity, cPs
θ_c	Equilibrium contact angle
σ_1	Surface Tension, mN/m
P	Maximum Load, N
P_1	Injection Pressure, MPa
P_2	Pressure at Flow Front, MPa
P_a	Profile
P_{ku}	Profile Kurtosis

P_q	Root Mean Square Profile
ρ	Density, kg/m^3
R	Radius, m
R_a	Roughness
t_{cure}	Pot Life of Adhesive, s
T_g	Glass Transition Temperature, ^oC
v	Flow Velocity, m/s
γ_{LG}	Liquid-Gas Interfacial Energy, J/m^2
γ_{SL}	Solid-Liquid Interfacial Energy, J/m^2
W_{SL}	Work of Adhesion, J/m^2

ACKNOWLEDGEMENTS

I would like to sincerely thank Prof. Hyonny Kim for his invaluable support and insight during my time as a graduate student and researcher at UCSD. Prof. Kim's unwavering support and patience while I performed research for his group was one of the greatest learning experiences of my life. He constantly made sacrifices helping me with the knowledge that I had a complex schedule within my personal life. I will always strive to have the patience and optimism that Prof. Kim exudes with all of his graduate and undergraduate students. Thank you for always helping me even when times were the toughest.

I would also like to give a special thanks Dr. Kostas Anagnostopoulos for his help with teaching me how to create FEA models for fracture mechanics and helping me develop the modified end notch flexure test. I would also like to thank Dr. Andrew Ellison for working jointly with me to learn new methods of non-destructive inspection and helping me perform X-ray CT imaging. Thank you, Mr. Barrett Romasko for working all those long days with me when it came to impact testing and performing ultrasonic inspection. I will always cherish our friendship made over the years we worked together. In addition to the folks at UCSD, I would like to thank the following people from NAVAIR who helped me invaluably with my research activities: Stephen Pacheco, Kurt Gaenzle, Paul Johnson and Dr. Eric Kim. These individuals from the Fleet Readiness Center Southwest Materials Engineering laboratory are not only industry experts, but took time out of their busy work schedules to teach me about multiple topics that would be pertinent to develop a new repair process. In addition, I would like to thank Mr. Ron Pangilinan and Fleet Readiness Center Southwest for funding me and allowing for the pursuit of my PhD while I was a full-time employee. Thank you.

I would like to give a special thanks to Mr. Bill Nickerson and Dr. Anisur Rahman for the financial and technical support provided by the Office of Naval Research for this study. In addition I would like to thank Mr. Fred Lancaster and the NAVAIR Multi-Platform Systems Air Vehicle Program for their support of this study.

Finally, I would like to thank my family for their understated and invaluable support over the years. Allowing me to work six days a week and helping raise my young children while I was in pursuit of this PhD is something I will never forget. Thank you, Mom and Dad, for giving the skills to persevere even in the most difficult of times and giving me the tools to succeed. Thank you to my children, Kohana and Niko, for giving motivation to complete this journey, and most importantly thank you to my loving wife, Dezarae, for supporting me even though it made your life infinitely more difficult and sacrificing for me.

Chapters 3 and 4 include material as it appears in the Impact Damage and Injection Repair Strength Restoration, 2021, Massey, Justin, Romasko, Barrett, and Kim, Hyonny, Proceedings of the 36th Annual American Society for Composites Technical Conference and Novel Enclosed Delamination Injection Repair Process for Strength Restoration, 2022, Massey, Justin, Romasko, Barrett, and Kim, Hyonny, Proceedings of the 37th Annual American Society for Composites Technical Conference. Also material from Characterization of Transverse Impact Damage and Internal Contamination of In-Service Composite Aircraft Skins, Massey, Justin, Ellison, Andrew, and Kim, Hyonny, Proceedings of the 2023 Composites and Advanced Materials Expo. In addition material from Advanced Composite Novel Delamination Injection Repair Procedure for Restoration of Laminate Mechanical Properties, Massey, Justin and Kim, Hyonny, in part is currently being prepared for submission for publication with the 2023 US-Japan Composite Symposium. Finally, unpublished material co-authored with Anagnostopoulos, Konstantinos and

Kim, Hyonny for A Comparison of Carbon/Epoxy Composite Interlaminar Laboratory-Based Delamination Methods to In-service Aircraft Damage. The dissertation author was the primary investigator and author for all of these papers.

VITA

Education

2009 Bachelor of Science, University of California, Santa Barbara

2011 Master of Science, University of California, Los Angeles

2023 Doctor of Philosophy, University of California San Diego

Experience

2009-2011 Aerospace Engineer, F/A-18 Fleet Support Team, Naval Air Systems Command

2011-2019 Senior Materials Engineer, Fleet Readiness Center Southwest, Materials Engineering Department, Naval Air Systems Command

2019-2023 Composite and Corrosion Division Head, Fleet Readiness Center Southwest, Materials Engineering Department, Naval Air Systems Command

PUBLICATIONS

Massey, J.T., Romasko, B., and Kim, H., "Impact Damage and Injection Repair Strength Restoration", Proceedings of the 36th Annual American Society for Composites Technical Conference, September 19-22, 2021, Virtual Conference.

Massey, J.T., Romasko, B., and Kim, H., "Novel Enclosed Delamination Injection Repair Process for Strength Restoration", Proceedings of the 37th Annual American Society for Composites Technical Conference, September 19-21, 2022, Tucson, AZ.

Massey, J.T., Ellison, A., Kim, H., "Characterization of Transverse Impact Damage and Internal Contamination of In-Service Composite Aircraft Skins", Proceedings of the 2023 Composites and Advanced Materials Expo, October 18-20, 2022, Anaheim, CA.

Massey, J.T., Anagnostopoulos, K., Kim, H., "A Comparison of Carbon/Epoxy Composite Interlaminar Laboratory-Based Delamination Methods to In-service Aircraft Damage", Manuscript in preparation.

Massey, J.T., Kim, H." Advanced Composite Novel Delamination Injection Repair Procedure for Restoration of Laminate Mechanical Properties", 2023 US-Japan Composite Symposium, abstract accepted and manuscript in preparation.

ABSTRACT OF THE DISSERTATION

Novel Quantitative Composite Delamination Injection Repair Procedure and Characterization for Strength Restoration

by

Justin Torasuke Massey

Doctor of Philosophy in Materials Science and Engineering

University of California San Diego, 2023

Professor Hyonny Kim, Chair

A common damage mechanism that occurs on polymer matrix composite (PMC) aircraft structures are delaminations which are interlaminar defects between composite plies. A current practice for repair of delaminations include injection using a repair resin. Injection repairs have traditionally been a faster, less expensive way to repair composite delaminations. However, the

aerospace industry and safety regulating authorities consider injection repair cosmetic and have not accepted it as a strength restorative process. Questions about quantifying the removal of internal contamination, how to characterize restored strength, and ensuring desired percentage of repair resin fill within the delaminations have been primary reasons why injection repairs have not been credited with strength restoration. Therefore, a new quantitative internal surface cleaning, preparation and repair process was developed for delaminated composite materials including utilization of a new test coupon and configuration.

First, laboratory manufactured fractures were successfully compared to delaminations taken from actual aircraft structures using advanced surface metrology. Laboratory manufactured delaminations methods include a novel modified end notch flexure coupons (ENF) loaded in Mode II for fracture propagation and a separate out of plane impact specimen. Multiple lay-up configurations were characterized and surface metrology results indicate that the ENF fracture surfaces was most closely related to the in-service damage due to statistical comparison of arithmetic mean (Pa) and root mean square (Pq) surface profilometry and arithmetic mean roughness (Ra) results.

Materials and process development was also conducted to create a novel injection repair procedure. First, intentional contamination procedures were successfully developed, verified, and introduced into simulated delaminations. Contamination removal and internal fracture surface preparation using solvent and atmospheric plasma cleaning procedures were remarkably successful in removing hydrocarbon contaminant archetypes from contaminated fractures. Real-time mass spectrometry providing quantifiable cleaning verification of hydrocarbon contamination removal was successfully implemented into the novel procedure. Destructive post-processing verification of surface cleaning by infrared spectrometry, and goniometry was successfully

completed. In addition, a modified low-viscosity injection resin was also developed for delamination infiltration and exhibited analogous shear strength characteristics to un-modified structural adhesive while achieving a >84% reduction in viscosity. After development of a simulated enclosed delamination modified ENF coupon, application of the surface cleaning and modified repair resin to the previously fractured and contaminated coupons were tested. After repair of the modified ENF coupons, mode II interlaminar fracture toughness (G_{IIc}) and calculated stiffness was quantitatively restored or increased for all coupon configurations. Fracture analysis was completed to verify desired cohesive repair resin or adherend matrix brittle fracture failure modes of repaired test specimens. Therefore application of the novel injection repair procedure provided quantifiable local mechanical property restoration that contributes to the overall repair of aerospace PMC structures to carry designed loads.

CHAPTER 1: INTRODUCTION

1.1. MOTIVATION

Advanced composite materials have been widely adopted in primary, secondary, and tertiary aerospace structures. Composite materials have many advantages over traditional metallic alloys, such as: tailorable (anisotropic) material properties, higher strength-to-weight ratio, non-corrosive, and extended fatigue life. However, a drawback of advanced composite materials is that they have low out-of-plane toughness compared to metallic alloys and advanced composites are laminated presenting new damage mechanisms such as delamination between material plies. Delaminations are a mode of failure where the materials fractures and separation of layers occur. Shown in Figure 1.1 is an example of multiple composite delaminations within a laminate.

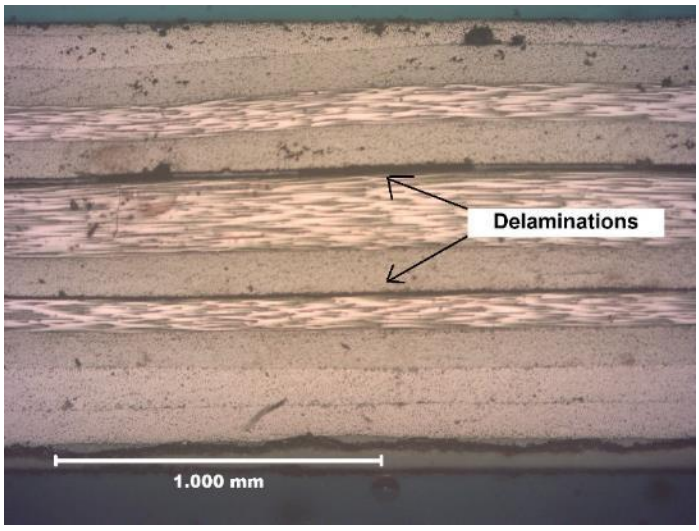

Figure 1.1. Example of advanced composite delamination

Delaminations often occur as a result from impacts, exposure of an edge to the airstream, defects from manufacturing, or coalescing micro-damage over time. The damage reduces the load carrying capability of the composite laminate and could potentially grow under load during in-flight operations leading to premature failure of aircraft components. Therefore it is preferable for all delaminations to be repaired to prevent the growth of damage or potentially restore lost strength. Enclosed damages less than 50 mm in diameter are of particular interest for repair. Current repair processes include a simple, fast, non-strength restoring resin injection method or a more invasive cutout repair which requires removal of the damaged laminate and repair with a structural load carrying repair patch that is bonded or bolted to the aircraft component. Injection repairs have traditionally been a faster, less expensive way to repair composite delaminations when compared to a cutout patch repair. Cutout of damage and using a patch to carry load also encounters its drawbacks including: addition of stress concentration due to cutout, often requires extensive engineering to verify repair, and requires more logistics for tooling and hazardous materials and specialized processing that may require extensive training.

The injection repair process incudes drilling holes to the depth reported by non-destructive inspection procedures (typically ultrasonic testing) and injecting and infiltrating the delaminated composite material with low viscosity epoxy repair resin that is assumed to “bond” the laminate plies back together and filling the delaminated void (see Figure 1.2). After injection and cure of the repair resin, the area is inspected to determine area filled and the process is repeated until the delamination is considered filled or repaired by the aircraft program.

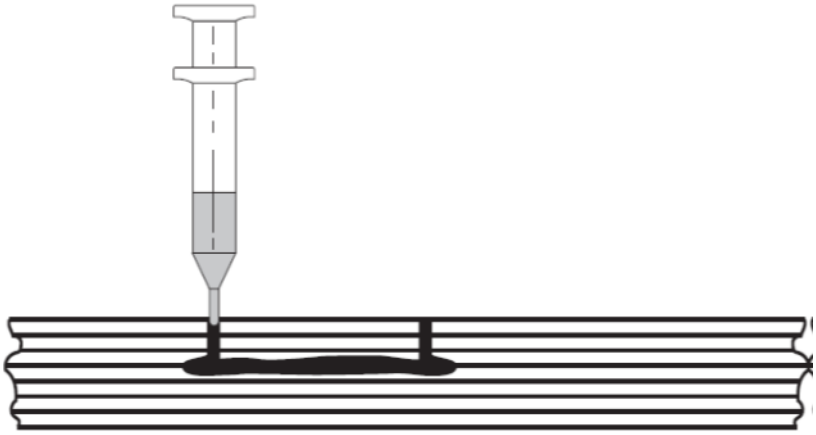

Figure 1.2. Example of injection repair of a delamination

Issues with this process are that it regularly does not completely fill the surface delamination and further inspection does not accurately describe the multi-layer damage geometry. Questions about quantifying and cleaning internal contamination from within the delamination, such as in-service fluid ingression, and ensuring percentage of repair resin fill within a delamination have been primary reasons why injection repairs have not been credited with strength restoration. Therefore a need exists to quantify contamination within a composite delamination and provide a method for cleaning the internal surfaces of the delamination prior to bonding with an injected adhesive.

1.2. OBJECTIVE

The main objective of this research is to determine the ability to quantitatively assess injection repair of delaminations in composite aircraft components, with the ultimate goal being to allow this repair method to quantitatively return strength to the component. The research conducted focuses heavily on: characterization of in-service delaminations and comparison to laboratory manufactured damage, identifying methods to better non-destructively inspect

delaminations, improve materials and processing for a novel repair procedure that quantitatively cleans and assess internal surface chemistry of delaminations prior to injection fill, and to qualitatively characterize and define a repaired delamination state while correlating damage state to local fracture toughness behavior of the laminate. Experimentation completed in support of the primary objective include: using viscosity and lap shear testing to assist in modification of repair resin for compatibility with injection into delaminations; development of contamination and contamination removal procedures for process testing using fluorescent dye and spectrometry; and modification of an existing end notch flexure test method to assess mode II fracture toughness of repaired composite laminates. All of the research focuses on carbon/epoxy unidirectional composite material, with three different laminate types investigated to determine the effectivity of the injection repair procedure with different fracture morphology. Results from experiments will assist in developing a more robust injection repair process that may result in quantitative strength restoration to delaminated composite laminates.

Chapter 2 provides background on previous work pertaining to: delamination of composites, delamination growth, composite repair procedures, and substantiation and evaluation of laminate characteristics as a result of delaminations and the effect of delamination repair. Chapter 3 defines the experimental set-up and procedure for both damage characterization and injection repair process development. Chapter 4 presents all of the experimental results from both damage characterization and injection repair process development testing. Chapter 5 provides a discussion of preliminary global mechanical testing results and requirements, transitional path forward for this research field, and conclusions about the research conducted.

1.3. NOVEL CONTRIBUTION

Although previous research has been conducted on the effectivity of injection repair of composite delaminations, the primary focus of those studies have either been centered on the development of low viscosity resins to better infiltrate and fill delaminations or to develop analysis techniques to determine a fluid flow model for injection fill. This previous work has supplemented in development of new repair procedures, however it does not address some main concerns including: comprehensive understanding of how well laboratory manufactured delaminations correlate to in-service delamination damage on aircraft components, quantification of contamination from in-service environment as it is related to resin bond quality for injection repairs, cleaning of contamination from internal delamination surfaces to improve repair bond quality, and quantifying local delamination repair mechanical property restoration.

This research will ultimately provide details in development of a novel process for repairing enclosed delaminations, however other novel contributions include comprehensively understanding delamination physical characteristics and comparing fracture mechanisms using analytical techniques. In order to characterize delaminations and develop new repair procedures, various parameters that effect repair materials and processes, such as composite laminate lay-up configuration, resin viscosity, and variation of contaminants were investigated. The variation of these parameters would allow for development of a process that more generalized and less configuration dependent. The outcome of this research will provide engineers with further understanding of how laboratory manufactured damage correlates to in-service aircraft damage, the effectivity of cleaning procedures on enclosed delaminations, and data that can be used to provide justification for mechanical property restoration of injection repaired delaminations.

Understanding the effectivity of these key topics will allow further implementation of injection repair to repair and restore strength to in-service aircraft, ultimately increasing aircraft repair capability and repairing composite aircraft components that would otherwise have previously been scrapped.

CHAPTER 2: BACKGROUND

This chapter is a literature review on topics related to the research of repair of delaminations in advanced composite materials. The topics include: a description of delamination defects in composite materials, how delaminations effect composite material mechanical properties, how delaminations are currently repaired, previous research conducted on materials and processes related to repair of composites, and previous research on conducted for evaluation of laminate characteristics as a result of delaminations and the effect delamination repair.

2.1. DELAMINATION OF POLYMER MATRIX COMPOSITES (PMC)

Delaminations are characterized as a separation between plies within a laminate material. In polymer matrix composite (PMC) materials, delaminations are often classified as a form of matrix cracking within the plane of the laminate [1]. Two primary types of delamination exist: 1. Edge Delaminations, where the delamination is open to the edge of a laminate; 2. Enclosed Delaminations, where the defect is fully encased within a laminate (see Figure 2.1).

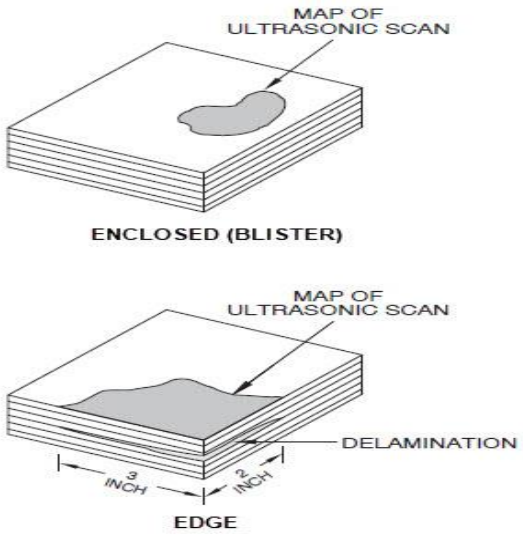

Figure 2.1. Classification of delamination types [1]

Multiple delaminations can also occur transversely through a laminate damage state and micro cracks exists between plies to connect multiple separated layers (see Figure 2.2). O'Brien [2] was an early researcher who characterized delaminations within carbon/epoxy composite laminates. O'Brien's research found that micro-cracking connects multiple delamination layers starts in plies 90 degrees from the loading direction.

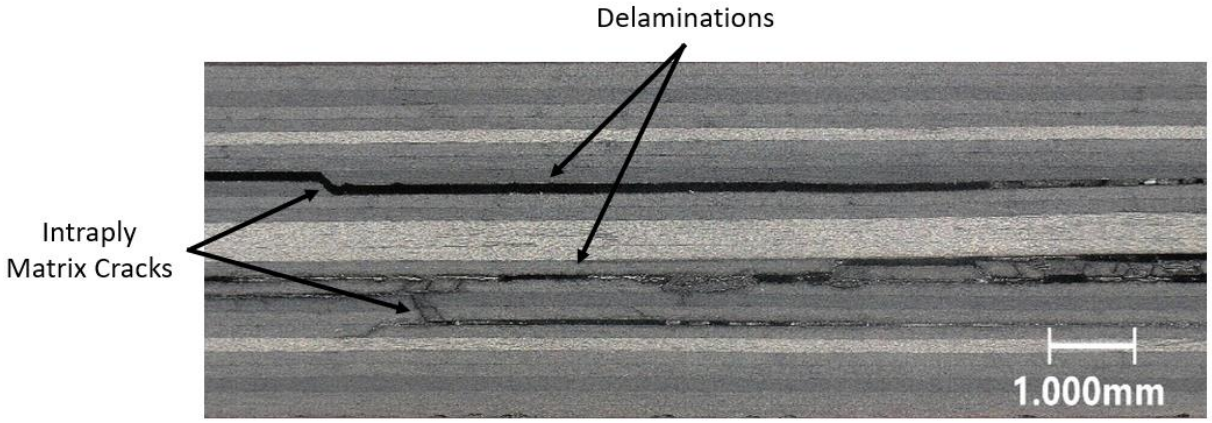

Figure 2.2. Microscopic image of a PMC delamination

Another major concern about delamination in composite laminates is the ability for the delamination to grow rapidly and eventually cause a premature failure of the composite laminate. O'Brien [2] also published a correlation of delamination size to laminate stiffness as shown in Figure 2.3. It was found that an increase in delamination will reduce the stiffness under static

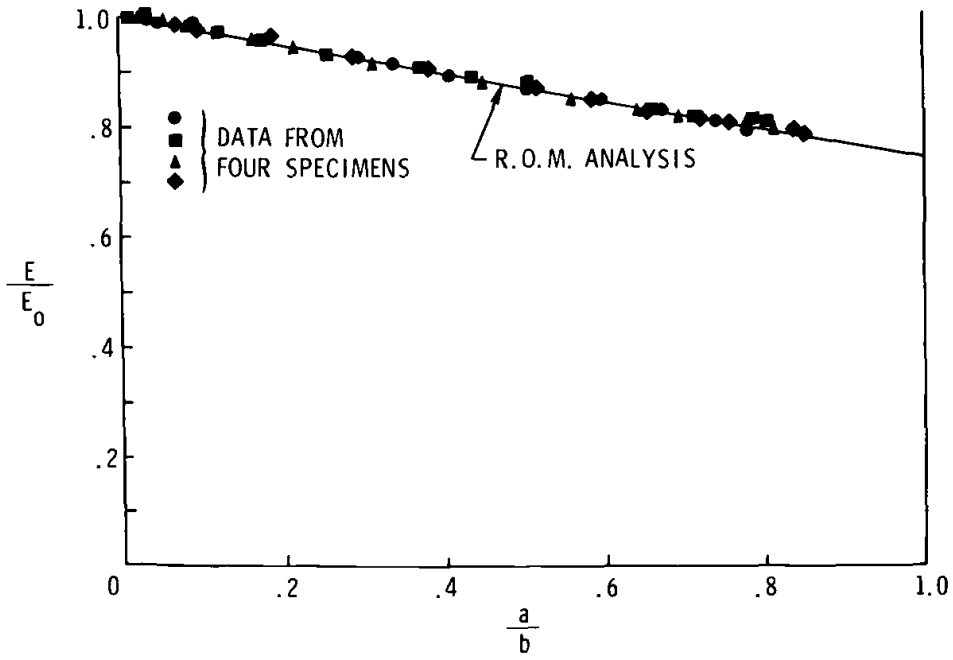

Figure 2.3. Stiffness as a function of delamination size [2]

and fatigue loading. This stiffness loss could cause premature failure of the laminate due to the inability to carry designed loads. This presents an issue with usage of highly loaded composites, such as implementation in aircraft flight control surfaces. Therefore characterization and understanding of delaminations has been broadly researched.

Delaminations are most often caused from impacts or as a defect from manufacturing. Impact damage causes delaminations as a result of the contact force causing interlaminar shearing forces within the PMC laminate. The matrix region in between lamina often has the lowest interlaminar shear strength and will fracture first when impacted. This localized shearing cause's damage and reduces the stiffness of the composite laminate at the mid-plane [3, 4]. Impacting PMCs also presents a transverse tensile load through the laminate causing intraply transverse micro-cracks and if the resulting impact force is high enough the transverse tensile loading will cause a breakout of plies on the opposite surface of the impact [5]. Therefore laboratory

manufactured delamination via impact have been widely researched to correlate the impact characteristic to composite damage size [6-12]. Impact testing has since been standardized by American Society of Testing and Materials (ASTM), in specification ASTM D7136 [11], where repeatable and accurate impacts could be used to reliably create delaminations in composite laminates for testing.

Manufacturing defects are most often found in PMC laminates due to porosity as a result of processing error. Voids may also be present within a laminate due to geometric constraints of laminate shape, such as a region where a ply termination may occur [13] or when a composite has curvature [14] as shown in Figure 2.4. When these defects are present, they coalesce during thermal or continuous physical loading of the laminate [15]. Figure 2.5 shows the evolution of microscopic defects that can turn into macroscopic delaminations and considerably reduce the use life of a PMC. Physical loading occurs when the composite laminate is subjected to operational loads, such as lift on a composite aircraft component. Thermal loading can provide residual stresses within the laminate due to the coefficient of thermal expansion during material curing and cool down [16]. In order to simulate manufacturing defects, inserts such as polytetrafluoroethylene (PTFE) or common wax paper have been utilized to simulate a delamination and corresponding air gap in composite laminates [17].

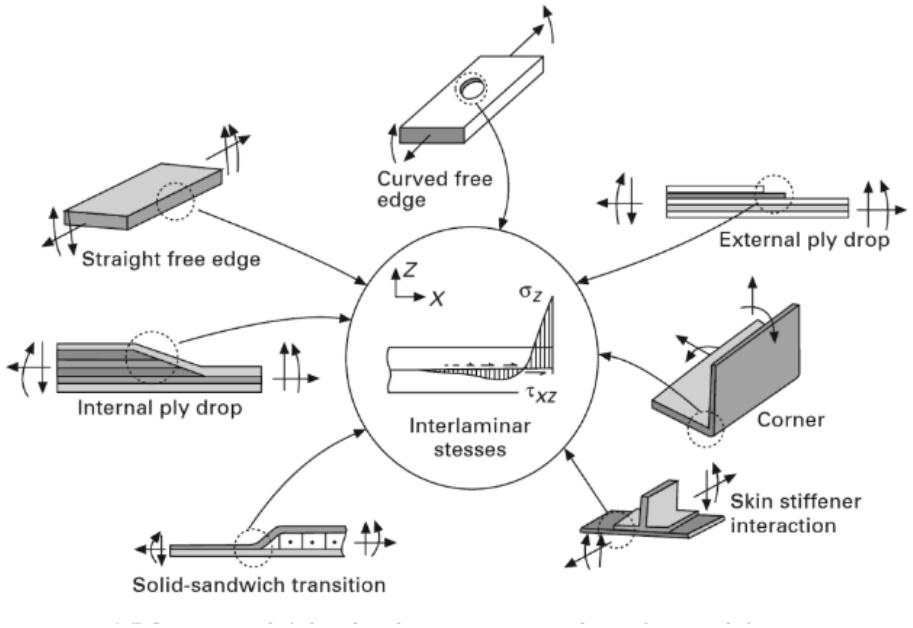

Figure 2.4. Sources of delaminations at geometric and materials discontinuities [13]

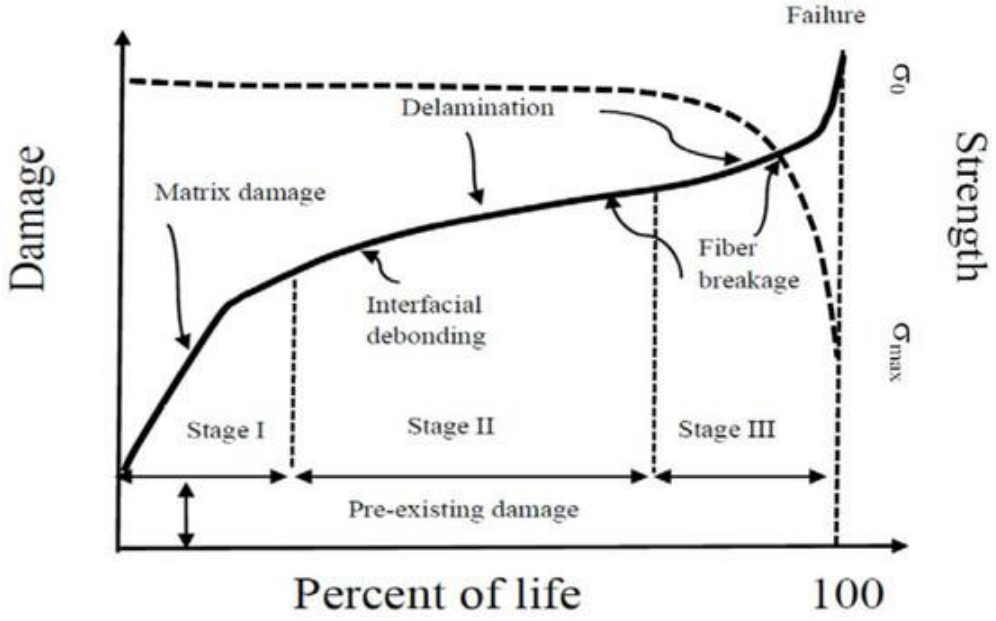

Figure 2.5. The schematic of damage development and the corresponding strength evolution under constant amplitude (CA) loadings [15]

PMC delaminations in carbon composites are typically barely visible to the naked eye and require non-destructive inspection techniques to identify location and severity of damage. The underlying delamination damage size and depth is most often characterized using ultrasonic testing (UT). UT uses a sound wave placed through the PMC material and parameters such as attenuation and speed are measured to determine the location of defects [18-20]. Delaminations within PMC materials are represented by air interfaces that transmit very little sound and provide a large reflection. UT can be completed using two primary methods: through transmission and pulse-echo. Through transmission is an inspection method where a transducer transmits a sound wave through the inspected material and a second transducer receives the sound. The second method, pulse-echo, is where a single transducer transmits an acoustic wave through the inspection material and the reflection of the sound within the material is received by the same transducer. In both cases, the acoustic wave that is received is analyzed to determine if sub-surface damage is present. In through transmission UT, lack of sound transmission or attenuation from the received sound wave is analyzed, often using reference standards to determine the area of a delamination. Pulse-echo is of particular interest to this research because that method can also use wave time of flight (TOF) to determine the depth of the damage from the inspection surface. Therefore when inspecting a PMC surface, pulse-echo can determine a delamination area by receiving a sound wave earlier than if it hit the back surface of the material as shown in Figure 2.6, where "E_P" is the full distance of the sound travelling through the thickness of the laminate and "D" is the distance to the delamination.

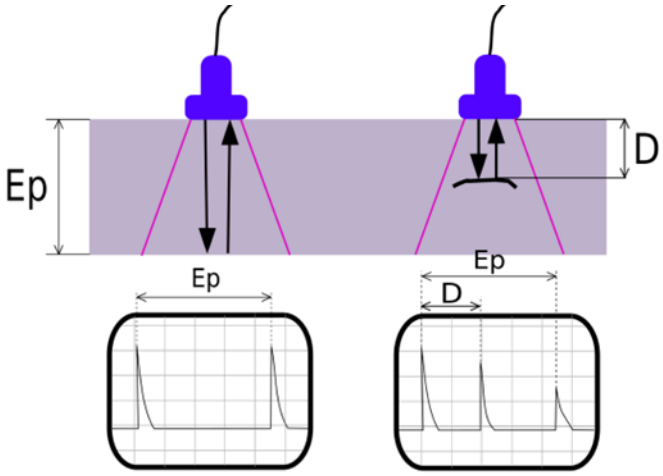

Figure 2.6. Pulse-echo ultrasonic testing and resultant waveform [19]

Although UT is the most prevalent inspection method for determining delaminations within a polymer matrix composite, the limitations of the inspection method are that only two-dimensional (2-D) representation are available of the defect that is closest to the inspection surface. Multi-level delaminations cannot be properly characterized because the portion of the delamination that is closest to the inspection surface will hide any underlying damage. However, developments have been made with X-ray computed tomography (CT), where three-dimensional (3-D) representation of a component can be achieved. X-ray CT is an inspection method taken from the medical industry [21-22], where many radiographs are taken as an object is rotated as shown in Figure 2.7.

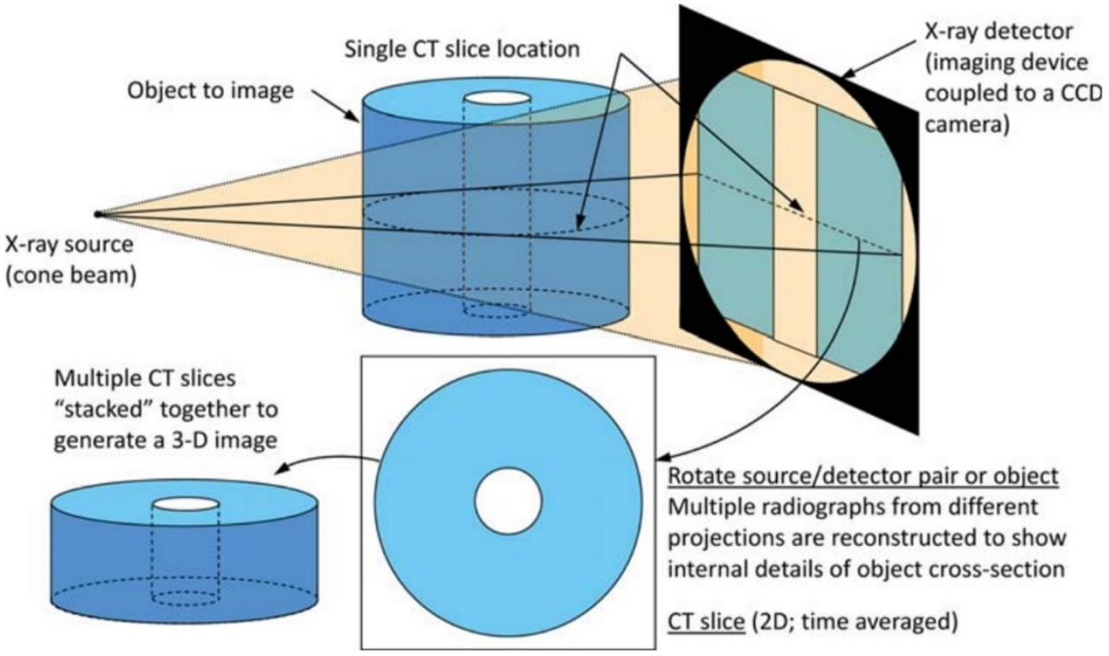

Figure 2.7. Schematic of X-ray CT imaging [21]

The X-rays are then reconstructed using software to create a 3-D representation of the inspected component. The resultant 3-D image is made up of high-definition voxels that represent material density. Recently, X-ray CT has been researched as a means to create a 3-D representation of composite delaminations as shown in Figure 2.8 [23-27], where the red coloring is the delamination closest to the surface and the green is the furthest away from the surface. Not only is a 3-D representation of the delamination damage state achievable using X-ray CT inspection, but 2-D through thickness profile and planar views can also be achieved to determine the exact depth a damage occurs. Some limitations of this inspection method are that: it is not as sensitive as ultrasonic testing where ends of defects are more clearly defined, there can be artifacts in the images as a result of X-ray processing, and post-processing of X-rays requires high computing power and takes hours and results in large data files (greater than 10 Gb). 3-D imaging of a

delamination can be utilized to determine the locations of where a laminate needs to be repaired and can assist in location of damage removal or processing locations.

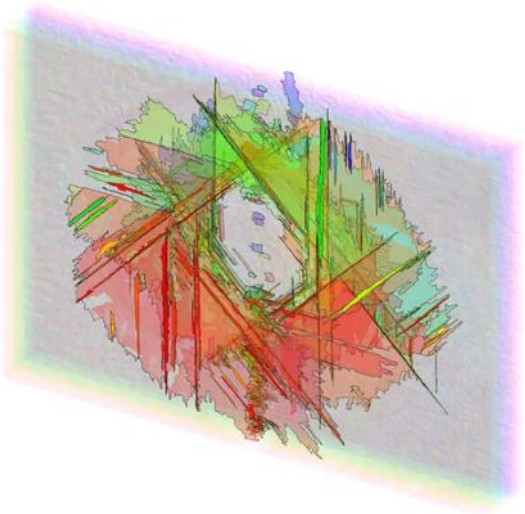

Figure 2.8. 3-D representation of composite delamination from X-ray CT inspection [27]

2.2. DELAMINATION GROWTH

In addition to characterization, it is also critically important to understand the fracture and growth mechanism associated with PMC delaminations. Linear Elastic Fracture Mechanics (LEFM) are often used to describe PMC delamination propagation. Three different fracture modes exist as shown in Figure 2.9, mode I (opening), mode II (in-plane shear), and mode III (out-of-plane shear). The critical values for each fracture mode relate to the fracture propagation within a composite laminate resulting in a delamination. Mode I fracture is where the delamination faces open away from each other, this is characterized in mechanical testing by the critical value of interlaminar fracture toughness (G_{IC}). Mode II fracture is where the two fracture faces slide over each other in the direction of the delamination growth and is characterized by the critical mode II interlaminar fracture toughness (G_{IIC}). Mode III is a fracture mode that is less common in

delaminations of composite, but it is when the fracture faces slide parallel to each other with respect to the open edge.

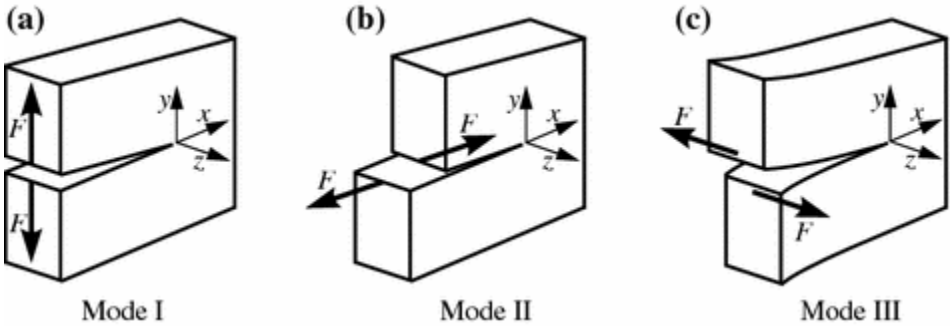

Figure 2.9. Three fracture modes

A commonly used theory for characterization of delamination growth in PMCs was the energy method. This method utilizes a version of Griffith criterion for brittle fracture, see equation (2.1), where the material's critical value of strain energy release rate (G_c) most accurately describes fracture growth, as shown by equation (2.2).

$$G(\sigma, \alpha) = G_c \tag{2.1}$$

$$G_c = G_{Ic} + G_{IIc} + G_{IIIc} \tag{2.2}$$

Furthermore, researchers have experimentally determined that G_C values correlate to the fracture mode in brittle PMCs as shown in Figure 2.10 [28].

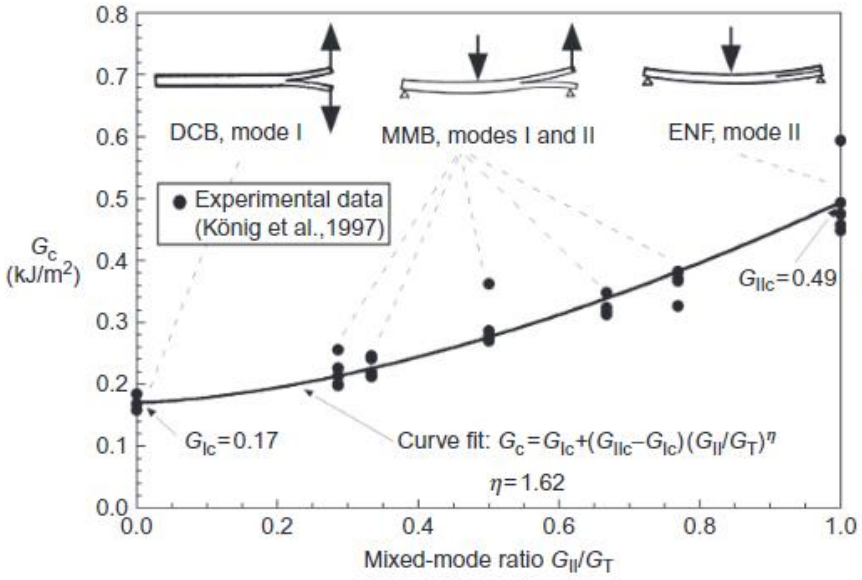

Figure 2.10. Critical strain energy release rate as a function of mixed-mode ratio for T900/914C PMC [28]

Since the adoption of the energy method using LEFM, there have been many different mixed mode fracture criteria developed to explain delamination growth. Reeder [29] was able to comprehensively compare the most accurate 2-D fracture criteria using a Power Law (see equation 2.3) and the Benzeggagh and Kenane (B-K) failure criterion (see equation 2.4).

$$\left(\frac{G_I}{G_{IC}}\right)^{\alpha} + \left(\frac{G_{II}}{G_{IIC}}\right)^{\beta} \geq 1 \tag{2.3}$$

$$G_c = G_{Ic} + (G_{IIc} - G_{Ic})\left(\frac{G_{II}}{G_T}\right)^{\eta} \tag{2.4}$$

His research found that both failure criterion was able to characterize mixed-mode fracture related to delamination fracture toughness, however both criteria were created before standardization of mode specific composite fracture testing. Three tests had since been created and standardized by

ASTM to capture pure mode I, pure mode II and mixed mode I/II fracture toughness. The Dual Cantilever Beam (DCB) test [30], was developed to provide pure mode I data by opening a pre-cracked composite coupon in transverse tension. Pure mode II data is typically generated using the End Notch Flexure (ENF) test [31] where the pre-cracked coupon is placed in 3-point bending which causes a compressive force on the loaded surface and tension on the bottom of the coupon. The compression on top of the coupon with the tension on the bottom causes a sliding mode at the mid-plane of the coupon giving a pure mode II fracture where the pre-crack is placed. The mixed-mode I and II data are generated using the mixed-mode bending (MMB) test [32]. The MMB test places the coupon in a 3-point bend at the mid-span location of the coupon along with placing the pre-cracked end into to transverse tension. This is practically a combination of the DCB and ENF coupon tests. All three tests were designed for composite materials to determine the material properties related to critical strain energy release rate, G_c, which has subsequently been correlated to the delamination fracture growth and propagation. Figure 2.11 shows schematics for the test configuration of each fracture toughness test and the corresponding coupon, where "a" is the initial crack length, "h" is the coupon thickness, "L" is the mid-span of the loading roller length, and "c" is the length between the loading roller and the load introduction coupling.

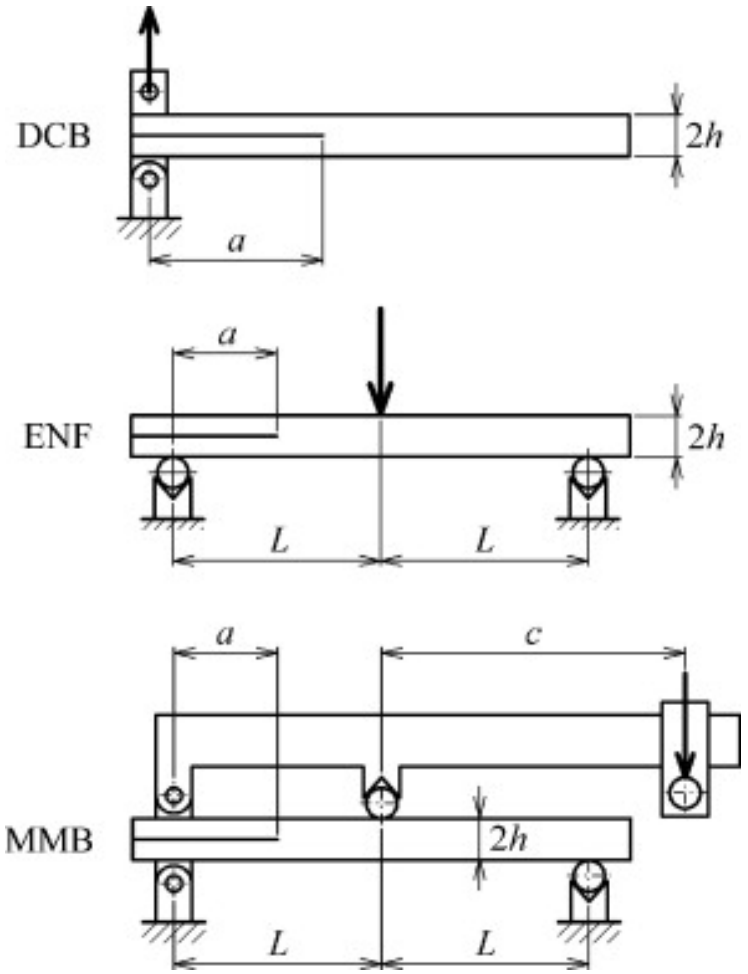

Figure 2.11. Schematic of Different Interlaminar Fracture Tests [33]

A testing has developed for capturing strain energy release rate in different composite fracture modes the data that was collected and shared was analyzed by Reeder [29] to determine the accuracy of the Power Law and B-K failure criterion. It was found that the B-K failure criterion was accurate in curve fitting mechanical test data as shown in Figure 2.10. Therefore the B-K failure criterion has been adopted by industry as a standard way to describe mixed mode I/II 2-D fracture behavior in PMC laminates [28, 34].

Delaminations often exceed the critical strain energy of the composite's matrix when sub-laminate buckling occurs due to compressive loading (see Figure 2.12). The occurrence of

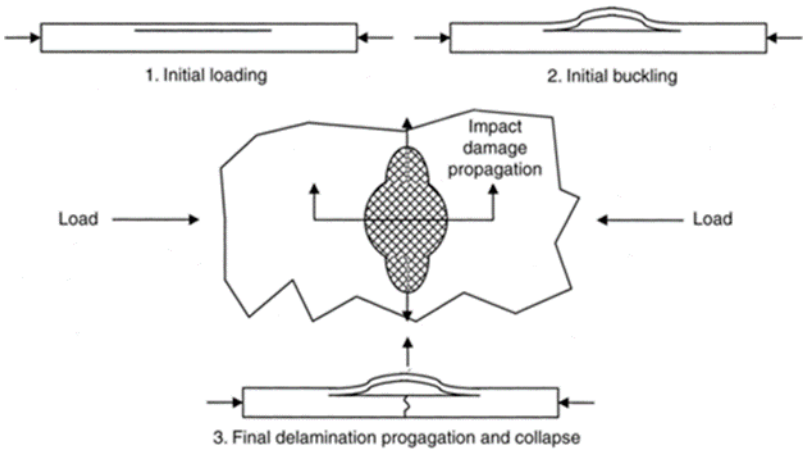

Figure 2.12. Steps of sub-laminate buckling within a composite laminate in compression [35]

sub-laminate buckling results in a mixed mode I and II fracture. When isolated, it has been found that mode I fracture in PMC laminates with pre-existing delaminations static growth critical [35-37]. Mixed mode I/II fracture within PMCs were found to grow critically under fatigue conditions [36]. Understanding the fracture mechanics of the delamination onset and growth and its relation to aircraft components is critical to ensure laboratory tests are representative of delaminations found on aircraft. Although mode I fracture is considered a critical fracture mechanism statically for PMC materials, it has been found that mode II fracture is typical for delaminations of aerospace components due to the PMC experiencing impact loading that translates to in-plane shear.

2.3. REPAIR OF DELAMINATIONS

As a result of previous research finding effective composite laminate mechanical property loss due to delaminations, in the 1980s, the U.S. Navy focused on the development of aerospace composite repairs [38, 39]. Two primary methods were developed to repair delaminations: 1.

Injection and 2. Cutout and Patch. The injection repair process incudes drilling multiple holes to the delamination depth reported by non-destructive inspection procedures (typically ultrasound) and injecting and infiltrating the delaminated composite material with low viscosity resin that is assumed to “bond” the laminate plies back together and filling the delaminated void. Figure 2.13 shows the set-up of an injection repair on a complex multi-level delamination. After injection and cure of the repair resin, the area is inspected to determine area filled and the process is repeated until the delamination is considered filled or repaired by the aircraft program [40].

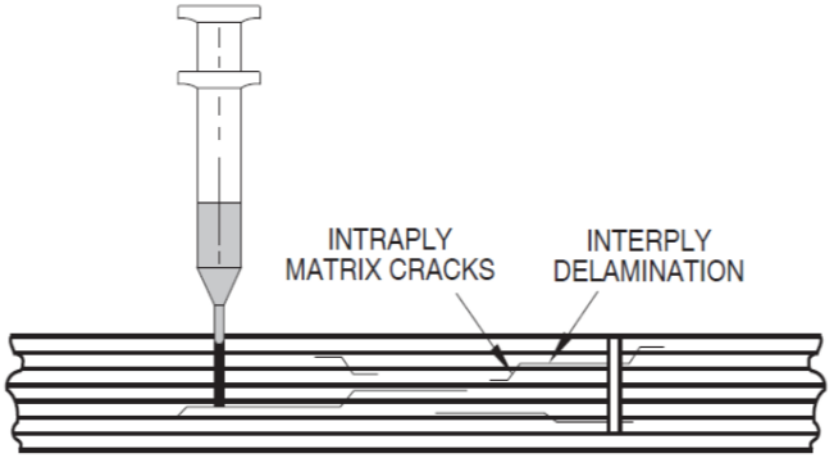

Figure 2.13. Schematic of injection repair of a delamination

The cutout and patch repair procedure includes a more invasive method where the delamination damage is removed by cutout of the damaged laminate and repaired by bonding or bolting a load carrying repair patch to the composite laminate [41]. Examples of cutout and repair can be seen in

Figure **2.14**, where the doubler repair is an externally bonded patch over the cutout area and the scarf repair is a carefully machined repair where the patch shape is manufactured to match the cutout taper and be flush with the parent material [42]. Industry recommendations are that the

delamination is approximately 50% filled and the injection holes are sealed to prevent moisture intrusion.

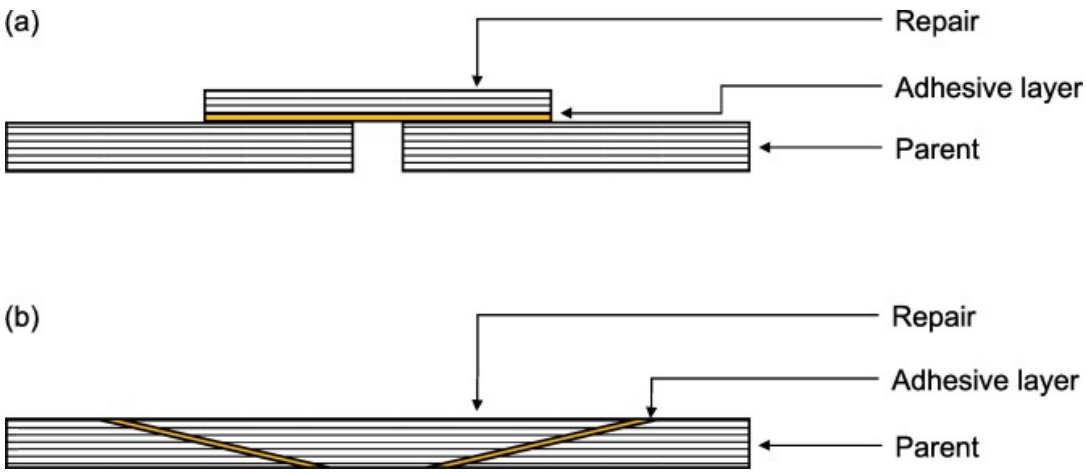

Figure 2.14. Examples of cutout and patch repairs. A. Doubler repair, B. Scarf repair [41]

Although both, the injection and cutout and patch repair methods, are routinely used for repair of composite aircraft, the injection repair is considered non-strength restoring, whereas the patch repair is considered load carrying.

However, because the injection repair method is simpler, faster, more cost effective, and less invasive than a cutout and patch repair, this repair method has been previously researched to determine if a strength restoring procedure could be developed [43-48]. One of the main constituents in injection repair is the repair resin used to inject into the delamination. Research and development of a low viscosity resin for injection repair has been heavily conducted [43-48], however the majority of the resins developed have not been commercially fielded. However Russell and Bowers conducted research that determined what characteristics of a resin were

required to successfully infiltrate an impact induced delamination that most research succeeding has utilized as a benchmark [43, 44]. The main contributing factors to the injection repair procedure were determined to be: viscosity of repair resin, pressure applied during injection, time to cure of resin, and size and permeability of the delamination. Understanding of these factors will result in an injection repair with maximum fill and potential strength restoration. Russell and Bowers found that the maximum viscosity that should be used to infiltrate up to 99% of micro cracks in an impact induced delaminations was 100 cP. It was also found that an area fills up to 90% previously achieved a strength restoration of 60-90% when correlated to compression after impact testing [40]. In conjunction to resin characteristics for injection repair, resin flow models have been developed to predict the feasibility to fill a delamination using an actively curing resin during the materials useable pot life [43, 45]. Russell and Bowers developed a 2-D resin flow model (equation 2.5) based on an idealized radial flow model for circular defects as shown in Figure 2.15, where the parameters are: t_{cure}= pot life of adhesive, P_1= injection pressure, P_2= Pressure at flow front, h= delamination thickness, R_1= radius of injection hole, R_2= radius of delamination, and η= viscosity of injection resin.

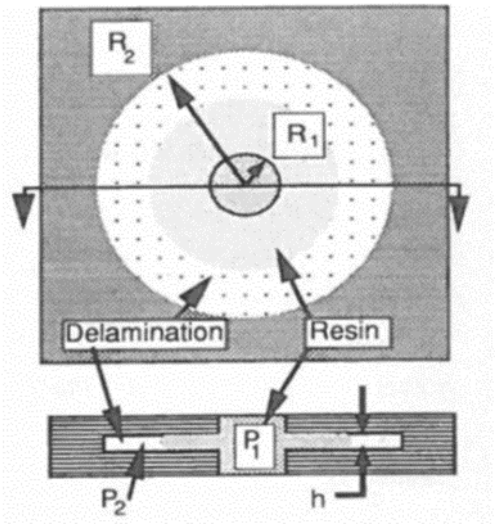

Figure 2.15. Schematic of Russell and Bowers injection repair flow model [43]

$$\int_{t_0}^{t_{cure}} \frac{1}{\eta} dt \geq \frac{3}{P_1 - P_2 h^2} \left[R_2^2 \left(2 \ln \left(\frac{R_2}{R_1} \right) - 1 \right) + R_1^2 \right] \tag{2.5}$$

Hautier [45] also developed a resin flow model for injection repair primarily based upon Darcy's law, equation (2.6). Where; L=delamination length and K= permeability constant. These flow models were used to ensure that the material does not reach a state of cure where the material is too viscous to infiltrate the delamination.

$$t = \int_0^L \frac{2\eta x}{K(x)\Delta P} dx \tag{2.6}$$

In addition to determination of resin flow characteristics, injection and drilling procedures have also been researched to determine optimized parameters for resin flow [46, 48]. Seneviratne, et al. [48], found that drilling parameters including: plunge speed, bit rotational speed, hole location,

and drill bit type all affected the ability to complete a successful injection repair. Additional procedural developments were that usage of vacuum assisted injection yielded superior infiltration with the prototype resin used in their study. Although materials and processes have been researched to determine key resin, injection, and drilling characteristics, this repair methodology is still considered non-strength restoring due to an unknown in-service contamination state within the delamination. Contaminants within the delamination such as in-service fluid ingression have previously been identified as reasons not to consider resin injection repair as strength restoring until these contaminants can be characterized and removed prior to repair.

2.4. PMC SURFACE CONTAMINATION AND PREPARATION

In order to have a successful injection repair, bond strength of the repair resin adhering to the existing parent laminate must be optimized. However, when aircraft are exposed to in-service environments, delamination internal surfaces can potentially be contaminated. Previous research has found that surface contaminants affect composite bond durability and integrity [49-51]. The contaminants of interest have been standardized for the aerospace industry, within Aerospace Material Specification, AMS7201 [52]. Oakley et al [50], found that the most common contaminants around aircraft can be broken down into archetype compounds that have an associated chemical class. The chemical classes that were investigated include: triglycerides, fatty acids, long chain esters, alcohol, surfactants, non-polar hydrocarbons, water soluble polymers, and inorganics. Of these chemical classes; non-polar hydrocarbons and inorganics are of particular interest due to their correlation to aircraft fluids and silicone-based manufacturing contaminants, respectively.

Removal of contaminants using surface cleaning or pre-treatment processes have been researched previously for PMCs [53-58]. Wingfield [53] surveyed nine different surface pre-treatment processes and found that removal of silicone and fluorocarbon contaminants to be of most importance. Hernandez et al. [55], found that cleaning procedures using solvents alone was not sufficient for structural adhesive bonding, whereas a combination of solvent wipe, sanding, then solvent wiping again yielded a superior bonding surface and partially recovered load carrying capacity. Fang et al. [54] found that atmospheric plasma and laser surface treatment techniques were adequate, but needed more development to be optimized for cleaning composite surfaces of aerospace contaminants. Although the previous research was primarily on flat plate contaminated surfaces, two primary surface preparation techniques that could be applied to internal surfaces of delaminations were found to be atmospheric plasma treatment or solvent cleaning.

Atmospheric plasma cleaning is of particular interest because it has the potential to clean internal surfaces of delaminations. Atmospheric plasma cleans PMC surfaces by incorporating oxidized functional groups (oxidation) that will either volatilize or provide chain scission of the surface contaminant [59-64]. An example of surface cleaning of contaminants and surface activation using atmospheric plasma is shown in Figure 2.16. This schematic shows that the atmospheric plasma cleans the surface using oxygen radicals from the plasma (1) and the resulting surface has active functional groups (2) to increase the quality of the adhesive bond (3).

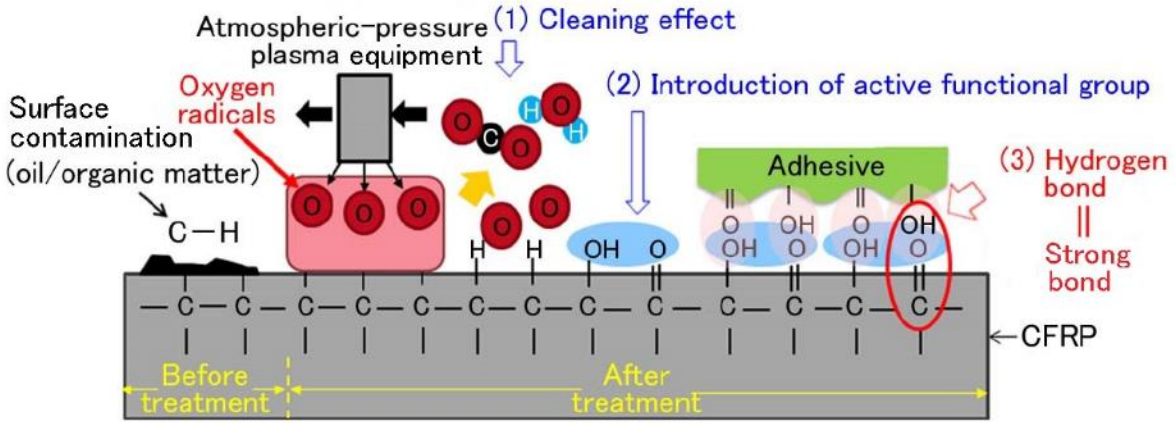

Figure 2.16. Schematic of atmospheric plasma treatment of composite surface [62]

Hydrocarbon, silicone and fluorocarbon contamination have been found to be cleaned using atmospheric plasma. Plasma cleaning breaks down contaminants into non-contaminating functional groups [60]. Dighton, et al [61], found that atmospheric plasma treatment can also break down silicone contamination into silica that is non-contaminating version of inorganic product that can exist on bonded surfaces. Roberts, et al [63] saw that atmospheric plasma would oxidize hydrocarbons into volatile species when treated with an oxygen rich plasma. The chemical reaction of the hydrocarbon to the plasma is shown in Figure 2.17.

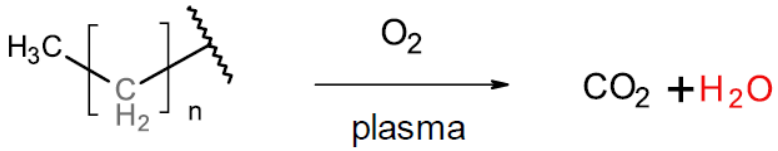

Figure 2.17. Oxidation of hydrocarbon by oxygen plasma [63]

In addition to cleaning contaminants from the PMC surfaces, atmospheric plasma can also provide a surface preparation. Atmospheric plasma accomplishes surface preparation by increasing

carbonyl groups on PMC surfaces [62]. Volatilization of the surface increases surface activation energy by also increasing the hydroxyl groups that can increase PMC bond strength to structural adhesives [65]. The ability to break down contaminants and increase surface activation energy is key to providing a clean and activated surface for polymer bonding. In order to determine if surfaces are clean and activated, two primary methods of inspection are utilized: 1. Contact Angle Goniometry and 2. Spectrometry.

Contact angle goniometry is a measurement technique that utilizes the Young-Dupré equation (2.7), where the equilibrium contact angle (θ_c) is defined as the angle between the liquid-gas interfacial energy (γ_{LG}) and the surface tension (γ_{SL}) as seen in Figure 2.18.

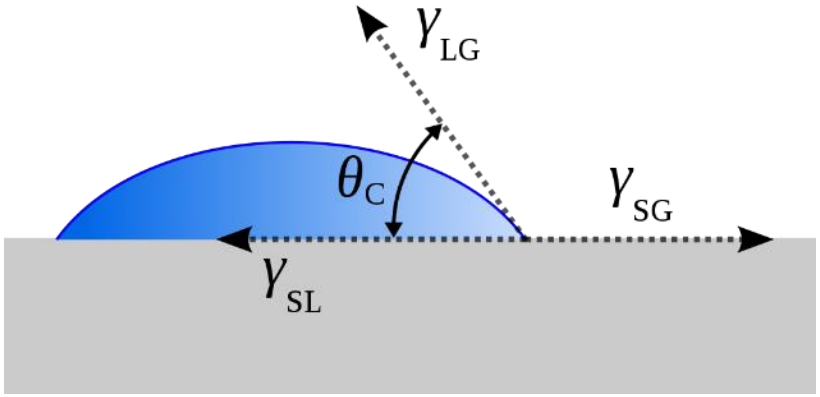

Figure 2.18. Schematic for Young-Dupré equation

$$W_{SL} = \gamma_{SL}(cos\,\theta_C + 1) \tag{2.7}$$

The work of adhesion (W_{SL}) of contaminated surfaces is typically lower for contaminated surfaces that are hydrophobic and increased for cleaned or activated surfaces. It has been researched that

water contact angle can be used to compare contaminated and cleaned/activated surfaces [60, 63]. Typically water contact angle is relative between a known clean versus a known contaminated surface, therefore standards or methods are required to complete a thorough analysis through water contact angle measurements. Also, water contact angle can only be applied to exposed surfaces where the water droplet can not be applied and measured.

Spectrometry is a generic term for the science of which spectra is produced when material interacts with or emits electromagnetic radiation. For surface chemistry investigations, multiple forms of spectrometry are available, however the two most commonly used are Fourier Transform infrared (FTIR) spectrometry and mass spectrometry. FTIR has been routinely used in studies to find organic compound contamination [63] and specifically finding them on PMC materials [53-56, 60-63, and 65-66]. FTIR consists of infrared (IR) radiation being passed onto or through a sample and the radiation is collected by a detector and then a Fourier Transform is applied to the IR signal creating a spectrum. Each of the peaks in the spectrum are representative of vibrations of molecules in the material that is being subjected to the IR radiation. An example of the molecular structure correlated to the FTIR spectrum is shown in Figure 2.19 [67].

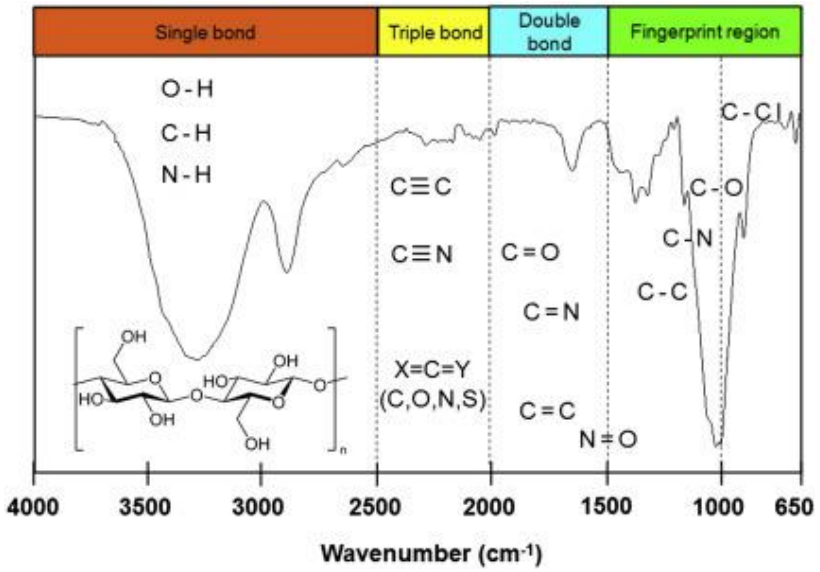

Figure 2.19. Example FTIR spectrum of cellulose with corresponding types of bonds [67]

Two primary collection techniques are used to determine if contamination is present on PMCs. This includes: Attenuated Total Reflectance (FTIR-ATR) and Diffuse Reflectance (DRIFTS). The two different techniques gather the molecular surface data differently as shown in Figure 2.20.

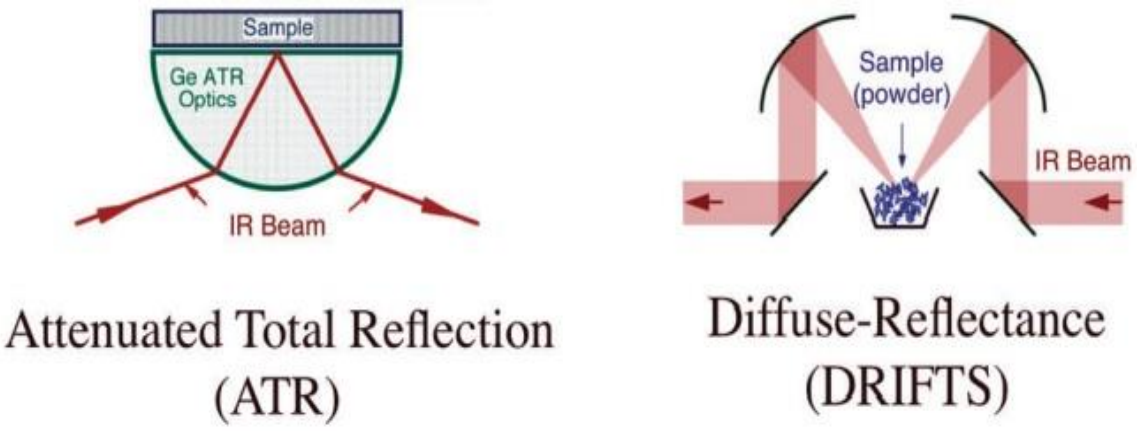

Figure 2.20. Type of FTIR collection methods [68]

FTIR-ATR utilizes a crystal where it is in contact with the sample and the IR signal travels through the crystal onto the sample surface and is reflected back through the crystal to the detector. This sampling technique is the most commonly used FTIR sampling method; however it is difficult to perform on rough or sanded composite surfaces. DRIFTS is where the IR beam is applied to the material surface through the air and the reflected light is collected by the detector, however only the light not directly reflected by the material is analyzed. This method is less precise than FTIR-ATR, however it is useful for in-situ IR analysis [68]. In Figure 2.21 and Figure 2.22 are examples of hydraulic fluid spectra being collected on PMCs by both DRIFTS and FTIR-ATR, respectively.

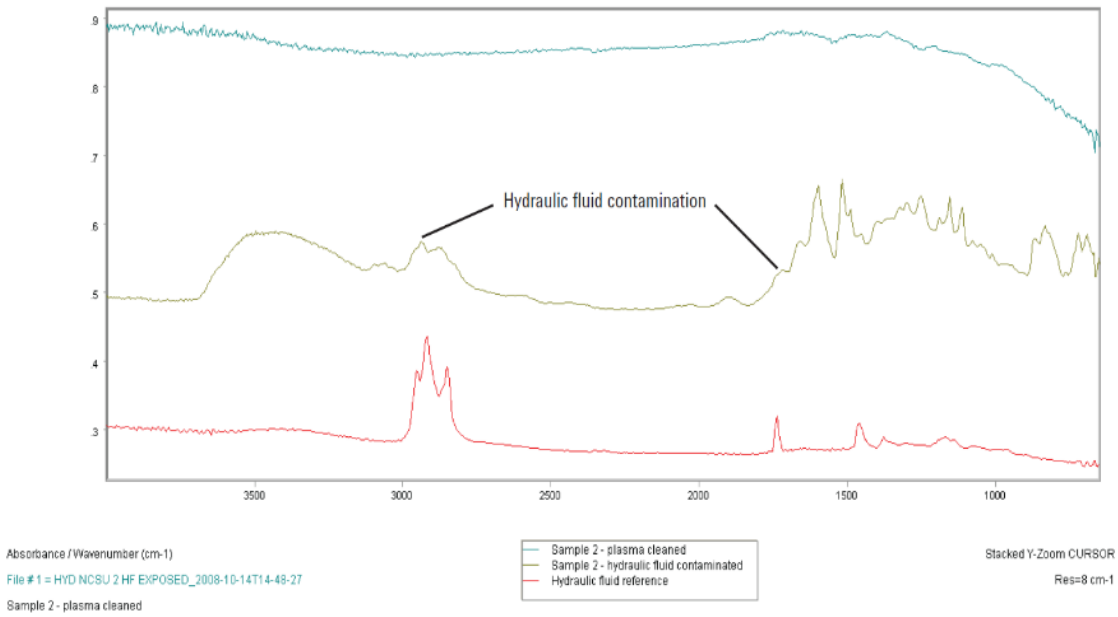

Figure 2.21. DRIFTS spectra of a cleaned and hydraulic fluid contaminated PMC [68]

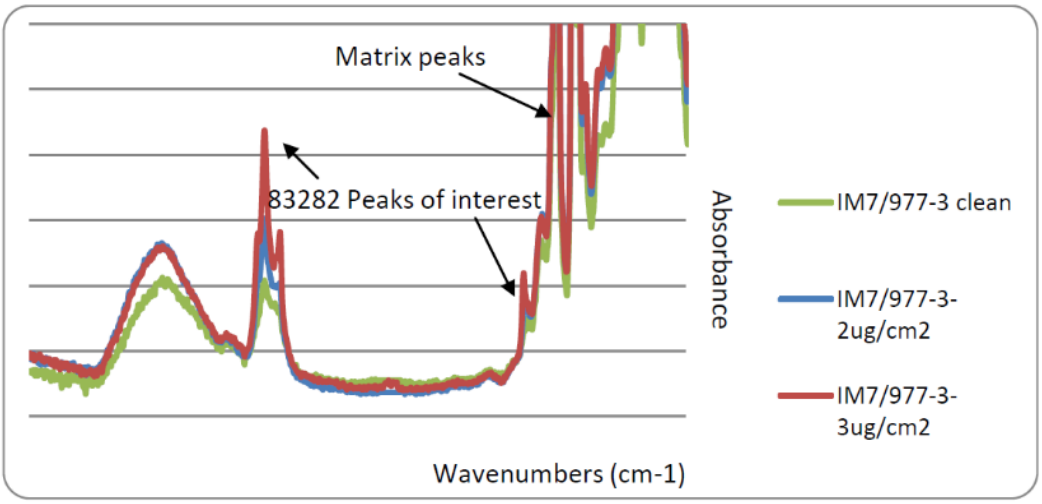

Figure 2.22. FTIR-ATR spectra of a cleaned and hydraulic fluid contaminated PMC [62]

In addition to FTIR spectrometry, mass spectrometry is another technique that has been used to determine if trace contaminants are on a material's surface [69, 70]. Mass spectrometry is a technique where a small sample is ionized, there are multiple ionizer options, and the ions are then sorted and separated by their mass and charge [70, 71]. The detector will determine the separated ions that are measured in mass/charge ratio and relative abundance and then displayed in a mass spectrum. Because mass spectrometry has been utilized since the early 1920's, the National Institute of Standard and Technology (NIST) has developed a very robust mass spectrum library that is available to the public and is routinely used to identify molecular compounds [72]. An example of a mass spectra of toluene is shown in Figure 2.23.

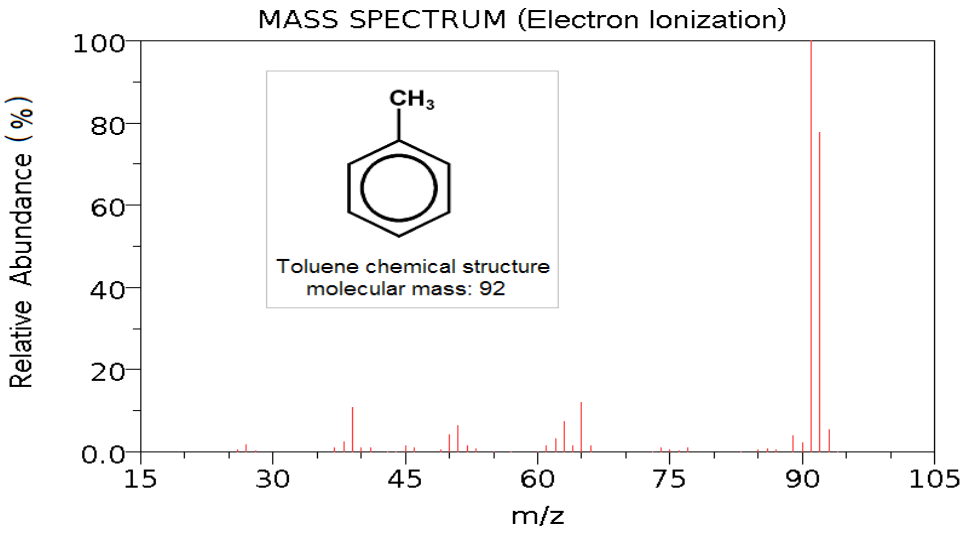

Figure 2.23. NIST defined mass spectrum of toluene [72]

Gas Chromatography is a very popular molecular separation technique that is performed in series with mass spectrometry to help with separating compounds prior to ionization, this type of instrumentation is call a gas chromatograph mass spectrometer (GC-MS). A schematic of a GC-MS is shown in Figure 2.24.

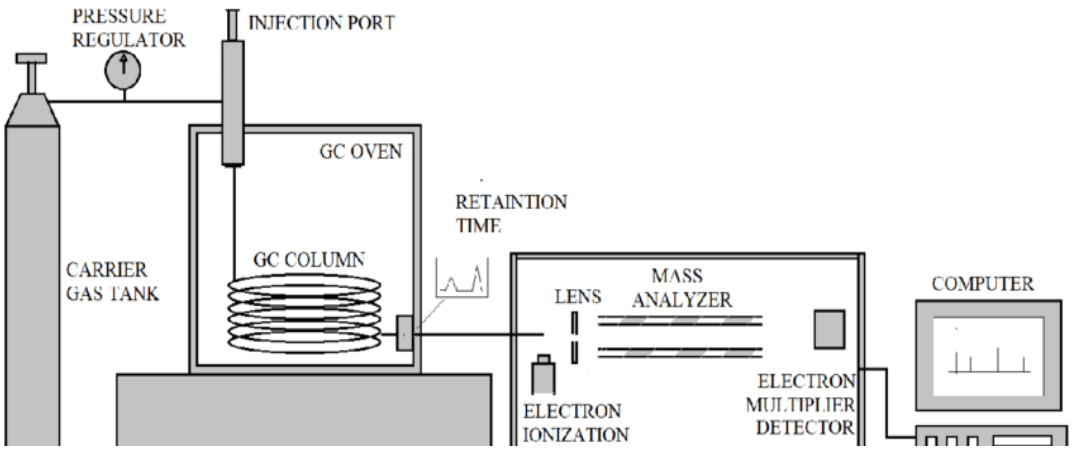

Figure 2.24. Schematic of GC-MS equipment [73]

The GC-MS works by taking a sample, such as a solvent carrying contaminants, and placing it into a vial, then an auto sampler will take a 1µL sample from the vial and inject it into a pressurized gas chromatogram capillary column that is temperature regulated in an oven. The heat from the oven will break down the sample in to molecular structures and the sample will elute the column at different retention times of which a detector will collect data and a chromatogram can be constructed. An example of a chromatogram is shown in Figure 2.25. The abundance is plotted versus the retention time for the sample collected.

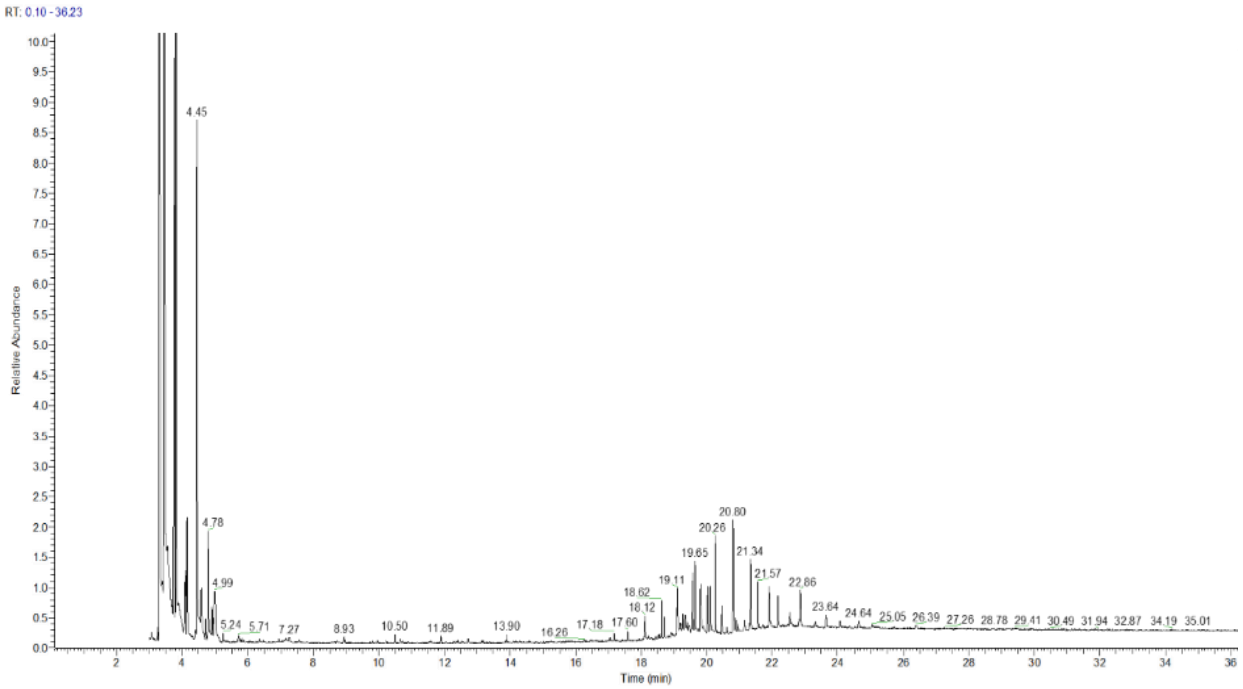

Figure 2.25. Example chromatogram of a PMC surface

The retention time peaks from the chromatogram can be compared to known compound retention times to identify molecules. Unknown molecular species, such as a mixture of contaminants on a composite surface, cannot be identified with gas chromatography alone. Therefore in a GC-MS

once the samples pass through the chromatogram it is transferred to the mass spectrometer, where the material is ionized and data is collected by the mass spectrometer detector. This robust process can be used to accurately identify surface contaminant species because two methods used synchronously are supplying information about the molecular structure. Both gas chromatograms and mass spectra have robust and large libraries maintain by NIST that can be used to identify molecular compounds. One drawback from this technique is that it is often performed as a post process inspection. Typically a wipe of any surface is analyzed by GC-MS before or after any surface preparation processes have been completed.

In order to provide real-time spectroscopic information during a process, the Quantitative Gas Analyzer (QGA) was developed by Hiden Analytical [74]. The QGA is a simplified mass spectrometer that was developed to perform gas and vapor analysis with a response time of 300 milliseconds. The QGA has a probe that collects vapor at atmospheric conditions and inputs the samples into a mass spectrometer. The probe line is heated to help with molecular separation prior to the vapor sample going to the ionizer. The QGA has two different detectors, an electron multiplier and a dual Faraday cup. The two different detectors allow the user to either target speed of analysis with the electron multiplier or target quality of analysis with the Faraday cup depending on the concentration of molecular species needing to be detected. The QGA can be used for in process monitoring of levels of specific target contaminants. This would be beneficial to ensure that surface preparation is processed properly by analyzing any vapor by product concentrations over time.

In summary, the literature review conducted found that delamination damage is caused by impact or pre-existing defects and growth mechanisms are classically defined using LEFM. It was also found a multitude of materials and processing variables are defined for practical inspection

and repair of delaminations. Topics that were not covered in this literature review are the effects of: laminate thickness, lay-up configuration, surface morphology, and comparison of unidirectional to woven PMC repair. This literature review provided a deep understanding of PMC delaminations damage and growth mechanism, current testing methods related to delamination growth, inspection and chemical analysis methods for defining delaminations and surface chemistry, and materials and processing requirements for repairing delaminations. Although multiple studies have been completed to define restoration of strength back into delaminated PMC laminates using injection repair, none have quantitatively defined processing parameters that could clean and prepare the delamination prior to injection with a structural repair resin. Therefore the research presented in this dissertation aims to provide novel methods for repair, quantitative characterization, and testing of delaminated PMCs with the main goal of strength restoration to the laminate.

2.5. KEY TECHNICAL CHALLENGES AND PROJECT ROADMAP

In order to successfully create an new injection repair procedure that could be used for repair of aerospace components, some primary ket technical objectives need to be be addressed by this study. In Figure 2.26 are the key technical challenges that must be addressed by scientific and engineering investigation to ensure the novel repair procedure is successful and encompassing to ensure strength restoration is achieved.

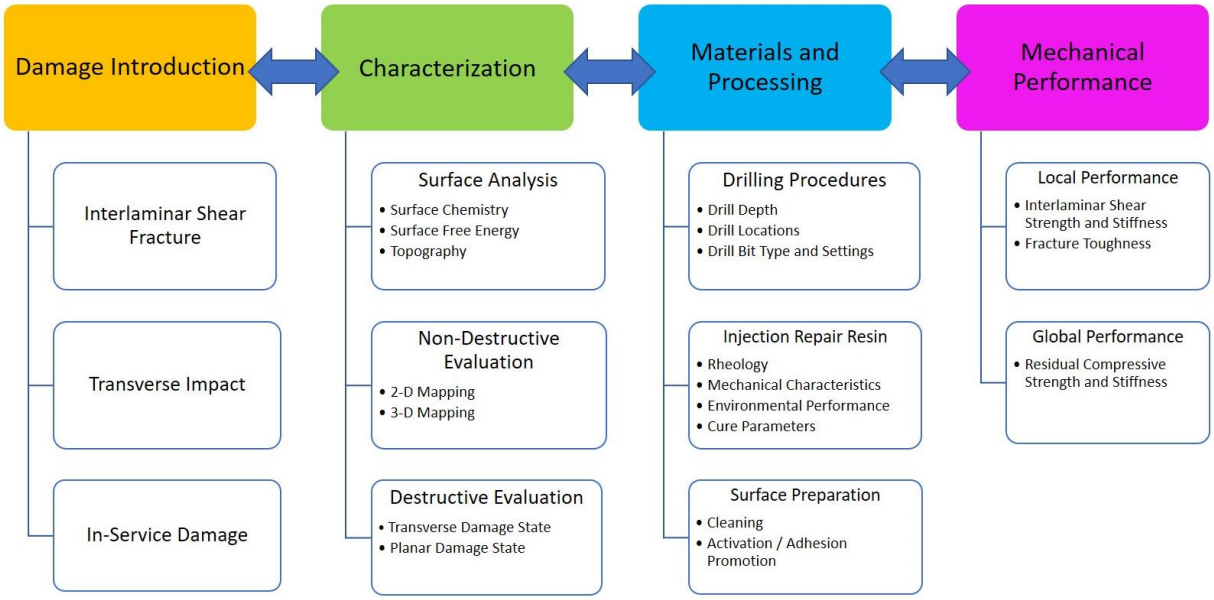

Figure 2.26. Delamination injection repair key technical challenge roadmap

The key technical challenges are segmented into four different topic areas: 1. Damage Introduction, 2. Characterization, 3. Materials and Processing, and 4. Mechanical Performance. These key technical challenges have arrows at the headers to show that the challenges must not only be addressed, but a feedback loop must be considered to ensure a robust solution is found.

Damage introduction is the first key technical challenge because understanding fracture mechanisms and characteristics of how damage is introduced into an aircraft component PMC laminates is important, but not thoroughly defined. However, also understanding the correlation between laboratory induced fractures to actual in-service damage is of importance to ensure laboratory testing accuracy. In addition, understanding the difference in resultant damage when comparing less complex 1-3 ply interlaminar shear fracture to highly complex multi-layer (greater than 3 plies) shear fracture induced by transverse impacts must also be considered, as not all damage to aircraft components are severe impacts (See Figure 2.27). Damage introduction also correlates with characterization because understanding the damage morphology along with the

chemical characteristics of a damaged surface is important to understand how to successfully repair a delamination.

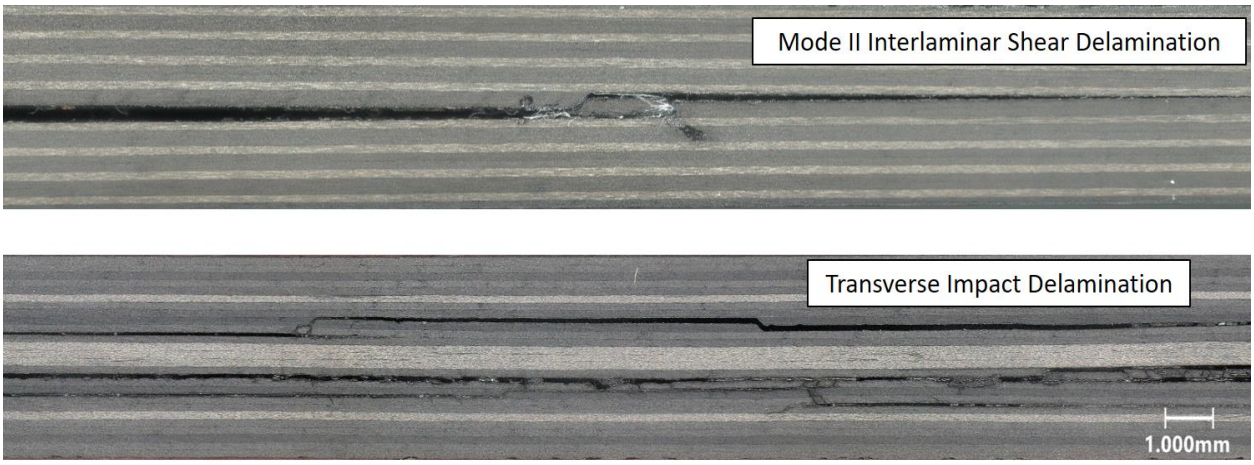

Figure 2.27. Examples of laboratory manufactured delaminations

Damage characterization is the second key technical challenge on the roadmap to developing a novel injection repair process. Understanding the extent and formation of the damage due to different damage initiation methods is important to correlate to laboratory fabricated delaminations to in-service damage. This can be done by non-destructive evaluation methods that provide 2-D or 3-D damage mapping through ultrasonic testing or X-ray computed tomography imaging. These methods could also be utilized to determine post-repair percent fill and effectivity of injection repair on delaminations. In addition, verifying non-destructive mapping with destructive characterization of transverse damage states through methods such as photo-microscopy can verify delamination damage structure. Furthermore, planar fractures surface comparison through destructive evaluation will reveal topographical similarities and differences through advanced metrology. In addition, surface chemistry evaluation methods such as

spectrometric evaluation for contaminants or measurement of surface free energy of delamination surfaces could be performed to determine cleanliness of surfaces or effectivity of surface preparation procedures. Injection repair materials and processes are tied to characterization because inspection of both, internal surface cleanliness and resin fill percentage must be quantitatively defined to identify a successful repair.

Materials and processing parameters are also a key challenge due to minimal research previously conducted for injection repairs. Procedures such as hole location and drill depth along with drill bit choice have been investigated minimally due to the current cosmetic classification of the repair. Hole location and drill depth must be investigated to determine optimal locations to fill complex damages. However, less emphasis on injection drill hole processing is required for less complex damages. Another key parameter for materials and processing is injection repair resin system choice or modification to meet infiltration and strength requirements. Factors such as viscosity, shear strength, cure cycle requirements, and environmental effects must be considered to determine if an injection repair resin meets aerospace requirements for structural composite repair. One particular novel area of interest is the potential of surface cleaning preparation of the internal surfaces of a delamination. This challenge area has been investigated minimally and has not been utilized for repair of aerospace structures. In order to determine if structural properties were returned to the delaminations by novel materials and processes, ultimately the mechanical performance of the repaired delamination configuration must be tested.

Finally, the mechanical performance of an injection repaired delamination must be determined by testing for restoration of mechanical properties. Local performance characterizing the effect of the novel repair on properties related to interlaminar shear fracture must be considered. The mechanical quantification of fracture related properties focuses on restoration of interlaminar

fracture toughness in a repaired laminate. This restoration of toughness can be correlated to the laminate's ability to withstand impact damage and flight loads. Further global quantification of strength restoration, specifically compressive strength, is also required to verify a novel injection repair procedure. However, current industry methods for testing repaired compressive strength are limited to impact damaged coupons and limited to complex delaminations. Performing mechanical assessment is the precipice requirement to correlate the effect of the novel injection repair process to restoration of mechanical properties into a composite aircraft component.

This study aims to complete testing and analysis to address all of the key engineering challenges shown in Figure 2.26. Although this study will address the different methods of damage introduction, damage characterization, and materials and process development, the objective of will ultimately provide a quantitative solution for restoring mode II fracture toughness by injection repair of interlaminar shear induced fractures. In addition, initial follow on work addressing drilling procedure development and global mechanical test assessment of complex impact induced delaminations will be addressed.

CHAPTER 3: EXPERIMENTAL TEST SET-UP

Three different prime contributions were completed as a result of experimentation: 1. Damage introduction 2. Damage characterization, 3. Repair materials and process development.

Damage introduction was completed by two techniques: 1. Mode II fracture via end notch flexure testing and 2. Impact Testing. In order to comprehensively define delamination damage and develop novel repair procedures, a modified ENF coupon was developed that would be used to represent delaminations. This includes three different lay-up configurations; unidirectional, quasi-isotropic, and cross-ply. The ENF coupon represents a mode II fracture surface that could be repaired. Mode II produces fracture surfaces representative of delamination induced by transverse impact to laminates. These coupon configurations will be used as the work-horse for both damage characterization and materials and process development. Impact testing was also utilized as a form of laboratory manufactured delaminations. This was completed to further define the damage state from interlaminar shear as a result of low-energy (less than 20J) transverse impact. Impact testing was a previously studied method of manufacturing delamination damage. Pre-existing delaminations were excised from previously in-service aircraft components. The components were donated by the U.S. Navy to assist with this research.

Damage characterization was completed to further define the existing damage state of delaminations excised from previously in-service aircraft components and compare to laboratory manufactured damage. The damages were characterized using non-destructive inspection, destructive inspection, and chemical analysis methods. Non-destructive inspection was primarily completed using ultrasonic pulse-echo testing and X-ray CT was also used to determine if the delamination damage could be characterized in 3-D using commercial off-the-shelf software. Destructive inspection included excising damage from the delamination samples and performing

optical and metrological analysis on the fracture surfaces. Surface metrology was compared for laboratory and in-service delaminations. Chemical analysis was also performed on the surfaces to determine if any contaminates were found on the in-service fracture samples surfaces. This includes performing molecular analysis of the surfaces using GC-MS.

Repair materials and process development required multiple types of experiments in order create a novel injection repair procedure. First step, was developing the modified ENF coupon to be repairable, so that it could be injection repaired and then re-tested and compared to undamaged laminate test results. Then a contamination method for internal surfaces of delaminations was developed using known aerospace contaminates. This was first completed using the exterior surface of a flat composite plate to determine the suitable contaminant solution. Then a novel injection approach was created to contaminate the internal surfaces of the modified ENF coupon which was verified using florescence dye and water contact angle (WCA) goniometry to identify contamination coverage. Surface preparation experiments were also conducted in a similar manner, where the removal of contaminants from a composite flat plate exterior surface was first used to determine contamination removal procedures, then the same procedures were completed on the internal surfaces of the modified ENF coupons. In order to verify removal of contaminant from the internal surfaces of the modified ENF coupon, QGA, WCA, and FTIR-ATR were utilized to determine if the surface was in fact cleaned. QGA readings were also developed on a flat plate and then used on the enclosed ENF coupon to verify removal of specific mass species correlated to hydrocarbon contaminant molecular structures. WCA and FTIR-ATR were used as a verification method where the coupons were filleted open and the internal surfaces of the ENF coupon were locally analyzed for remaining contaminants and to verify if the surface was cleaned.

In conjunction with performing injection cleaning and repair procedures of the PMC laminate, a finite element analysis was also conducted to ensure that the resulting injection pressures would not progress the delamination. This was a parametric analysis completed for multiple delamination sizes and depths to understand the behavior of the laminate, so that resulting process development would be beneficial for repair of multiple configurations of enclosed delaminations.

In addition to development of an internal cleaning and surface preparation process for the delaminations, modification of the injection resin was also completed via experimentation. Hysol's EA9396 epoxy resin was identified as the primary resin used for injection repairs within industry. However the viscosity of the neat resin was 3600 cPs, which was determined to be too high to successfully infiltrate the delamination using current injection repair methods. Therefore resin modification and cure parameter experiments were conducted to determine how lowering the viscosity of the resin with diluents and the resulting cure cycle would affect the mechanical performance of the cured resin. Single lap shear and viscosity testing, in addition to cure parameter testing using Barcol hardness were completed.

To determine local laminate level mechanical property restoration, the developed internal surface preparation and modified injection repair resin were applied to a previously fractured ENF coupon and cured. This repaired version of the modified ENF coupon was then tested in the same manner as the baseline laminate coupons to determine if mode II fracture toughness was restored to the laminate. Once tested, the coupons were carefully cut apart so that the fracture surface were exposed and analyzed using advanced digital microscopy and the scanning electron microscope (SEM) at high magnification (>1000x).

Although the majority of the experimentation was completed on the modified ENF delamination coupon configuration, some work was completed on the more complex impact damage coupons. Drill hole location experiments were completed to determine drill hole patterns that were beneficial for injection repair and verified using a gas leak test. Also, preliminary compression after impact mechanical testing was completed to determine the global mechanical effects that the delamination has on the PMC laminate. Although preliminary testing was completed on repair of the impact specimens, further work to develop the repair procedures for complex delaminations would be required.

3.1. SPECIMEN DESIGN AND DAMAGE INITIATION

Modified ENF coupon and impact testing coupons were designed to ensure that multiple laminate configurations were examined during this study. Damage initiation was completed using different methods to ensure that different degrees of composite delamination damage were captured. Delaminations were also collected from previously in-service aircraft components.

3.1.1. **Modified End Notch Flexure (ENF) Testing**

PMC Coupon Testing

Modified ENF coupons were utilized for two different delamination production methods: 1. PTFE Insert and 2. Mode II fracture. Panels were fabricated using three different 24-ply lay-up configurations as shown in Table 3.1.

Table 3.1. ENF test panel configurations

Panel Type	Layup; Pre-Crack is PTFE Insert Located Adjacent to Central Ply
Unidirectional	$[0]_{24}$
Quasi-Isotropic	$[-45/0/45/45/0/-45/45/0/-45/-45/0/45]_S$
Cross-Ply	$[0/90/0/90/0/90/0/90/0/90/0/90]_S$

The average thickness of each panel was 3.2 mm. The unidirectional panel type is consistent with the ASTM D7905 [31] coupon configuration which results in a 0º/0º ply interface at the mid-plane. Robinson [75] previously demonstrated successful usage of a quasi-isotropic laminate with a 45º/45º mid-plane ply interface for dual cantilever beam testing. The quasi-isotropic coupon configuration was also utilized for ENF testing in this project. The cross-ply lay-up created a 90º /90º ply interface at the mid-plane. A 127 mm wide layer of PTFE coated woven fiberglass release film, Airtech's Release Ease 234TFNP, was placed at the mid-plane of the laminate to serve as a crack starter for ENF testing. ENF test specimens were cut from the larger panels into 228.6 mm long x 50.8 mm coupons using a wet diamond blade tile saw. Each specimen had a 63.5 mm release film crack starter at one end. The delamination production region is behind the PTFE insert where the crack propagation occurred as shown in Figure 3.1.

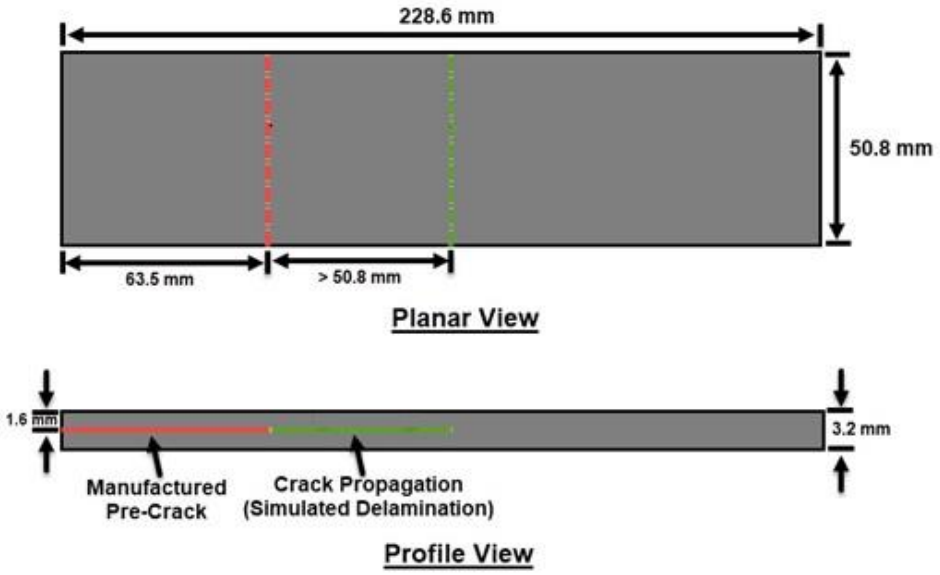

Figure 3.1. Modified ENF coupon configuration

ENF testing was conducted following the ASTM D7095 specification. However, because delaminations of 50.8mm or larger were of particular interest in this study, slight modifications were introduced to increase the fractured surface to simulate a large delaminated area. The modifications include changing the width of the specimens to be nominally 50.8 mm (from 25.4 mm in the ASTM specification). Additionally, the specimens were tested 1 to 3 times each in order to propagate the crack length to be a minimum of 50.8 mm. A schematic of the testing fixture can be seen in Figure 3.2.

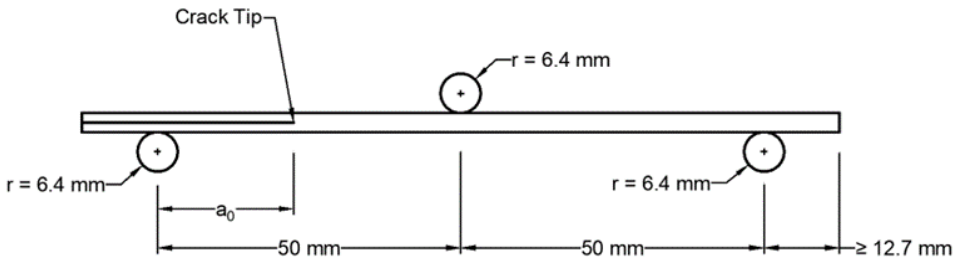

Figure 3.2. ENF test fixture schematic

The cylindrical loading surface and supporting surfaces each had a radius of 6.4 mm. The distance from loading surface to support surface was 50 mm. The distance from the left side supporting surface to the crack tip mark (a_0) was 30 mm when propagating the crack. However, a_0 was also varied to 20 mm and 40 mm in order to acquire compliance information for both the non-precracked and precracked tests. The coupons were loaded to a set value within the linear-elastic region for the compliance calibration, this load was nominally 450 N. The test set-up used in the lab, as well as a specimen during loading, can be seen in Figure 3.3.

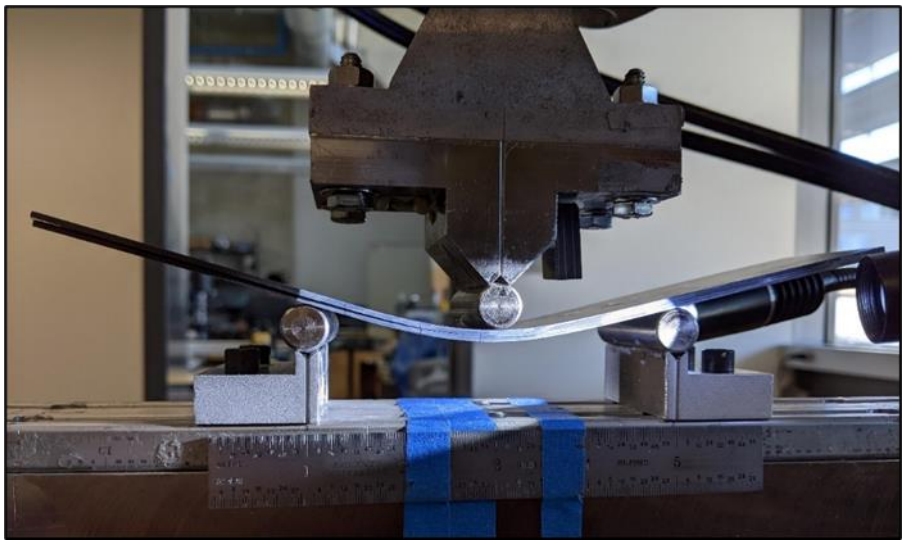

Figure 3.3. Laboratory ENF test fixture set-up and specimen during testing

For the crack propagation, the specimens were loaded until a crack was observed through a drop in load and in some cases an audible crack. The specimens were flipped over, shifted left (in Figure 3.2, keeping a_0 at 30 mm) and loaded again to extend the cracks further than 50.8 mm. Shown in Figure 3.4 are the load versus displacement plots for loading the same ENF coupon five times. Similar loading profiles were observed for loading of the same coupon.

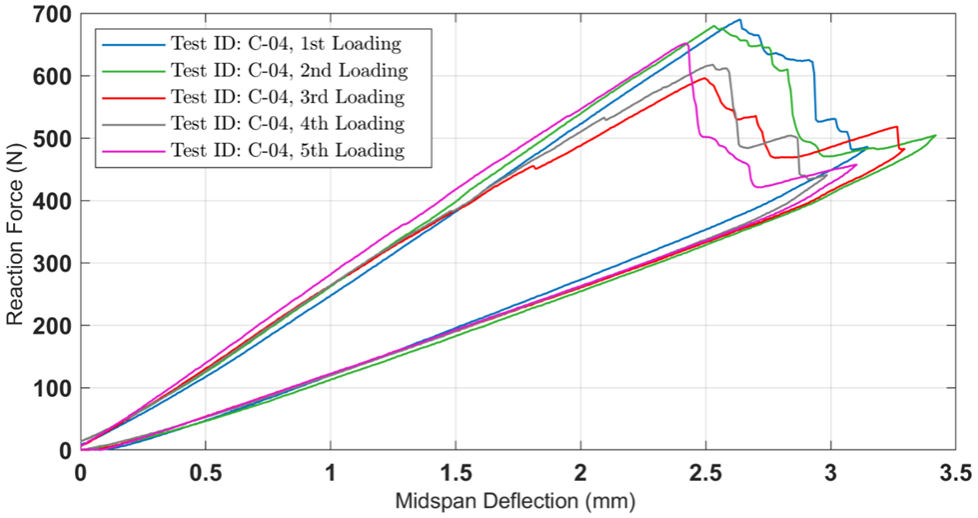

Figure 3.4. Load v. displacement plot of multiple loading of same modified ENF coupon

Aluminum Modified ENF Neat Resin Testing

In addition to the modified ENF testing completed for PMC fracture, an aluminum adherend coupon was utilized to determine the mode II fracture toughness of the injection repair resin by itself. Two 305 mm x 229 mm x 3.18 mm thick 2024-T3 aluminum panels were prepared using a grit blast prior to sol-gel technique. The panel surfaces were blasted using a 40-micron silica media blast at a 45° angle from greater than 0.3 m away until the entire surface was matte in finish. The surface was then blown clean with compressed air and then 3M's, AC130-2 sol-gel adhesion promoter, was applied using a natural bristle brush to the blasted surfaces for 3 consecutive minutes keeping the surface wet and then allowed to cure at ambient room temperature for one hour. Next, Solvay's BR6747-1 epoxy bond primer was applied to the bonding surface and allowed to set at room temperature for 1 hour. The primer was then cured at 121°C for 1 hour, using a ramp rate of 1-3°C/min for heat up and cool down. 0.2 mm thick Flashbreaker tape was applied around the edges and a 13 mm wide strip down the middle of the aluminum panels was placed as a shim. Flashbreaker tape was used a as a shim to create nominal values for bondline

thickness at 0.2 mm for cured coupon configurations. EA9396 diluted with 10% acetone was brush applied to the bonding surfaces. The panels were sandwiched and put into a platen press at 20 psi and set for 5 days at room temperature. The panels were then cured at 88°C for 1 hour, using a ramp rate of 1-3°C/min for heat up and cool down. Once the panels were cured, they were cut into 50.8 mm x 229.0 mm wide modified ENF coupons using a waterjet. Figure 3.5 shows the aluminum modified ENF coupon for neat resin fracture testing. Coupons were pre-cracked at approximately 50.8 mm using steel wedges. Pre-crack distance was verified using optical microscopy and all fractures were verified to within the adhesive layer.

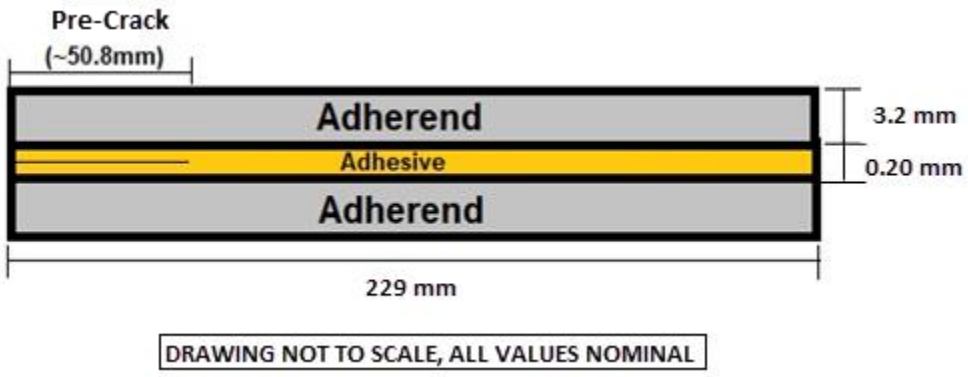

Figure 3.5. Aluminum neat resin modified ENF coupon configuration

Aluminum modified ENF coupons were tested in the same manner as PMC modified ENF coupons, however they were only fractured once. After fracture, the coupons were split open for visual and microscopic inspection of failure modes.

3.1.2. **Impact Testing**

As a collaborative component contributing to this research project, impact testing was primarily completed by Romasko [12], further details of the impact test procedures and damage mapping can be found in his Master's thesis. Impact delamination test specimens were fabricated and impacted to produce delamination zones that were greater than 50 mm in diameter. Three laminate configurations were created, their layups, effective moduli can be seen in Table 3.2. The nominal cured thickness of all panels was 3.2 mm. The laminate configurations were chosen as commonly used layups in Naval aircraft.

Table 3.2. Impact delamination specimens

Laminate Configuration	Layup	Effective Modulus (GPa)	Thickness (mm)
Hard (H)	$[45/-45/0/0/45/-45/0/0/45/-45/0/0/\underline{90}]_S$	114	3.2
Medium (M)	$[45/-45/0/0/45/-45/0/45/-45/0/45/-45/\underline{90}]_s$	79.2	3.2
Soft (S)	$[45/-45/0/45/-45/90/45/-45/0/45/-45/90/\underline{90}]_s$	58.6	3.2

The specimen size was determined according to the ASTM D7136 [11] test method. The specimens had nominal dimensions of 100 mm by 150 mm with the 0° direction aligned with the long side of the specimens. These specimens were cut from the panels using a wet diamond blade tile saw. The specimens were impacted in the manner defined by ASTM D7136, via a low velocity drop weight (pendulum impact) as shown in Figure 3.6. Coupons were impacted at 10J, 15J, 20J, and 40J to determine size of resultant delamination.

Figure 3.6. Pendulum impactor set-up

The impactor tip had a force-measuring instrumented hemispherical hardened steel tip with a 25.4 mm diameter. The pendulum impactor had an arm length of 1,402 mm, and a total mass of 4.8 kg and was set up with a laser photogate to measure actual incoming head velocity just prior to the impact event as well as rebounding velocity. NDI of damaged specimens was performed using ultrasonic pulse echo test methods to map the delamination location boundary using gel-coupled A-scan, as marked in Figure 3.7. The delamination size is defined as the length of the longest axis measured from the A-scan mapped damage (see Figure 3.7).

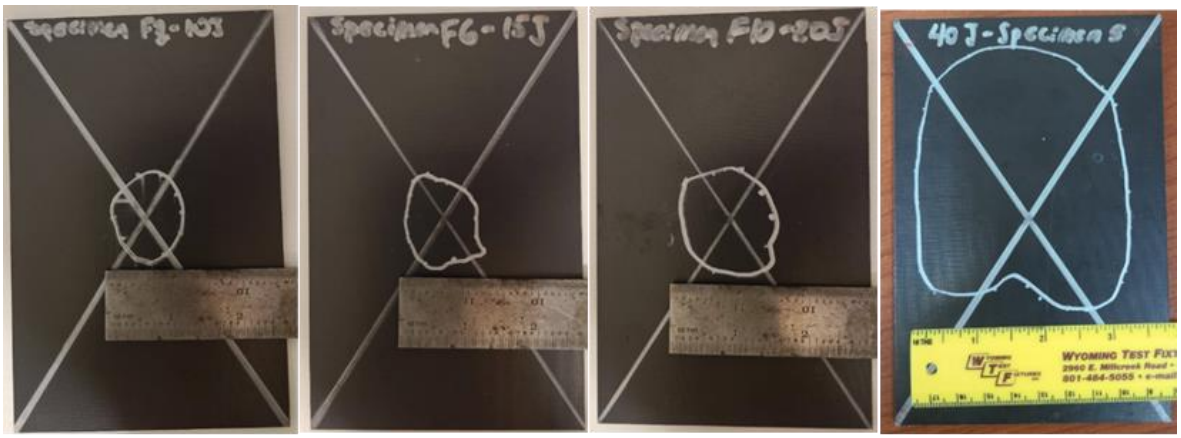

Figure 3.7. Impact damage size (A-Scan) for range of energy (10, 15, 20, and 40 J left to right)

Once specimens were impacted and characterized using NDI, they were sectioned using a lapidary trim saw equipped with a diamond coated blade into 5 sections as shown in Figure 3.8. Middle sections where impact occurred were identified as delaminated and were filleted open using a scalpel for analysis. Side sections were kept intact and utilized for inspection of the delamination through thickness profile.

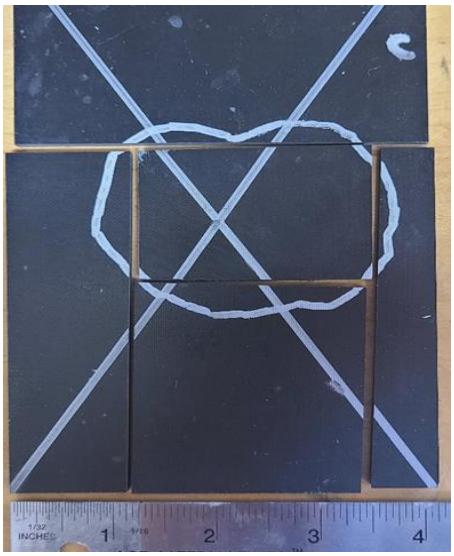

Figure 3.8. 20J impact specimen sectioned for microscopic observation

3.1.3. **In-Service Delaminations**

Five delamination samples were donated by the U.S. Navy from previously in-service fixed winged aircraft components, Figure 3.9 shows examples of excised delaminations. All five samples were each taken from different aircraft components, all with a sandwich construction of two composite skins with aluminum core substructure bonded with film adhesive. Skins were constructed with AS4/3501-6 or IM7/977-3 carbon/epoxy composite material. Backside undamaged skins, aluminum core, and film adhesive were removed by sanding with a 90-degree angle grinder equipped with 180 grit aluminum oxide sanding disks. Blue film adhesive was removed until only the black composite skin was remaining.

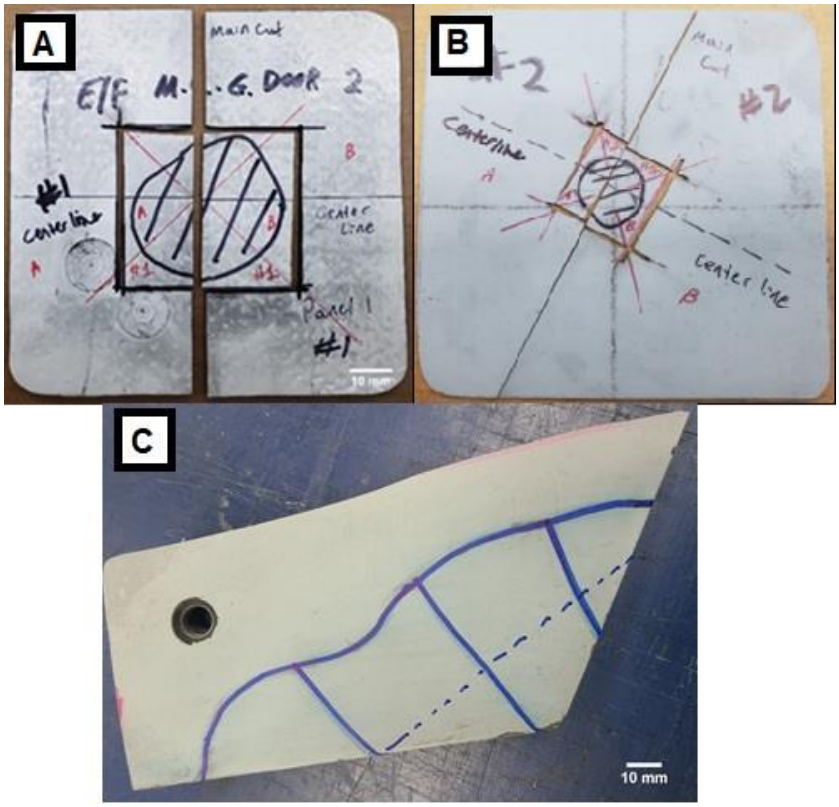

Figure 3.9. In-Service delaminations excised from aircraft components. A. 12-ply enclosed delamination, B. 5-ply enclosed delamination, C. 12-ply edge delamination

Delaminations were previously identified by the U.S. Navy using pulse-echo ultrasonic testing. Table 3.3 exhibits the lay-up for each specimen and the approximate damage area and depth for each delamination identified with traditional A-scan pulse-echo ultrasonic testing procedures [20].

Table 3.3. In-service delamination sample information

Sample	Material	Delamination Type	Lay-up	Thickness (mm)	Approx. Damage Size (mm^2)	Depth (mm)
IS-1	IM7/977-3	Enclosed	12 Plies $[45/-45/0/90/0/90]_S$	1.57	916.8	0.53
IS-2	AS4/3501-6	Enclosed	5 Plies [45/-45/90/-45/45]	0.89	83.2	0.79
IS-3	IM7/977-3	Edge	12 Plies $[45/-45/0/90/0/90]_S$	1.57	149.23	0.13
IS-4	AS4/3501-6	Enclosed	5 Plies [45/-45/90/-45/45]	0.89	24.5	0.71
IS-5	AS4/3501-6	Enclosed	5 Plies [45/-45/90/-45/45]	0.89	59.3	0.38

3.2. DAMAGE CHARACTERIZATION

Delaminations were characterized using non-destructive, destructive, and chemical analysis testing. Non-destructive testing was completed to characterize the depth and size of the delaminations prior to machining the samples. Destructive testing was used to determine through thickness damage morphology and planar surface characterization. Chemical analysis was used to analyze the surface chemistry of the internal surfaces of the delaminations.

3.2.1. **Non-Destructive Inspection**

Non-destructive inspection on delamination coupons was completed using three different methods: 1. Pulse-echo ultrasonic testing by hand, 2. Pulse-echo ultrasonic testing by robotic submersion tank, and 3. X-ray computed tomography.

Pulse-Echo UT by Hand (A-Scan)

Coupons were inspected for delaminations and repair resin bondline integrity using pulse-echo ultrasonic testing. Single-sided ultrasonic scanning, via A-scan presentation, was performed by hand using a Mistras PocketUT system equipped with a 3.5 MHz, 6.4mm diameter delay line and transducer (see Figure 3.10). All scanning was coupled with glycerin gel. A standard was used with known defects of which 50% screen height attenuation within the A-scan were considered areas of delamination. The A-scan waveform for inspecting the coupons can be found in Figure 3.11. The area in between the front surface and back surface signal would increase in amplitude if there was a defect present.

Figure 3.10. Pulse-echo ultrasonic A-scan hand inspection test set-up

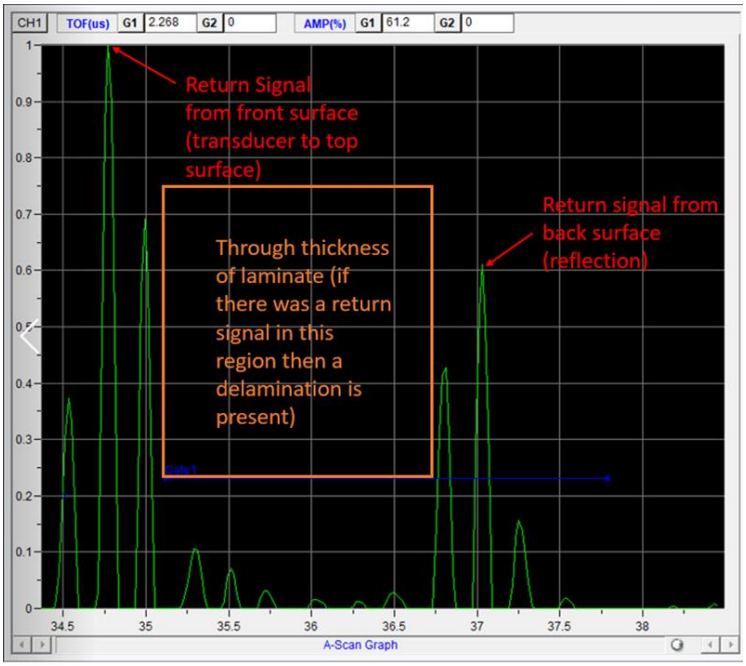

Figure 3.11. A-scan waveform for inspecting PMC delaminations [12]

Pulse-Echo Robotic UT (C-Scan)

Single-sided robotic pulse-echo immersion tank ultrasonic scanning, with C-scan presentation, was performed with a Mistras PocketUT system with a scan resolution of 0.127 mm per scan-line and a 10 MHz spherical focus transducer. The submersion tank scanning setup is shown in Figure 3.12. Time-of-flight (TOF) values between the first and second reflections of the signal to the transmitting transducer were the primary features used to determine delamination depth and location.

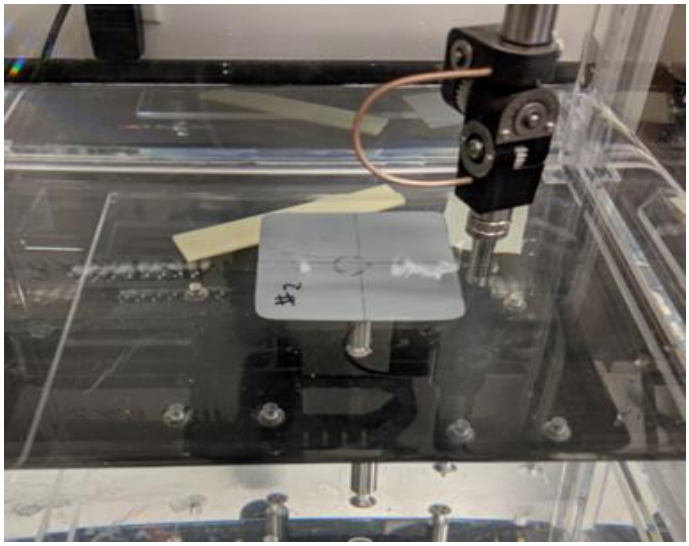

Figure 3.12. Ultrasonic submersion tank scanning setup

An example UT scan TOF C-scan plot is shown in Figure 3.13. Medium gray values indicate an undamaged region and darker values indicate shallower delaminations. UT scanning was used to determine the major axis of the damage feature to select the location and angle of the sectioning cut for micrograph inspection.

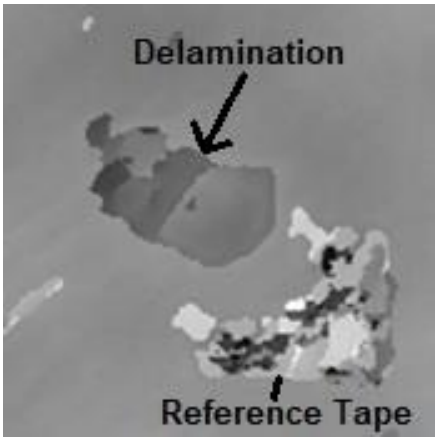

Figure 3.13. UT TOF C-scan presentation of sample IS-2

X-ray Computed Tomography

X-ray CT was conducted using facilities at the Naval Air Warfare Center Aircraft Division Materials Laboratory (Patuxent River) on in-service and laboratory impacted delamination specimens to determine if 3-D representation of damage was possible using commercial off the shelf software. X-ray CT images were collected with Northstar Imaging X5000 XCT system. The X5000 system operating parameters include: 150kV, 500µA, with a focal spot size of 50 µm, projections of 3600, and two frames averaged. A detector shift subpixel routine to improve resolution and continuous scanning. The resulting CT resolution varied between 22-16 µm. Set-up of specimen in X-ray CT is shown in Figure 3.14

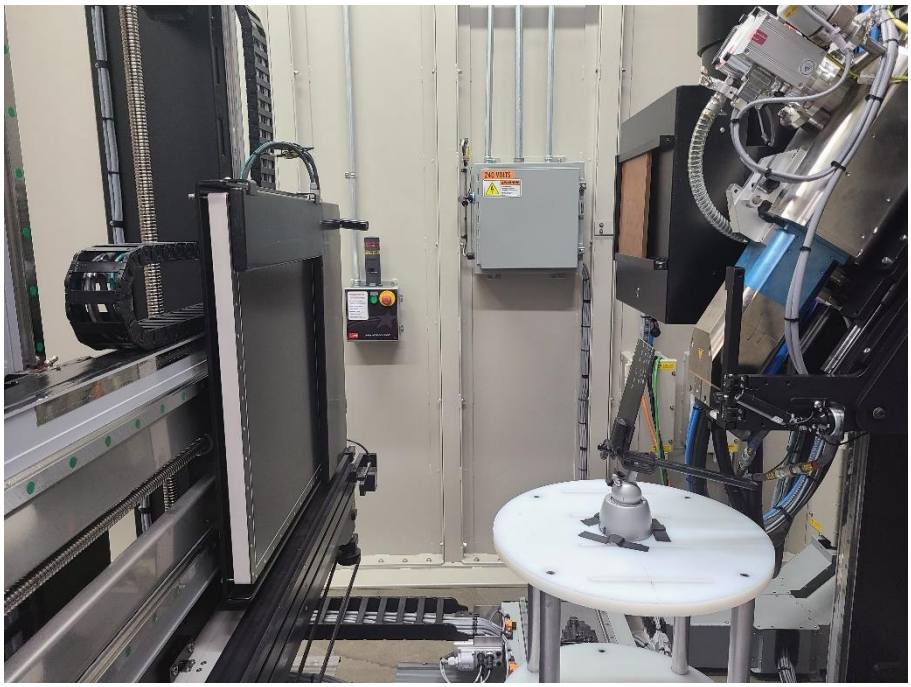

Figure 3.14. X5000 X-ray CT set-up for scanning composite panels

CT post-processing of previously in-service delamination was performed with the Software ImageJ [27] for viewing and analysis of orthogonal slices. Example orthogonal slices are shown

for Specimen IS-4 where in Figure 3.15a shows a planar slice that emphasizes damage features such as delaminations and Figure 3.15b shows a through-thickness slice that emphasizes the distribution of damage through the composite laminate.

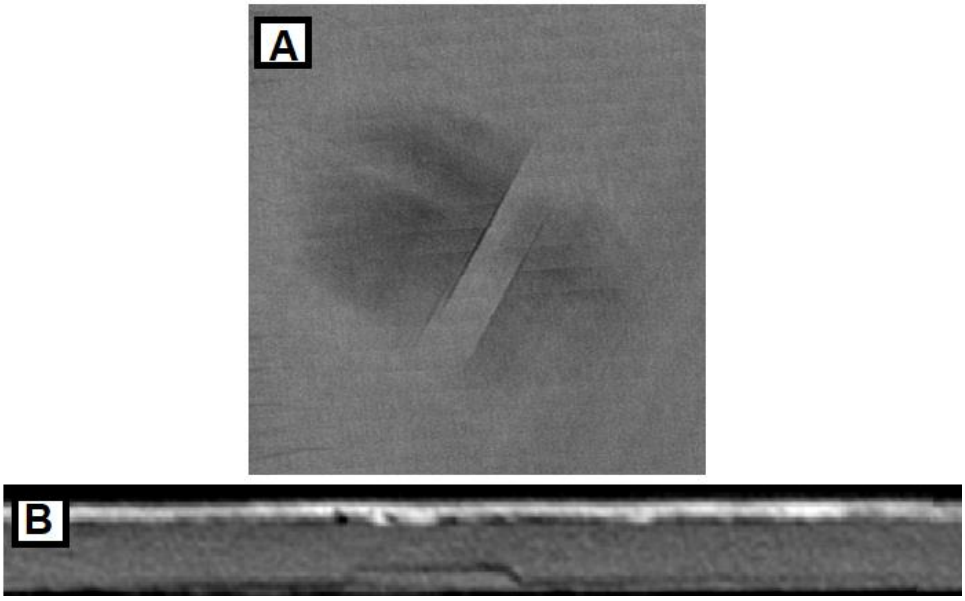

Figure 3.15. Example orthogonal CT slices taken from specimen IS-4. a) Planar view of the laminate showing a delamination and matrix cracks. b) A through-thickness slice showing delamination near the back surface

3.2.2. **Destructive Inspection: Optical Analysis and Profilometry**

Delamination samples were cut using a dry non-abrasive diamond coated laboratory saw along a prescribed main cut axis for the photomicrograph sections as shown in Figure 3.16. The perimeter of the delamination was cut out using a Dremel rotary tool equipped with a diamond coated cut wheel. One half of the delamination was used for physical damage visual characterization through photomicrography and the other for surface contamination

characterization. The excised delamination half was then mounted using clear mounting epoxy and polished down to a 1µm finish.

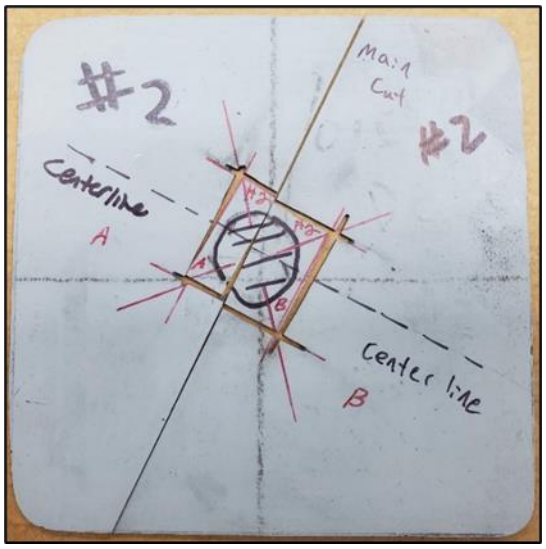

Figure 3.16. Excision of delamination for photomicrographs and surface analysis

Photomicrographs and surface characterization was performed using a Keyence VHX-7000 digital microscope. Photomicrographs were taken of both the through thickness profile of the delaminations and a planar view of the internal fracture surfaces of the delamination after it was fileted open. Profile and planar view photomicrographs were taken at 80x and 20x zoom, respectively. For profile and planar views of entire delaminations, two-dimensional (2-D) and three-dimensional (3-D) picture stitching with photomicrographs was achieved through the Keyence VHX software suite.

Profilometry of the delamination planar surfaces was completed by the Keyence software line profile function on 3-D images for each sample. Line profiles were taken in both the 0° and 90° directions on all delamination samples. Five-line profiles were taken in each measurement

direction per sample at 20x zoom. An example of the line profile locations for both 0° and 90° are shown in Figure 3.17.

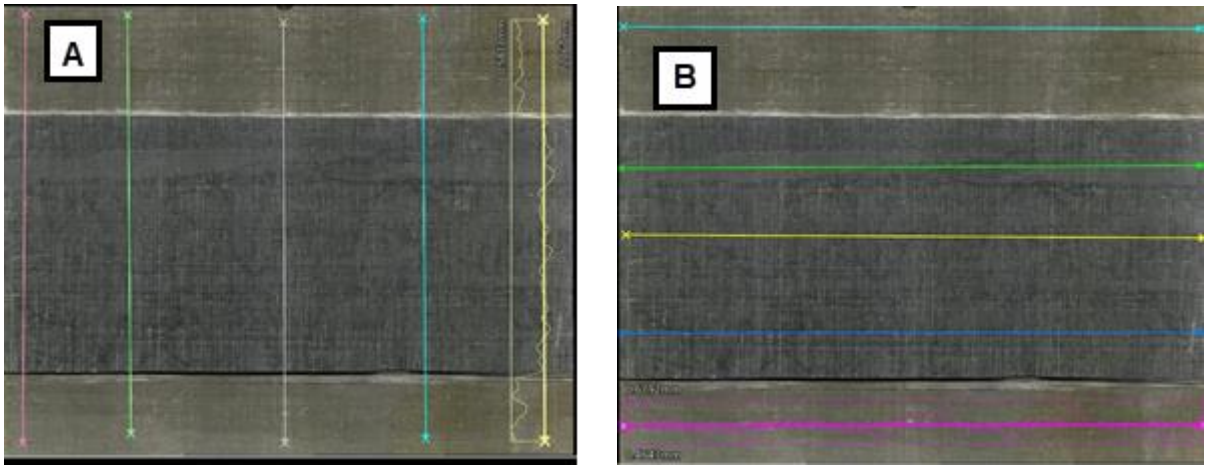

Figure 3.17. Example of line profile locations for delamination samples. (A) 0° direction; (B) 90° direction

Raw data for profilometry measurements were extracted, then filtered and analyzed using True Map 6, surface texture analysis software. For surface roughness measurements, five readings were taken in both 0° and 90° measurement directions using 100x zoom for each sample. The line roughness function within the VHX software was utilized to determine the average roughness (Ra) on each surface. Digital surface roughness readings were verified for measurement sensitivity using the Pocket Surf portable surface roughness tester.

3.2.3. **Surface Analysis Using Gas Chromatography Mass Spectrometry (GC-MS)**

GC-MS was used to inspect internal fracture surface of the delamination for trace contaminants such as hydrocarbons, ester oils, or silicones. The remaining excised in-service

delamination sections were cut to the exact perimeter of the outlined delamination using the Dremel rotary tool with a 5 mm diameter cut wheel. The delaminations were filleted into two halves by inserting a thin blade into the delaminated sections and pulling apart out of plane using tweezers under a stereo microscope. The internal delaminated surfaces were exposed and a previously hexane washed cotton swab was used to collect samples from both of the delaminated surfaces. Four wipes were performed on each open surface and the cotton swab was washed with 6mL of high purity liquid chromatography grade Hexane into a vial. 400 µL were taken from the vial and placed into GC-MS vials with a 400 µL glass column and a Teflon membrane. Sample collection was completed for each of the four excised delaminations and one baseline manufactured sample.

GC-MS data collection was conducted on a Thermo-Fisher Trace 1310 Gas Chromatography unit equipped with a TR-5 column and a TSQ 8000 Evo mass spectrometer. A tri-plus auto sampler taking 1 µL measurements was used for data collection. Each sample measurement was processed with method programmed with the following parameters: hold at 40°C for three minutes, then ramp at 16°C per minute up to 330°C and hold for 15 minutes. A 3-minute latency delay was used for the hexane solvent.

3.3. MATERIALS AND PROCESS DEVELOPMENT EXPERIMENTATION

In order to develop a novel injection repair procedure, experiments and analysis developing materials and processes were completed. Some of these experiments had to be invented in order to obtain relevant processing information. Materials and process development testing and analysis includes: injection pressure analysis, surface contamination and cleaning processing, surface

chemistry assessment, resin viscosity modification, development of modified ENF coupon for injection repair testing, fracture analysis using microscopy.

3.3.1. **Injection Pressure Analysis**

The development of injection repair processes includes concerns about pressurization of the delamination that could induce growth of the fracture. Injection of cleaning products such as solvent, plasma, or resin could progress the delamination if the processing pressure is too high.

First a pressure analysis was conducted to determine if the hand applied pressure from a syringe or the machine-applied pressure from the atmospheric plasma unit would further damage the composite laminate when injecting into the existing delamination. To conduct such an analysis, the input pressure into the delamination must first be calculated. First the pressure from a syringe was calculated using the modified Bernouilli's equation (3.1) as depicted in Figure 3.18. This equation has assumptions that the height is negligible and the flow is inviscid, incompressible, and laminar.

$$P_2 = P_1 + \frac{1}{2}\rho(v_1^2 - v_2^2) \tag{3.1}$$

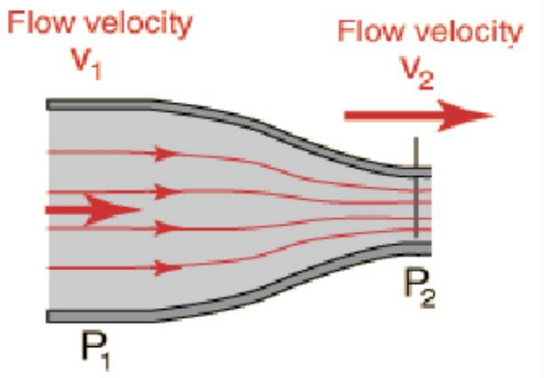

Figure 3.18. Bernoulli's equation flow diagram

The flow exit pressure (P_2) is the important experimental variable to determine if the exit pressure from the source into the laminate exceed the maximum allowable pressure prior to crack propagation. The variables are defined as: input pressure (P_1), input flow velocity (v_1), output flow velocity (v_2), and fluid density (ρ). The syringe, as shown in Figure 3.19, was assumed to be a 50 mL syringe with a 27.62 mm diameter body equipped with a 20-gauge needle (0.603 mm needle diameter).

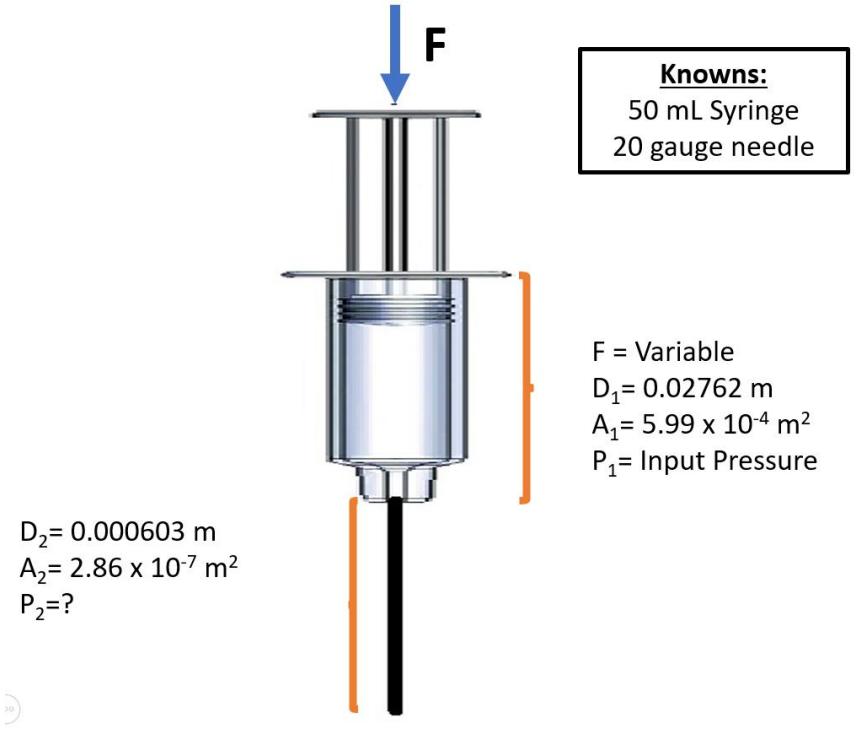

Figure 3.19. Syringe injection pressure calculation schematic

The input forces were determined from three different sources: 1. The maximum pressure the syringe body could withstand prior to rupture, resultant input force is 516.25 N [76]; 2. The maximum pressure of the plunger seal, resultant force is 30 N [77]; 3. The maximum syringe

pressure typically observed from a human, resultant force 103.24 N [78]. The pressure from the plasma unit was previously determined by the equipment manufacturer using the maximum settings for the minibeam head. Three different fluid densities were analyzed: 1. Helium-oxygen plasma (1.429 kg/m^3); 2. EA9396 epoxy (1140 kg/m^3); 3. Reagent grade Acetone (784 kg/m^3). Volumetric flow rates of 5x10^{-6} m^3/s for epoxy and acetone were used to calculated fluid velocity which was experimentally determined by timing the expulsion of the fluids from a syringe. The volumetric flow rate of 173000 mm^3/s for plasma was used and is determined from the settings on the plasma unit. The resultant P_2 injected into the delamination determined from the calculations are found in Table 3.4 The different P_2 are correlated to the differing injection pressures where P_{2a} is from maximum pressure of syringe body input pressure, P_{2b} is from maximum pressure of the plunger seal input pressure, and P_{2c} is from human induced input pressure.

Table 3.4. Injection pressure calculation results

Fluid	**P_{2a} (MPa)**	**P_{2b} (MPa)**	**P_{2c} (MPa)**
Helium Plasma	0.0695		
EA9396	0.684	0.0948	0.00588
Acetone	0.739	0.0391	0.0498

The atmospheric plasma had a resultant pressure of 0.0695 MPa entering the composite laminate and this was a single data point because the atmospheric plasma machine does not rely on input force from a human. The resultant pressure exiting the syringe needle for EA9396 was highest calculated when applying enough pressure to rupture the syringe body at 0.684 MPa. The same trend was found for the acetone with a resultant pressure of 0.739 MPa. The maximum pressure

that can be applied prior to rupturing the syringe plunger seal for EA9396 repair resin was 0.0948 MPa, which higher than when using acetone. The maximum pressure applied by hand for the injection syringe had an exit pressure of 0.00588 MPa using EA9396 and 0.0498 for acetone. Although the rupture pressure of the syringe body is a possibility and a conservative way to analyze the injection pressure, most operators have force feedback when the syringe is pushed and will likely never reach a pressure that breaches the syringe body. Also based upon the calculations, the plunger seal pressure was less than the maximum syringe body pressure making it so that the plunger seal would fail before the syringe body failed in any case. Therefore the most practical applied pressure to the composite laminate would be the calculation result P_{2c}. However this study will explore all three input force configurations.

The pressure input previously determined could be used to compare to a finite element analysis (FEA) model. Therefore an FEA model was created in Abaqus software to determine the effects of injection pressure at different sizes and depths through the laminate. Analysis was completed on a circular shaped delamination using the virtual crack closure technique (VCCT) method within the FEA. Fracture properties of IM7/977-3 carbon/epoxy composite material used were previously determined from past studies [79, 80]: $G_{IC} = 220$ J/m^2; $G_{IIc} = G_{IIIC} = 1000$ J/m^2; $\eta = 1.8$. This single plane delamination analysis was completed at various depths locations, z, relative to the thickness, h, as shown in Figure 3.20.

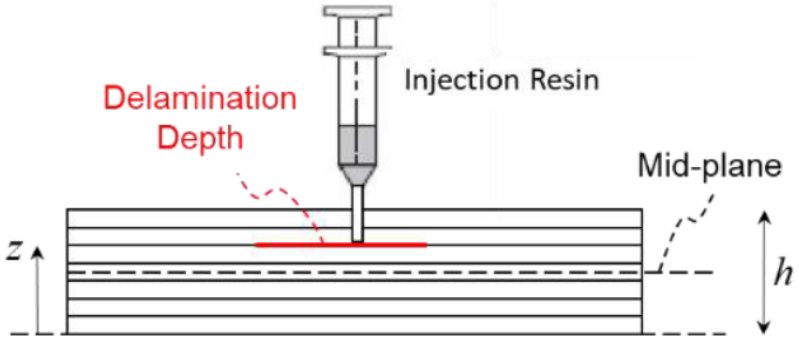

Figure 3.20. Delamination depth analysis case

Two 25-ply laminate configurations were analyzed include a "hard" and "soft" laminate having percent 0º/±45º/90º ply content of 48%/48%/4% and 32%/64%/4%, respectively. Delamination diameters of 2a = 25, 50, and 100mm size were defined and internal pressure was increased until the critical strain energy release rate was met with mixed mode fracture growth criterion (equations 3.2 through 3.4).

$$\frac{G_T}{G_c} > 1 \tag{3.2}$$

$$G_c = G_{Ic} + (G_{IIc} - G_{Ic}) \left(\frac{G_{II}}{G_T}\right)^{\eta} \tag{3.3}$$

$$G_T = G_I + G_{II} \tag{3.4}$$

The goal of the FEA model is to determine the pressure at which the crack tip propagates using the mixed mode fracture growth criterion. Delamination internal pressure (blister pressure) schematic is shown in Figure 3.21, along with an example result from the VCCT FEA model.

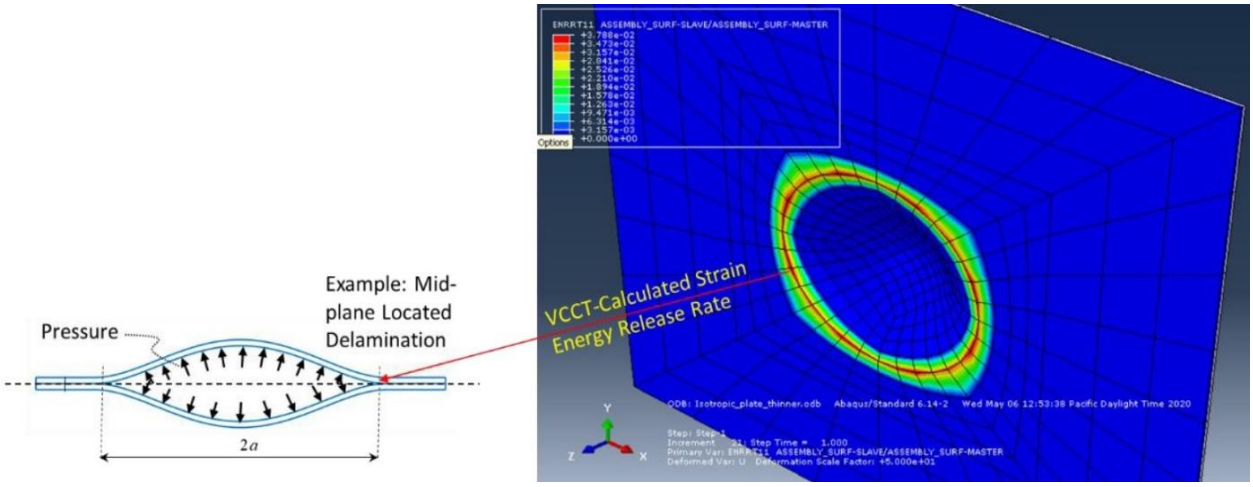

Figure 3.21. Finite element analysis virtual crack closure technique model for circular-shaped delamination growth

3.3.2. Surface Contamination and Cleaning Process Development Testing

Contamination Testing

Two different aircraft fluid contaminants were down selected from AMS 7201[52] based upon previous findings from in-service aircraft maintained by NAVAIR. These two contaminants include: 1. MIL-PRF-83282 hydraulic fluid and 2. MIL-PRF-7808 lubricating oil.

Contamination testing was conducted with an iterative process starting with a flat plate discriminator panel to determine contamination coverage. Due to the high viscosity of both selected fluids, a dilution with solvent was required to ensure the contaminant could be injected and achieve total coverage within the delamination. Contaminant fluids were mixed with varying volumes of isooctane (2, 2, 4-Trimethylpentane) solvent to determine the minimum required volume fraction of contaminant to ensure adequate coverage of the internal surface of the

delamination while lowering the surface activation energy to prevent bonding. Five separate contaminant solutions mixed with solvent were created consisting of: 5, 10, 15, 20, and 30% contaminant by volume. A 279 mm x 83 mm IM7/977-3 flat composite panel was sanded and partitioned into five 2000-3500 mm^2 sections. 100 µL of each contaminant was placed into each region using a pipette and spread evenly using an aluminum spatula as shown in Figure 3.22.

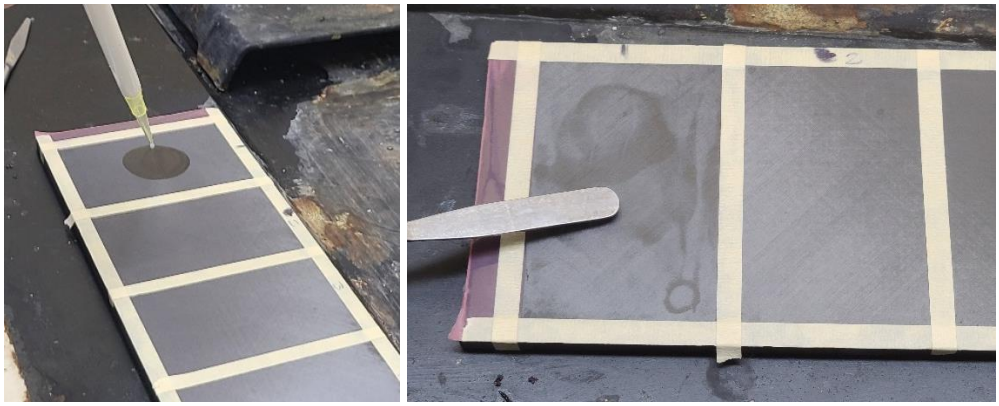

Figure 3.22. Contaminant application on flat plate

The contaminant solution was allowed to dry for 24 hours at room temperature. Each contamination region on the test panel consisted of a different amount of contamination coverage as shown in Figure 3.23. Shown in Table 3.5 are the calculated contamination coverage for each region. A hydraulic fluid, lubricating oil, and solvent densities of 827,510 µg/cm^3, 987,030 µg/cm^3, and 690,000 µg/cm^3 were used, respectively. After drying, water contact angle (WCA) measurements were taken at five different locations within each contamination region using the Brighton Science's Surface Analyst 3001 portable goniometry instrument.

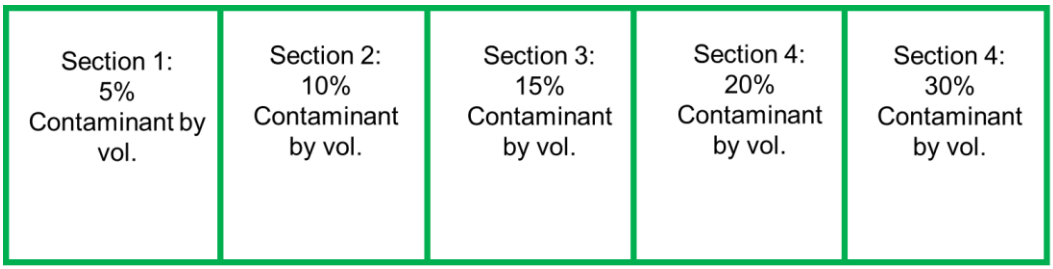

Figure 3.23. Flat plate contamination discriminator panel test regions

Table 3.5. Flat plate contamination panel coverage

Section	Contaminant	Contaminant Volume Fraction	Mixed Density ($\mu g/cm^3$)	Contaminant Coverage ($\mu g/cm^2$)
HF-1	Hydraulic Fluid	0.05	696,876	152.8
HF-2	Hydraulic Fluid	0.1	703,751	365.6
HF-3	Hydraulic Fluid	0.15	710,627	475.9
HF-4	Hydraulic Fluid	0.2	717,502	699.3
HF-5	Hydraulic Fluid	0.3	731,253	1004.5
L-1	Lubricating Oil	0.05	704,852	100.7
L-2	Lubricating Oil	0.1	719,703	226.7
L-3	Lubricating Oil	0.15	734,555	349.8
L-4	Lubricating Oil	0.2	749,406	482.7
L-5	Lubricating Oil	0.3	779,109	705.7

Enclosed contamination testing was also performed to ensure contaminant coverage on the inside of a delamination. Two previously tested and fractured ENF coupons were utilized. The coupons were sealed around the edges using Hysol's EA9394 epoxy and Flashbreaker tape. Two #40 (2.5 mm) diameter holes were drilled into the coupons at locations shown in Figure 3.24 to a depth of 1.6 mm. A 10% by volume mixture of each contaminant was mixed with a droplet of fluorescent dye. 3 mL of each contaminant was injected into independent coupons through the drilled holes using a 20-gauge diameter hypodermic needle attached to a syringe. The coupons were allowed to dry at room temperature for 24 hours after injection. The coupons were then cut with a lapidary saw equipped a diamond coated blade to the end of the fracture region and split

into two and inspected using WCA measurements on the inside of the previously enclosed fracture region. 10 WCA measurements were taken on each coupon at five locations on each side of the specimen as shown in Figure 3.24. The area of contamination was also visually inspected with a black light to determine area of coverage from contaminant injection.

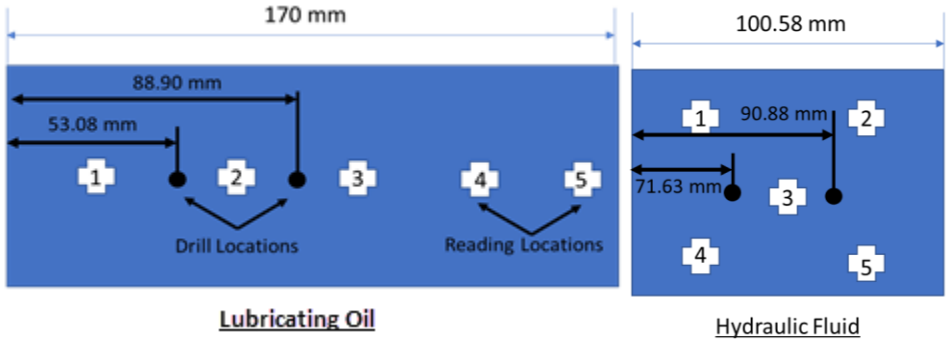

Figure 3.24. Drill holes and WCA reading locations on internal contamination coupons

Delamination Cleaning Process Development

Delamination cleaning process development was also completed using an iterative process to prove out cleaning solutions on a contaminated flat plate prior to cleaning contaminated enclosed fractures. An identical flat composite plate used for contamination testing was utilized to determine the effectiveness of contamination cleaning techniques. 100 µL of each contaminant were placed and spread into each of the five 2000-3500 mm^2 sections. Both methyl isobutyl ketone (MIBK) solvent and a helium-oxygen atmospheric plasma were used as contamination removal techniques. A Surfx Atomflo 500L atmospheric plasma unit equipped with a minibeam head was used for all plasma cleaning processes as shown in Figure 3.25.

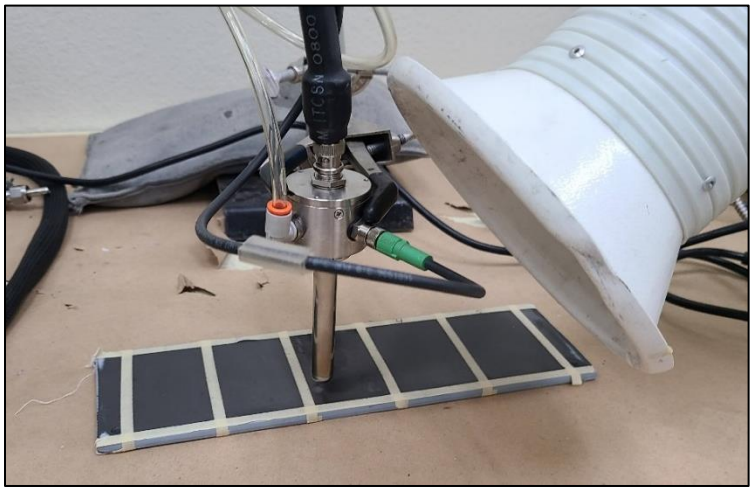

Figure 3.25. Atmospheric plasma cleaning contamination on a flat plate

The atmospheric plasma treatment was completed using the following parameters: 60 W power, 30.0 L/min. helium, and 0.15 L/min oxygen flow rate. Five different contaminant removal techniques were used on the panel as shown schematically in Figure 3.26.

Section 1: MIBK Solvent Wipe	Section 2: MIBK Solvent Wipe w/ 10 sec Plasma Exposure	Section 3: Plasma Exposure until Visual Removal.	Section 4: Plasma Exposure for 10 sec per Spot.	Section 5: Plasma Exposure for 15 sec per Spot.

Figure 3.26. Flat plate contamination removal discriminator panel test regions

Solvent wipe was completed by first wiping the region using a rymplecloth soaked with MIBK then dry wiping with rymplecloth until no discoloration was found in the cloth. For all

plasma exposures, five locations in each section were exposed to the plasma for the allotted time, with four exposures in each location.

After flat plate cleaning process development was completed, enclosed ENF coupons sealed around the edge and injected with contaminant were utilized to determine effectiveness of cleaning procedures on enclosed delaminations with contaminant present. Enclosed contaminant coupons were first injection with a 10% contaminant by volume and allowed to off-gas for 1 week. The same coupons were then subject to an acetone rinse using approximately 10 mL of acetone to rinse the gross contamination from the interior of the ENF coupon. 5 mL was applied via syringe to each hole within the coupon. The acetone rinsed coupons were allowed to settle at room temperature for a minimum of 24 hours. Each coupon was then purged for 5 seconds with high purity Nitrogen gas at 60 kPa by injecting into one of the two drilled holes prior to further preparation using atmospheric plasma. A SurfX Atomflo 500L atmospheric plasma unit equipped with a minibeam head was used for all plasma cleaning processes. The plasma head was sealed using sealant tape to prevent back flow of carrier gas and sealed to the coupon surface with a high temperature silicone O-ring. A Helium-Oxygen Plasma was injected into one of the drilled holes using a high temperature silicone rubber gasket to separate the plasma head from the composite laminate as shown in Figure 3.27. The plasma unit was set at 60W power, 10 L/min. Helium (He) flow rate, and 0.15 L/min. Oxygen (O_2) flow rate. Plasma treatment was conducted for 10-20 minutes on each hole of each coupon.

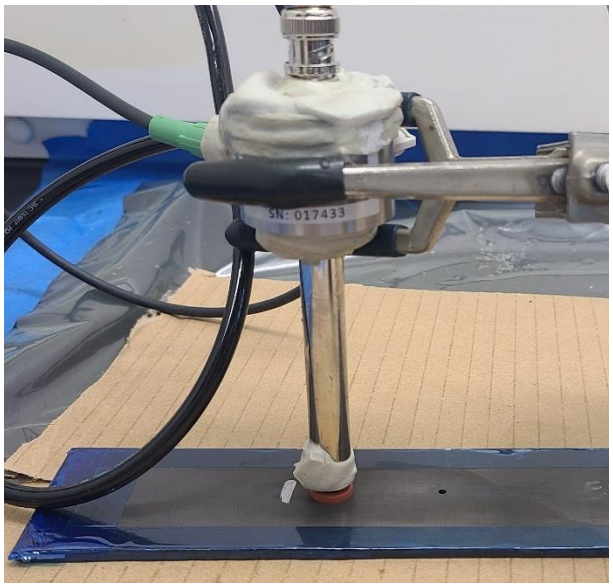

Figure 3.27. Plasma cleaning modified ENF coupon

3.3.3. **Surface Preparation Verification Testing**

Fourier Transform Infrared Spectrometry Verification

A Thermo-Fisher Nicolet Fourier Transform Infrared spectrometer equipped with an Attenuated Total Reflectance (ATR) accessory was used to inspect the internal surfaces of the simulated delaminations. Coupons were cut at the end of the delamination, opened, and analyzed with a diamond ATR crystal which was pressed on the laminate surface using a 15 N probe clutch. A background spectrum was collected every 10 minutes and 32 scans were collected per sample location. 16 sample locations were collected per coupon as shown in Figure 3.28. A control sample was collected on a known contaminated panel for reference when analyzing FTIR data.

Figure 3.28. FTIR analysis locations on ENF process development coupon

Quantitative Gas Analysis

The Quantitative Gas Analyzer (QGA) from Hiden Analytical is a mass spectrometer that provides real time data for vapor or gas analysis. The QGA is equipped with a tether probe that is used as an inline detector for analysis of vapor/gas byproducts of processes. In order to determine the byproduct from the delamination cleaning process, the QGA spectroscopic method was first developed on the outer surface of a flat composite panel that was contaminated with lubricating oil. A chamber was placed over the contaminant with a port hole for the atmospheric plasma and another port hole to hook up the QGA probe to take readings of the byproducts filling the chamber (see Figure 3.29). The chamber was sealed with sealant tape to ensure that all byproduct vapors and gasses from the plasma cleaning process were captured and read by the QGA. In order to determine the primary byproducts of the process, the Faraday detector of the QGA was utilized to document all mass spectra responses from 1-200 amu. The spectra were then analyzed for primary byproducts of lubricating oil using the Mass Spectra Handbook [71] and the material safety data sheet. Once the primary byproducts were identified, a separate method was developed within the QGA software (EGASoft) that would use the Secondary Electron Multiplier detector for specific

process monitoring of the contaminant material. This would include using a background subtract feature to remove any contributions from ambient air.

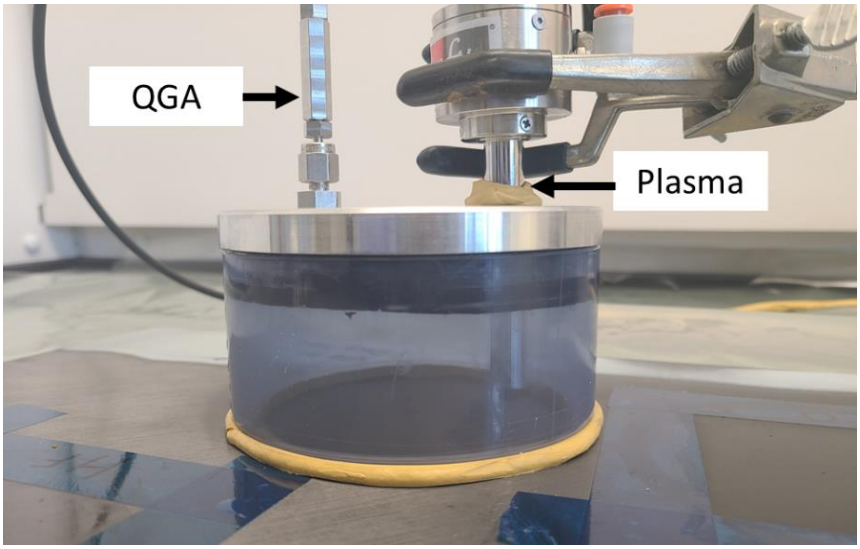

Figure 3.29. QGA contamination removal verification test set-up

For monitoring the plasma cleaning of the enclosed ENF coupons, the QGA probe was placed next to the opposite hole of the atmospheric plasma (see Figure 3.30) to provide gas analysis of byproducts leaving the delamination. QGA mass spectra data was collected for the same time duration as the plasma treatment. Spectra collected were of only the byproduct masses over time.

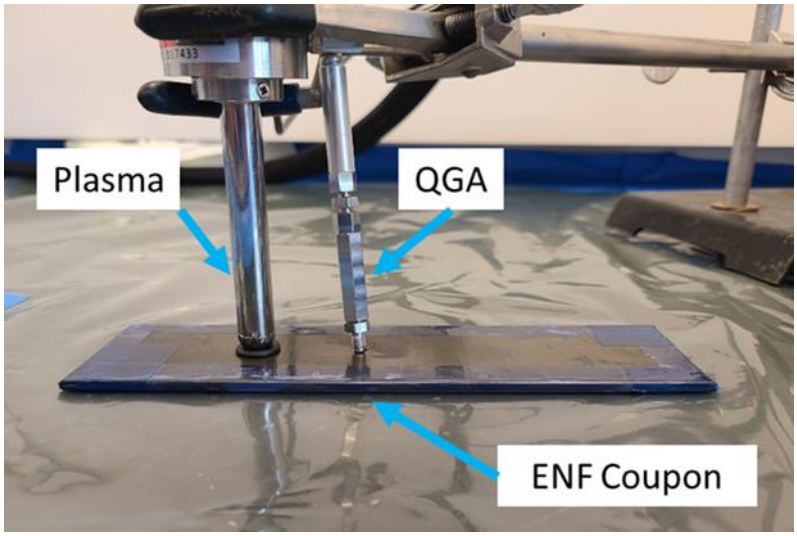

Figure 3.30. Plasma cleaning and QGA monitoring of enclosed ENF coupon

3.3.4. **Resin Modification Testing**

The two-part epoxy resin EA9396 was identified by the U.S. Navy as the primary injection resin used for repair of aircraft, however the resin viscosity was too high (>3500 cPs) to achieve a fill of more than 50% without multiple iterations of resin injection and drilling. Therefore resin modification testing was completed to determine if a diluent could be used with the recommended material to both achieve low viscosity while retaining shear carrying capability. EA9396 was modified using either acetone or methylethylketone (MEK) as solvent diluents to lower the viscosity of the repair resin. Three primary experiments were completed for resin modification testing: 1. Tensile Single Lap Shear, 2. Viscosity via Brookfield viscometer, and cure parameter verification with Barcol hardness testing.

Tensile Single Lap Shear

Single Lap Shear coupons were manufactured per ASTM D1002 [81] using 1.6 mm thick 2024-T3 aluminum that were surface prepared using grit blast prior to application of sol-gel and bond primer. Coupons were cured in a platen press under 0.17 MPa pressure using a bonding fixture for 1 hour at 88°C. Coupons were then mechanically tested per ASTM D1002 at room temperature ambient conditions. Table 3.6 shows the sample sets manufactured to test the effect of solvent dilution of EA9396 epoxy.

Table 3.6. EA9396 adhesive modification lap shear sample set

Sample Set	Solvent	% by Weight Solvent
LS-BL	N/A	N/A
LS-ACE-10	Acetone	10
LS-ACE-20	Acetone	20
LS-ACE-25	Acetone	25
LS-MEK-20	MEK	20
LS-MEK-25	MEK	25

Viscosity Testing

Viscosity testing was conducted on a Brookfield DV-E viscometer equipped with a #1 Spindle. The Spindle rotational speed was completed at 20 rpm. A 500 mL sample was required and two replicates were completed. Due to the large volume required for each sample, only EA9396 diluted with 10% or 20% acetone by volume were tested. All testing was completed over a ten-minute period at room temperature ambient conditions. Figure 3.31 shows the test set-up of the Brooksfield viscometer.

Figure 3.31. Brookfield viscometer testing set-up

Cure Parameter Testing

Cure parameter testing was completed by mixing approximately 30g of each modified adhesive blend and pouring into a 75mm diameter plastic cup for cure. The cap was placed on the cup and sealant tape was applied to the cap edge to prevent volatile leakage. The cup was then placed in an air circulating oven and the cure cycle was completed for each sample. Table 3.7 shows the epoxy solution and cure cycles for each sample. All samples were cured at 88°C after room temperature hold except the baseline sample (CP-1). The manufacturers recommended cure cycle was 66°C, however the 88°C cure cycle is most commonly used to ensure the glass transition temperature is above the service temperature for military aircraft [82]. Therefore it was recommended to implement an 88°C cure to all specimens. Once the cure cycle was completed, the sample was bisected using a diamond coated blade in a laboratory lapidary saw. The cut

surfaces for the sample were then polished with up to 600 grit sandpaper and polishing compound and then visually inspected for porosity.

Table 3.7. Cure parameter testing matrix

Sample	Dilution (% acetone)	Room Temp. Hold (hrs.)	Cure Temp (°C)
CP-1	0	0	66
CP-2	30	16	88
CP-3	20	16	88
CP-4	10	16	88
CP-5	10	120	88

In addition to visual inspection for porosity, the samples were also tested using a Barcol Hardness tester in accordance with ASTM D2583 [83]. Barcol Hardness is a process verification test that is completed on thermoplastic materials to determine the polymer degree of cure. Higher Barcol hardness readings are typically correlated to higher epoxy degree of cure. Ten Barcol hardness readings were taken per a cure parameter testing sample when surface was not too porous for measurements. Figure 3.32 shows a schematic of the Barcol hardness tester and a picture of the test being completed.

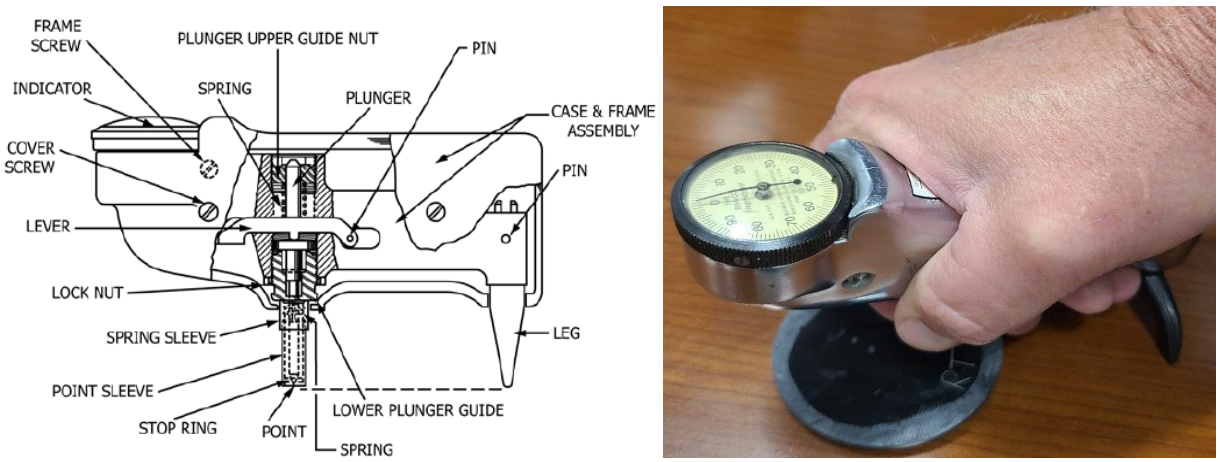

Figure 3.32. Barcol hardness impressor diagram (Left) and impressor in use (Right)

3.3.5. **Injection Repair Process and Repaired ENF Coupon Testing**

Novel Injection Repair Process

The final dimensions of the modified ENF process development coupon is nominally shown in Figure 3.33. Coupons had PTFE tape placed in the "manufactured pre-crack section" and sealed around the open edges using Hysol's EA9394 epoxy adhesive. Pressure sensitive tape was then placed over the sealed edges as a secondary barrier. These sealed coupons would be used for

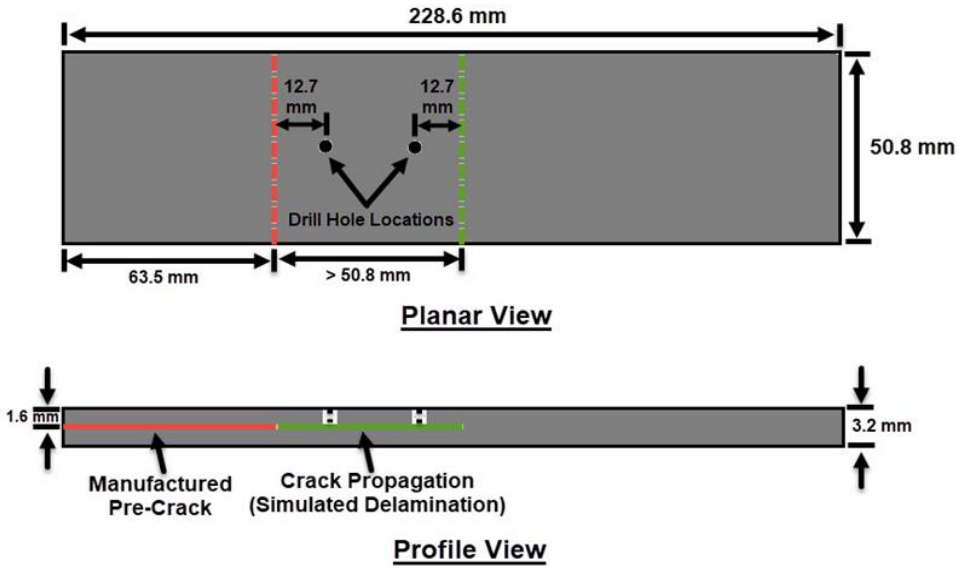

Figure 3.33. Drill hole locations for injection repair process verification testing

testing the novel injection repair process. Sample sets of three coupons were prepared for four different test configurations utilizing two different contaminants and three different laminate configurations as shown in Table 3.8. These configurations included: 1. Baseline (testing pristine IM7/977-3 laminate), 2. Injection repaired, 3. Contaminated (injection repaired with contaminant present), and 4. A set that was contaminated, cleaned, and repaired using the novel repair process. Lubricating oil and hydraulic fluid were utilized to simulate a contaminated delamination from in-service usage.

Table 3.8. Modified ENF repair test matrix

Sample Set	Lay-up	Contaminant	Cleaned?	Repaired?	Repair Resin Dilution (by weight)
ENF-UNI-BL	Unidirectional	No	No	No	N/A
ENF-QUASI-BL	Quasi-Isotropic	No	No	No	N/A
ENF-CROSS-BL	Cross-ply	No	No	No	N/A
ENF-UNI-RPR-20%	Unidirectional	No	No	Yes	20% Acetone
ENF-QUASI-RPR-20%	Quasi-Isotropic	No	No	Yes	20% Acetone
ENF-CROSS-RPR-20%	Cross-ply	No	No	Yes	20% Acetone
ENF-UNI-RPR	Unidirectional	No	No	Yes	10% Acetone
ENF-QUASI-RPR	Quasi-Isotropic	No	No	Yes	10% Acetone
ENF-CROSS-RPR	Cross-ply	No	No	Yes	10% Acetone
ENF-UNI-CONT-LO	Unidirectional	Lubricating Oil	No	Yes	10% Acetone
ENF-QUASI-CONT-LO	Quasi-Isotropic	Lubricating Oil	No	Yes	10% Acetone
ENF-CROSS-CONT-LO	Cross-ply	Lubricating Oil	No	Yes	10% Acetone
ENF-UNI-CONT-HF	Unidirectional	Hydraulic Fluid	No	Yes	10% Acetone
ENF-QUASI-CONT-HF	Quasi-Isotropic	Hydraulic Fluid	No	Yes	10% Acetone
ENF-CROSS-CONT-HF	Cross-ply	Hydraulic Fluid	No	Yes	10% Acetone
ENF-UNI-CL-LO	Unidirectional	Lubricating Oil	Yes	Yes	10% Acetone
ENF-QUASI-CL-LO	Quasi-Isotropic	Lubricating Oil	Yes	Yes	10% Acetone
ENF-CROSS-CL-LO	Cross-ply	Lubricating Oil	Yes	Yes	10% Acetone
ENF-UNI-CL-HF	Unidirectional	Hydraulic Fluid	Yes	Yes	10% Acetone
ENF-QUASI-CL-HF	Quasi-Isotropic	Hydraulic Fluid	Yes	Yes	10% Acetone
ENF-CROSS-CL-HF	Cross-ply	Hydraulic Fluid	Yes	Yes	10% Acetone
AL-EA9396	Aluminum	N/A	No	Yes	10% Acetone

The novel process performed to repair the simulated delaminations in this study was seven steps. These steps are outlined in the repair flow chart in Figure 3.34.

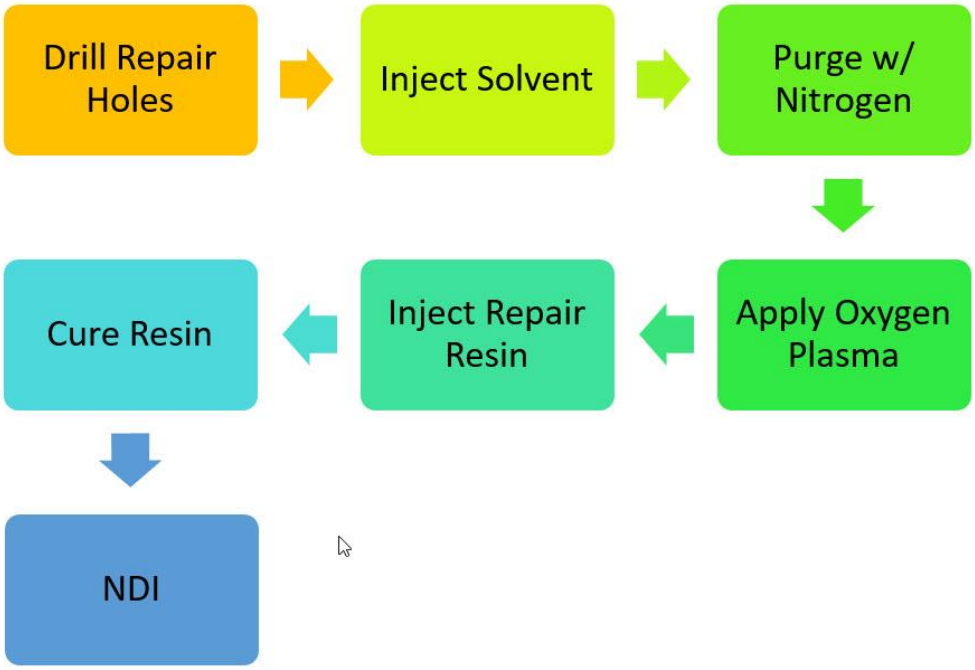

Figure 3.34. Novel injection repair process flowchart

Step 1: Drill Repair Holes: A minimum of two #44 drill bit (2.18 mm diameter) holes will be drilled within the delamination to the depth identified by non-destructive inspection of the defect. If defect depth information is not available, drilling to a depth within two plies of the backside surface was used.

Step 2: Inject Solvent: Acetone was injected to flush out any large contamination that may be within the delamination. This includes using a minimum of 10 mL of acetone to manually flush through the delamination using a 20 mL syringe equipped with a 14-gauge needle (2.1 mm diameter). The solvent was allowed to air dry and evaporate over 24 hours.

Step 3: Purge w/ Nitrogen: As a pretreatment just prior to plasma cleaning, **e**ach delamination would be injected with high purity compressed nitrogen gas at 0.34 MPa for a minimum of five seconds. This is used to flush and make inert the inside of the delamination to ensure the atmospheric plasma treatment is used to clean the surfaces and not attach to oxygen atoms from air within the cavity.

Step 4: Apply Oxygen Plasma: Oxygen plasma is applied to one of the drilled entry point holes using a SurfX Atomflo 500 atmospheric plasma unit equipped with a minibeam head. The plasma head is sealed to the hole using a high temperature O-ring creating a 2 mm standoff distance. The plasma unit was set at 60W power, 10 L/min. Helium (He) flow rate, and 0.15 L/min. Oxygen (O_2) flow rate. The delamination was treated for 20 minutes in each of the two entry point holes.

Step 5: Inject Repair Resin: The diluted EA9396 injection repair resin was placed into a 20 mL syringe equipped with a 14-gauge needle (2.1 mm outer diameter). A minimum of 5 mL of injection resin was placed into each entry hole until the resin would come out the opposite hole. This process was repeated one more time for each hole.

Step 6: Cure Resin: After resin injection, the resin was allowed to set at room temperature for 24 hours. Once the resin was set, it was cured at 88°C for 1 hour with a ramp rate of 1-3°C/min.

Step 7: NDI: Post repair processing, the ENF coupons were inspected for bondline integrity using pulse-echo ultrasonic testing. Single-sided ultrasonic A-scanning was performed by hand using a Mistras PocketUT system equipped with a 3.5 MHz, 6.4mm diameter delay line and transducer

coupled with glycerin gel. A standard was used with known defects of which 50% screen height attenuation within the A-scan were considered areas of disbond. Only areas of repair were inspected on each ENF coupon.

After the modified ENF coupons were inspected, the EA9394 used for sealing the edges was machined off using a lapidary saw with a diamond coated blade. Any remaining adhesive was removed with a 90° angle grinder equipped with a 180 grit sanding disk. The modified ENF coupons were tested in the same manner as described in section 3.1.1. After testing was completed, the coupons were cut using a lapidary saw with a diamond coated blade behind the fracture front and opened for the fracture surface to be analyzed by microscopic observation and fractography.

3.3.6. **Fracture Surface Characterization**

Two primary methods were used to analyze the fracture surfaces using microscopy. The first was digital microscopy to complete surface observation and analysis from 20-2500x. The second was scanning electron microscopy that was completed at high magnification >2500x.

Digital Microscopy

Photomicrographs characterization was performed using a Keyence VHX-7000 digital microscope. Photomicrographs were a planar view of the internal fracture surfaces of the delamination repair region after it was filleted open. Planar view photomicrographs were taken at 20x zoom, however high magnification at 2500x was utilized to observe the fractography of the surface. 2-D picture stitching with surface enhancing high dynamic range features were utilized to ensure high magnification photomicrographs were in focus. In some cases 3-D picture stitching was utilized to determine the field of depth for features such as voids or lifting tears of adhesive.

Scanning Electron Microscopy

A TESCAN Vega 3 scanning electron microscope (SEM) was used to complete high magnification imaging of the planar fracture surfaces from the post-tested modified ENF coupons. SEM setting were: variable pressure chamber at 10 Pa, accelerating voltage at 20 kV, and magnification between 0-900x. A backscatter detector was utilized to complete backscatter electron imaging of the surface to better provide contrast in material and topography. Samples were prepared by wrapping edges with carbon tape to help prevent surfaces from charging due to the high voltage used for imaging. Samples were placed on a platen and imaged without further processing to ensure the surface was not disturbed after testing.

Chapter Acknowledgements

Chapter 3 included material as it appears in the Impact Damage and Injection Repair Strength Restoration, 2021, Massey, Justin, Romasko, Barrett, and Kim, Hyonny, Proceedings of the 36th Annual American Society for Composites Technical Conference and Novel Enclosed Delamination Injection Repair Process for Strength Restoration, 2022, Massey, Justin, Romasko, Barrett, and Kim, Hyonny, Proceedings of the 37th Annual American Society for Composites Technical Conference. Also material from Characterization of Transverse Impact Damage and Internal Contamination of In-Service Composite Aircraft Skins, Massey, Justin, Ellison, Andrew, and Kim, Hyonny, Proceedings of the 2023 Composites and Advanced Materials Expo. In addition material from Advanced Composite Novel Delamination Injection Repair Procedure for Restoration of Laminate Mechanical Properties, Massey, Justin and Kim, Hyonny, in part is currently being prepared for submission for publication with the 2023 US-Japan Composite

Symposium. Finally, unpublished material co-authored with Anagnostopoulos, Konstantinos and Kim, Hyonny for A Comparison of Carbon/Epoxy Composite Interlaminar Laboratory-Based Delamination Methods to In-service Aircraft Damage. The dissertation author was the primary investigator and author for all of these papers.

CHAPTER 4: EXPERIMENTAL RESULTS

In order to address the key engineering challenges discussed in section 2.5, experimental and analytical testing was completed. Each key engineering challenge required multiple types of experimental tests or analysis to determine a viable solution, these experiments are outlined in Figure 4.1.

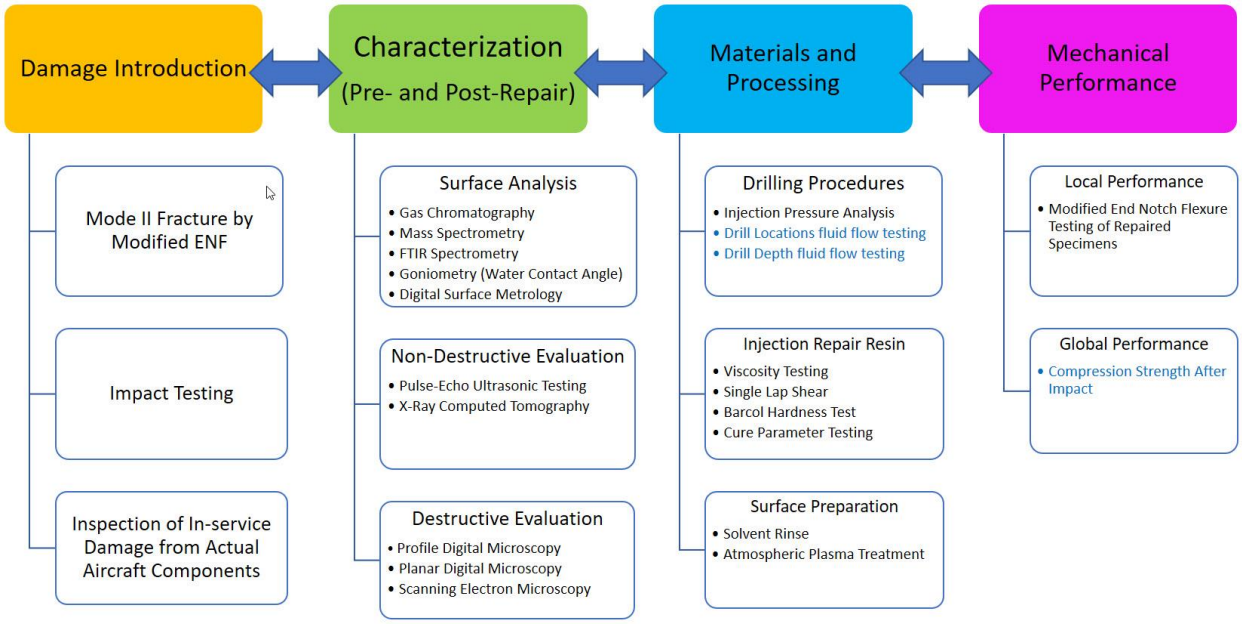

Figure 4.1. Experimentation roadmap of results completed in this study

The key experimental contributions of this study are in each bubble attached below the key engineering challenge. The results of each set of experiments were considered a step toward the goal of creating a novel strength restoring injection repair procedure. Experiments names with blue text are currently being investigated, however preliminary work has been conducted and is discussed in Chapter 6. This Chapter will address and go into depth the results completed for all experiments colored with black text in Figure 4.1.

4.1. IN-SERVICE AIRCRAFT DELAMINATION DAMAGE CHARACTERIZATION

In order to develop a novel injection repair process, first, in-service delaminations described in section 3.1.3 were investigated and characterized to better plan a path forward for repair process development. The characterization of the damages would help determine the topography of fractured surfaces and potential contaminants to better scope repair development. Characterization also helped develop and test potential characterization methods that could be used in the final procedure as a quality check.

4.1.1. **Microscopic Observation**

Photomicrograph of sectioned in-service specimens shown in Figure 3.9 measurement results are shown in Table 4.1. Delamination length was measured for each specimen in one dimension along the cut line axis. Samples IS-1, IS-2, and IS-4 are of similar length. All samples have multi-level delaminations through the thickness, therefore the delamination ply interfaces are denoted for each specimen in Table 4.1. Ply 1 is characterized as the outer moldline ply beneath the paint (usually the outer exterior surface). Maximum delamination opening gaps were also recorded for each sample and are reported in Table 4.1. Maximum delamination sample thicknesses were found to be consistent between specimens IS-1, IS-2, and IS-4, however specimen IS-3 had a larger delamination opening gap likely due to the location of the delamination being on the edge of the component without any substructure support.

Table 4.1. Photomicrograph measurement results

Sample	Length of Delamination (mm)	Delamination Ply Interfaces	Max. Delamination Opening Gap (mm)
IS-1	33.38	4/5, 7/8, 8/9	0.051
IS-2	13.97	2/3, 3/4, 4/5	0.050
IS-3	49.36	7/8, 9/10, 10/11, 11/12	0.252
IS-4	11.42	2/3, 3/4, 4/5	0.052
IS-5	8.69	1/2, 2/3, 3/4, 4/5	0.045

Figure 4.2 shows photomicrographs for specimens IS-1 and IS-2 that were constructed from multiple photographs combined using imaging software. Both specimens exhibit the aforementioned multi-level delamination planes that occurred within all specimens. For this specimen, multiple overlapping layers of delamination can be seen in addition to several ply matrix cracks which can be seen connecting delaminations at different layers.

a)

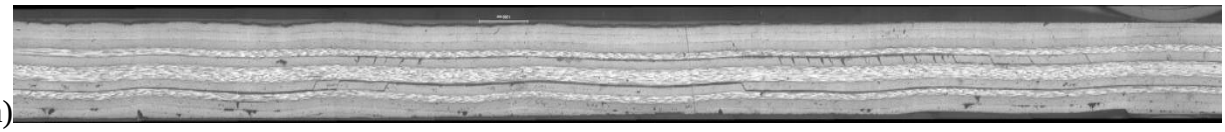

b)

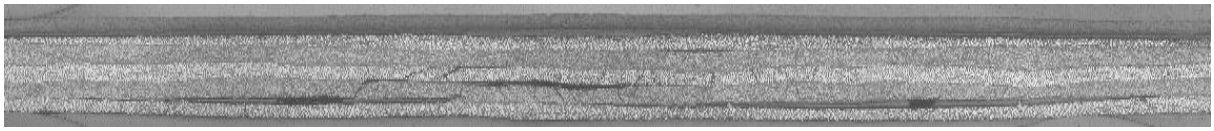

Figure 4.2. Micrograph imaging of (a) Specimen IS-1 and (b) Specimen IS-2

4.1.2. **Ultrasonic Pulse-Echo Testing**

Damage extents were calculated from UT scan TOF maps by detecting the edges of the damage envelope by comparison with the average TOF value from the surrounding undamaged regions. This damage extent determination is shown in Figure 4.3 for Specimen IS-5. Extracted damage sizes are given in Table 4.2. One of the limitations of single sided UT scanning is the

inability to detect delaminations beneath shallower damage (i.e., shadowed) so the damage extent values calculated from the UT scans are only based on the projected damage shape and do not take into account potential additional hidden delaminations.

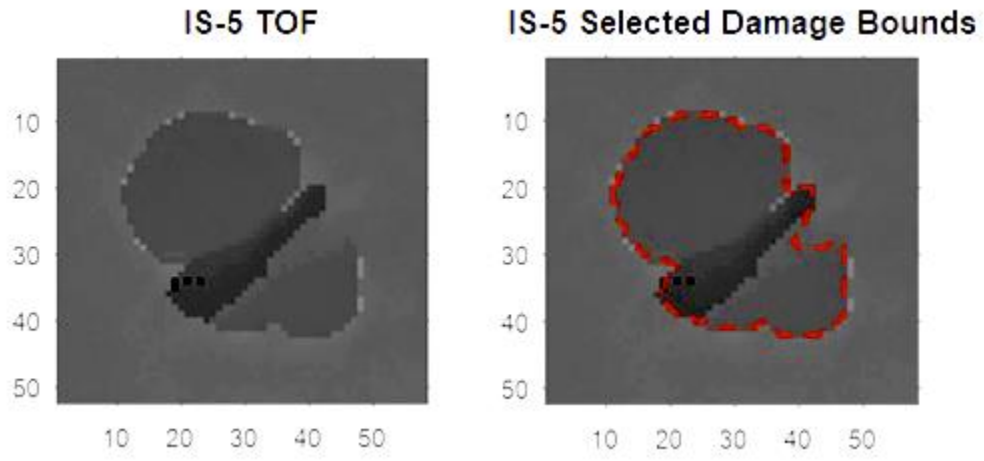

Figure 4.3. Determination of damage extent from UT TOF maps for Specimen IS-5. Units plotted are given in numbers of scans (at 0.125 mm per scan point)

Table 4.2. Ultrasonic testing damage sizing

Sample	Thickness (mm)	Approx. Damage Size (mm^2)	Depth (mm)
IS-1	1.57	916.8	0.53
IS-2	0.89	83.2	0.79
IS-3	1.57	149.23	0.13
IS-4	0.89	24.5	0.71
IS-5	0.89	59.3	0.38

4.1.3. **X-ray Computed Tomography (CT)**

To analyze X-ray CT data sets, the automatic segmentation method developed in Ellison and Kim [27] was used to attempt to separate damage by interface and ply. This method extracts

the specimen from the surrounding void, divides the interior into approximate ply and interface locations, and uses binary thresholding to identify damaged material. However, due to limited contrast, resolution, and uneven sanding of the back surface, automated applications of CT segmentation procedures were unable to produce clear layer-by-layer damage maps for each ply and interface. X-ray CT segmentation results are shown for each interface in Figure 4.4 for Specimen IS-5. Some noise can be seen in the delamination maps, particularly for the back-side ply shown in Figure 4.4, where dashed line streaks can be seen which are due to the uneven sanding of the specimen during the removal of the aluminum core. However, these segmented damage maps provide a solid baseline that could be compared to scan results after an injection repair procedure to determine how well the in-fill has performed at each layer.

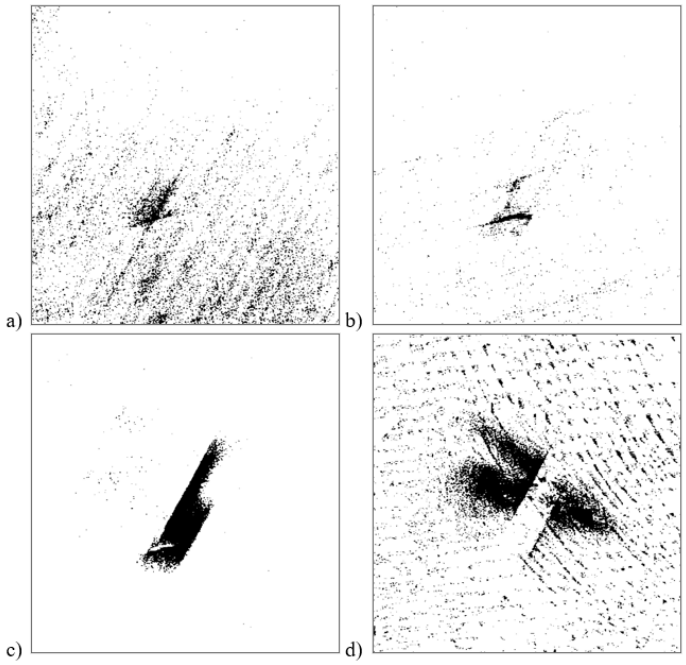

Figure 4.4. CT scan segmentation delamination results for Specimen 4: a) Delamination between plies 1 and 2, b) delamination between plies 2 and 3, c) delamination between plies 3 and 4, d) delamination between plies 4 and 5. Damage maps are binary projections of the damage state where black pixels indicate delamination between layers

4.1.4. **Comparison Between Physical Damage Characterization Methods**

Physical damage characterization was performed with three different methods: destructive sectioning and microscopy, ultrasonic pulse-echo, and X-ray computed tomography scanning. Each of these methods presented difficulties and potential advantages. In order to compare these results the differences in characterization dimensionality need to be bridged. Microscopy provides a high-quality view of the damage along a single 1-D line, UT scanning provides a 2-D damage depth characterization, and CT scanning provides a 3-D damage characterization. An example comparison between the different characterization methods is shown in Figure 4.5 for Specimen IS-2 where the UT results shown in Figure 4.5a have been annotated along the cutting plane to create a parallel with the microscopy image along the cut. The microscopy image shown in Figure 4.5b has been similarly annotated showing a similarity with UT results in terms of relative depths and lengths of delaminations along the cutting line. Compared to the microscopy results, the information given by the UT scan contains only a single layer of delamination at each point and is limited in its ability to capture matrix cracking as seen in the microscopy results.

a)

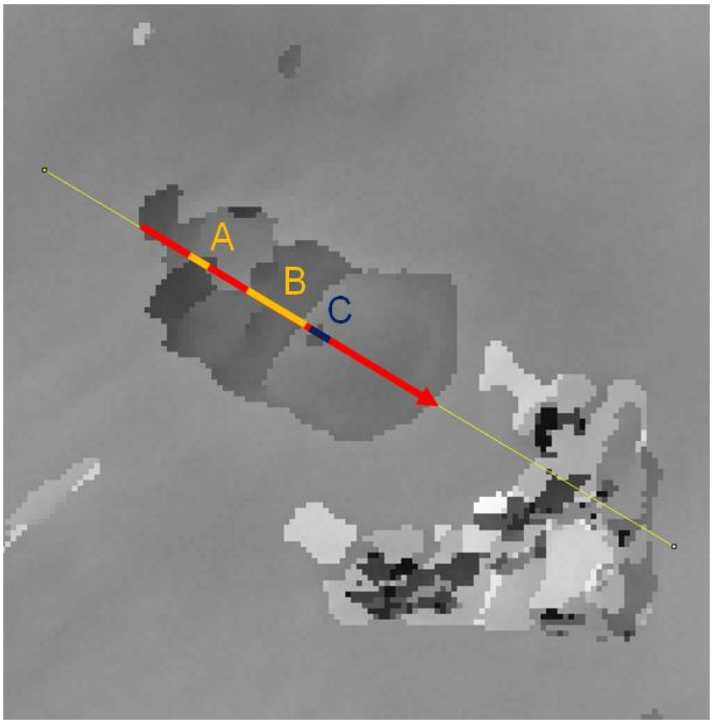

b)

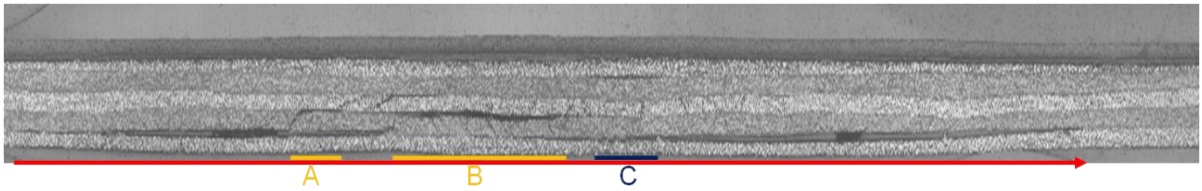

Figure 4.5. Annotated a) UT scan results and b) microscopy results color coded by the presence of delamination along the reference cutting line and the depth of the shallowest delamination as would be detected by UT scanning

4.1.5. **GC-MS Surface Analysis**

Gas chromatograms and mass spectra and were collected for each of five different specimens. Baseline coupons that were fabricated from the same material that was excised from the in-service components. The specimen was sanded with 180 grit aluminum oxide sandpaper and used to serve as a control specimen for comparison. Figure 4.6a exhibits the control gas chromatogram collected from the laboratory fabricated sample. Plotted is the relative abundance versus the retention time. The control chromatogram shows distinct peaks between 17.60 and

23.64 minutes. Peaks up to five minutes could be considered residual hexane solvent that may not have fully escaped the gas chromatography tube. Figure 4.6b-e show the resultant chromatograms from delamination Specimens IS-1 through IS-5, except IS-3. IS-3 was excluded due to the specimen being procured after surface analysis was completed on other specimens. All figures were normalize scaled to 3 $x10^9$ for relative abundance. In comparison, there does not appear to be a significant peak that indicates contamination between the samples collected from the inside of the delaminations. Peaks in the baseline sample appear to have a higher abundance possibly due to residual sanding residue left behind from sample preparation. Mass spectra were inspected at retention times: 17.60, 18.63, 18.71, 19.11, 19.58, 19.81, 20.11, 20.47, 22.17, 22.86, and 23.97 seconds using Xcalibur software accessing the NIST mass spectra library. Figure 4.7 shows an example of a mass spectra collected at a specific retention time, 20.47 seconds, from the chromatogram. The mass spectra were inspected for common ions for hydrocarbon and silicon contamination found at mass-to-charge ratios (m/z) between 29-101m/z and 476-1440 m/z, respectively [71, 72]. 100 μL reference samples were created for the following known contaminants: corrosion preventative compound, jet fuel, lubricating oil, hydraulic fluid and hydraulic fluid. These reference samples are known hydrocarbon archetype contaminants that were compared with the spectra taken form the in-service delaminations. The gas chromatogram for the contaminants exhibited strong spectra responses for all contaminants. Appendix A has the collected GC-MS chromatogram for the in-service samples. Gas chromatography retention times for the known contaminant reference samples were compared to the in-service samples and significant hydrocarbon or silicone-based contamination were not found on any of the four specimens. Mass spectra were analyzed from the highest response chromatogram spectra and could

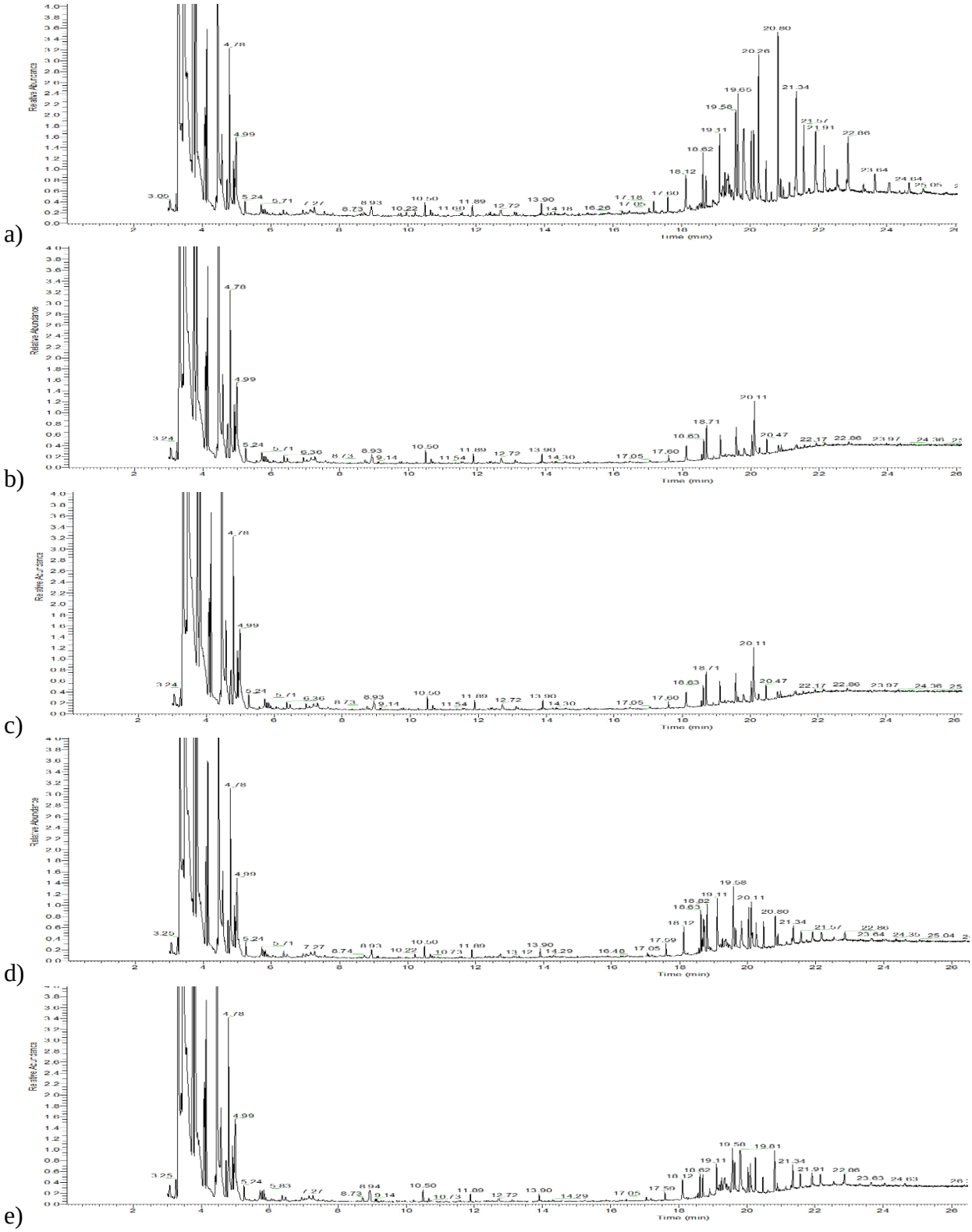

Figure 4.6. Baseline gas chromatography spectra of control and delamination surfaces: a) Sanded control, b) Delamination specimen IS-1, c) Delamination specimen IS-2, d) Delamination specimen IS-4, e) Delamination specimen IS-5

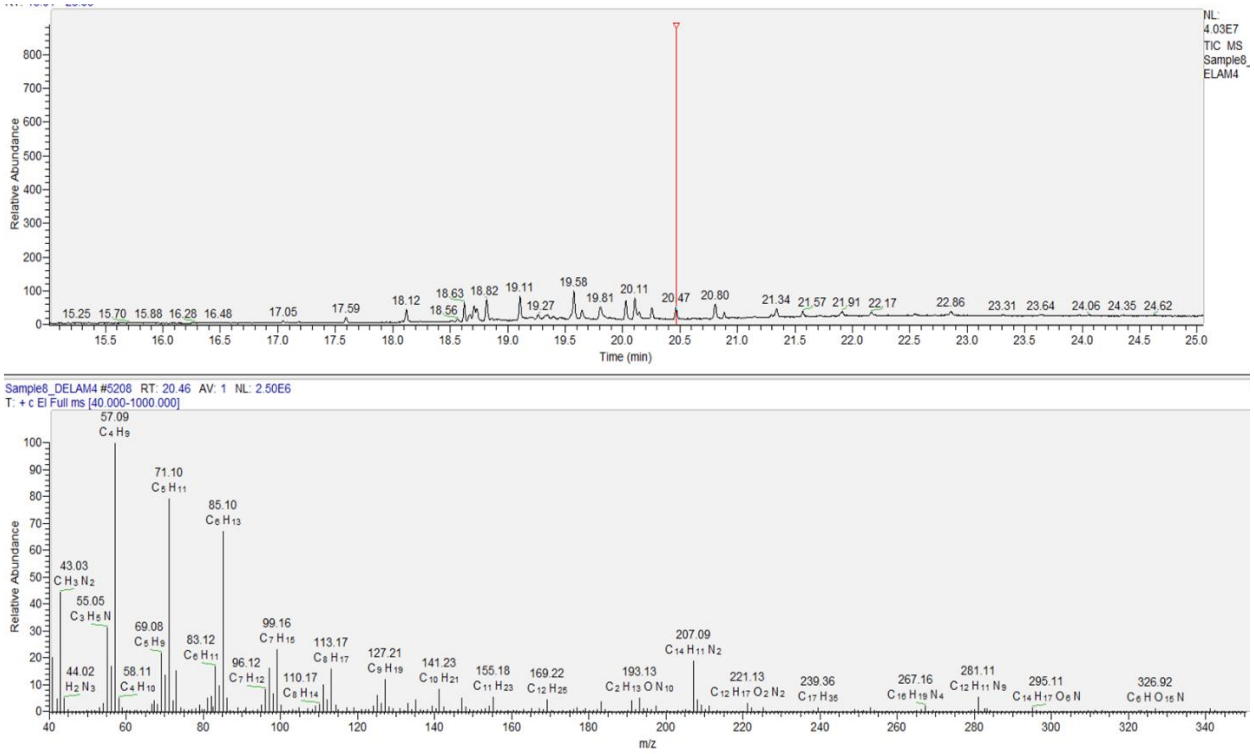

Figure 4.7. GC-MS chromatogram (top) and resultant mass spectra at 20.47 sec

not be correlated to the hydrocarbon archetype reference samples or silicone archetype from the NIST reference library.

Although the excised in-service delamination were analyzed and hydrocarbon or silicone based contamination we not found through GC-MS analysis, the results from the reference sample exhibited a strong response in both gas chromatography and mass spectrometry. Therefore these in-service delaminations pulled from Navy aircraft may not be representative of components in area exposed to large amounts of hydrocarbon compounds, such as a door next to the landing gear system or flight control actuators. However, contamination that may hinder bonding of the injection resin to the internal surfaces of the delamination remain a concern, if the repair is to be considered strength restoring. Although mass spectrometry is a proven method for evaluating

surfaces for hydrocarbon and silicone contamination archetypes, it requires destructive inspection and cannot be performed during an injection repair procedure, therefore a real-time surface analysis system would be required to investigate delaminations for contamination. In addition, further work must be completed to investigate a larger variety of delaminations throughout the aircraft to gain more insight to fluid contamination within delaminations.

4.2. CHARACTERIZATION AND COMPARISON OF LABORATORY MANUFACTURED DELAMINATION METHODS WITH IN-SERVICE DAMAGE

In order to better define the test specimens and procedures used to develop a novel injection repair process, characterizing the laboratory manufactured fracture surfaces and comparing to actual in-service delaminations was important to ensure the coupon-level testing is representative of fractures that are to be repaired on actual aircraft. Therefore comparing the delamination surface characteristics produced by different fracture methods was completed and referenced to in-service delamination surfaces prior to testing novel injection repair procedures.

4.2.1. **Impact Testing Results**

Impact testing was completed as an established method for creating delaminations through transverse impacts. An extensive study on impact of PMC materials was completed as part of Romasko's MS thesis [12] which complement and supports this project's overall aims. More exhaustive reporting of the impact testing results can be found in Romasko's MS thesis and this is a summary of the efforts as it relates to the development of a novel injection repair procedure. From the impacts panel test results it was found that the 10 to 20 J impact energy range created the delamination diameter sizes between 6 to 50 mm (as shown in Figure 3.7). The 40 J impacted specimens had very large delaminations (> 50 mm dia.), which were deemed to be outside of the repair scope for injection

repair. However the 40J specimens could be used to characterize complex delaminations surfaces due to the multi-layer damage including backside breakout of surface plies. Specimens have subsequently been impacted at ranges of 10, 15, and 20 J to be repaired. In Table 4.3, the test matrix is shown, summarizing completed impact tested specimens.

Table 4.3. Impact testing matrix

Panel Type	Layup	Thk. (mm)	Qty. Planned [Tested]:			
			10 J	15 J	20 J	40 J
H	$[45/-45/0/0/45/-45/0/0/45/-45/0/0/\underline{90}]_S$	3.3	9	9	9	2
M	$[45/-45/0/0/45/-45/0/45/-45/0/45/-45/\underline{90}]_s$	3.3	9	9	9	--
S	$[45/-45/0/45/-45/90/45/-45/0/45/-45/90/\underline{90}]_s$	3.3	9	9	9	--

As seen in Table 4.3, a total of 83 specimens were impacted, resulting damage was mapped by hand-held gel-coupled ultrasonic A-scans to find the extent of damage (See Figure 3.7). The delamination size versus impact energy for all tested specimens and panel types is summarized in Figure 4.8. Results show that the damage area of the laminate type S tends to exhibit larger damage size, for a given impact energy. It is seen that panel H and panel M have delamination sizes that fall within the delamination diameters of interest; however, panel S begins to exceed the 50 mm upper boundary that is being pursued for the injection repair. As panel S is the softest laminate of the three layup types, it is the most susceptible to damage. Error bars are the standard deviation to delamination size measured. However, the impacted specimens at this level will still be attempted to be repaired in the future of this study.

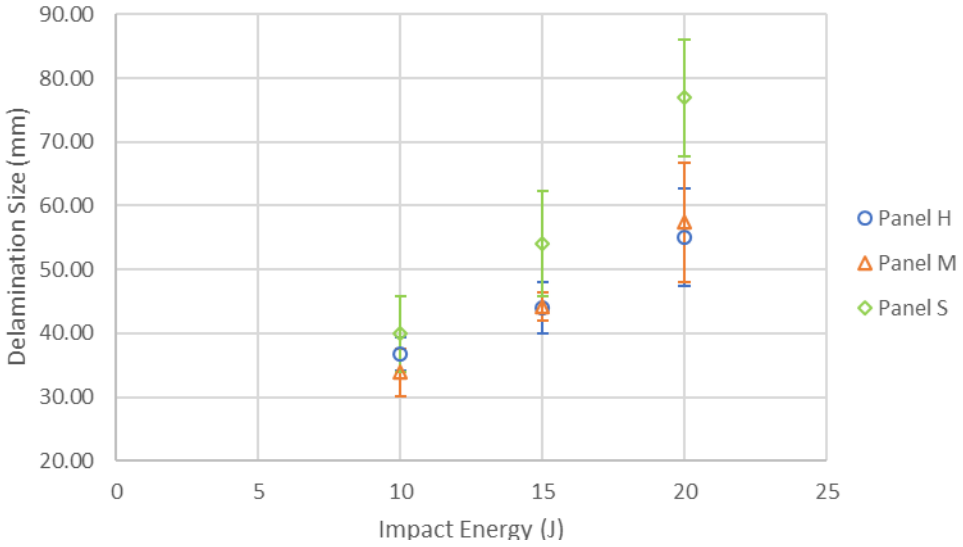

Figure 4.8. Delamination size versus impact energy of specimens from 10-20 J

As a result of the impact testing, fractures induced by transverse impact produce such a complex multi-planar delamination and damage state that a simpler coupon configuration utilizing a modified ENF coupon was chosen to first be used as a simpler, but representative platform for repair process development.

4.2.2. **Modified ENF Baseline Fracture Testing Results**

Modified ENF Testing was conducted as described in section 3.1.1 on baseline laminate coupons with a PTFE film crack starter. Laminate cracks were tracked using a loupe and verified with a microscope. Baseline test sets were completed for all ENF laminate configurations. Mode II critical fracture toughness (G_{IIC}) was determined for pre-cracked (PC) test configuration in accordance with ASTM D7905. The compliance calibration method utilizing Equation (4.1) for and PC testing configurations to determine the G_{IIC}.

$$G_{IIC} = \frac{3mP^2a_o^2}{2B} \tag{4.1}$$

First, the load versus displacement curves of the different initial crack lengths (a_o) at 20 mm, 30 mm, and 40 mm were plotted to determine the slope of each case. The compliance (C) is the inverse of slope for each load versus displacement plot. An example of a load versus displacement plot to determine the different compliance for each initial crack length can be found in Figure 4.9.

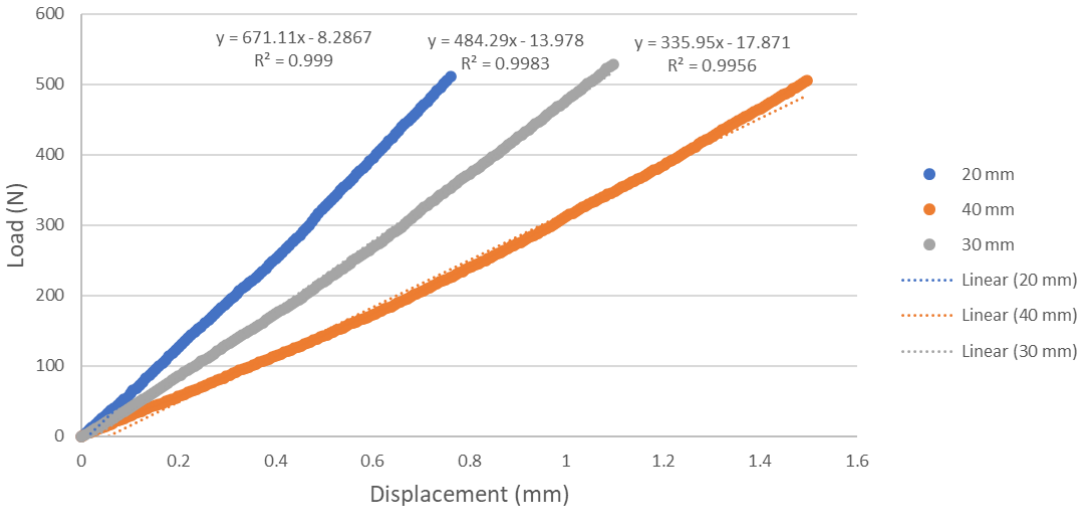

Figure 4.9. Sample load versus displacement plot to determine compliance of ENF coupon

Once the compliance of each initial crack length load case was determined, it was plotted versus a_o^3 for the multiple compliance calibration tests. The compliance calibration coefficient (m) is found through the slope of the partial least squares fit of multiple compliance calibration tests as shown in Figure 4.10.

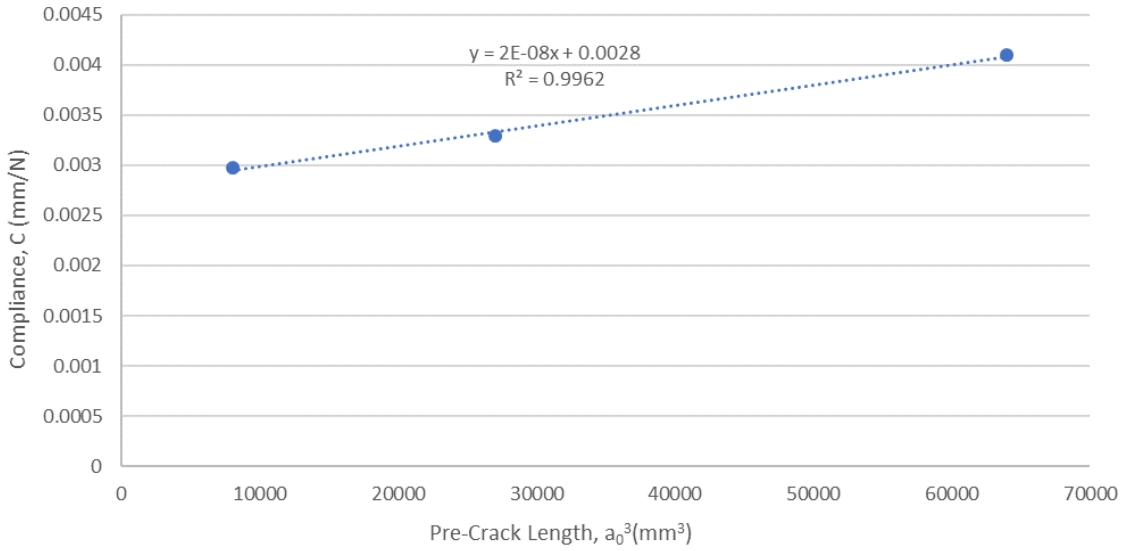

Figure 4.10. Compliance calibration partial least squares fit

A separate m coefficient was determined for each PC fracture test set. Maximum load (P) and specimen width (B) are also factored into the G_{IIC} calculation. All baseline coupons were loaded and fractured between two to three times and a consistent maximum load was obtained. Since consistent test values were obtained for all baseline coupon fractures, average fracture values are displayed in this study. Table 4.4 shows the average results of modified ENF: specimen width, crack length, failure load, compliance calibration coefficient, and resultant $G_{IIC.}$ Data is an average collected from 45 data points for each panel type.

Table 4.4. Baseline modified ENF results

Panel Type	Specimen Width (mm)	Avg. Crack Ext. Length (mm)	Avg. Failure Load (N)	Compliance Coeff., m	Avg. G_{IIC} (J/m^2)	StDev (J/m^2)
Unidirectional	50.9	25.8	1484.6	$2x10^{-8}$	857	213
Quasi-Isotropic	50.9	23.0	1257.2	$3x10^{-8}$	1302	410
Cross-Ply	51.0	19.4	972.5	$3x10^{-8}$	831	401

The average crack extension length for all specimen lay-up configurations was approximately the same due to standard deviations of crack extensions for unidirectional, quasi-isotropic, and cross-ply panel types being 8.5 mm, 7.3 mm, and 5.3 mm, respectively. The average load decreased from 1484.6 N with unidirectional coupons, down to 1257.2 N for quasi-isotropic and 972.5 N for cross-ply. Although the average failure load decreased depending on the lay-up configuration, the average G_{IIC} was approximately equivalent between unidirectional and cross-ply laminates and higher with quasi-isotropic laminates. This shows that the compliance calibration is imperative when determining the G_{IIC}. The quasi-isotropic sample set had a higher average G_{IIC} due to the increase in compliance calibration coefficient when compared to the unidirectional and cross-ply laminate configurations.

Since consistent test values were obtained for all baseline coupon sample set fractures and only pre-cracked mode II fracture values are displayed in this study. Shown in Figure 4.11 is an example of the load versus displacement curve for the pre-cracked modified ENF baseline PMC testing for each laminate configuration. These curves were consistent within each sample set.

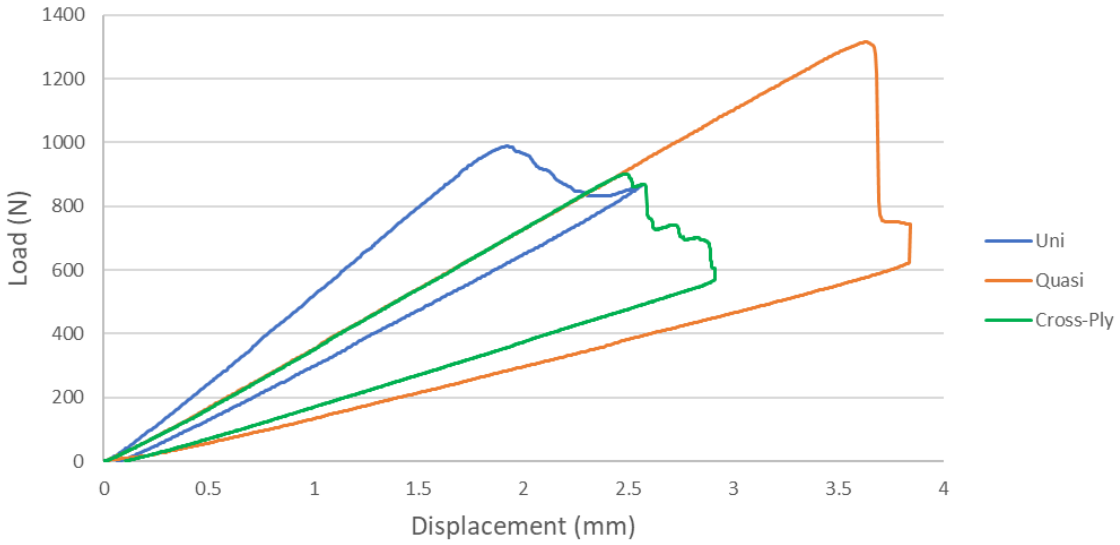

Figure 4.11. Load vs. displacement curve of baseline PMC laminate modified ENF coupons

The load versus displacement curves show that the unidirectional laminate had the highest stiffness of 543 N/mm while the quasi-isotropic and cross-ply laminates had almost identical stiffness of 371 N/mm prior to fracture. The stiffness for all coupons lowered after fracture when comparing the slopes in the elastic region and to the unloading slope.

4.2.3. **Microscopic Profile Cross-Section Analysis**

A key interest is to understand whether lab-created delamination surfaces are representative of in-service delamination. Samples of modified ENF, impact tested, and in-service delaminations were cut to collect microscopic through thickness profiles images of the delamination cross-sections. The profile view of the samples was utilized to verify traverse formation of the damage including characterization of multi-ply damage. Profile views of the delaminations are shown in Figure 4.12 through Figure 4.14. Delamination locations are described as the first ply being the top ply shown in each photomicrograph.

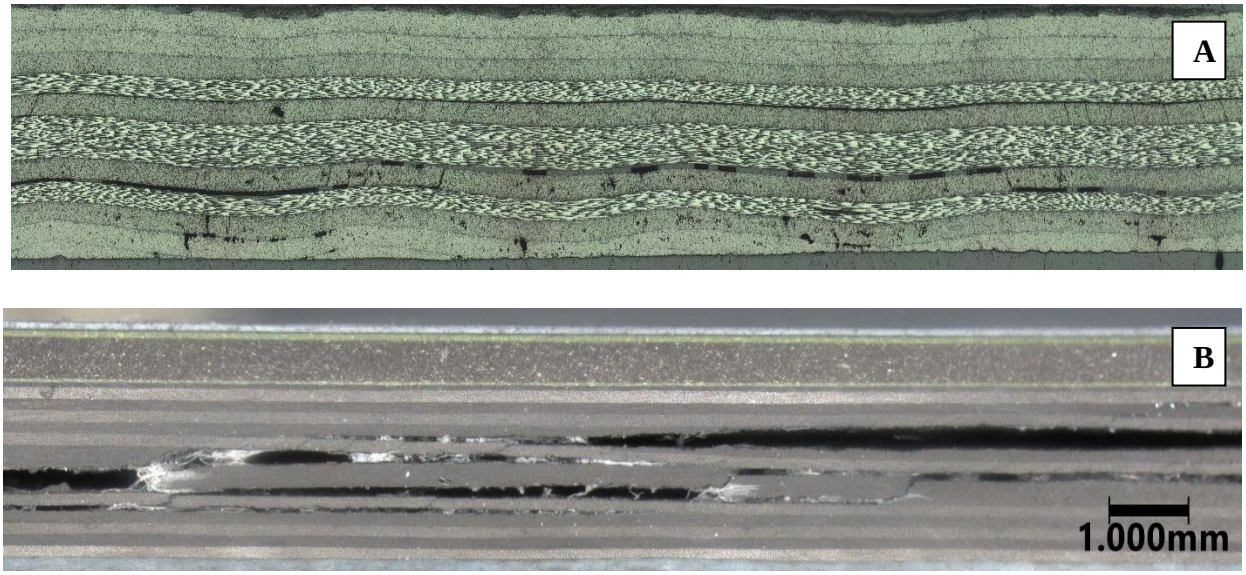

Figure 4.12. In-service delamination fracture profiles: A. Enclosed delamination, B. Edge delamination

The enclosed in-service delamination shown in Figure 4.12A exhibits a multi-level damage, including delaminations observed between: plies 4 and 5 (90°/0° interface), plies 7 and 8 (90°/0°), and plies 8 and 9 (0°/90°). Transverse micro-cracks are also observed in ply 5 (0°) and ply 8 (0°). The "pyramid" shape of the multi-level damage indicates that the enclosed delamination was initiated through a transverse impact. The profile photomicrograph of the in-service edge delamination (Figure 4.12B) also shows a multi-layer damage. Delaminations are observed between: plies 4 and 5 (90°/0°), plies 5 and 6 (0°/90°), plies 7 and 8 (90°/0°), and plies 8 and 9 (0°/90°). Transverse microcracks were observed within plies 4 through 9.

The fracture shown in the PTFE insert (Figure 4.13A) and unidirectional ENF sample (Figure 4.14B) were primarily confined at the mid-plane depth of the laminate between the 12^{th} and 13^{th} (0°/0°) plies. For the PTFE insert there is a blunt ending to the simulated fracture (see right side of Figure 4.13A). For the unidirectional ENF sample, as the fracture grew within the

coupon during loading, there was no evidence of crack front moving between plies or into either sub-laminate. The crack propagation within the quasi-isotropic ENF coupon is shown in Figure 4.13C. The fracture first appears between plies 13 and 14 (45°/0°). The coupon was then unloaded, flipped and loaded again, where the fracture propagated as a transverse micro-crack back up to between plies 11 and 12 (0°/45°). The movement of fracture between plies is due to coupon being loaded and then flipped and loaded again. Once flipped and loaded, the inverse shear created between the two sub-laminates as a result of the mode II loading caused a 45° transverse micro-crack and relocation in depth of the crack front. The relocation of the crack is due to the change in interlaminar shear principal stresses from flipping the coupon and re-loading.

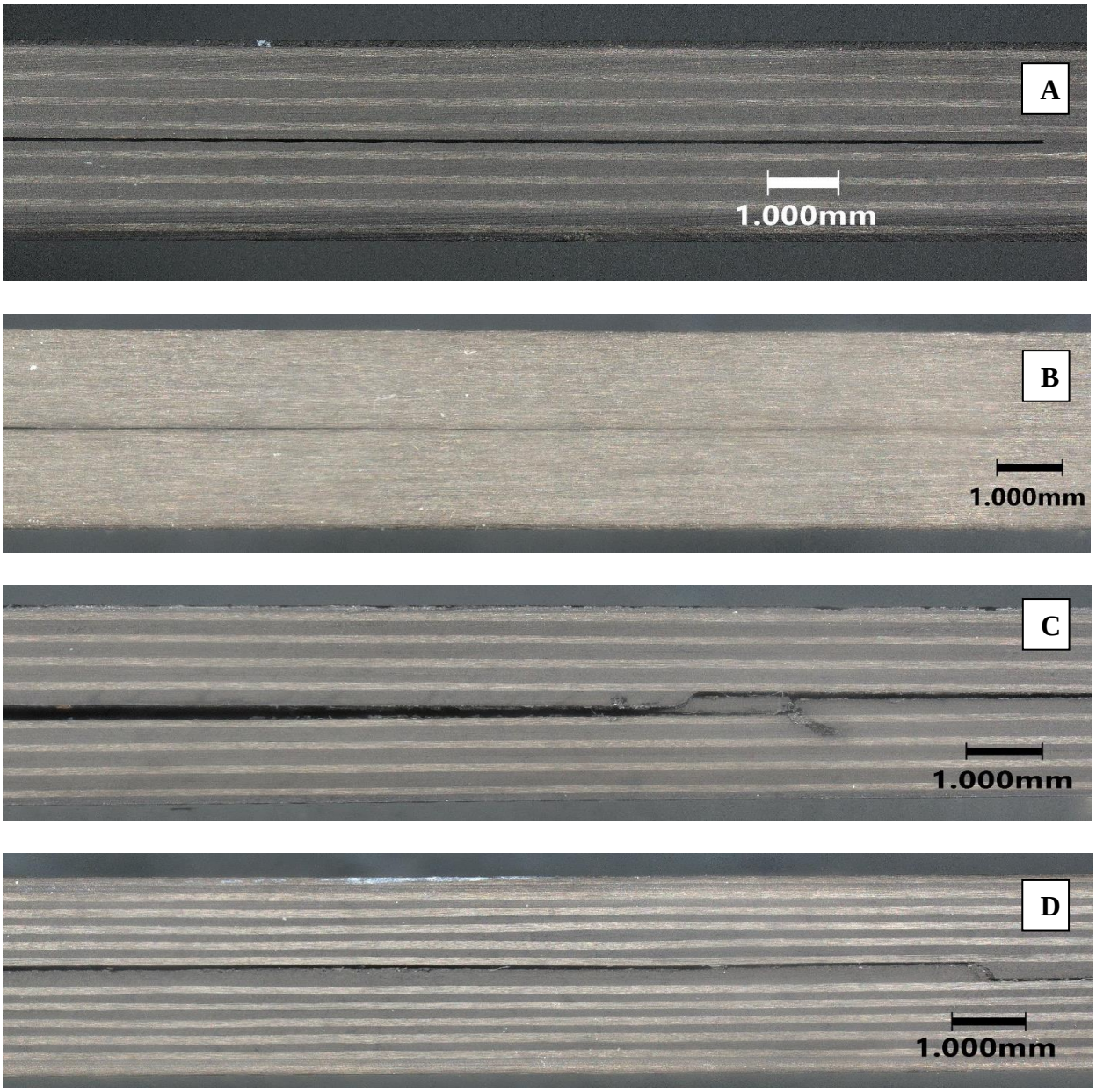

Figure 4.13. ENF Delamination fracture profiles: A. PTFE insert, B. Unidirectional ENF, C. Quasi-Isotropic ENF, and D. Cross-Ply ENF

For the cross-ply ENF specimen (Figure 4.13D), the crack profile characteristics exhibit a fracture that starts between plies 13 and 14 (90°/0°). The fracture stays between plies and 13 and 14 until the coupon is unloaded, flipped, and loaded again. The fracture then migrates back up to

between plies 12 and 13 (0°/90°). The coupon was unloaded, flipped again, and loaded for a third time where the crack migrated back to between plies 13 and 14. This migration of the crack front was caused by the changing shear force within the laminate due to flipping the coupon during mode II loading, much like the behavior of the cracks found in the quasi-isotropic ENF coupons, however the progression of the crack in the cross-ply ENF coupons was more pronounced due to the 0°/90° cross-ply lay-up where the crack was able to navigate transversely through the 90° plies.

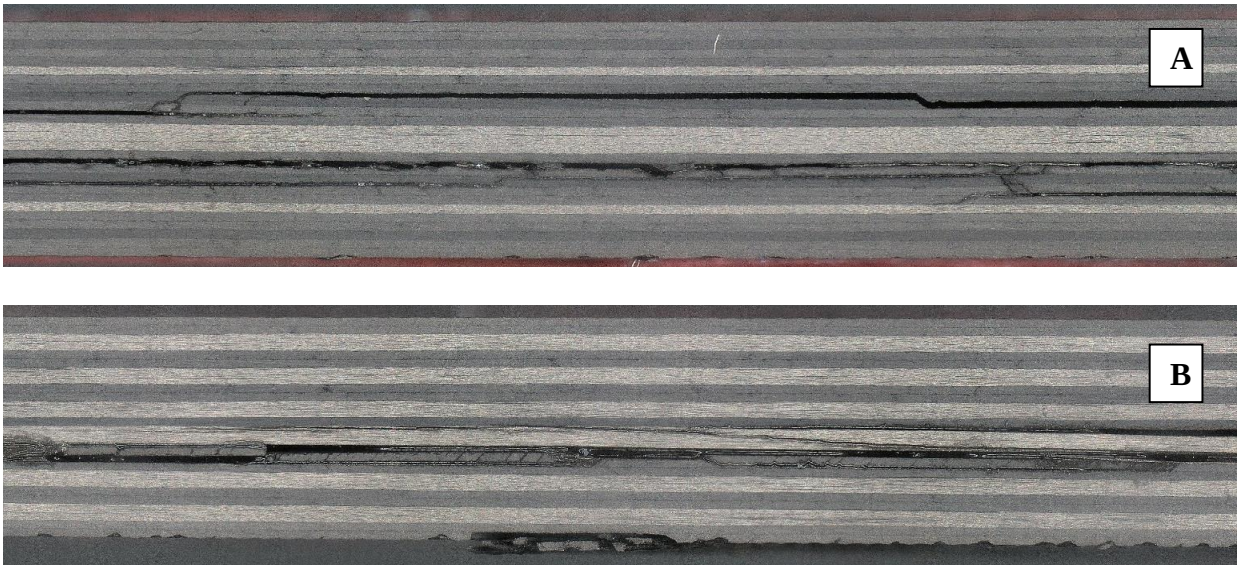

Figure 4.14. Lab impacted delamination fracture profiles: A. 20J impact and B. 40J impact specimens

The fracture created in the 20J impact specimen (Figure 4.14A) exhibits a multi-level delamination state. Delaminations were exhibited between the interfaces of the following plies: 8 and 9 (-45°/0°), 9 and 10 (0°/45°), 10 and 11 (45°/-45°), 14 and 15 (90°/-45°), 15 and 16 (-45°/45°), 16 and 17 (45/0°), 17 and 18 (0°/-45°), and 18 and 19 (-45°/45°). Several of the delaminations overlapped and transverse microcracks were also observed in multiple plies connecting the delaminations in a tiered pyramid pattern indicative of an impact damage. The 40J impact

specimen (Figure 4.14B) also exhibited a complex multi-level delamination, however less fractures were observed compared to the 20J impact specimen. Delaminations were observed between the interfaces of the following plies: 12 and 13 (-45°/90°), 13 and 14 (90°/-45°), 15 and 16 (45°/0°), 16 and 17 (0°/-45°), and 17 and 18 (-45°/45°). The delaminations observed in the 40J impact panel did not initiate until the 12th ply from the impact surface, whereas the 20J impact specimen had delaminations observed start at the 8th ply from the impact surface. The 40J impact coupon did have some backside breakout of the 25th ply due to the force of the impact. This may be why less damage was contained within the laminate.

The ENF coupons exhibited the least complex cross-sectional damage when compared to the impact and in-service delaminations. The quasi-isotropic and cross-ply ENF coupons had relatively simple multi-level delaminations. However, the coupons subjected to laboratory impact damage appeared to be highly complex damage states compared to the in-service delaminations, with multiple damage layers including breakout of damage on the backside of the coupon as seen in the 40J impact specimen. Therefore from the side profile view perspective, the laboratory impact delaminations are more aggressive than the extracted in-service and modified ENF fractures.

4.2.4. **Microscopic Planar Surface Analysis**

Delaminated specimens from: in-service components, modified ENF, PTFE insert, and impact coupons were excised and filleted open to expose the planar fracture surface. Three-dimensional representation of each delamination surface was captured using the digital microscope as described in section 3.2.2 with 3-D rendering capability as shown in Figure 4.15 through Figure 4.17.

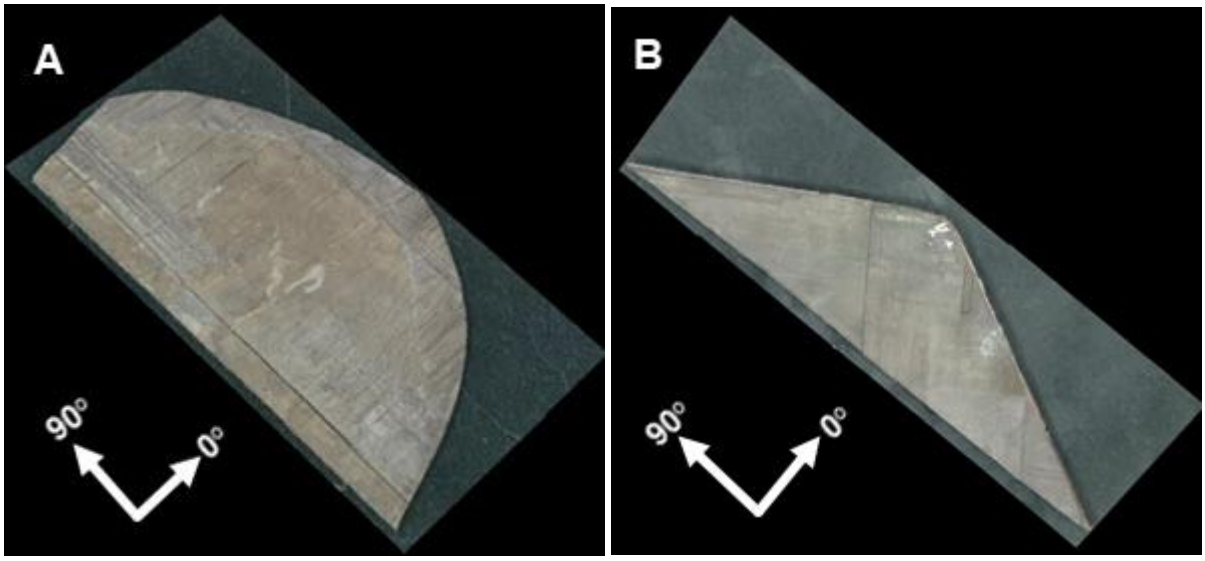

Figure 4.15. In-service delamination 3-D isometric fracture surface planar views: A. Enclosed delamination, B. Edge delamination

The in-service enclosed delamination (Figure 4.15A) also exhibits multi-ply damage; however the primary exposure is the 0° ply. Areas of ply stripping, which are regions of the ply lifted and missing, are found toward the edge of the specimen where 90° plies are exposed. The in-service edge delamination surface Figure 4.15B) exhibits a multi-ply damage by exposing both 0° and 90° plies on the surface. The ply orientations observed are consistent with the depth of the delaminations and ply orientations found when inspecting the profile of the damage.

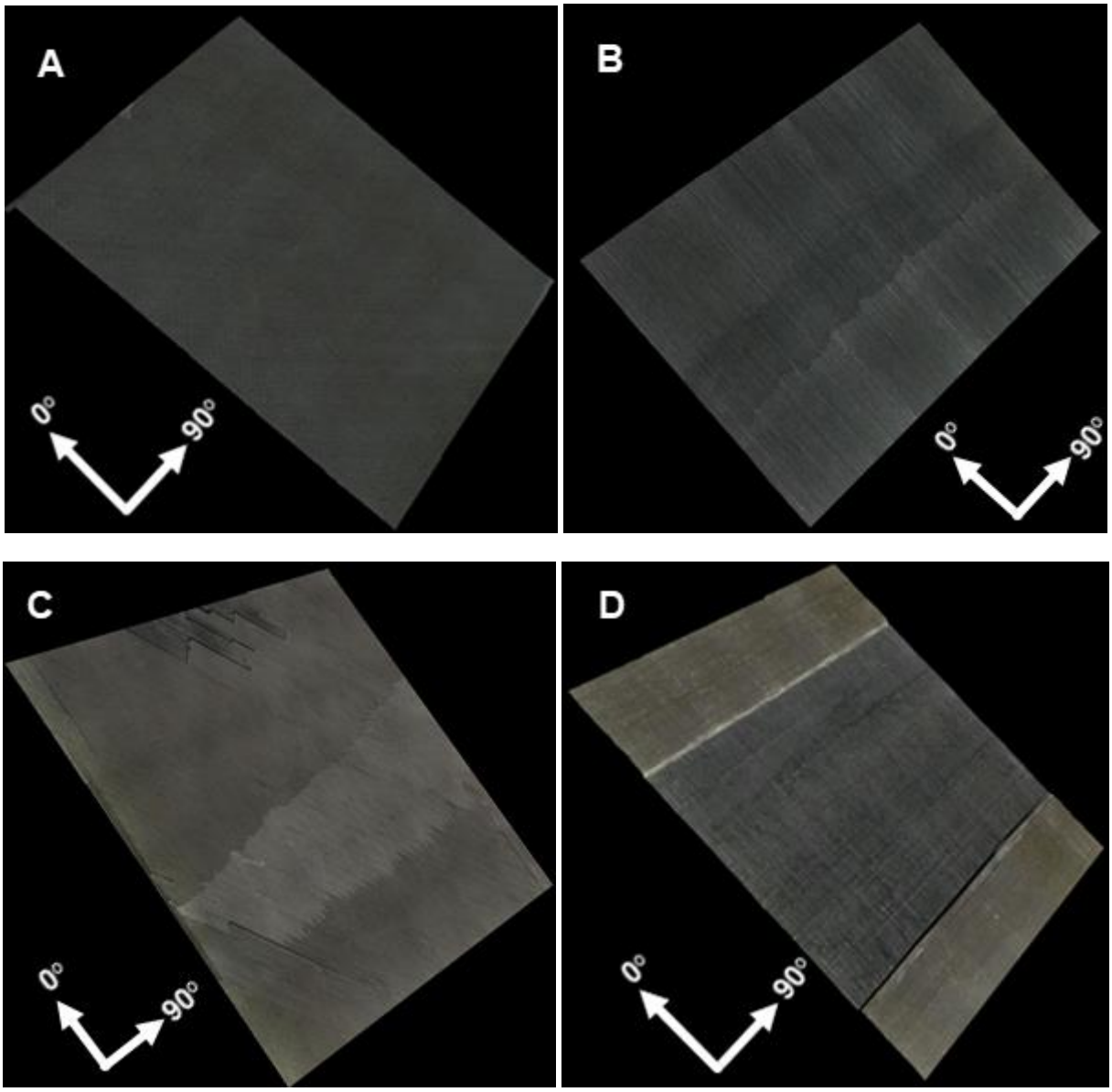

Figure 4.16. ENF delamination 3-D isometric fracture surface planar views: A. PTFE insert, B. Unidirectional ENF, C. Quasi-isotropic ENF, and D. Cross-ply ENF

The PTFE insert manufactured delamination surface is shown in Figure 4.16A. A minor pattern, due to the fiberglass carrier cloth used in the PTFE insert was observed on the delamination surface. There was no fracture as a result of using the Teflon insert, therefore all surfaces were found to be an intact epoxy layer. The unidirectional ENF coupon (Figure 4.16B) displays only 0° ply orientation, however there is a color change on the fracture surface. This color change is

consistent with the measured end of fracture front from ENF testing. When the coupon was flipped and loaded for the second time the fracture progressed and appears as a lighter color. This is due to the coupon experiencing mode II fracture in the opposite direction in the second fracture region, therefore the fracture of the matrix in each region experienced the opposite sliding mode. There was no change in ply depth observed. The quasi-isotropic ENF coupon fracture surface (Figure 4.16C) displays a multi-ply damage state, however all plies exposed were found to be in 45° ply orientation. The change in fracture depth for the quasi-isotropic ENF coupon was also consistent with the end of the fracture front, this being caused by the coupon being loaded, flipped, and loaded again. Although at the top of the coupon the multi-ply damage is observed, lower on the surface is discoloration consistent with the unidirectional coupon where the fracture front was confined to the same ply interface. The cross-ply ENF coupon (Figure 4.16D) exhibits a multi-ply fracture. The fracture is extremely organized, where the coupon was loaded and the fracture front ended is where the ply orientation changes. The coupon was flipped after each loading and the fracture depth also changed at each loading. It can be seen in Figure 4.16D where the top region is the 90° ply #13, then the middle region is the 0° ply #11, and the bottom region is again ply #13.

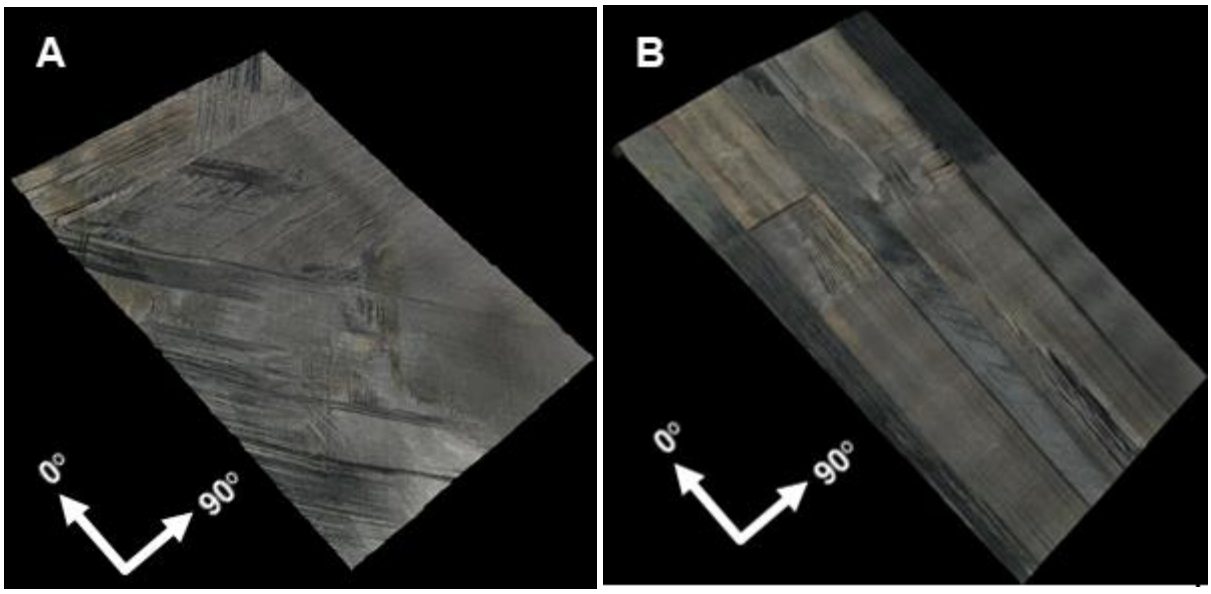

Figure 4.17. Impact delamination 3-D isometric fracture surface planar views: A. 20J lab impact, and B. 40J lab impact specimen

The 20J impact specimen fracture surface (Figure 4.17A) exhibited a multi-layer delamination. Areas of: 90°, 45°, and -45° plies were observed. The high complexity of this impact damage revealed multiple plies at different depths and was consistent with the ply orientations found in the profile photomicrography. The 40J impact specimen fracture surface (Figure 4.17B) also exposed multiple ply orientations primarily exposing 0°, -45°, and 90° plies. The panel was segmented in the 0° direction, where the fracture traveled furthest due to the impact. This was primarily observed in the 15^{th} and 16^{th} ply interface when inspecting the profile of the delamination. Although the segmentation was consistent along the 0° ply orientation, the depth varied along the 90° axis of the coupon.

The three-dimensional planar micrographs were able to qualitatively display the different ply orientations and fracture surfaces of the delamination samples. The in-service delaminations exhibited multi-layer damage however only one to three differing plies were exposed. The unidirectional ENF and PTFE crack initiator coupons, had a single plane of delamination surface

exposed. The quasi-isotropic and cross-ply ENF coupons also both had one to three differing plies exposed. Both 20J and 40J impact coupons displayed very complex multi-layer (> 3 plies) damages with complex depth changes and varying ply orientations exposed.

4.2.5. **Delamination Fracture Surface Metrology**

The delamination coupons were also analyzed using the digital microscope surface metrology features. Surface profilometry and roughness were captured for all coupon fracture surfaces in the 0° and 90° directions. An example of a profile location is shown in Figure 4.18, taken on an example cross-ply modified ENF coupon in the 90° direction. The resulting raw profile data is shown in Figure 4.19. The raw data for profilometry data was processed in accordance with ASME B46.1 [84], using a Gaussian filter with weighting function in equation (4.2).

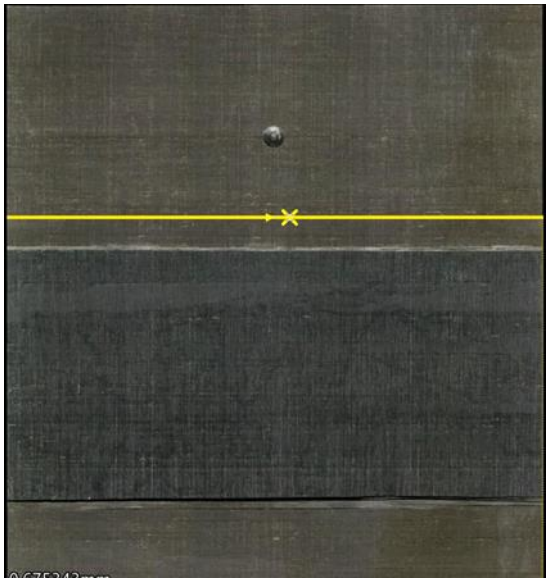

Figure 4.18. Example profile location on a cross-ply modified ENF fracture surface

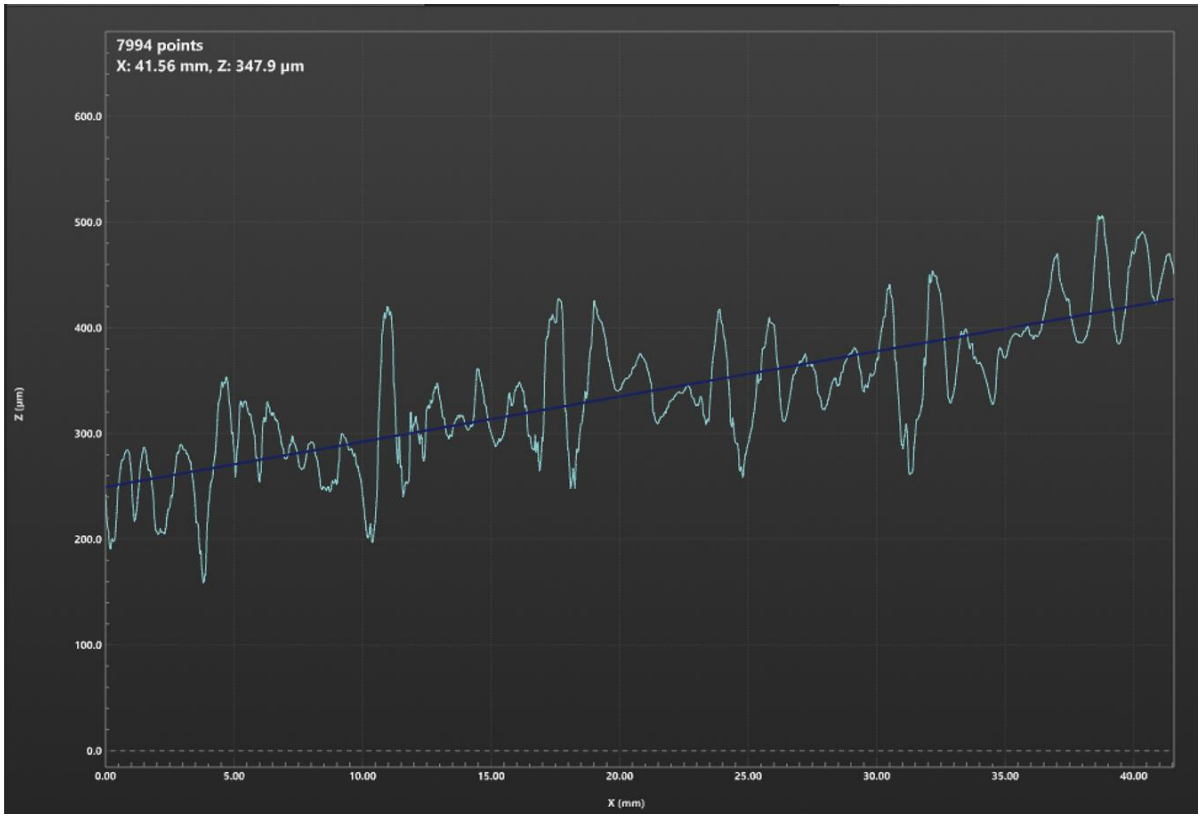

Figure 4.19. Delamination profilometry measurement raw data

$$z'(x_1) = \int_{-\infty}^{+\infty} S(x)\, z(x + x_1) dx \qquad (4.2)$$

Where, $z(x+x_1)$ is the unfiltered profile as a function of position near a point x_1, $z'(x_1)$ is the filtered profile calculated for x_1, and S(x) is the weighting function. All raw data collected for profilometry of the fracture surfaces was filtered with a long-wavelength cutoff (λ_c) of 0.8 mm and a short wavelength cutoff (λ_s) of 2.5µm. An example of the filtered profilometry data is shown in Figure 4.20.

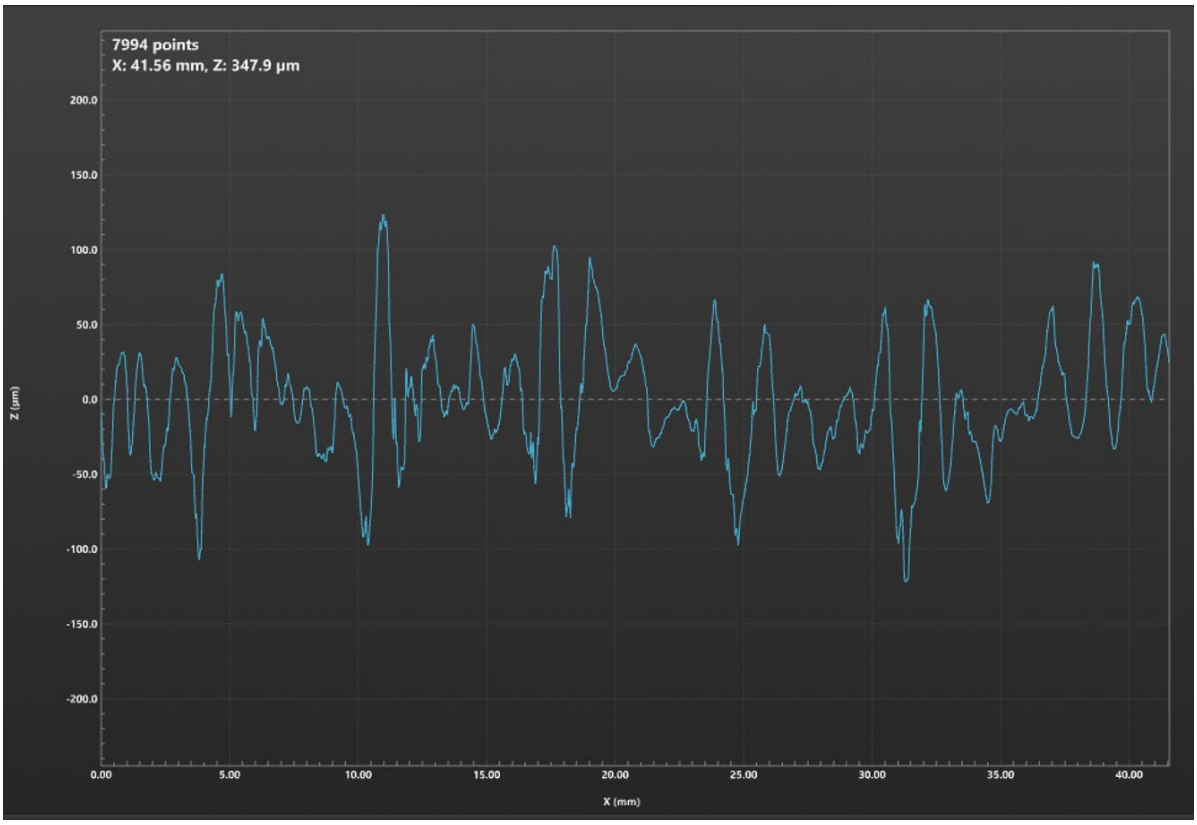

Figure 4.20. Filtered delamination profilometry data

Once the profilometry data was filtered, it was analyzed for: the arithmetic mean profile (P_a) and roughness (R_a) found using equation 4.3, root mean square profile (P_q) using equation 4.4, and the Kurtosis (P_{ku}) to measure the height distribution of the surfaces using equation 4.5.

$$P_a, R_a = (1/L)\int_0^L |Z(x)|dx \tag{4.3}$$

$$P_q = \left[(1/L)\int_0^L Z(x)^2\,dx\right]^{1/2} \tag{4.4}$$

$$P_{ku} = \frac{1}{P_q^4}\left[\frac{1}{L}\int_0^L Z^4(x)dx\right] \tag{4.5}$$

"Z(x)" is the profile height function and "L" is the evaluation length. The sampling lengths used for profilometry was equivalent to "λ_c". Sampling lengths used for roughness analysis was 0.8 mm. Results of the metrological analysis of the arithmetic average surface profile and root mean square profiles taken along the 0° and 90° direction are shown in Figure 4.21 and Figure 4.22, respectively.

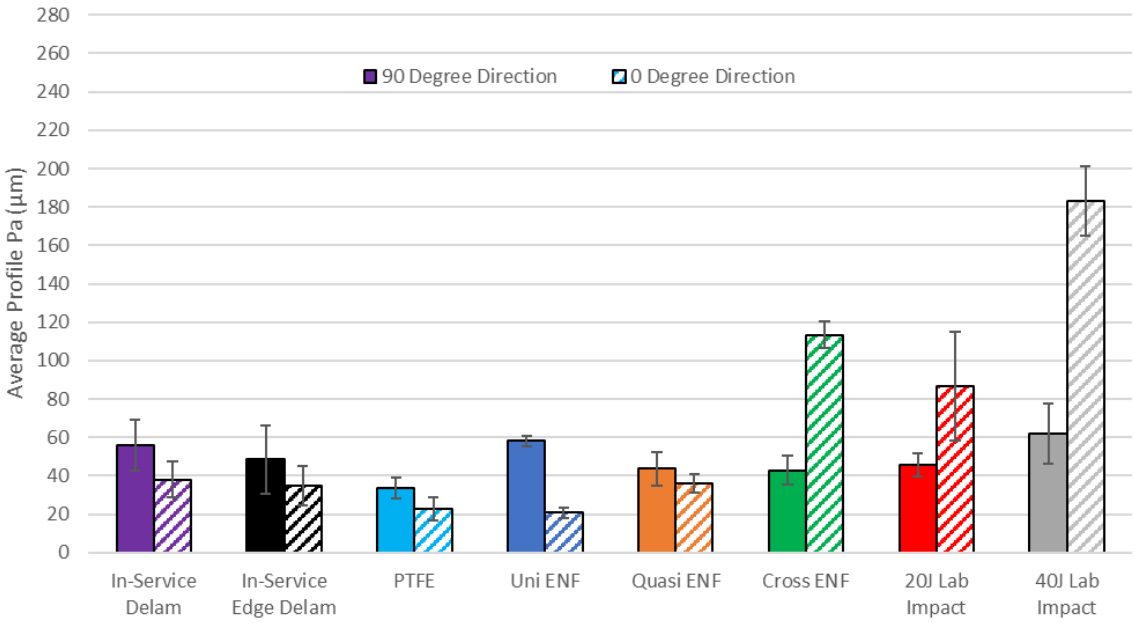

Figure 4.21. Arithmetic average profilometry (P_a) values of delamination surfaces

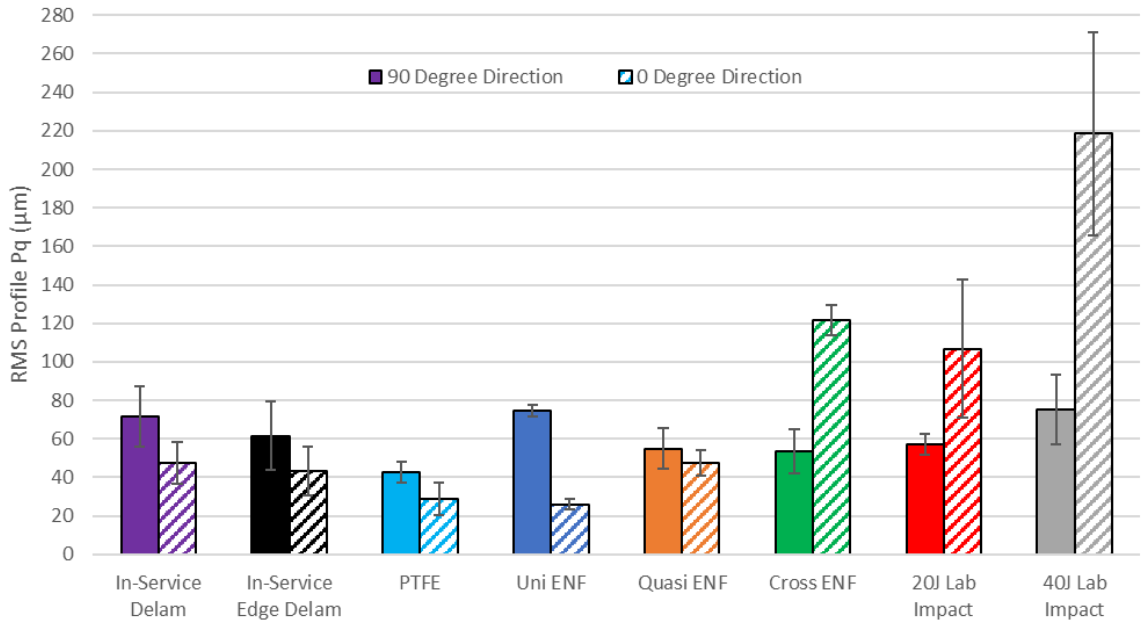

Figure 4.22. Root mean square profilometry (P_q) values for delamination surfaces

The arithmetic average and root mean square profile measurements exhibited similar data trends for all delamination coupons, however the RMS measurements results consistently had larger profile measurements for all coupon configurations. The unidirectional ENF coupon exhibited approximately 300% larger profile changes in the 90° direction when compared to the 0° direction measurements. The 0° direction was aligned completely with the coupon fiber direction; therefore the 0° direction measurements did not cross perpendicular over the fibers on the fracture surface and thus a smoother surface topography resulted. The quasi-isotropic coupon exhibited a more consistent profilometry between the 0° and 90° measurements, where the 90° direction arithmetic average profile (Pa) was 16% larger than the 0° measurement and root mean square profile (Pq) was 13% larger in the 90° direction compared to the 0° direction. The cross-ply ENF coupon surface profile had a much larger change in measured primary profile (Pa and Pq) due to the 0° direction measurements being 250% larger than the 90° profile measurements. This

large change in profile is attributed to the observed multi-ply transverse fracture that occurred at the mid-plane of the coupon, creating a large step-like feature within the delamination coupon. This was previously observed in both profilometry and the areal damage characterization. The delamination created by the PTFE insert also exhibits a surface profile where the 90° direction measurements are on average 33% larger than the 0° measurements. This is a byproduct of the woven cloth used within the PTFE insert, leaving a surface pattern after curing.

The previously in-service enclosed delamination exhibited primary profile measurements that were larger in the 0° measurement direction when compared to the 90° direction by 47% and 51% for Pa and Pq, respectively. The edge delamination also exhibited a change due to the Pa and Pq measurement direction, approximately a 30% decrease in primary profile measurements when comparing 90° measurements to 0° measurements. The consistency of the damage profile for in-service delamination is comparable to the PTFE delaminations when comparing the change in profilometry with respect to measurement direction. The only coupon to have a more consistent fracture surface profile with respect to the measurement direction was the quasi-isotropic ENF coupon. The in-service delamination profile depths are more comparable to the quasi-isotropic ENF fracture coupon where the average difference in Pa measurement was 5.18μm. The PTFE facture surface had an average difference in Pa of 9.85μm.

Impact specimens also exhibited a large disparity in surface morphology when comparing the measurement direction. The 20J impact specimen had a greater than 86% increase in primary profile measurements going from the 90° to 0° direction measurements. The 40J impact specimen had an even larger increase in profile measurements where both Pa and Pq increased 190% going from 90° to 0° direction measurements. The complex multi-level damages created by the impacts also result in profilometry measurements that have a larger transverse height measurement due to

the depth of the damage. This increased damage state increased the surface texture and surface profile measurements. Although the impact damages showed an increase in overall profile measurement depth when compared to other fracture coupons, the lay-up of the coupon must also be taken into account for directional fracture and changes in the surface profile with respect to measurement direction.

In addition to the profilometry analysis completed on the amplitude parameters of the delamination surfaces, a Kurtosis analysis was performed on the amplitude averages to determine the sharpness of the fracture surface profiles. The results of the profilometry kurtosis (P_{ku}) are shown in Figure 4.23.

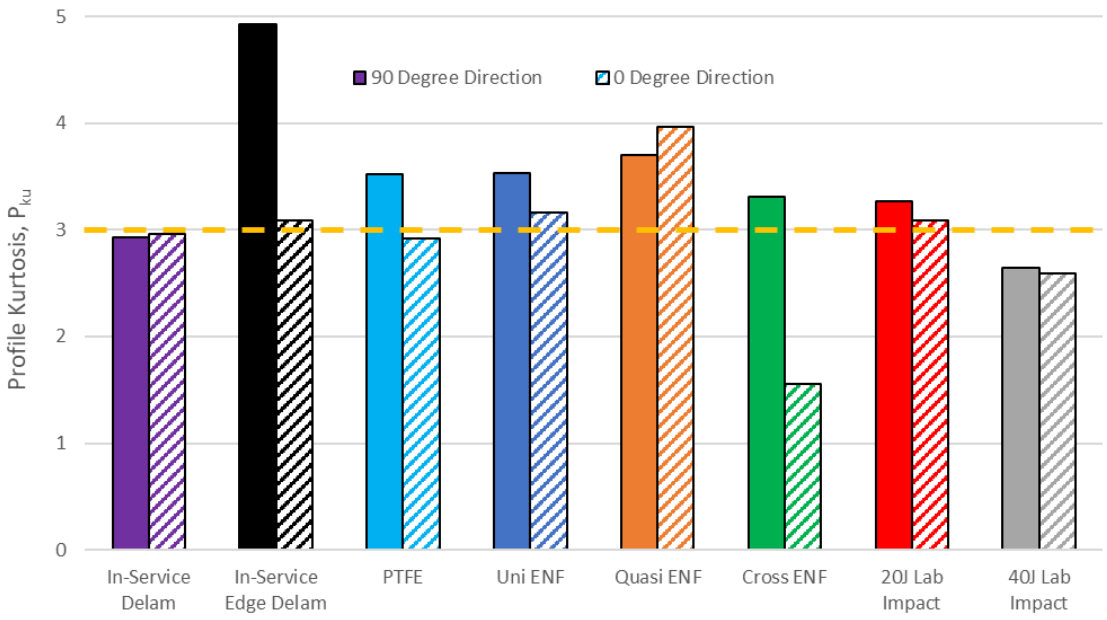

Figure 4.23. Profilometry kurtosis (P_{ku}) analysis of delamination surfaces

The yellow line at P_{ku} = 3 indicates the value for normal height distribution of a surface profile. This indicates that the closer the P_{ku} is to 3, that sharp points and indented points are more likely to co-exist on the surface. A normal distribution was found on the majority of the collected profilometry sample sets as indicated in Figure 4.23. However there were multiple sample sets where P_{ku}< 3 such as: cross-ply ENF 0° direction and both measurement directions for the 40 J impact specimen. These samples indicate that the average surface height distribution is above the mean plan or more even, indicating a more plateaued surface. The two cases found are where there was deeper transverse micro cracking with plateaued regions, creating a stepped region. This was verified when inspecting the delamination profile and planar surfaces. Surfaces where P_{ku}> 3 indicated a more spiked surface where quick and abrupt transitions were observed. This was found in the Unidirectional ENF specimens for profiles taken along the 90° direction, both quasi-isotropic ENF, PTFE along the 90° direction, and edge delamination along the 90° direction measurements. These surfaces were found to have areas where quick and abrupt height measurements were found, such as: the surface perpendicular to 0° fracture within the unidirectional ENF coupon, ply stripping areas of the quasi-isotropic ENF and edge delamination samples. The PTFE surface changes are due to the surface impression from the fiberglass carrier cloth creating resin peaks.

In addition to surface profilometry, the delamination surfaces were also measured for their arithmetic average roughness (R_a). Roughness measurement results for both the 90° and 0° direction are shown in Figure 4.24. The roughness observed for all samples had a higher measurement in the 0° direction. The highest R_a measurements were observed in the 90° direction on the: unidirectional ENF, 20J impact, and 40J impact coupons. The roughness measured in the 0° direction was statistically comparable for the PTFE, unidirectional, quasi-isotropic, and cross-

ply ENF fracture surfaces. This measurement was taken along the primary fiber direction for all ENF coupons except the PTFE sample, indicating a relatively smooth surface. The quasi-isotropic ENF surface has a 90° direction roughness that is statistically comparable to the same direction roughness measurements of the in-service edge delamination and in-service enclosed delamination. The edge delamination and the 40J impact specimens also had similar R_a measurements greater than 2µm. The 20J specimen had the largest 0° direction R_a at 4.3µm.

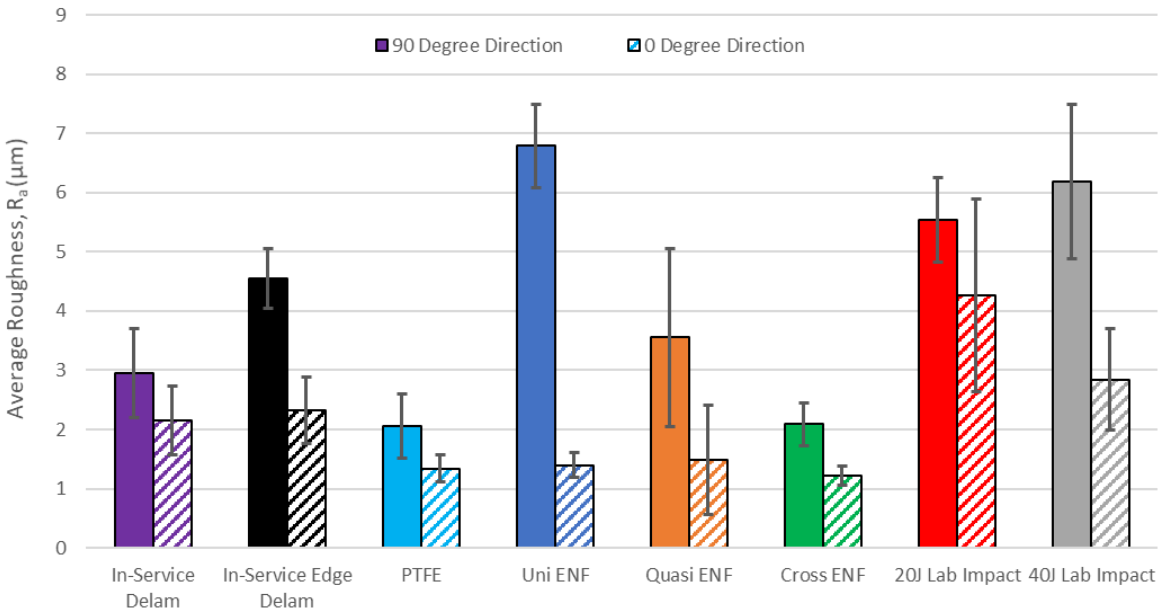

Figure 4.24. Arithmetic average roughness (R_a) of delamination surfaces

Surface metrology results indicate that the quasi-isotropic modified ENF delamination surface was most comparable to the in-service delaminations. This indicated that the quasi-isotropic ENF delamination surface is a representative of an in-service fracture when comparing laboratory manufactured delamination methods. Unidirectional modified ENF fractures may not be the best representation of aircraft delaminations due to the high directionality of the surface

profile and roughness. Cross-ply modified ENF fractures were also had highly directional surface profiles that were not comparable to the in-service delamination measurements. The impact induced delaminations directionality of fracture was consistent with the in-service delamination, however both impact samples had greater surface profile and roughness measurements. The surface metrology surface analysis techniques were found to be an effective way to quantitatively demonstrate equivalence between two fracture conditions created by different sources.

4.3. MATERIALS AND PROCESS DEVELOPMENT EXPERIMENTATION RESULTS

In order to complete development of a novel delamination injection repair procedure for repair and mechanical property restoration of PMC laminates as described in section 3.3.5, the materials and processes required must be established to ensure the procedure is robust for use in various repair scenarios. This includes being able to use the processes on: multiple types of PMC materials, on aircraft components in close proximity to contaminants, in locations that have higher service temperature requirements (greater than 82°C), be able to withstand design flight loads including interlaminar shear in the composite laminate, and have the ability to complete procedures in limited access areas where cutout and patch repairs may not be viable.

4.3.1. **Injection pressure FEA results.**

Different laminates were defined to compose percent 0/90/±45 degree ply orientation content of 48%/48%/4% and 32%/64%/4%, adjusting groupings of 0^o piles, or arranging where interfaces with 45/-45^o ply groups were located. Results are presented here for FEA models described in section 3.3.1 predicted the pressure causing further delamination growth. All laminates had the 90^o ply at the center. For the 48%/48%/4% family, specific laminates are listed

in the legend of Figure 4.25. This figure plots the threshold pressure for delamination growth for the eight different laminates, with 50 mm delamination diameter, and at varying through-thickness location of the delamination (i.e., each point in the plot is a separate FEA model). Among the different laminates that could compose a 48%/48%/4% layup, the configurations with all 0^o plies and 45/-45^o plies lumped together yielded the lowest threshold pressures. These are considered the "worst case" scenario and a fitting line was drawn through the bottom set of points to represent the entire population of results. The strongest controlling parameter is clearly depth location of the delaminated sub-laminate. Specifically, if just one ply was delaminated pressure for further increasing the delamination could be as low as 0.23 MPa.

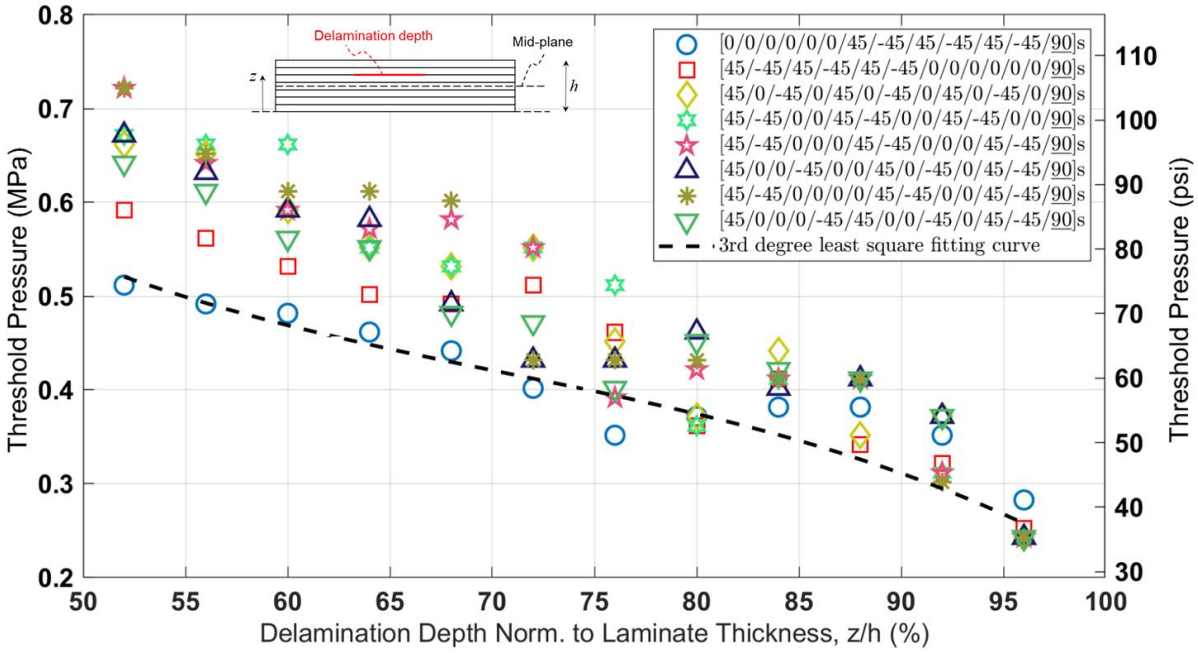

Figure 4.25. Threshold pressure for 50 mm diameter delamination growth onset; various 25-Ply configurations of 48%/48%/4% layup IM7/977-3

Similar to the results in Figure 4.26, a series of many FEA models (over 500 in total) were run for other delamination size cases, for both layup types. The “worst case” fitting line representing the entire population of results was extracted from plots similar to Figure 4.25, to produce the summary of FEA models plotted in Figure 4.26 which gives an overall view how the threshold pressure is affected by various geometry parameters and layup configurations. Figure 4.26 shows that threshold pressure strongly depends on and decreases for larger sized delamination. Furthermore, threshold pressure is lower as the delamination depth is located closer to the surface (i.e., thinner sub-laminate) for the 25 and 50 mm delamination size, but relatively insensitive to delamination depth for the larger 100 mm delamination. The maximum sized delamination that this injection repair method is intended to be used is up to 50.8 mm, corresponding to a threshold pressure of ~ 0.26 MPa for the delamination being located at one ply distance from the surface. These results provide key information on the operational range of safe injection pressures that can be applied, to avoid further growth of the delamination during injection of solvent, plasma, and resin.

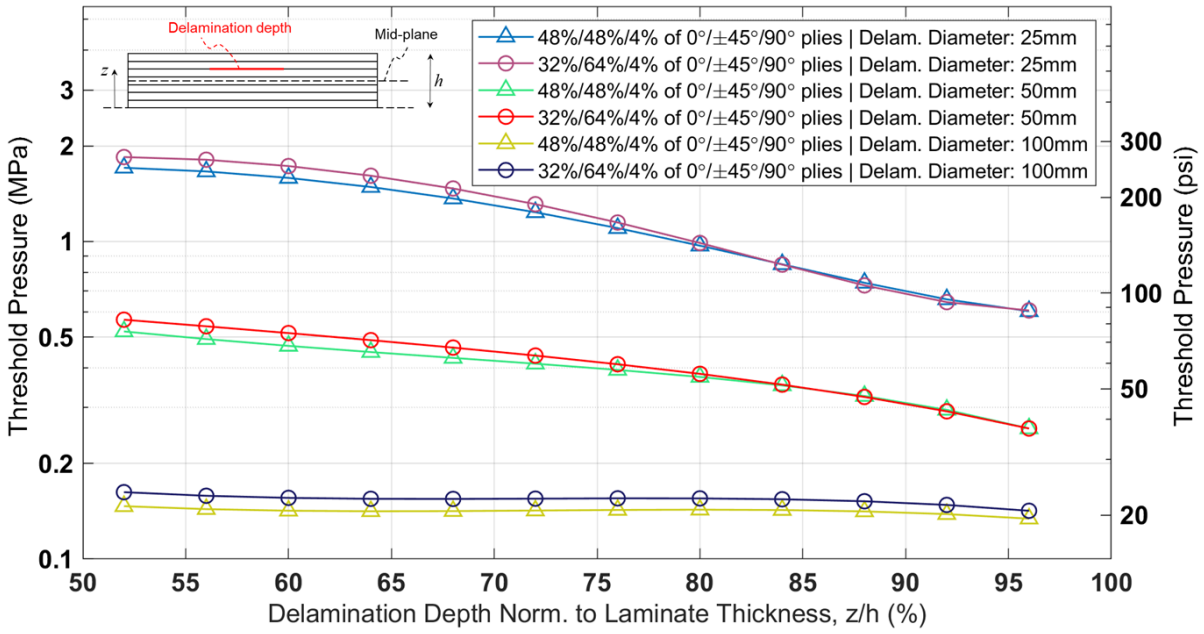

Figure 4.26. Summary of FEA models predicting delamination growth threshold pressure for 25-ply IM7/977-3

Comparing the FEA results to injection pressure calculation results, the most conservative approach syringe pressure application of 0.739 MPa, would exceed the maximum allowable pressure for both 50 mm and 100 mm diameter delaminations. However, it was previously discussed that the plunger seal maximum pressure would be exceeded prior to the syringe body and that maximum pressure was 0.0948 MPa, which would be less than any of the configurations analyzed by FEA. The maximum atmospheric plasma pressure of 0.0695 MPa would also never exceed the delamination growth threshold pressure for any of the configurations analyzed.

4.3.2. **Contamination Testing Results**

In order to create a test configuration representative of gross in-service contamination of a PMC delamination, testing was completed to determine the lowest viscosity that could be achieve by diluting a contaminant with solvent. The importance of lowering the viscosity of contaminants

was imperative to ensure that full infiltration of a test delamination coupon could be completed without encountering capillary effects to prevent full coverage. First, flat plate testing was completed to determine the lowest percentage of contaminant that could be used with solvent dilution while maintaining a lowered surface activation energy within the PMC fracture surface. Next, the down-selected contaminant was utilized to develop an injection contamination process to ensure full contaminant coverage within the enclosed delamination.

Flat Panel Contaminant Testing

Flat panel contamination testing was completed with five different contaminant solutions (see section 3.3.2). Each contamination region on the test panel consisted of a different amount of contamination coverage and WCA measurements were taken in each area. WCA can be used to determine the work of adhesion on the surface in accordance with the Young-Dupré equation (see Figure 2.18 and equation (1.7). Lower WCA (Θ_C) and higher W_{ls} correlate to a better adhesion. A water surface tension of Y_{SL} = 72.8 mN/m was used for all calculations. The WCA measurement and surface activation energy results for flat plate contamination testing are shown in Table 4.5**.** Sample BL-1 was a baseline sample where a WCA reading was taken on an uncontaminated and sanded IM7/977-3 unidirectional composite surface resulting in a work of adhesion of 123.2 mN/m. This sample would be used as a reference for all other contaminated samples. All Hydraulic Fluid (HF) contaminated samples, were on average 94.3 mN/m or lower except sample HF-1, which had a work of adhesion of 101 mN/m. All lubricating oil samples exhibited statistically similar results ranging from 100.8 to 104.3 mN/m work of adhesion regardless of the contaminant volumetric fraction. All contaminated samples exhibited an 18% or more reduction in work of adhesion when compared to the baseline sample. As a result, 0.10 volumetric fraction of each

contaminant was selected for enclosed contamination testing to ensure surface contamination meeting steady state work of adhesion results (i.e., higher concentration of contaminant did not affect the W_{ls}).

Table 4.5. Flat plate contamination WCA testing results

Sample	Contaminant	Contaminant Volume Fraction	Contaminant Coverage (μg/cm^2)	WCA (Θ_C) Avg. (°)	St. Dev	W_{ls} (mN/m)
BL-1	None	NA	N/A	46	4	123.2
HF-1	Hydraulic Fluid	0.05	152.8	67	2	101.0
HF-2	Hydraulic Fluid	0.1	365.6	73	1	94.3
HF-3	Hydraulic Fluid	0.15	475.9	74	1	92.9
HF-4	Hydraulic Fluid	0.2	699.3	73	1	93.8
HF-5	Hydraulic Fluid	0.3	1004.5	71	1	96.5
L-1	Lubricating Oil	0.05	100.7	64	3	104.3
L-2	Lubricating Oil	0.1	226.7	67	1	100.8
L-3	Lubricating Oil	0.15	349.8	67	2	101.7
L-4	Lubricating Oil	0.2	482.7	66	1	101.9
L-5	Lubricating Oil	0.3	705.7	65	2	103.3

Enclosed Delamination Testing Results

Enclosed contamination coupons (see section 3.1.1) were exposed to a 10% contaminant by volume mixture infused with a droplet of fluorescent dye to determine coverage when injected into a fractured modified ENF coupon simulating a simple delamination. Shown in Figure 4.27 is a photograph of internal surfaces of the delaminated coupons once fully split in half and viewed under black light.

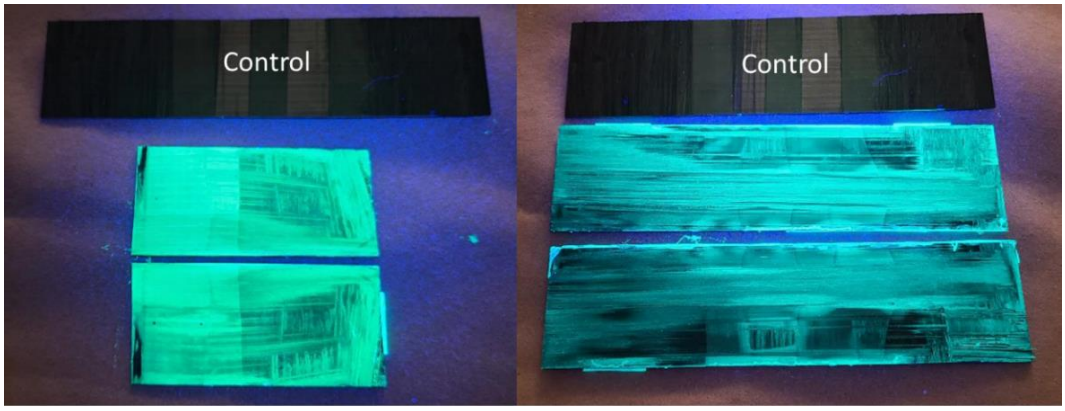

Figure 4.27. Enclosed contamination coupons with fluorescent contaminant under ultraviolet light

The top specimen is taken from a control sample that was not previously exposed to the injected contaminant. Both the hydraulic fluid and lube oil contaminated coupons appeared to have approximately 100% coverage of the internal surfaces of the delamination. Ten WCA readings were also collected on both panels from each specimen. The average WCA were 78±4° for the hydraulic fluid sample and 74±6° for the lubricating oil sample. These values are consistent with the values collected from the flat panel contamination testing for steady state contamination values.

4.3.3. **Delamination Cleaning Process Development Results**

A novel delamination cleaning procedure was developed based on testing completed and reported on in this section. First, a contamination removal method using solvent and atmospheric plasma was developed using the externally-accessible surface of a flat panel, much like the contamination testing completed in section 4.3.2. Once contamination removal procedures were developed on a flat panel, they were down selected and applied to a pre-fractured and contaminated modified ENF coupon to determine cleaning efficacy. The cleaning procedures were verified using WCA analysis and FT-IR inspection after cleaning procedures were concluded. In addition,

development of a procedure using QGA mass spectrometer was completed to determine real time contamination removal data.

Flat Panel Contamination Cleaning Process Development Results

The flat plate contamination removal panel was treated in five areas with different contamination removal techniques as previously shown in Figure 3.25. Visual indication was a component of the assessment of contamination removal processing. As shown in Figure 4.28, it can be seen that there is a color change in the areas where the contaminant was removed. The contaminant remaining on the flat panel surface is shown as “dark glossy” when compared to the contaminant removed regions which are “gray flat” in appearance. In Figure 4.28, Section 1 of the panel, a slight glossiness remains even after solvent wiping the surface multiple times. In section 2, the area was solvent wiped and atmospheric plasma treated. Section 2 areas where the plasma treatment occurred exhibit a matte appearance. This same matte appearance is found in Sections 3 to 5, where the plasma exposures occurred, however the rest of the region appeared to be highly contaminated since plasma was applied on to those select spot locations, as described in section 3.3.2.

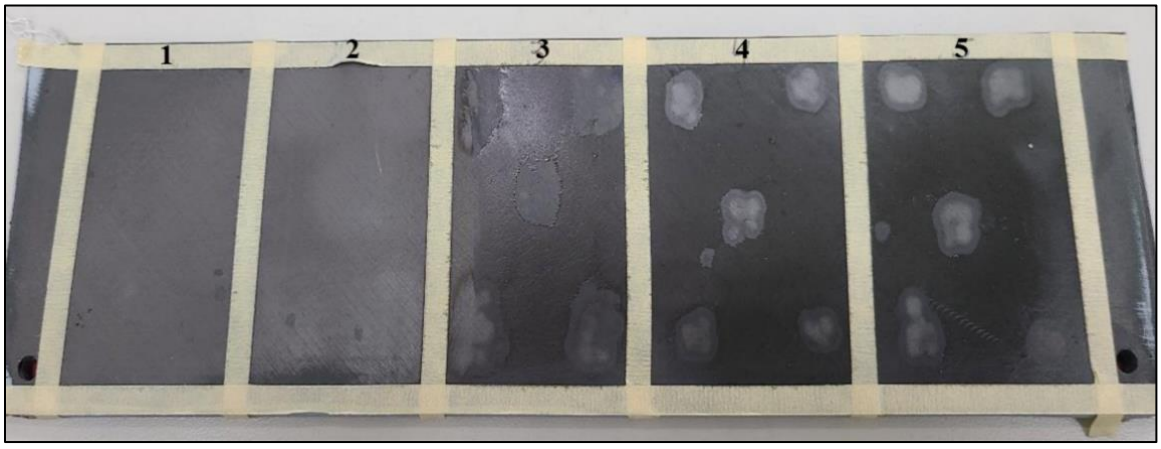

Figure 4.28. Lube oil contamination discriminator panel after cleaning processes

WCA readings were taken in the regions where the cleaning techniques were spot applied. The results for the WCA readings can be found in Table 4.6. Solvent wipe with MIBK for both hydraulic fluid and lubricating oil appeared to increase the W_{ls} value when compared to results found during the contamination study. The contamination W_{ls} results were previously found to be an average of 94.3 mN/m and 100.8 mN/m, for hydraulic fluid and lubricating oil respectively. HF-R-2 and LO-R-2 sections were both cleaned using solvent prior to plasma exposure. This resulted in a W_{ls} value of 144.3 mN/m for hydraulic fluid and 144.7 mN/m for lubricating oil removal. This is a greater than 40% increase in work of adhesion. Also, larger areas were affected by the cleaning when compared to plasma cleaning only as shown in Figure 4.28. Plasma with visual indication of removal was complete within eight seconds for each contamination sample, however the areas treated still had lower W_{ls} values when compared to other plasma exposure sections. Sections with plasma only exhibited an increase in work of adhesion with some of the highest W_{ls} values, however the cleaning area was much smaller than the solvent and plasma treatment combined. Therefore when conducting further cleaning procedures for enclosed damage samples, solvent flush prior to plasma exposure will be conducted.

Table 4.6. Flat plate contamination cleaning WCA results

Sample	Contaminant	Removal Technique	Plate Section #	WCA Avg. (°)	St Dev.	W_{ls} (mN/m)
HF-R-1	Hydraulic Fluid	Solvent Wipe	1	57	1	112.5
HF-R-2	Hydraulic Fluid	Solvent + 15 sec Plasma	2	11	3	144.3
HF-R-3	Hydraulic Fluid	Plasma Until Visual Removal	3	35	8	132.4
HF-R-4	Hydraulic Fluid	Plasma 10 Sec.	4	13	3	143.7
HF-R-5	Hydraulic Fluid	Plasma 15 Sec.	5	10	1	144.5
LO-R-1	Lubricating Oil	Solvent Wipe	1	49	3	120.6
LO-R-2	Lubricating Oil	Solvent + 15 sec Plasma	2	9	1	144.7
LO-R-3	Lubricating Oil	Plasma Until Visual Removal	3	27	7	137.7
LO-R-4	Lubricating Oil	Plasma 10 Sec.	4	25	3	138.8
LO-R-5	Lubricating Oil	Plasma 15 Sec.	5	15	4	143.1

Flat Panel Quantitative Gas Analysis (QGA) Contamination Removal Results

A flat plate surface contaminated with lubricating oil or hydraulic fluid (See section 3.3.3) was utilized to determine the molecular byproducts of plasma cleaning contaminants from the composite surface. Shown in Figure 4.29 is the spectra collected during cleaning of the lubricating oil contaminant. Masses of: 4 (He), 28 (N_2), and 32 (O_2) amu were removed due to large responses from ambient air and the helium being the major byproduct of the generated plasma. All spectra were background subtracted in an attempt to remove any environmental induced spectral responses.

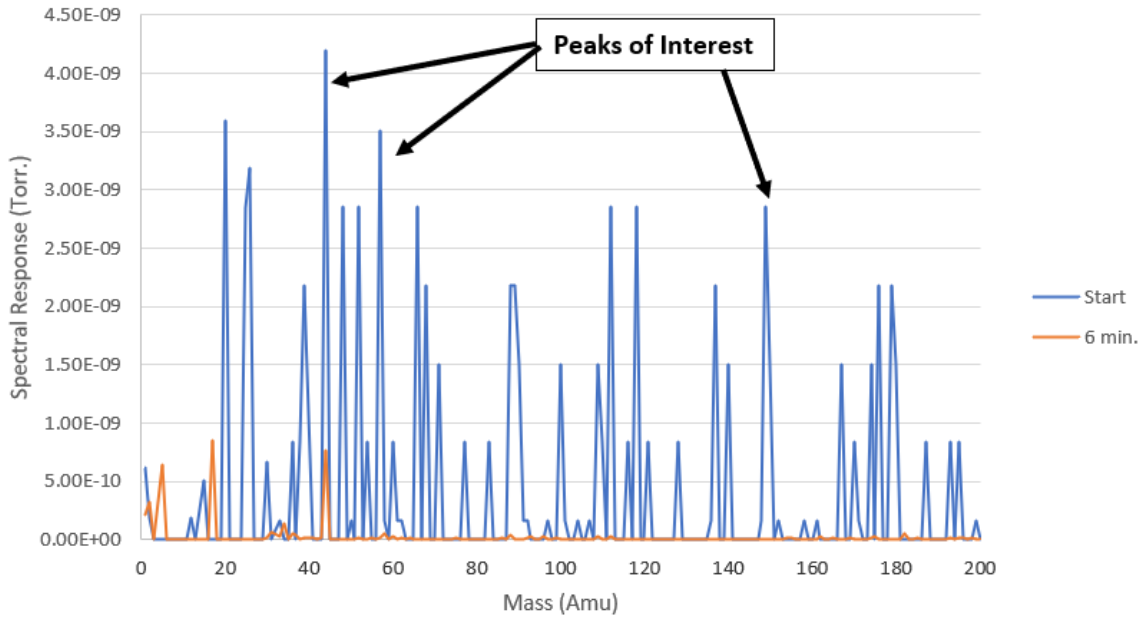

Figure 4.29. Mass spectra of lubricating oil before and during plasma cleaning

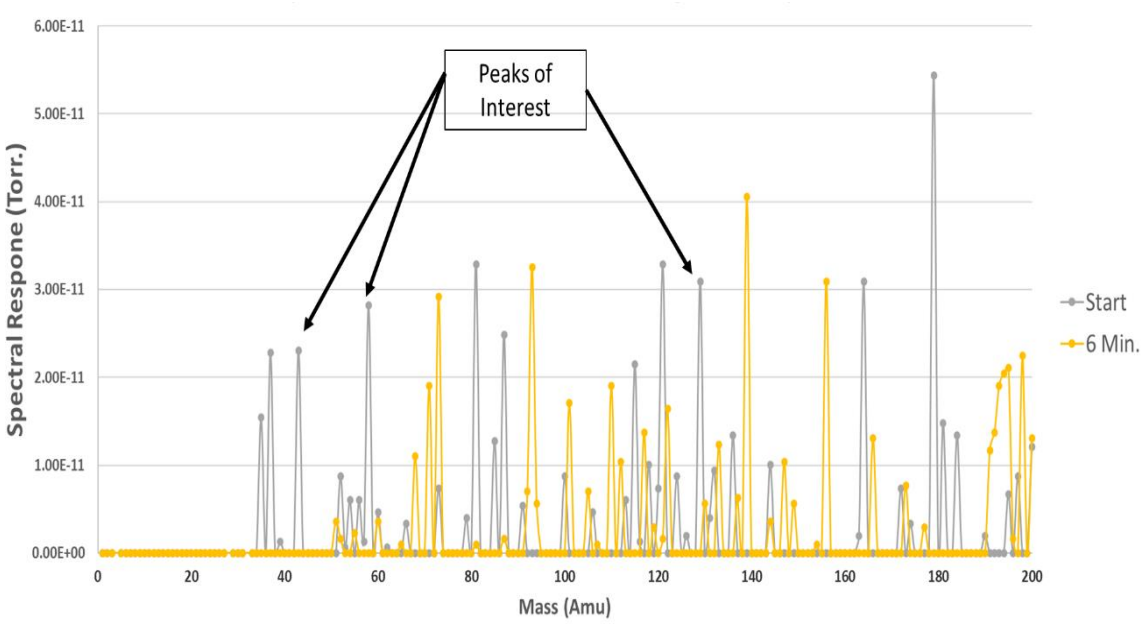

Figure 4.30. Mass spectra of hydraulic fluid before and during plasma cleaning

Specific mass peaks were investigated based upon the constituent materials identified within the safety data sheets for each contaminant material. This includes tracking the molecular peaks for specific hydrocarbon compounds such as C_4H_7 (43/44 amu) and C_4H_9 (57/58 amu). For the lubricating oil sample, the peak at 156 amu is another molecular compound commonly found in lubricating oil, polyol ester [85]. The hydraulic fluid sample also has an identifying peak at 129 amu that represents an ester commonly found in MIL-PRF-83282 hydraulic fluid. The spectrum collected using the dual Faraday detector are shown in Figure 4.29 and Figure 4.30 corresponds to the start of the cleaning process and after six minutes. For the removal of lubricating oil as shown in Figure 4.29, at t = 0 min. (shown in blue) and t = 6 min (shown in range), there is a large change in the resulting spectrum. Most of the mass spectral response was removed after six minutes of helium-oxygen plasma application or lowered by an order of magnitude.

For the hydraulic fluid contamination removal observed in Figure 4.30, please note the average response was two orders of magnitude less than the lubricating oil sample. Although a weaker response was recorded which in turn created more scatter in molecular response, the peaks of interest found at 43, 44, 57, and 58 amu showed a major reduction in response when comparing t = 0 min. (shown in grey) and t = 6 min. (shown in yellow).

In addition, the spectral responses at 156 amu for lubricating oil and 129 amu for hydraulic fluid were two orders of magnitude weaker in mass spectra response for each respective material at both time intervals. This is likely due to the electron ionization method used in the QGA and that the constituents at 156 and 129 amu were also considered secondary confirmation peaks. Therefore the targeted molecular species at 43, 44, 57, and 58 were found to reduce during plasma exposure for both lubricating oil and hydraulic fluid would then be used for real-time process

monitoring. A method for using the QGA was created for both contaminants to track the peaks of interest in real time during plasma cleaning of the process development coupons.

Enclosed Delamination Cleaning Process Development Results

Enclosed ENF coupon delaminations were first injected (see section 3.3.2) with a contaminant (lubricating oil or hydraulic fluid) to ensure a worst-case scenario of a highly contaminated delamination. Next, the enclosed ENF coupon was cleaned using an acetone flush of injecting 10 mL into each hole in the coupon and the acetone was allowed to dry for a minimum of 24 hours. Next the coupon was purged with nitrogen and then plasma treated using the atmospheric oxygen plasma. During the plasma treatment the coupon was monitored using a QGA for contamination removal and verified after opening the coupon using WCA measurements and FTIR analysis.

The QGA was placed on the opposite hole from the plasma treatment injection to analyze escaping byproducts of the cleaning process. The method developed for the real-time tracking contamination removal were completed within the QGA system's EGASoft software package. The method was developed for removal of the lubricating oil and hydraulic fluid contaminant tracking masses at: 43, 44, 57, and 58 amu. The SEM detector was used for in-line process monitoring due to the higher sensitivity and all spectra were background subtracted. Shown in Figure 4.31 and Figure 4.32 are typical responses for removal of hydraulic fluid and lubricating oil contamination, respectively, as documented by the reduction in monitored chemical masses of interest.

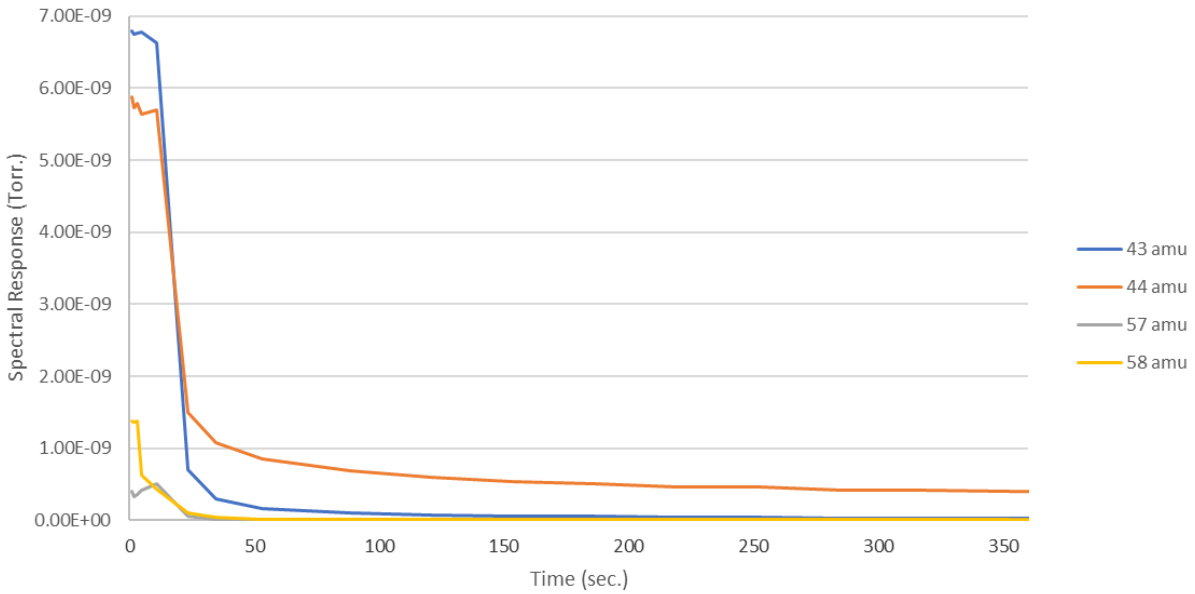

Figure 4.31. QGA Response of hydraulic fluid plasma treatment in modified ENF coupon

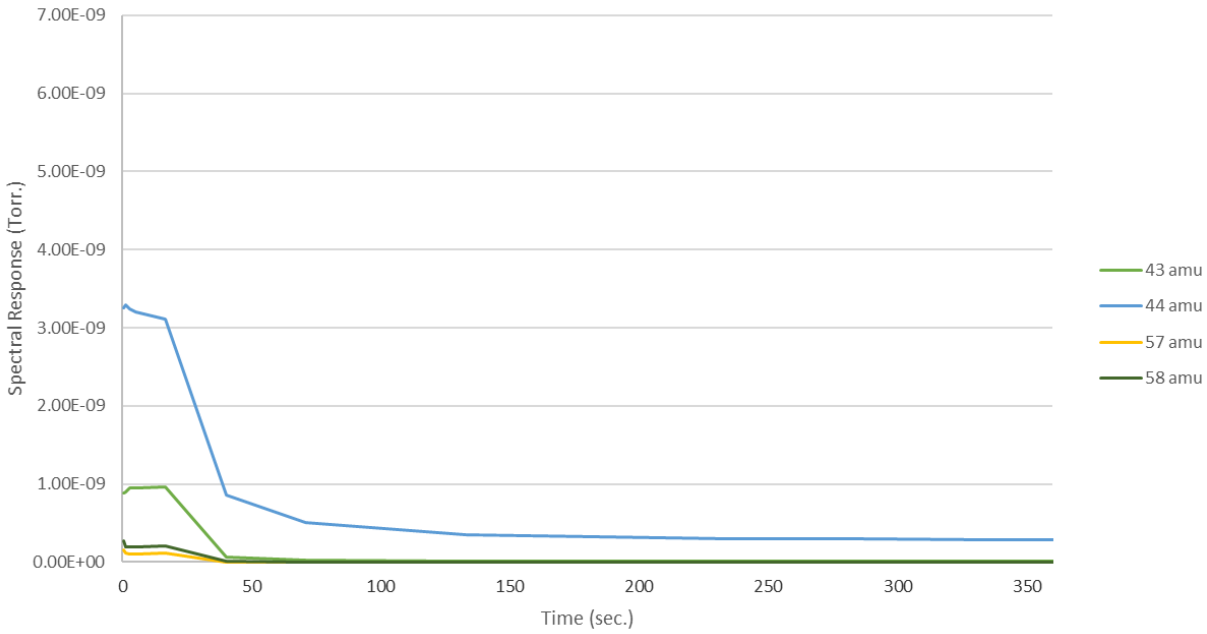

Figure 4.32. QGA response of hydraulic fluid plasma treatment in modified ENF coupon

It was observed that the spectral response for hydrocarbon constituents (43, 44, 57, and 58 amu) after plasma exposure elicited a lowered response in the lubricating oil coupon with a maximum response at $3.25x10^{-9}$ Torr compared to the hydraulic fluid coupon at $6.80x10^{-9}$ Torr. However the plasma exposure reduced the response of all tracked masses on both coupons. 43, 57, and 58 amu masses exhibited a response within approximately 100 seconds where steady state reduction was achieved. After approximately 200 seconds steady state reduction was reached for 44 amu. Although reduction of C_4H_7 (43/44 amu) and C_4H_9 (57/58 amu) hydrocarbon compounds were monitored and found to have steady state response after 200 seconds, the plasma exposure was kept on at 20 minutes (10 minutes each hole) to ensure all internal areas of the coupon were thoroughly cleaned.

In addition to real-time spectrometry, the enclosed delamination coupon was opened immediately after plasma cleaning and analyzed using WCA. Ten readings were taken for each of the lubricating oil and hydraulic fluid contamination removal coupons. Readings were taken in areas between the drill holes and within 12 mm forward and aft of the drill location. Shown in Figure 4.33 and Figure 4.34 are examples of the location of the WCA readings.

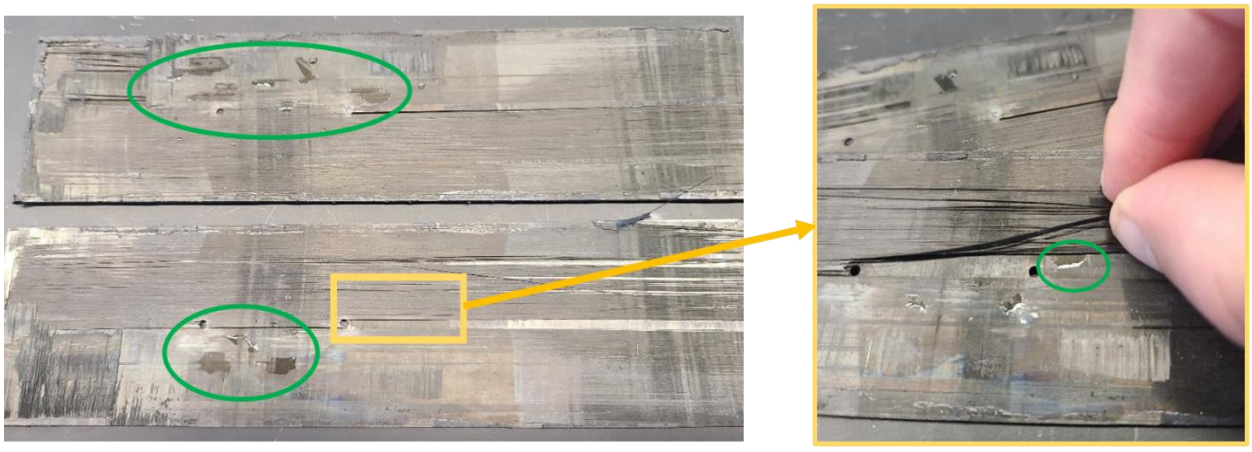

Figure 4.33. WCA readings after atmospheric plasma treatment of lubricating oil contaminated modified ENF coupon

Figure 4.34. WCA readings after atmospheric plasma treatment of hydraulic fluid contaminated modified ENF coupon

The resulting WCA data for the lubricating oil contaminated and cleaned coupon was <5° for all sites analyzed. The detectable limit of the Surface Analyst unit is 5°, therefore the cleaning of lubricating oil was considered successful. Also shown in Figure 4.33 is a close-up of a reading taken under the fractured fibers within the coupon. This reading was also <5°, exhibiting that the solvent-plasma cleaning process was infiltrating below the immediate surface of the coupon. Although, the hydraulic fluid contaminated coupon had <5° readings in all areas in between the two drill holes, there was a single reading aft of the drill holes where an average 72° WCA resulted. This area was found to still be contaminated (see Figure 4.34, circled in red) and further cleaning would be required to ensure removal of contaminants.

In order to further verify contaminant removal, FTIR spectrometry was utilized to inspect the modified ENF processing coupon surfaces after cleaning. This was completed by inspecting each of the three modified ENF panel type fracture surfaces after plasma cleaning. This was achieved for both lubricating oil and hydraulic fluid contaminated samples. Shown in Figure 4.35

through Figure 4.40 are the results of 16 areas (see Figure 3.28 for locations) that were inspected with FTIR on each coupon after cleaning a contaminated ENF process development coupon. The coupons were treated with an atmospheric plasma for 20 minutes each (10 minutes on each injection hole).

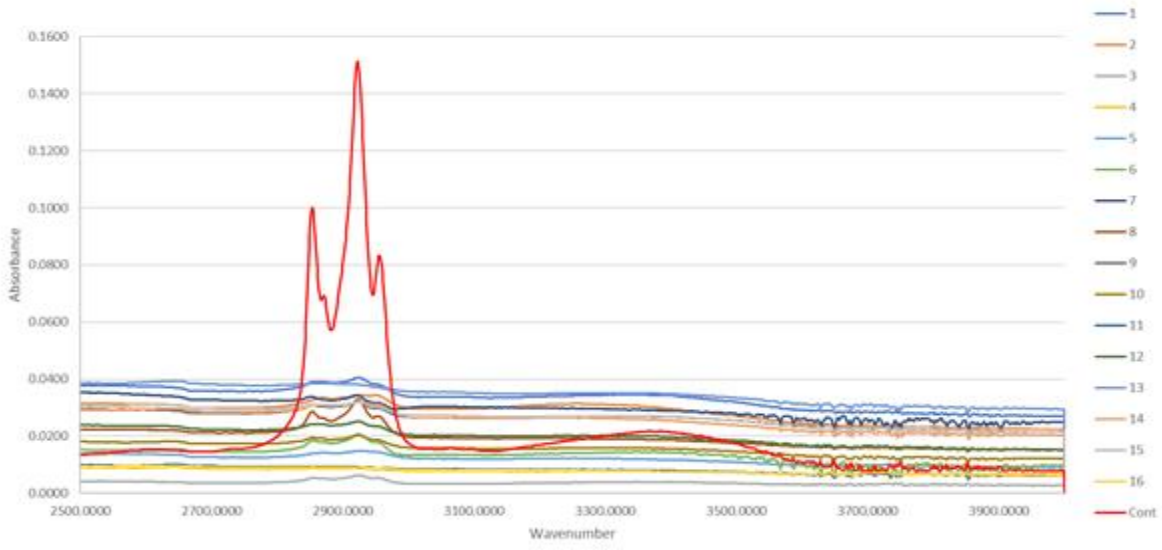

Figure 4.35. Hydraulic fluid contamination removal FTIR results on unidirectional ENF coupon

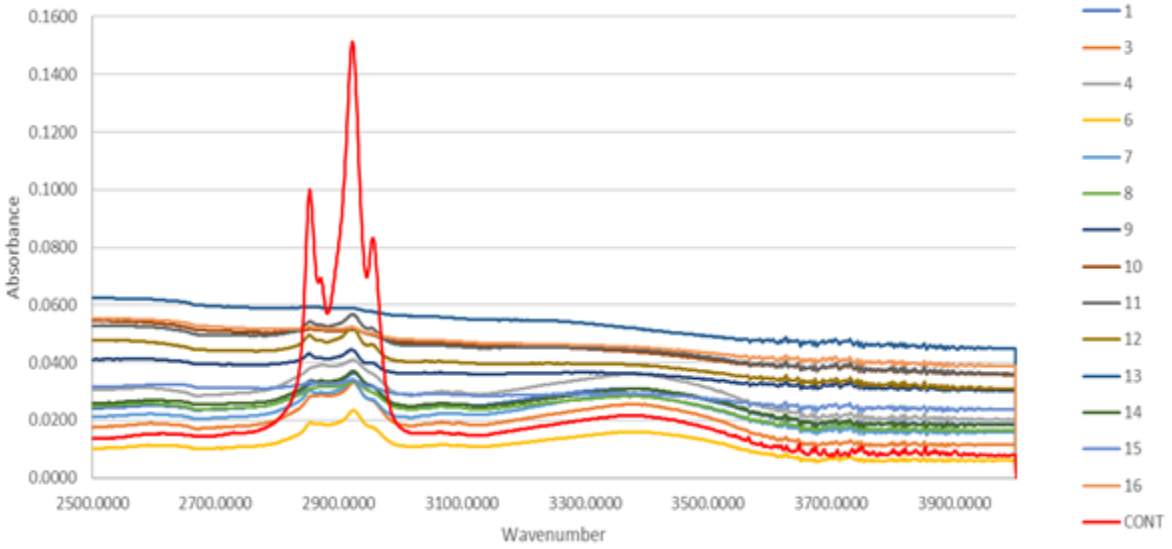

Figure 4.36. Hydraulic fluid contamination removal FTIR results on quasi-isotropic ENF coupon

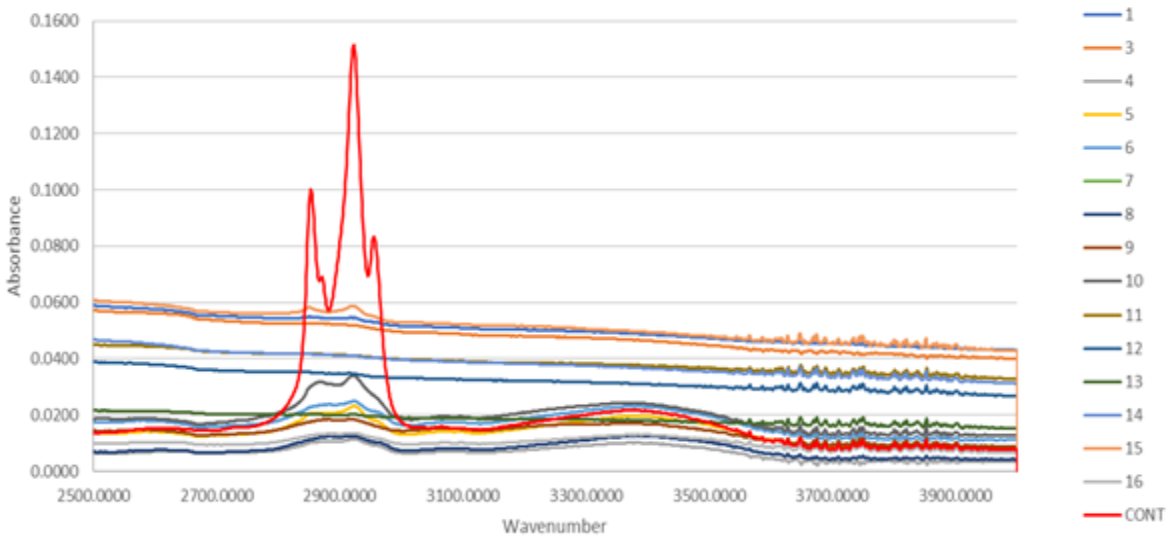

Figure 4.37. Hydraulic fluid contamination removal FTIR results on cross-ply ENF coupon

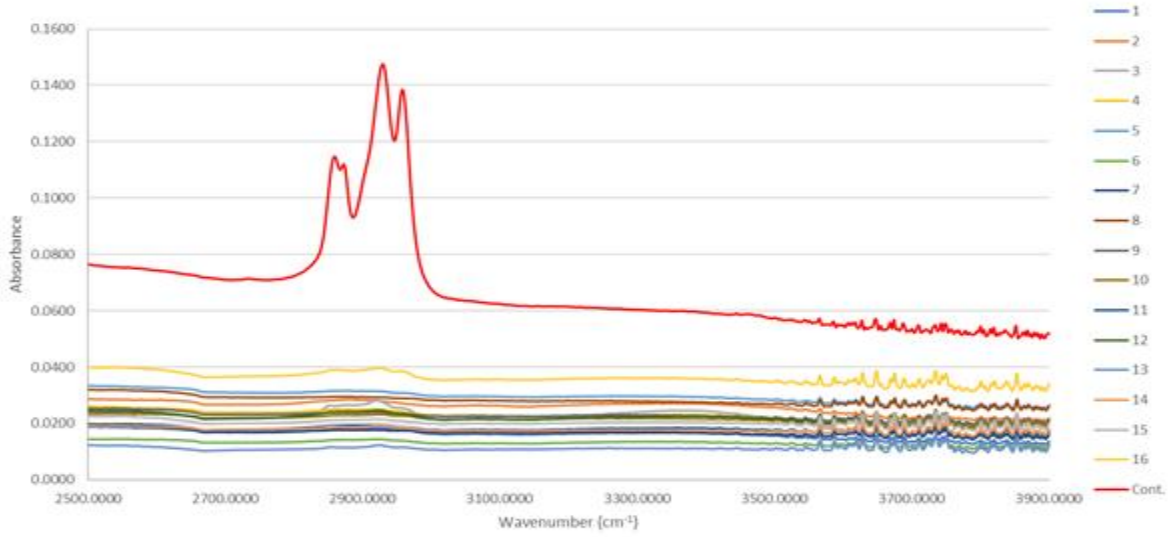

Figure 4.38. Lubricating oil contamination removal FTIR results on unidirectional ENF coupon

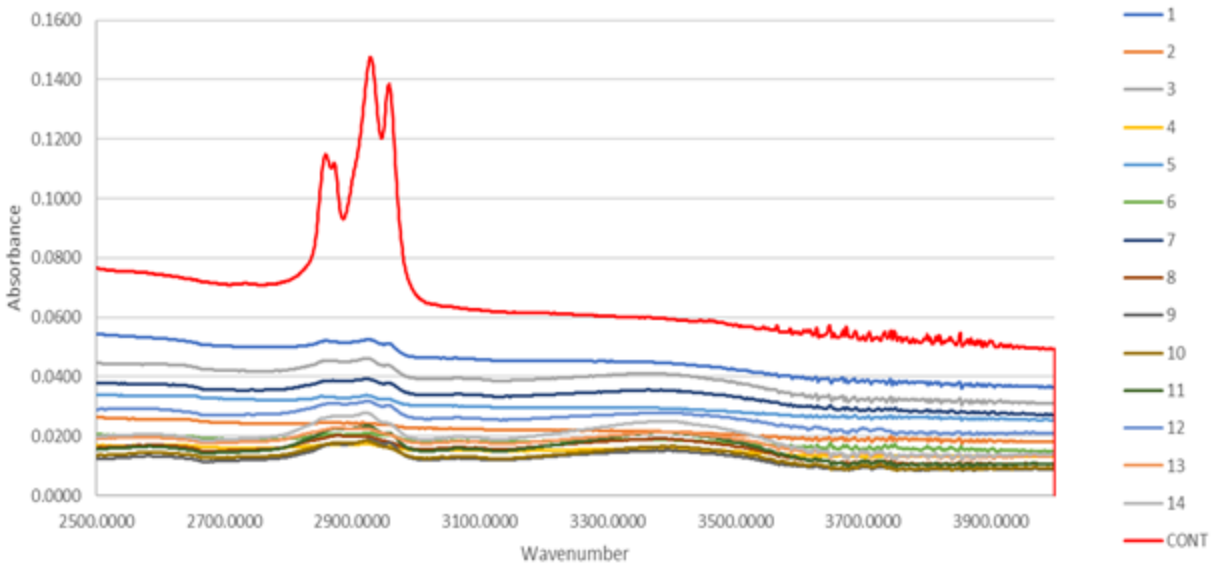

Figure 4.39. Lubricating oil contamination removal FTIR results on quasi-isotropic ENF coupon

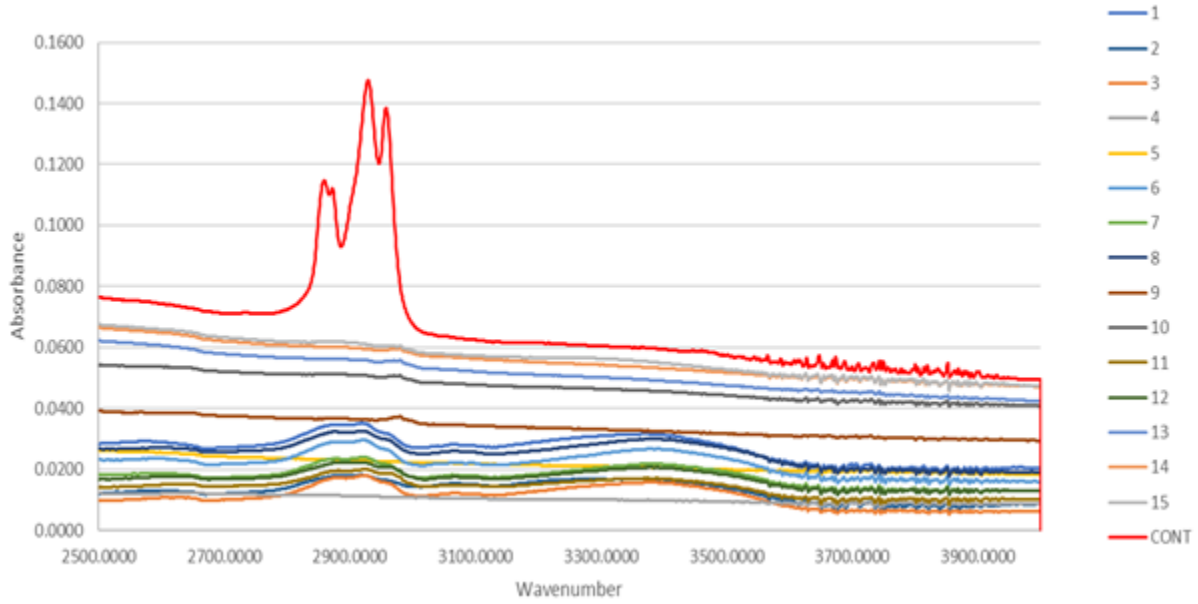

Figure 4.40. Lubricating oil contamination removal FTIR results on cross-ply ENF coupon

The data in Figure 4.35 through Figure 4.40 was truncated to only show 2500-3900 cm^{-1}. This truncation was to purposefully highlight the primary contamination constituent which is the hydrocarbon triplet, located between 2850-3000 cm^{-1} that is exhibited by the red spectra found in

each figure. The contaminant, denoted by "CONT.", in each figure is the result of performing FTIR-ATR spectrometry analysis on the contaminant, lubricating oil or hydraulic fluid, by itself. Each coupon was analyzed for the hydrocarbon triplet to determine if the coupon still had contaminants on the surface. The entire triplet was required to be identified in order to be deemed contaminated. In Figure 4.35, the unidirectional ENF coupons that was contaminated with hydraulic fluid exhibit readings cleaned of hydrocarbon contaminants for the entire coupon except at location 8. There was trace amounts of contaminant found near the edge of the coupon. Although no clearly defined triplets were found in Figure 4.36, peaks between 2850-3000 cm^{-1} were observe and could potentially be hydraulic fluid trace contaminant located at multiple sites (6 out of 16), however there was a major reduction in IR signature compared to the control spectra. Therefore hydraulic fluid was being cleaned; however the plasma may need to be applied for a longer period of time. The cross-ply FTIR-ATR results shown in Figure 4.37. There was no defined triplet found on this coupon surface, however a doublet was found at location 9. This doublet is not considered hydrocarbon contamination.

In Figure 4.38 through Figure 4.40 the coupons were all contaminated with lubricating oil prior to plasma cleaning. The hydrocarbon triplet for lubricating oil is shown in each spectra plot for reference. The three spectra peaks identified from the hydrocarbon triplet are required to deem any location of the coupon to be contaminated. In all three ENF coupon configurations, there was no trace contaminants of lubricating oil observed after atmospheric plasma cleaning. Therefore the procedure to remove lubricating oil contamination with solvent and plasma was verified.

Solvent flush prior to plasma cleaning was verified to significantly reduce or remove the presence of hydrocarbon contamination within a simulated enclosed delamination. It was observed that hydraulic fluid requires a more extensive treatment period to eradicate the contaminant

completely. Although trace amounts of hydraulic fluid were found in locations within the quasi-isotropic ENF coupon, there was a significant reduction in the contaminant, therefore a follow-up coupon with further cleaning of this lay-up configuration was completed using 40 minute (20 minutes at each injection hole) plasma treatment instead of 20 minutes to remove the trace contaminants. The resulting spectra from 40 minute plasma cleaned spectra are found in Figure 4.41 through Figure 4.43.

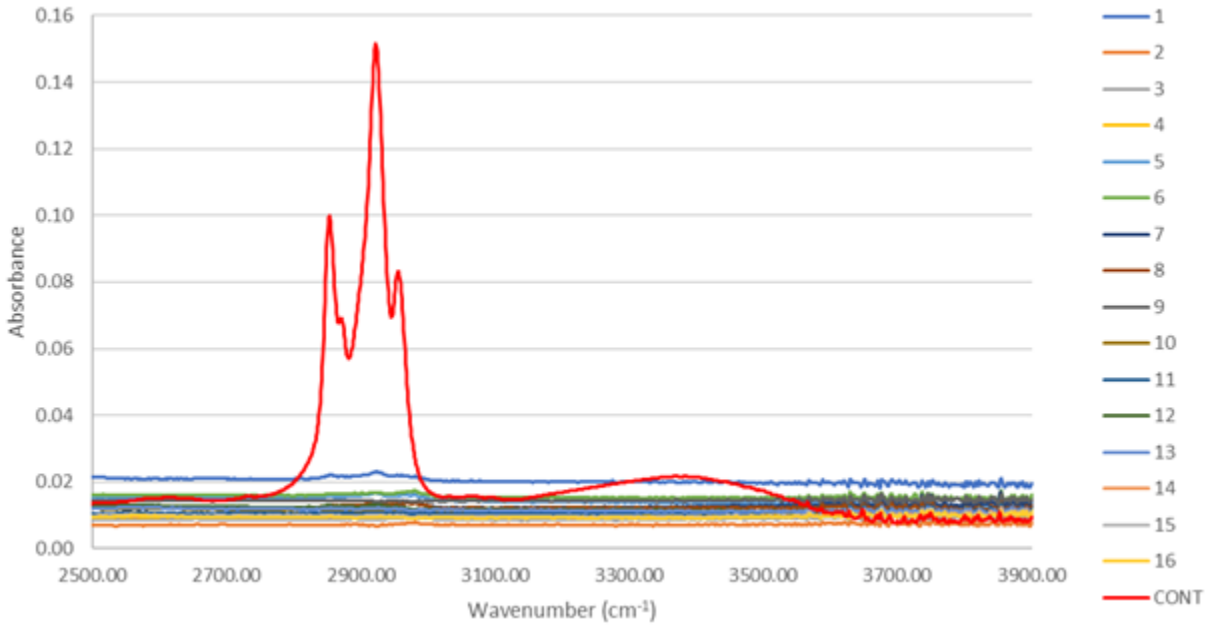

Figure 4.41. Hydraulic fluid contamination removal FTIR results on unidirectional ENF coupon after 40 minutes

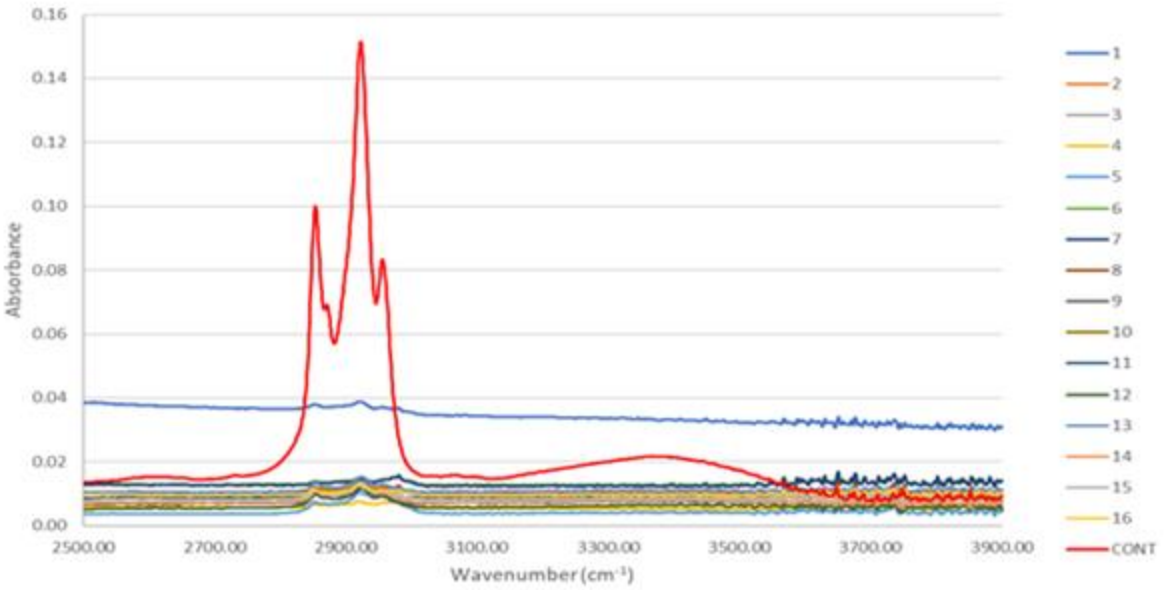

Figure 4.42. Hydraulic fluid contamination removal FTIR results on quasi-isotropic ENF coupon after 40 minutes

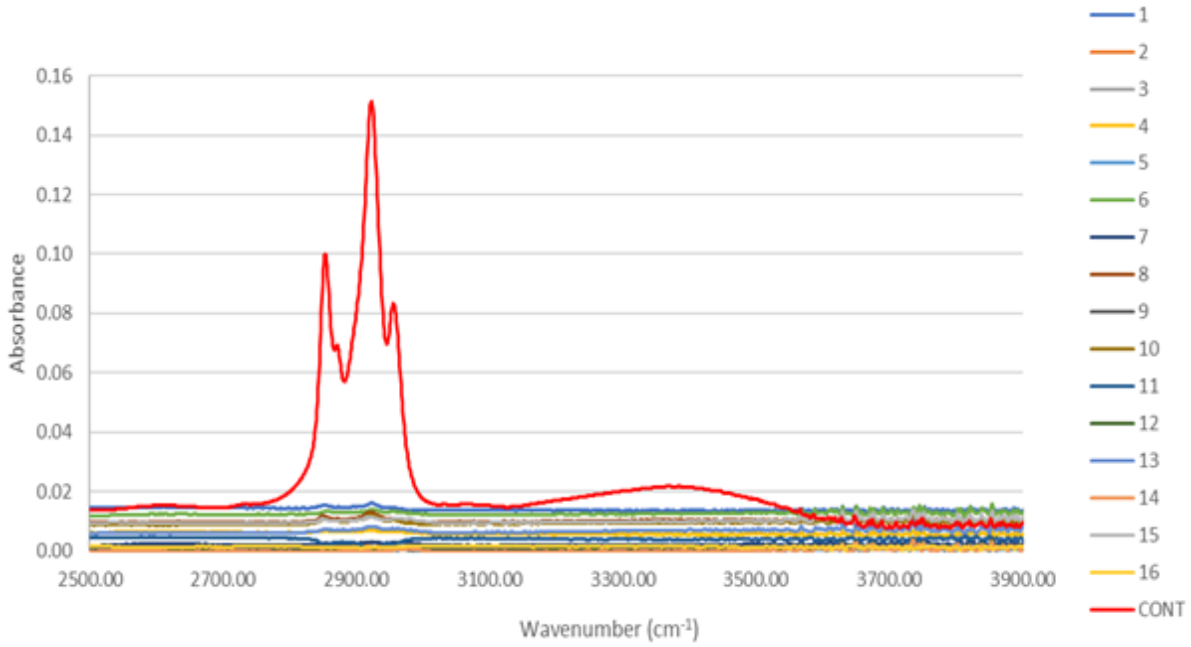

Figure 4.43. Hydraulic fluid contamination removal FTIR results on cross-ply ENF coupon after 40 minutes

Results from the 40 minute plasma treatment clearly exhibit a cleaned PMC surface where the hydrocarbon triplet associated with hydraulic fluid was removed. The absence of a pronounced triplet between 2850-3000 cm^{-1} signifies that the hydraulic fluid contaminant was removed after 40 minutes of treatment and significant reduction was observed in peak absorbance compared to the 20 minute plasma treated hydraulic fluid samples. In addition, it was conclusive that Lubricating oil was thoroughly cleaned after solvent flush and atmospheric plasma cleaning for 20 minutes due to no trace contaminants being left behind. Therefore, utilization of a 40 minute plasma treatment was performed for all subsequent contamination removal coupons (both hydraulic fluid and lubricating oil) including modified ENF testing.

4.3.4. **Resin Modification Testing Results**

Resin modification testing was completed to determine if the recommended injection resin, Hysol's EA9396, could be modified to lower the viscosity while maintaining mechanical properties. Single lap shear, viscosity, and cure parameter testing were completed to develop a lower viscosity version of EA9396 that would be more advantageous to injection repair of delaminations.

Single Lap Shear Testing

Single lap shear testing of the EA9396 adhesive was completed on six different sample sets as described in Table 3.6 to determine the effect of solvent dilution with acetone or methyl-ethyl-ketone (MEK) on adhesive shear strength. The results from single lap shear testing per ASTM D1002 are shown in Figure 4.44 (BL indicates to baseline EA9396 and ACE denotes acetone). Error bars shown on the plot are the standard deviation for each sample set.

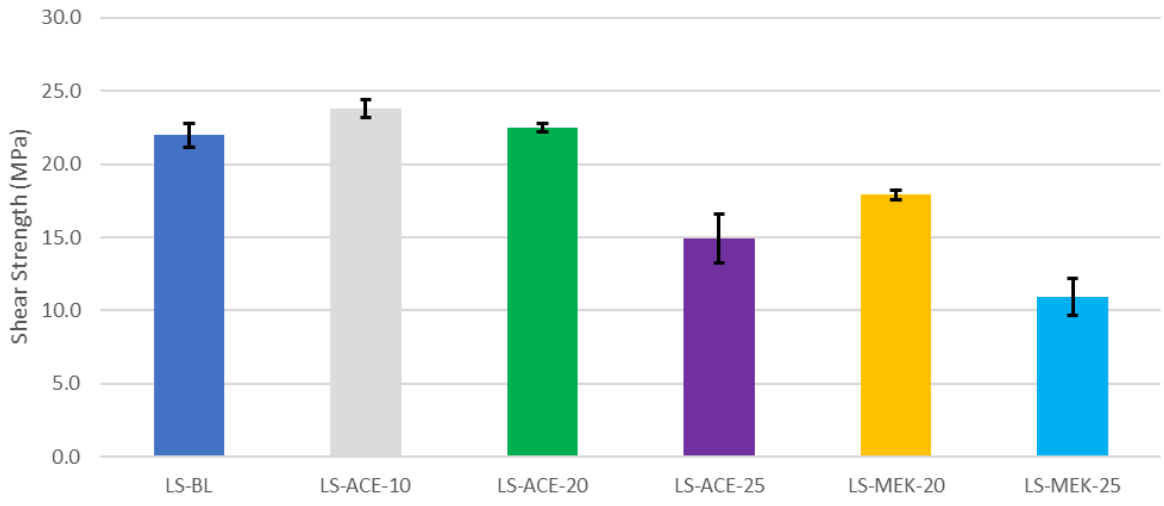

Figure 4.44. Repair resin modification single lap shear test results

Shear strength test results for the baseline (LS-BL) set, where neat EA9396 resin was used, had an average strength of 22.0 MPa. All other samples set, except the LS-ACE-20 and LS-ACE-10 samples sets, had a shear strength reduction as a result of the solvent dilution. Sample set LS-ACE-20, had an average shear strength of 22.5 MPa and LS-ACE-10, had and average shear strength of 23.8 MPa was within standard deviation of the baseline sample set. Failure modes for all coupon test sets can be seen in Appendix B. It was observed that all test sets had cohesive failure within the adhesive in the lap shear region, however it was determined that all of the coupons exhibited porosity in the adhesive flash locations as shown in Figure 4.45 and circled in Figure 4.46. Due to the superior lap shear performance of the acetone diluted sample sets, only the porosity of the acetone diluted samples were investigated using the cure parameter testing to determine if it was a byproduct of solvent dilution or mixing of the adhesive.

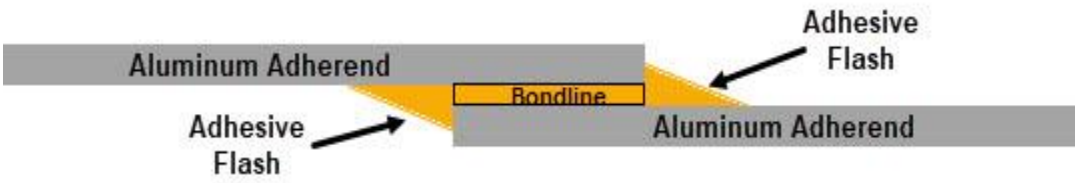

Figure 4.45. Single lap shear profile displaying flash locations

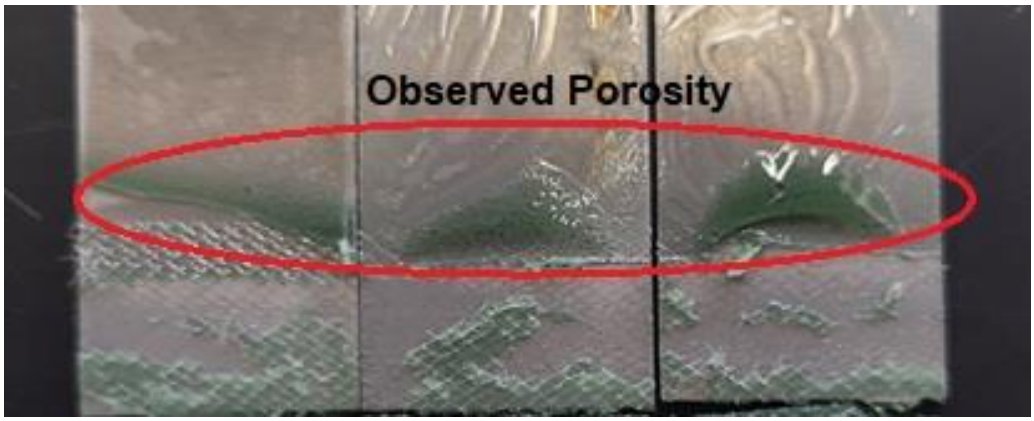

Figure 4.46. Porosity in single lap shear adhesive flash (LS-ACE-20 pictured)

Cure Parameter Testing

Cure parameter testing using resin pucks was completed to determine if diluted EA9396 would cure with induced porosity due to the solvent diluents being introduced into the repair resin. Experimental set-up of cure parameter testing coupon is described in section 3.3.4 and list of test samples are shown in Table 3.7. Example of the cure parameter resin pucks after cure can be seen in Figure 4.47.

Figure 4.47. Cure parameter testing of diluted EA9396 resin puck coupons

Figure 4.48 through Figure 4.52 show the macroscopic cross-section of each cure parameter coupon and a 100x zoom photomicrograph where micro-porosity was present. Cure parameter coupon CP-1 (undiluted EA9396 resin) was cured using the manufacturer recommended cure cycle of 1 hour at 66°C with no room temperature hold. CP-1 showed little to no visual indications of porosity in the macroscopic inspection (see Figure 4.48), however micro-porosity was observed in the 100x magnification microscopic photographs.

A 1 hour cure cycle at 88°C after a 16 hour room temperature hold was completed on samples CP-2 through CP-4. The 1 hour at 88°C is a repair cure cycle developed for use of the EA9396 epoxy resin on 220°F service temperature aircraft [82] and the 16 hour room temperature hold was utilized to allow the acetone to vaporize out of the diluted mixture prior and for the EA9396 to gel. Samples CP-2 (30% acetone dilution) and CP-3 (20% acetone dilution) were cured at 88°C for 1 hour after a 16 hour room temperature hold, show major porosity in the cured coupon (see Figure 4.49 and Figure 4.50), therefore no microscopic visual inspection was completed. Sample CP-4 (10% acetone dilution) was cured at 88°C for 1 hour after a 16 hour room temperature hold, exhibited porosity on the surface of the coupon around the edges and micro-porosity was observed in the photomicrograph of the coupon cross-section. The porosity in all coupons was not observed after the 16-hour room temperature hold, but appeared after the elevated temperature

cure at 88°C was completed even if the coupon appeared gelled. It was determined that the cure temperature at 88°C was above the boiling point of acetone at 56°C. Therefore it was determined that a longer solvent room temperature off-gas period was required to prevent the solvent from boiling and creating porosity in the repair resin.

Due to the porosity issues found with the 16 hour room temperature hold, CP-5 (10% acetone dilution) was room temperature held for 120 hours (5 days) prior to elevated temperature post-cure at 88°C. 5 days is the manufacturer's recommended room temperature cure cycle for EA9396 and would allow the adhesive to cure, then the 88°C would increase the glass transition temperature of the epoxy resin to be used on high service temperature (greater than 82°C) aircraft components. The macroscopic visual inspection did not indicate any surface porosity and microscopy revealed minor porosity found in the cross-section of the coupon (see Figure 4.52).

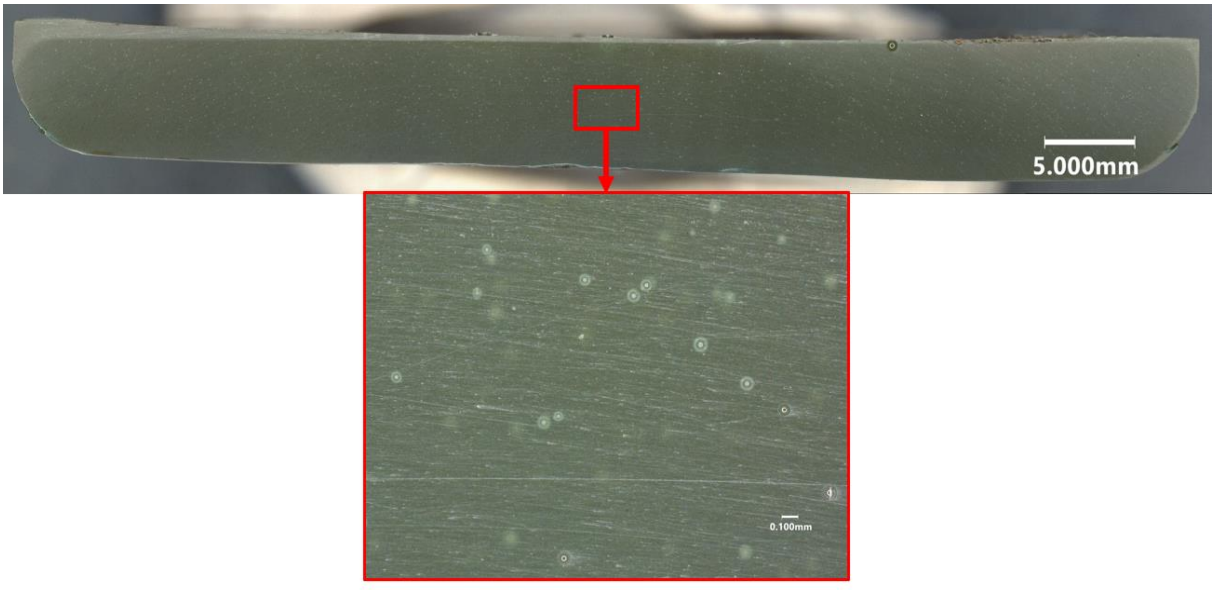

Figure 4.48. CP-1 (undiluted EA9396) cure parameter coupon at 5x with 100x zoom photomicrograph

Figure 4.49. CP-2 (30% acetone diluted EA9396) cure parameter coupon section

Figure 4.50. CP-3 (20% acetone diluted EA9396) cure parameter coupon section

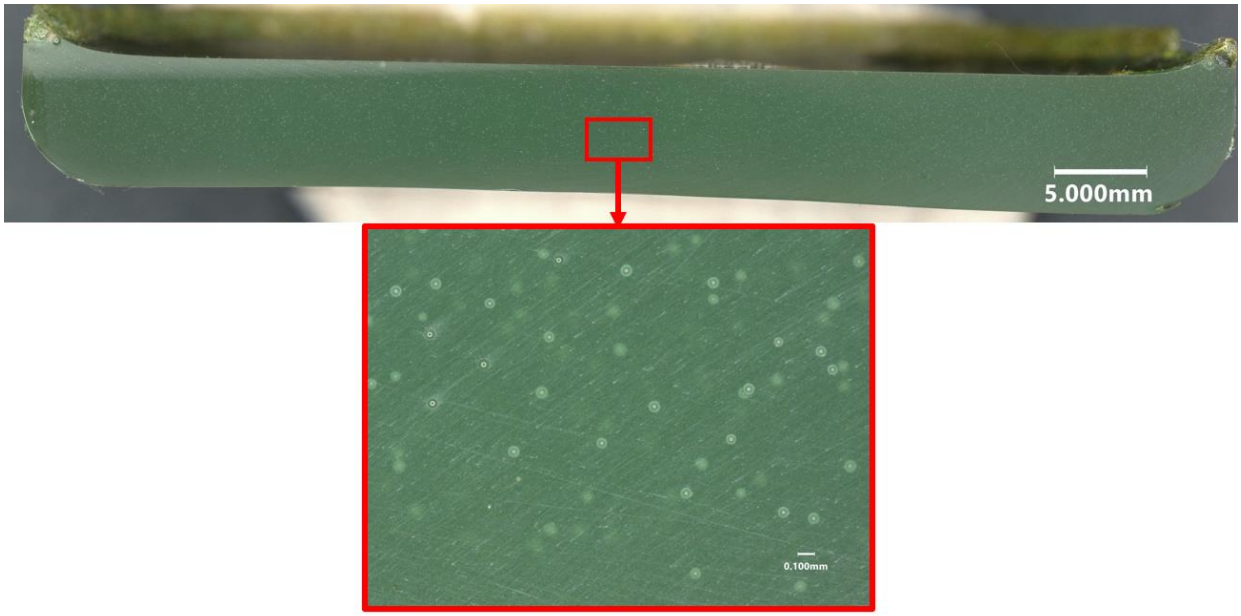

Figure 4.51. CP-4 (10% acetone diluted EA9396) cure parameter coupon at 5x with 100x zoom photomicrograph

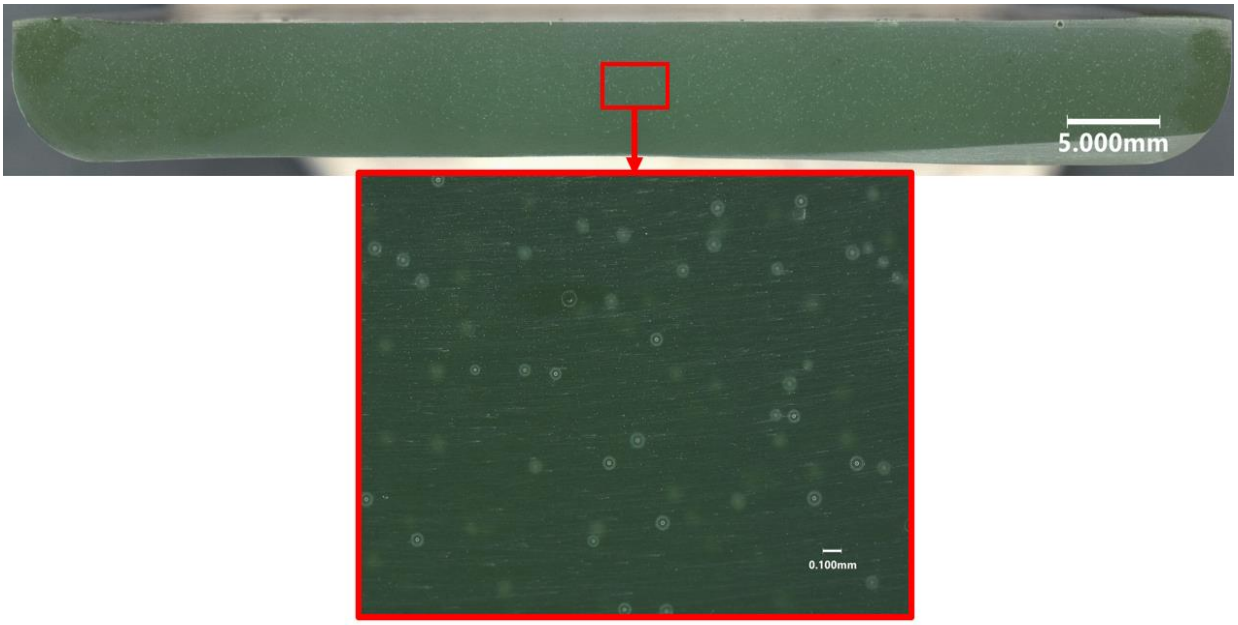

Figure 4.52. CP-5 (10% acetone diluted with 5 day room temperature cure) cure parameter coupon at 5x with 100x zoom photomicrograph

Due to the variability in cure cycle parameters for coupons fabricated, Barcol hardness was completed on the CP-1 and CP-5 coupons. Results of Barcol hardness readings are shown in Figure 4.53. The Barcol hardness testing is used to correlate the glass transition (Tg) of the epoxy to the hardness reading.

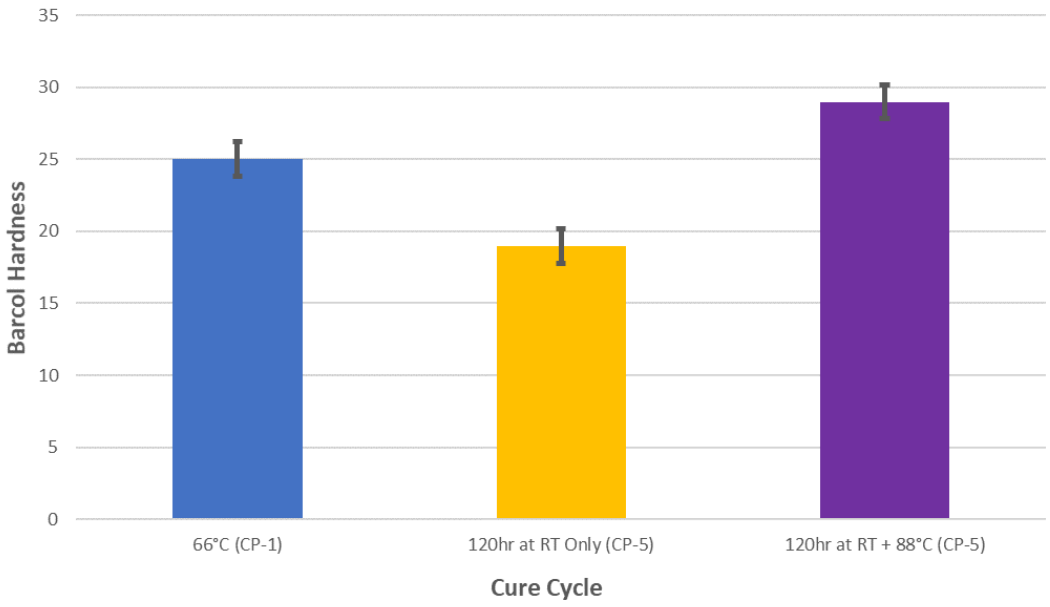

Figure 4.53. Cure parameter coupon Barcol hardness results

Coupon CP-1 (baseline cure cycle) was tested after the 66°C cure cycle was completed and had an average Barcol hardness of 25B. After the 120-hour room temperature hold for the CP-5 coupon, Barcol hardness was measured to be 19B. Once the CP-5 coupon was post cured at 88°C, it was re-tested and the Barcol Hardness increased to 29B. Therefore based on the Barcol testing, the Tg of the diluted EA9396 material was highest when post-cured at 88°C.

Viscosity testing was also completed to determine the effect of the diluent when compared to the 3600 cPs of the base mixed undiluted EA9396 resin. Results of viscosity testing over a ten-minute period are shown in Figure 4.54.

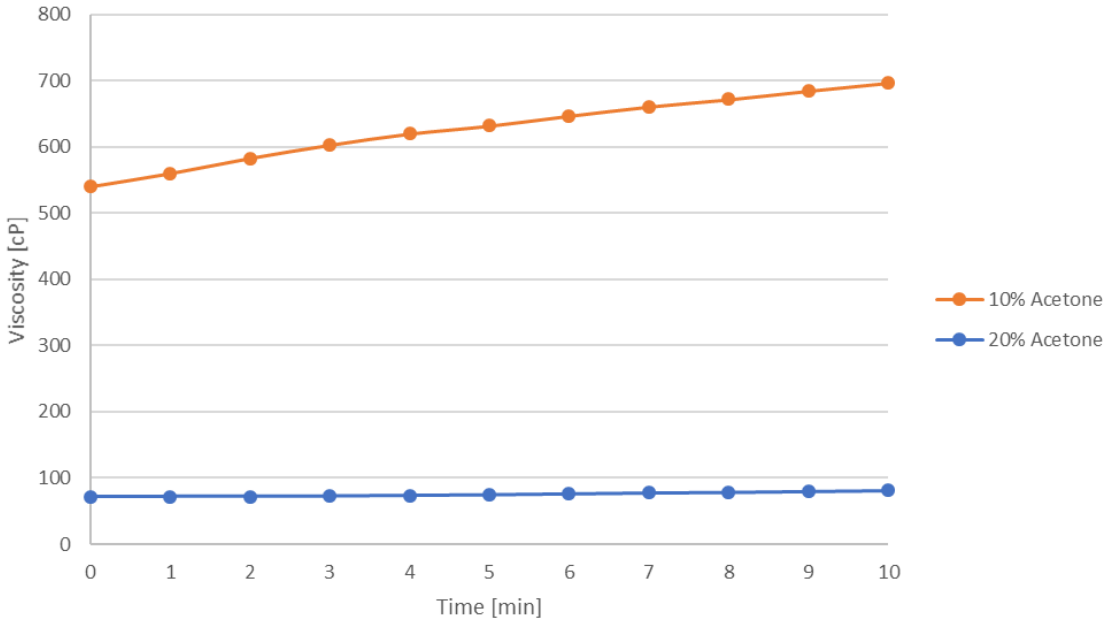

Figure 4.54. Diluted EA9396 Brooksfield viscosity test results

The 10% acetone dilution by weight viscosity test resulted in a viscosity increasing over time between 540-697 cPs. This is an 85% decrease in resin viscosity when compared to the baseline mixed EA9396. The EA9396 diluted with 20% acetone by weight had a viscosity of between 71.5 and 81.5 cPs over the 10-minute test period. As previously discussed, a viscosity of less than 100 cPs was targeted to ensure maximum fill of complex impact delaminations [43] and the 20% diluted EA9396 was able to meet that criterion. However, concerns remain about the ability of the 20% acetone to fill a delamination without gross porosity. Therefore both 10% and 20% diluted EA9396 were both evaluated with the modified ENF repair testing.

In order to verify that the viscosity of the diluted EA9396 injection repair resin will infiltrate a 50.8 mm delamination prior to gelling of the adhesive, the Russell [43] injection (equation 2.5) repair flow model was utilized. The following variables were input into the model: $t_0 = 0$, t_{cure}= 300 s, η= 697 cPs (for 10% dilution), P_1=P_2= 0.0059 MPa, R_1= 2.1 mm, R_2= 50.8 mm, and h=0.252 mm. It was calculated that both the 10% and 20% acetone dilution levels pass the repair flow model verification. Although 10% acetone dilution does not meet the 100 cPs viscosity recommendation from Russell's work, it does meet flow model requirements and was utilized as a repair resin for this study.

4.3.5. **Modified ENF Mechanical Testing Results**

Three different laminate configurations of modified ENF testing (see specimen and test description in section 3.3.5) were completed to determine the effectivity of the novel injection repair process to restore mechanical properties of delaminated PMCs. Baseline PMC testing was previously discussed in section 4.2.2. Also, an aluminum modified ENF coupon was utilized to determine the G_{IIC} of the modified injection repair resin in isolation from composite interlaminar failure modes. Finally, the fractured PMC modified ENF coupons were repaired using the novel injection repair process and re-tested to determine the restoration of mechanical properties to the delaminated composite. A summary of modified ENF test sets and configurations could be found in Table 4.7. Figure 4.55 is a key to the nomenclature of the sample set names.

Table 4.7. Modified ENF test matrix

Sample Set	Lay-up	Contaminant	Cleaned?	Repaired?	Repair Resin Dilution (by weight)	# of Coupons Tested
ENF-UNI-BL	Unidirectional	No	No	No	N/A	3
ENF-QUASI-BL	Quasi-Isotropic	No	No	No	N/A	3
ENF-CROSS-BL	Cross-ply	No	No	No	N/A	3
ENF-UNI-RPR-20%	Unidirectional	No	No	Yes	20% Acetone	3
ENF-QUASI-RPR-20%	Quasi-Isotropic	No	No	Yes	20% Acetone	3
ENF-CROSS-RPR-20%	Cross-ply	No	No	Yes	20% Acetone	3
ENF-UNI-RPR	Unidirectional	No	No	Yes	10% Acetone	3
ENF-QUASI-RPR	Quasi-Isotropic	No	No	Yes	10% Acetone	3
ENF-CROSS-RPR	Cross-ply	No	No	Yes	10% Acetone	3
ENF-UNI-CONT-HF	Unidirectional	Hydraulic Fluid	No	Yes	10% Acetone	2
ENF-QUASI-CONT-HF	Quasi-Isotropic	Hydraulic Fluid	No	Yes	10% Acetone	1
ENF-CROSS-CONT-HF	Cross-ply	Hydraulic Fluid	No	Yes	10% Acetone	2
ENF-UNI-CL-HF	Unidirectional	Hydraulic Fluid	Yes	Yes	10% Acetone	3
ENF-QUASI-CL-HF	Quasi-Isotropic	Hydraulic Fluid	Yes	Yes	10% Acetone	3
ENF-CROSS-CL-HF	Cross-ply	Hydraulic Fluid	Yes	Yes	10% Acetone	3
ENF-UNI-CONT-LO	Unidirectional	Lubricating Oil	No	Yes	10% Acetone	1
ENF-QUASI-CONT-LO	Quasi-Isotropic	Lubricating Oil	No	Yes	10% Acetone	2
ENF-CROSS-CONT-LO	Cross-ply	Lubricating Oil	No	Yes	10% Acetone	0
ENF-UNI-CL-LO	Unidirectional	Lubricating Oil	Yes	Yes	10% Acetone	3
ENF-QUASI-CL-LO	Quasi-Isotropic	Lubricating Oil	Yes	Yes	10% Acetone	3
ENF-CROSS-CL-LO	Cross-ply	Lubricating Oil	Yes	Yes	10% Acetone	3
AL-EA9396	Aluminum	N/A	No	Yes	10% Acetone	3

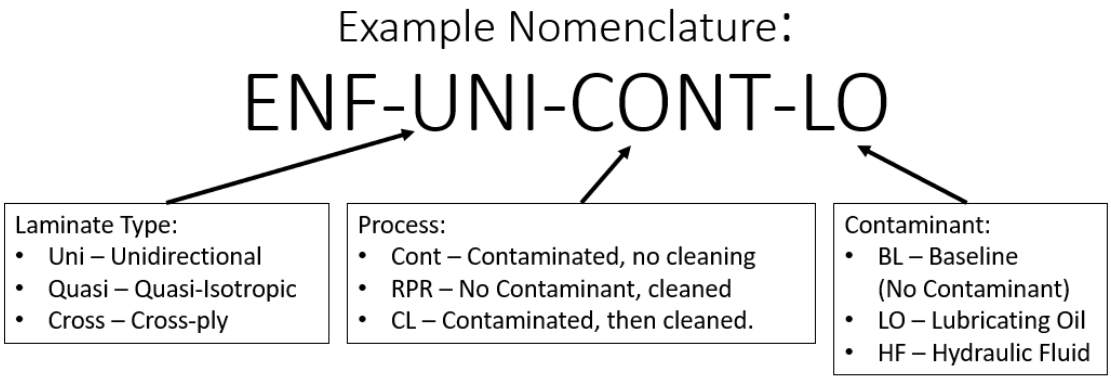

Figure 4.55. Modified ENF sample set nomenclature

The sample set configurations shown in Table 4.7 include variation in: lay-up, contaminant, and if the coupon was repair, if the cleaning surface preparation procedure was applied, if the coupons was repaired, and the number of samples tested for a set. In the case where a coupon was subjected to contamination (CONT or CL sample sets), an injection of the contaminant using the same process outlined in section 3.3.2 for enclosed contamination was completed. The sample sets that were subjected to the cleaning surface preparation procedure (RPR and CL sample sets) were subjected to the entire novel injection repair procedure in accordance with section 3.3.5. The minimum amount of coupons tested per a set was primarily three, however for some of the contaminated sample sets only one to two samples were tested because the bond was so weak in the repair that the coupon did not stay intact during set-up in the test rig. G_{IIC} was determined for pre-cracked (PC) test configuration in accordance with ASTM D7905 and in the same manner as discussed in section 4.2.2. All coupons that were not able to be tested due to the weak repair bond, were considered to have a $G_{IIC} = 0$. All plots in this section are representative views of the data collected and the number of tested specimen represented is provided in Table 4.7.

Aluminum Modified EA9396 Baseline Test Result

Aluminum baseline modified EA9396 tests were completed using a wedge pre-cracked coupon configuration instead of using a PTFE film (see specimen and test description in section 3.3.5 and Figure 3.5). A representative load versus displacement curve for the aluminum modified EA9396 sample set is shown in Figure 4.56.

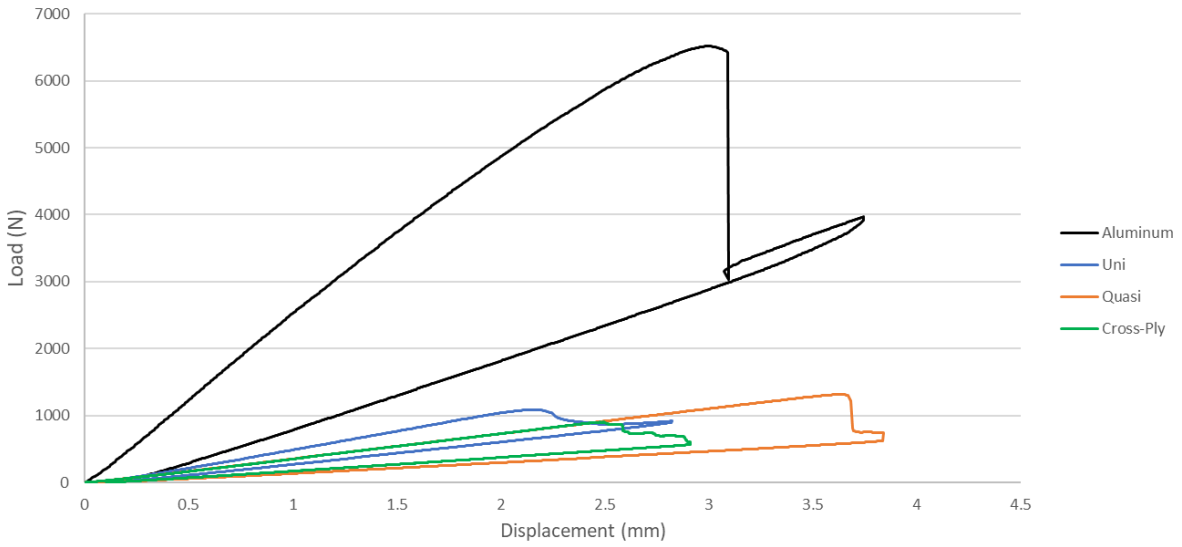

Figure 4.56. Load vs. displacement curve of aluminum EA9396 and baseline PMC modified ENF coupons

The modified EA9396 bonded aluminum ENF coupon had a stiffness of 2531 N/mm, which was 682% higher than the quasi-isotropic PMC laminate and 467% higher than the unidirectional and cross-ply PMC laminates. This increase in stiffness was primarily due to the larger thickness of the aluminum samples at 6.6 mm (to avoid yielding of the aluminum) when compared to the 3.11 mm average thickness of PMC coupons. The average calculated G_{IIC} for the aluminum EA9396 was 3410 ± 645 J/m^2 (three specimens tested). This shows that the modified EA9396 epoxy injection resin has a G_{IIC} that is approximately 200-400% greater than the IM7/977-

3 PMC laminate mode II interlaminar fracture toughness of 831-1301 J/m^2 (see section 4.2.2 for results).

20% Solvent Diluted Resin Repaired PMC Laminate Modified ENF Test Results

In the first iteration of PMC repaired laminate modified ENF testing, a 20% acetone by volume modified EA9396 injection resin was utilized due to the low viscosity. Samples sets ENF-UNI-RPR-20%, ENF-QUASI-RPR-20%, and ENF-CROSS-RPR-20% were all repaired with the 20% diluted EA9396 injection resin. Shown in Figure 4.57 is an example plot of the load versus displacement for a specimen from each of the sample sets.

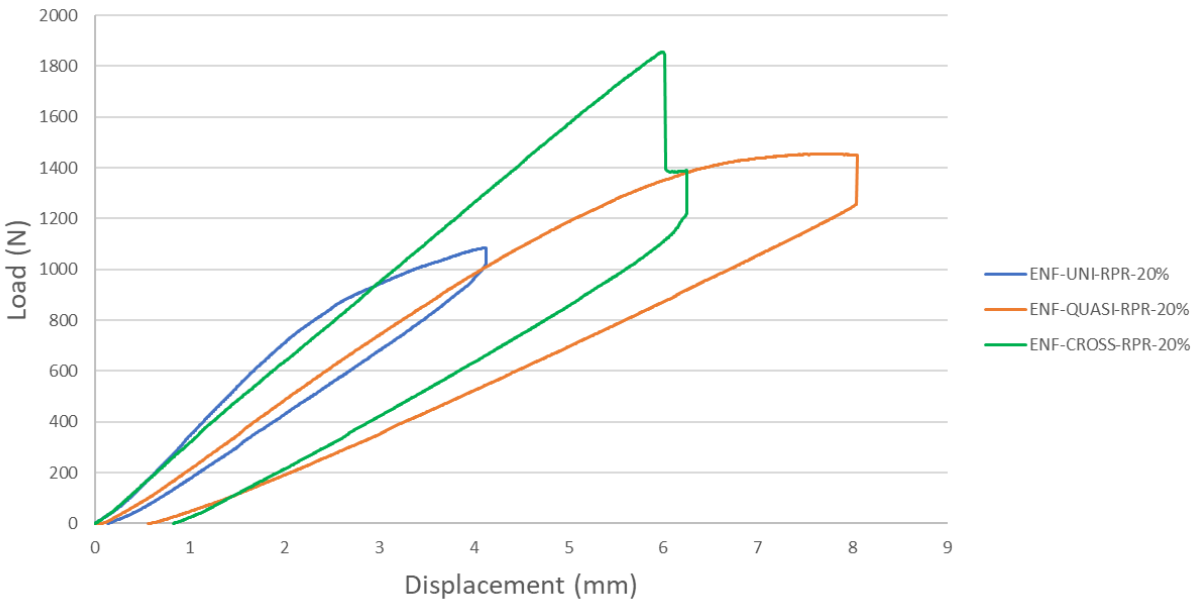

Figure 4.57. Load vs. displacement curve of 20% acetone diluted EA9396 repaired ENF coupons

The stiffness of the 20% acetone diluted EA9396 repaired ENF coupons were lower compared to the baseline coupons. The unidirectional sample set (ENF-UNI-RPR-20%) had a

stiffness of 320 N/mm which is 220 N/mm less than the baseline ENF specimens (see section 4.2.2 for data). The ENF-QUASI-RPR-20% and ENF-CROSS-RPR-20% both also had a stiffness reduction compared to the baseline coupons of 80 MPa and 122 MPa, respectively. Although the stiffness reduction was observed, the G_{IIC} increased for all laminate configurations as shown in Figure 4.58.

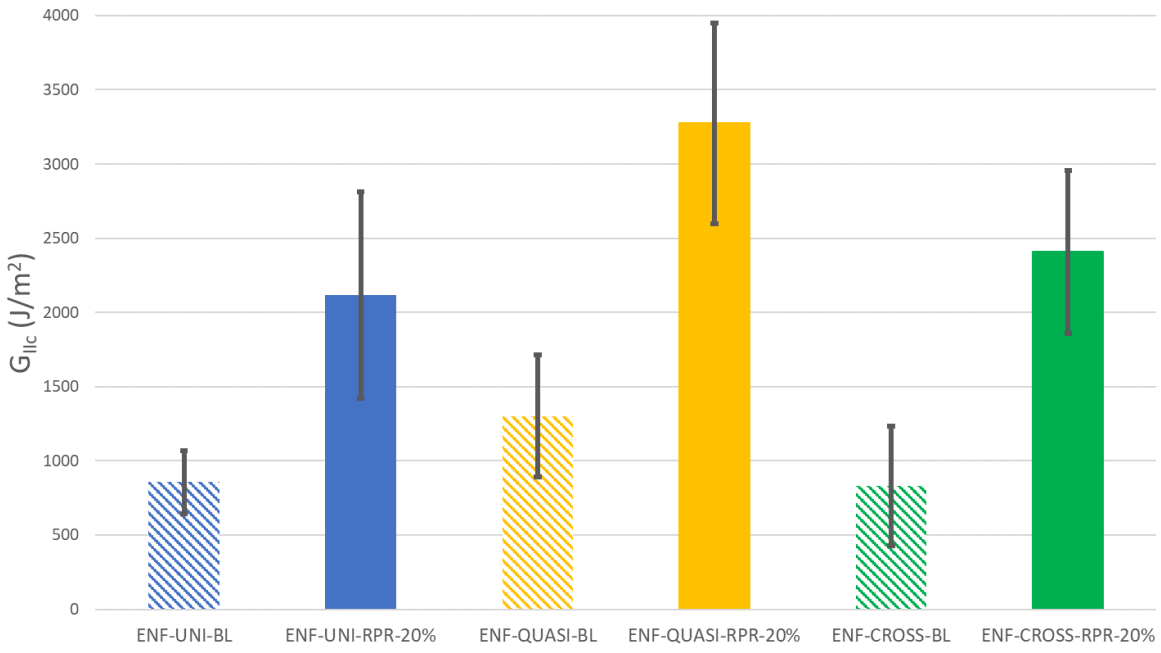

Figure 4.58. 20% acetone diluted repaired modified ENF test results

All of the 20% acetone diluted EA9396 repaired ENF coupons had a remarkable increase in G_{IIC} when compared to the baseline laminate ENF coupons (shown with striped bars). ENF-UNI-RPR-20% had a 155% increase in G_{IIC} compared to the baseline laminate value. ENF-QUASI-RPR-20% and ENF-CROSS-RPR-20% had 152% and 181% increases in G_{IIC}, respectively. Although the 20% acetone diluted ENF coupons resulted in a higher mode II fracture toughness, there are concerns about the large drop in coupon stiffness. Therefore the fracture

surfaces were investigated prior to any further modified ENF repair testing. Shown in Figure 4.59 are representative coupons of the post-fractured repaired surfaces.

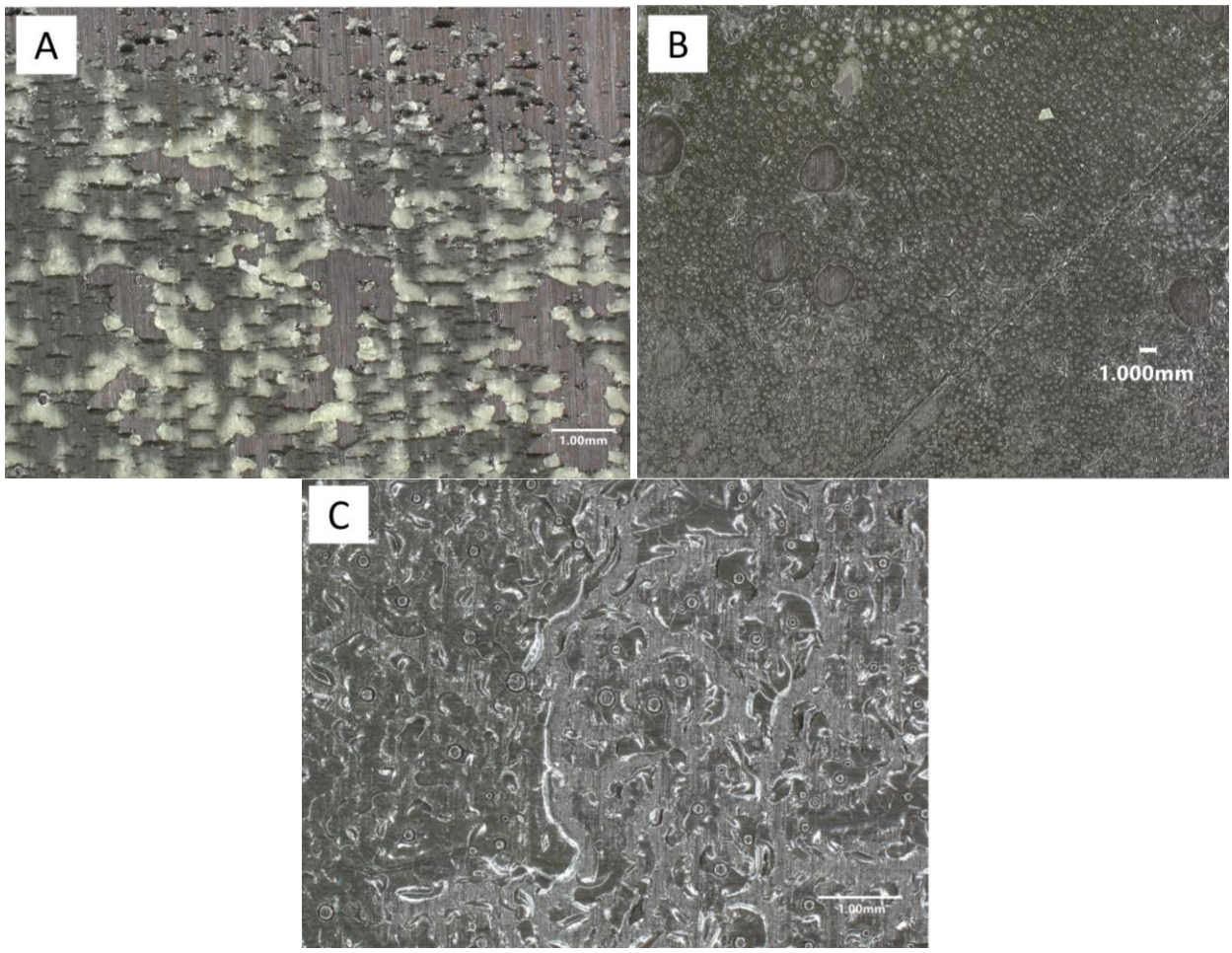

Figure 4.59. 20% acetone diluted EA9396 modified ENF injection repair coupon fracture surface (20x Zoom). A. Unidirectional B. Quasi-isotropic C. Cross-ply

The fracture surfaces of all of the coupons reveal major porosity within the bondline of all of the 20% acetone diluted repair specimens. Although the porosity may have had a toughening effect to increase the mode II fracture toughness of the sample, the reduction in stiffness and increase in porosity were of concern. It is likely that due to the porosity in the bondline, the repair would fail prematurely in fatigue. Therefore further repair testing would be conducted with 10%

acetone diluted EA9396 and gelled with a five day room temperature hold prior to cure at 88°C would be pursued as a path forward as a result from the cure parameter testing.

10% Solvent Diluted Resin Repaired PMC Laminate Modified ENF Test Results

15 different modified ENF sample sets were tested to determine the effectivity of the novel injection repair procedure with a 10% acetone diluted EA9396 injection repair resin. A summary of these sample sets can be seen in Table 4.7.

Shown in Figure 4.60 are representative load versus displacement curves for each of the unidirectional PMC laminate sample sets that were repaired with 10% acetone dilution EA9396 repair resin.

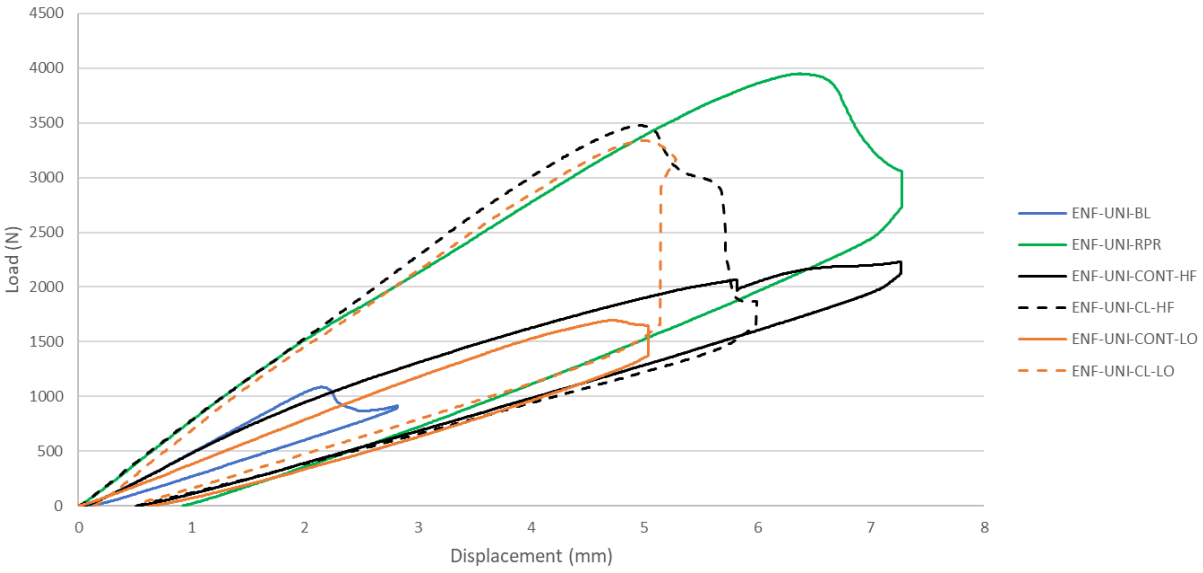

Figure 4.60. Load vs. displacement curve of unidirectional modified ENF coupons

The load versus displacement curves shows two primary trends when comparing the measured stiffness of the repaired ENF coupons to the baseline laminate sample set. The repaired

or cleaned and repaired sample sets had a stiffness greater than the baseline laminate (shown in Figure 4.60 by the green, dashed orange, and dashed black lines). The stiffness of these sample sets involving contamination plus cleaning (CL) or no contamination at all (RPR) was consistent residing between 770- 794 N/mm. However, the sample sets that were contaminated and left unclean prior to repair resin injection (ENF-UNI-CONT-LO and ENF-UNI-CONT-HF) had a 26% reduction in stiffness when compared to the baseline laminate. During testing for contaminated samples, there was no noticeable load drop or audible cracking due to crack extension. Therefore crack extension was visually tracked and determined by observing a change in stiffness denoted as an inflection point from the load versus displacement curve. An example of how the maximum load was extracted from the load versus displacement plot for the contaminated coupon sample set is shown in Figure 4.61.

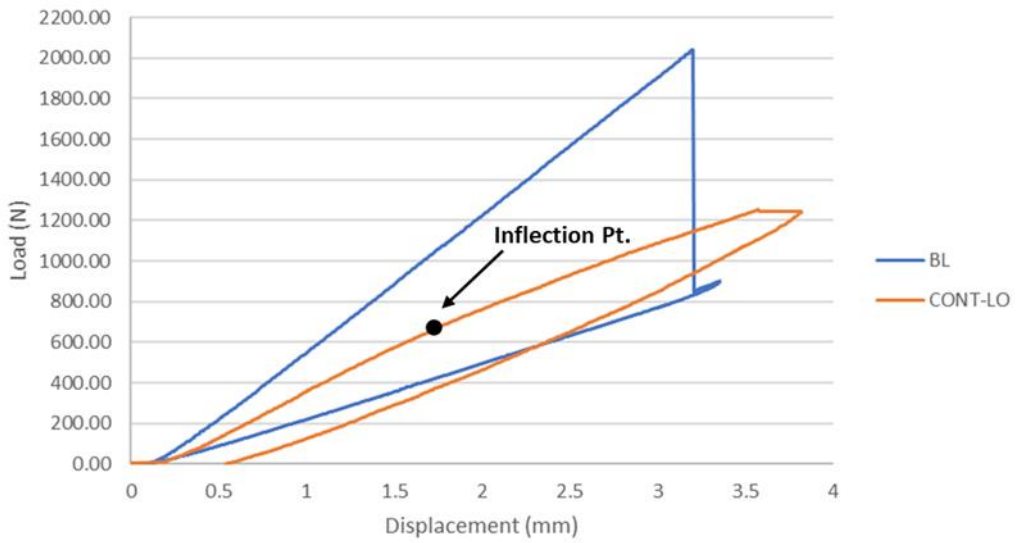

Figure 4.61. Example load vs. displacement curve contaminated sample set maximum load identification

The two samples for ENF-UNI-CONT-LO were both investigated for maximum load using the load versus displacement plot. The change in stiffness during testing after the inflection point was determined to have a slope of 303 N/mm. The slope of the unloading for the cracked baseline coupon had a similar slope of 294 N/mm. Therefore it is likely that after the inflection point, the ENF coupon was not loading into the bonded repair region (i.e. absence of bonding) and the load was being carried by the flexure of the two sub-laminates acting as if stacked together and then loaded per ENF configuration (with no bond).

The results for the unidirectional modified ENF samples sets are shown in Figure 4.62. Also included in this figure is the G_{IIC} value of the aluminum EA9396 (AL-EA9396) to compare the neat resin test values to the data collected from the unidirectional modified ENF testing.

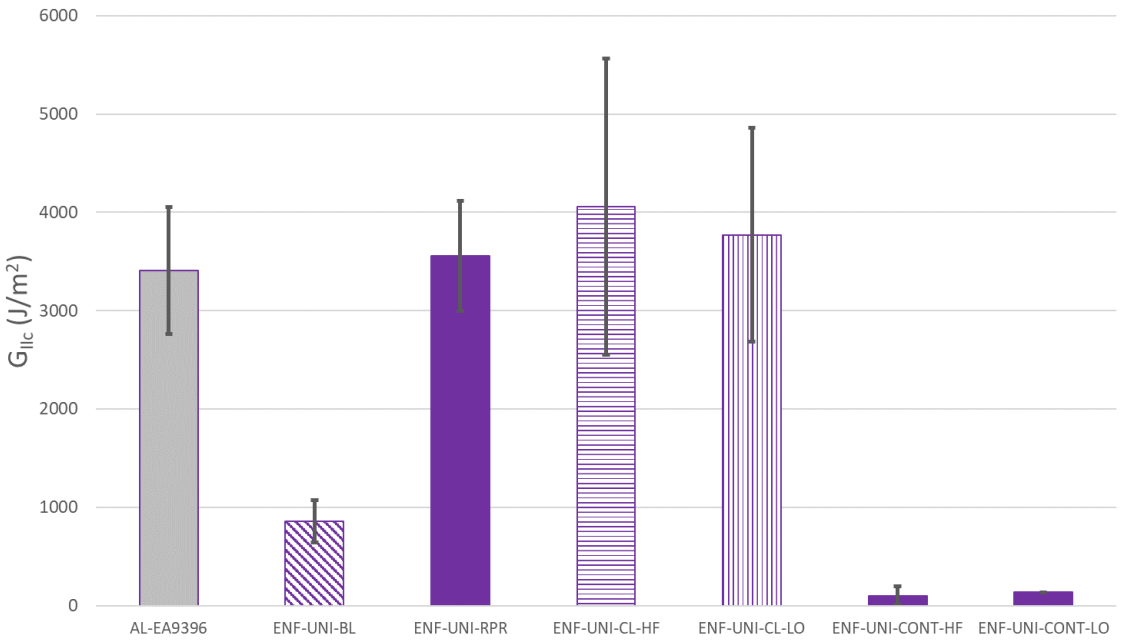

Figure 4.62. Modified ENF unidirectional test results

The average G_{IIC} for the baseline (pristine laminate) sample set of the IM7/977-3 material (ENF-UNI-BL) was 857 J/m^2. The baseline value would serve as the threshold requirement for coupons that were repaired using the new injection repair procedures. The previously discussed, aluminum 10% dilution EA9396 modified ENF test set had a G_{IIC} of 3410 J/m^2, which was a 298% increase in mode II fracture toughness compared to the baseline laminate. The sample set that was fractured and repaired (no contamination applied), ENF-UNI-RPR, is shown in Figure 4.62 with a solid bar, had an average G_{IIC} of 3555 J/m^2. This was approximately the same mode II fracture toughness of the neat injection repair resin with aluminum adherends. The sample set that was contaminated with hydraulic fluid, cleaned and repaired using the novel injection repair process (ENF-UNI-CL-HF, horizontal striped bar), had an increased average G_{IIC} of 4059 J/m^2, which is a 374% increase compared to the baseline laminate testing. Samples that were contaminated with lubricating oil and cleaned prior to injection repair (ENF-UNI-CL-LO) has an average G_{IIC} of 3771 J/m^2. All of the sample sets that were repaired, either without contamination or cleaned prior to injection repair, exhibited a large increase (>298%) compared to the baseline laminate. Although these sample sets had large increases in mode II fracture toughness, the average G_{IIC} is consistent with the values collected when testing the neat modified repair resin. The contaminated and cleaned sample sets also had the highest standard deviation compared to other sample sets, however the increase in G_{IIC} was statistically significant.

In order to test the effect of the novel injection repair process on laminates that are more representative of lay-ups found on aircraft, quasi-isotropic modified ENF testing was completed. Figure 4.63 shows an example of the load versus displacement curves for the each of quasi-isotropic modified ENF sample sets.

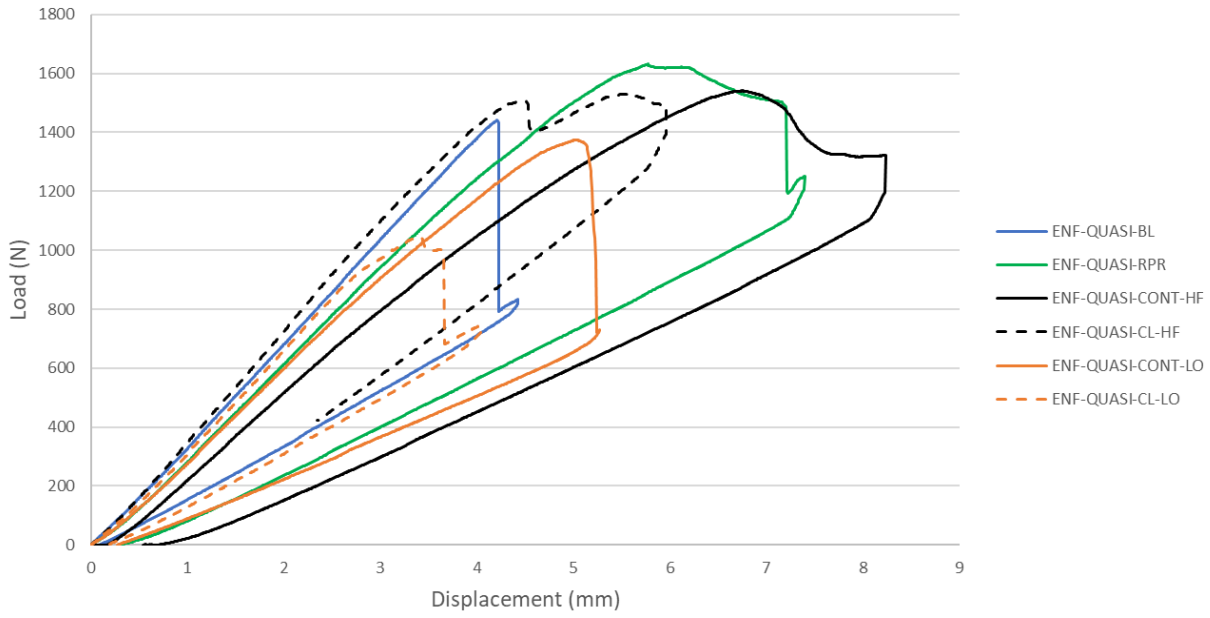

Figure 4.63. Load vs. displacement curve of quasi-isotropic modified ENF coupons

The quasi-isotropic modified ENF testing did not exhibit as much discrepancy in stiffness between samples sets. The ENF-QUASI-RPR, ENF-QUASI-CL-HF, and ENF QUASI-CL-LO coupon sample sets that were representative of non-contaminated or contaminated and cleaned delaminations, have similar stiffness to the baseline laminate. However the contaminated samples sets (ENF-QUASI-CONT-LO and ENF-QUASI-CONT-HF) did not have a considerable reduction in coupon stiffness as seen in the unidirectional coupon testing. The non-contaminated or cleaned coupons had stiffness ranging between 325-375 N/mm, whereas the contaminated coupons had stiffness between 283-308 N/mm. The reduction in contaminated coupon stiffness was approximately 12% compared to baseline laminate properties.

Mode II fracture toughness results for the quasi-isotropic modified ENF coupon are shown in Figure 4.64.

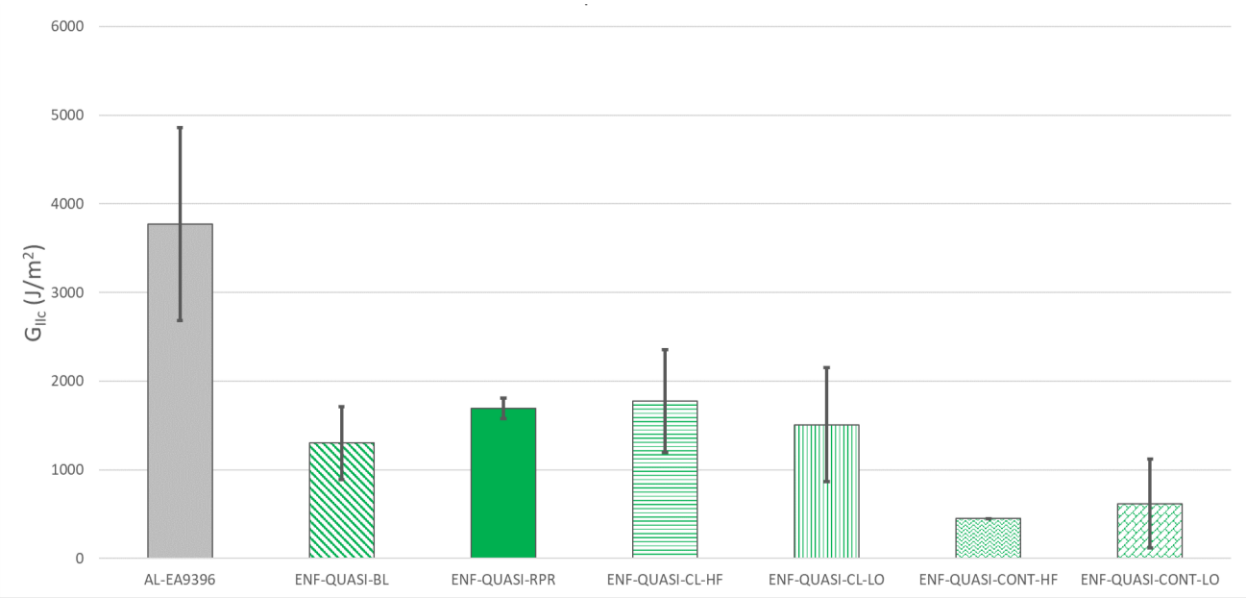

Figure 4.64. Modified ENF quasi-isotropic test results

Overall the calculated G_{IIC} for the modified ENF quasi-isotropic test coupons was lower than the unidirectional configuration. Although the quasi-isotropic baseline sample set (ENF-QUASI-BL) at 1302 J/m^2 was on average higher G_{IIC} than the unidirectional samples set (ENF-UNI-BL) at 857 J/m^2, the repaired configurations appeared to have lower overall values than the unidirectional repaired configurations. The quasi-isotropic non-contaminated or contaminated and cleaned samples sets: ENF-QUASI-RPR, ENF-QUASI-CL-HF, and ENF-QUASI-CL-LO, all had higher average G_{IIC}, however the results were statistically within range of the baseline sample set and lower than the neat repair adhesive aluminum modified ENF coupons. This is a change compared to the unidirectional sample set that had a minimum increase of 298%, however the average test results for cleaned and repaired modified ENF coupons do meet the threshold of restoring mode II fracture toughness to the baseline testing results. Failure mode analysis will further expound why the test results are similar to the baseline laminate. The (no cleaning) contaminated samples set, ENF-QUASI-CONT-HF and ENF-QUASI-CONT-LO, both had lower

average G_{IIC} compared to the baseline sample set, however the ENF-QUASI-CONT-LO sample set was statistically within range. It must be noted that two of the ENF-QUASI-CONT-HF and one of the ENF-QUASI-CONT-LO coupons could not be tested because the coupons fell apart due to weak bonds while handling prior to testing. This indicates that the contaminated and un-cleaned condition results in little to no interlaminar shear strength, therefore the actual G_{IIC} is close to 0 for this state.

A cross-ply laminate modified ENF coupon was tested to determine the ability for the novel injection repair process to infiltrate a 0/90° fractured surface with micro-gaps for fluid to flow. First, the ability for the simulated delamination to retain stiffness as a result of the injection repair was considered. Figure 4.65, displays example load versus displacement for each cross-ply sample set.

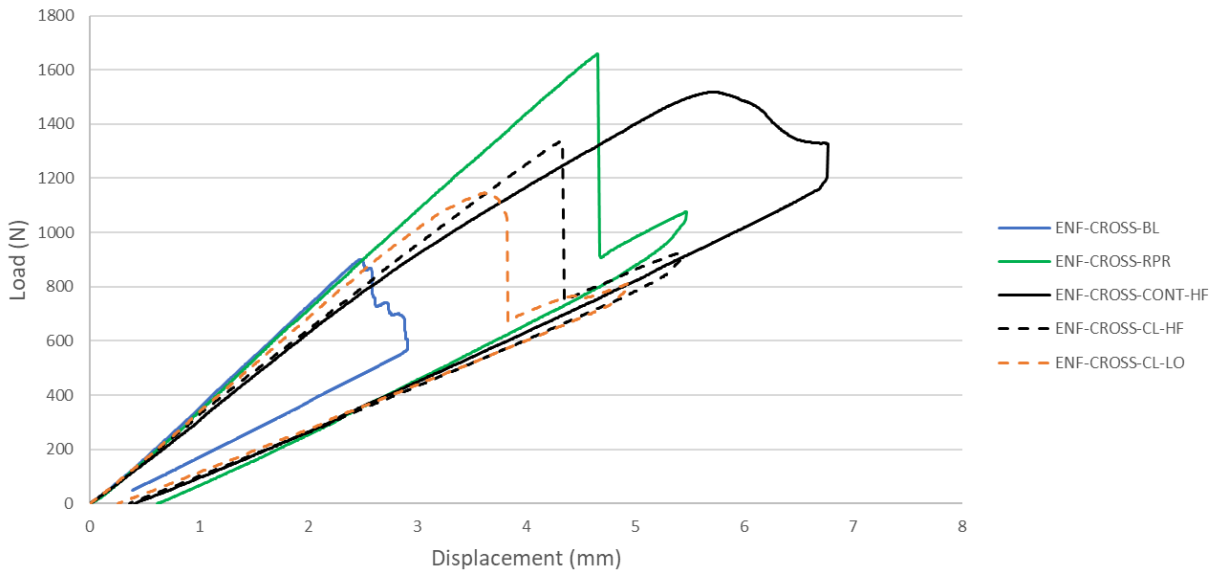

Figure 4.65. Load vs. displacement curve of cross-ply modified ENF coupons

The stiffness calculated for cross-ply sample sets as a whole were similar compared to the quasi-isotropic modified ENF laminate configurations. The stiffness observed between the cross-ply sample sets was between 361-321 N/mm for all sets that were not left contaminated. The hydraulic fluid contaminated sample set (ENF-CROSS-CONT-HF) had a stiffness of 304 N/mm. In addition, the hydraulic fluid contaminated sample set exhibited similar behavior when being loaded, where there was no major drop in load carrying capability unlike the rest of the cross-ply sample sets. The lubricating oil contaminated sample set could not be tested because all samples fell apart within the test fixture and could not carry load (so G_{IIC} values are zero for these samples).

The calculated G_{IIC} results for all cross-ply modified ENF sample sets can be seen in Figure 4.66. Overall average G_{IIC} of the cross-ply samples sets was lower than the unidirectional, but higher than the quasi-isotropic sample sets. The baseline cross-ply sample set (ENF-CROSS-BL) had an average value of 831 J/m2 that was within standard deviation of both the unidirectional (ENF-UNI-BL) and quasi-isotropic (ENF-QUASI-BL) baseline sample sets. The repaired or cleaned and repaired sample sets configuration of: ENF-CROSS-RPR, ENF-CROSS-CL-HF, ENF-CROSS-CL-LO were on average higher than the cross-ply baseline laminate test results with values of 2178, 2346, and 2011 J/m2, respectively. This was an average increase of 142% in mode II fracture toughness compared to the baseline sample set. These cross-ply repaired or cleaned and repaired sample sets were lower on average mode II fracture toughness than the same configuration in unidirectional sample sets and higher than the quasi-isotropic sample sets.

However, the standard deviation, shown by the error bars, were large enough for the ENF-CROSS-RPR, ENF-CROSS-CL-HF, ENF-CROSS-CL-LO sample sets to be within the lower end of repaired unidirectional (ENF-UNI-RPR, ENF-UNI-CL-HF and ENF-UNI-CL-LO) and aluminum sample set (AL-EA9396) range and within the higher end of the repaired quasi-isotropic

(ENF-QUASI-RPR, ENF-QUASI-CL-HF and ENF-QUASI-CL-LO) and baseline cross-ply sample sets (ENF-CROSS-BL). This could be a result of the coupon failure mode being more within the adhesive for the higher G_{IIC} results or propagating more within the parent laminate for the lower G_{IIC} results. Further investigation of the failure modes was conducted in section 4.3.6. The lone contaminated sample set, ENF-CROSS-CONT-HF, had hydraulic fluid contamination and an average G_{IIC} of 274 J/m2, which was a 67% reduction compared to the baseline laminate sample set. The lubricating oil contaminated sample set, ENF-CROSS-CONT-LO, did not record a G_{IIC} because all samples did not bond and could not be tested.

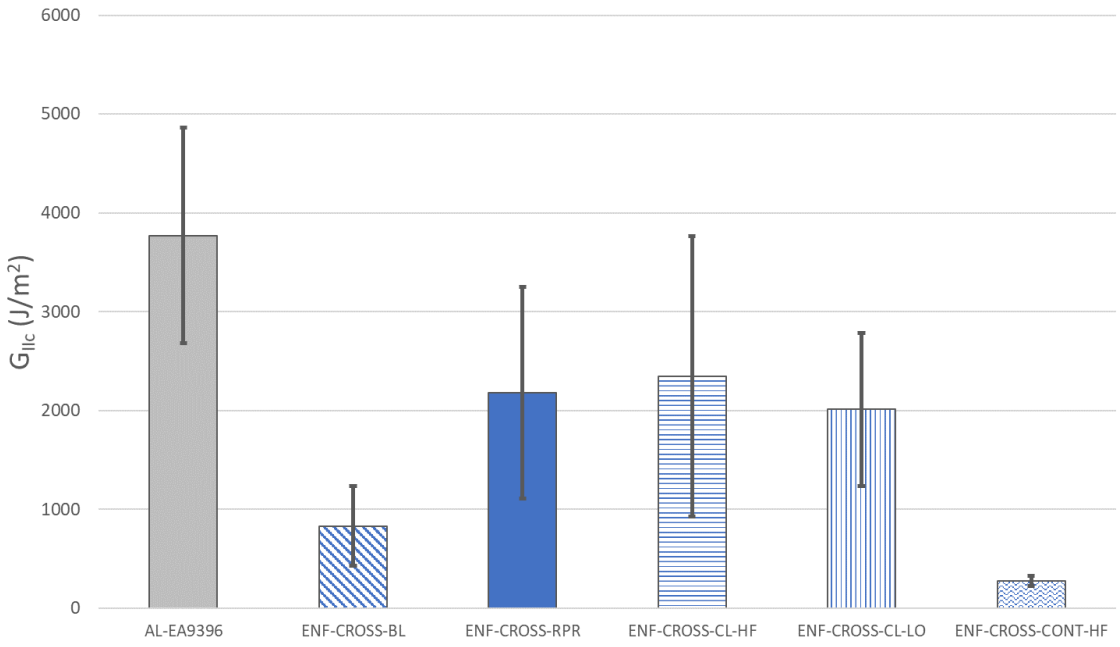

Figure 4.66. Modified ENF cross-ply test results

The modified ENF testing of the repaired laminate configurations revealed that in all cases where the laminate was repaired (no contamination) or cleaned (after contamination) and repaired

using the novel injection repair process, the G_{IIC} was fully recovered or increased. The results also display that coupons which were left contaminated and injected with the diluted repair resin without cleaning had significantly lowered (even zero) G_{IIC} compared to the baseline sample sets for each laminate configuration. These intuitive results, show that the contaminant is affecting the bond between the repair resin and the parent PMC laminate. In addition, it was found that the diluted EA9396 repair material has a higher G_{IIC} compared to the IM7/977-3 laminate. In conjunction it was found that the unidirectional repair laminates had G_{IIC} values in the same range as the neat resin tests, whereas the quasi-isotropic repaired laminates had G_{IIC} values more closely resembling the baseline laminate values. In addition, the repaired cross-ply laminates had values in between the unidirectional and quasi-isotropic modified ENF values.

4.3.6. **Modified ENF Microscopy, Fracture Surface, and Scanning Electron Microscope Analysis Results**

In order to fully understand the results from the modified ENF testing, a failure mode analysis of the coupon fracture surfaces was done. This analysis was conducted by performing fractographic analysis of the profile and planar fracture surfaces using both digital microscopy and scanning electron microscopy (SEM). Digital microscopy and SEM were able to conduct both low magnification (20-100x) and high magnification (300x-2500x) analysis. Photographs of profile and planar fracture surfaces of coupons are representative depictions of multiple specimens replicating the same condition. The number of specimens tested for each sample set is listed in Table 4.7 and the photographs in this section are representations of each batch of coupons.

Microscopic Profile Analysis

Figure 4.67 shows a profile of the repaired with 10% acetone diluted EA9396 ENF coupons (specimens labeled RPR) prior to fracture. This is the pristine coupon after the novel injection repair was conducted and prior to testing. Figure 4.67 shows that the modified adhesive was able to fully infiltrate and fill the coupon as indicated by the visible resin-filled zone (line) along the mid-plane. There are minor areas of porosity that may be inherent to the process, however a greater than 90% fill was observed. This was also verified with post repair non-destructive inspection using ultrasonic testing.

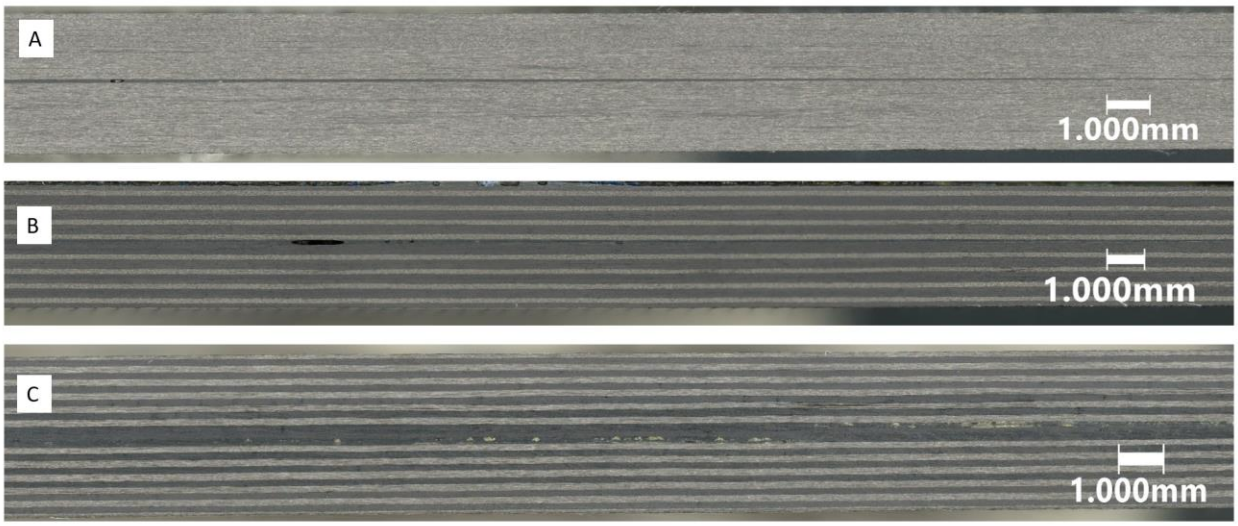

Figure 4.67. Profile view of repaired modified ENF coupons. A. Unidirectional, B. Quasi-isotropic, C. Cross-ply for EA9396 diluted with 10% acetone

In addition to inspecting the injection repair resin fill, the bondline for the repair was measured for each of the sample sets. In Table 4.8, the aluminum, uncontaminated, or cleaned and repaired ENF sample set data was presented for bondline thickness. The contaminated coupons were not measured due to the lack of bond for most coupons. This data was collected using a micrometer

and subtracting the baseline laminate thickness that was recorded prior to fracture from the repaired configuration thickness. Aluminum samples were measured using a measuring microscope in three sections of each coupon and averaged for all three measurements. The injection bondline repair thickness measurements were very consistent for all unidirectional repair configurations being 0.11 mm. This was approximately 4% of the total thickness of the coupon. Quasi-isotropic coupons had an average of 0.21 mm for repaired, 0.19 mm for lubricating oil cleaned and repaired, and 0.20 mm for hydraulic fluid cleaned and repaired coupons. This is approximately 8% of the coupon thickness. Cross-ply modified ENF coupons has the thickest bondlines at 0.37, 0.37, and 0.34 mm for sample sets ENF-CROSS-RPR, ENF-CROSS-CL-LO, and ENF-CROSS-CL-HF, respectively.

Table 4.8. Modified ENF repair bondline thicknesses

Sample Set	Lay-up	Avg. Bondline Thickness (mm)
ENF-UNI-RPR	Unidirectional	0.11
ENF-UNI-CL-LO	Unidirectional	0.11
ENF-UNI-CL-HF	Unidirectional	0.11
ENF-QUASI-RPR	Quasi-Isotropic	0.21
ENF-QUASI-CL-LO	Quasi-Isotropic	0.19
ENF-QUASI-CL-HF	Quasi-Isotropic	0.20
ENF-CROSS-RPR	Cross-ply	0.37
ENF-CROSS-CL-LO	Cross-ply	0.37
ENF-CROSS-CL-HF	Cross-ply	0.24
AL-EA9396	Aluminum	0.24

The bondlines for Cross-ply laminate modified ENF coupons were 12% of the total thickness of the coupon. The aluminum coupons had a 0.24 mm average bondline thickness.

Once the coupons were tested in ENF, photomicrographs of the profiles were also taken to determine location of the crack propagation and shape of the crack. Note that on, a few of the profile photographs, some white areas may be present which is not fully removed left over white

paint from tracking the crack propagation during testing. Figure 4.68 shows a profile section of the modified aluminum ENF coupon AL-EA9396.

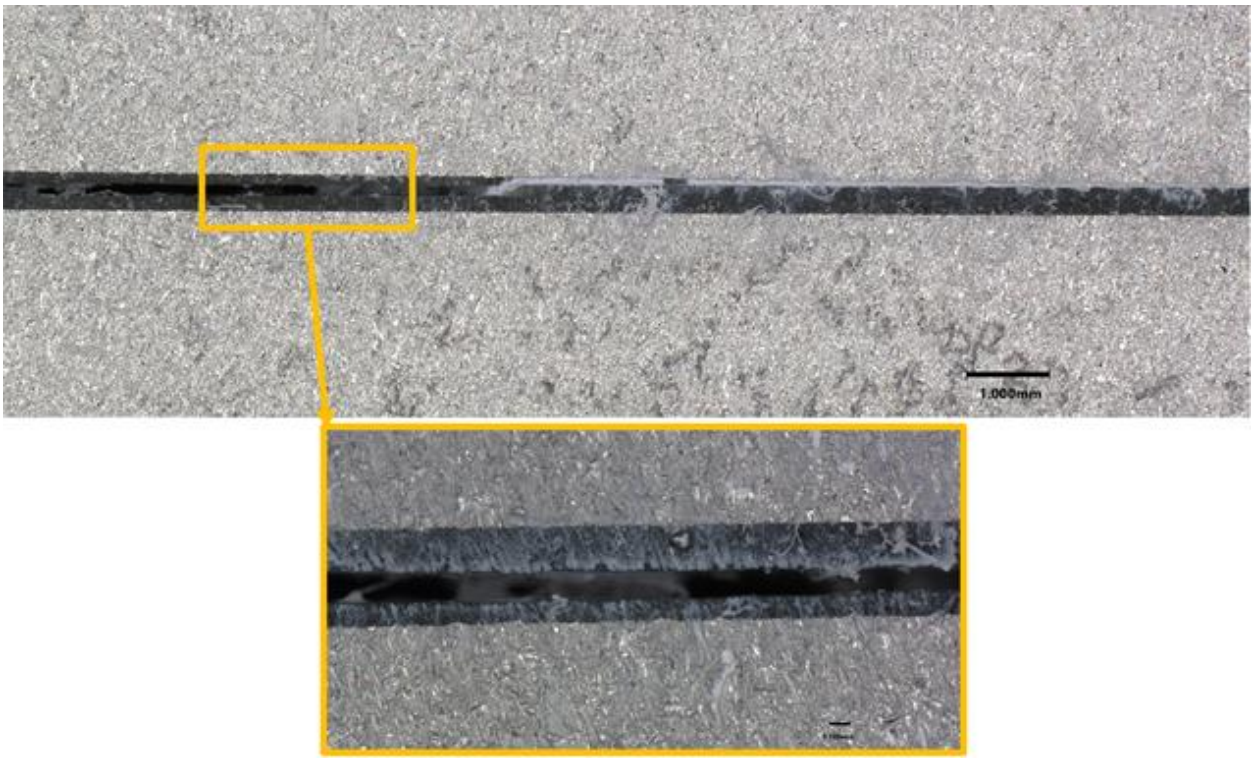

Figure 4.68. Profile view of post-tested aluminum EA9396 modified ENF coupons

In the profile section of the aluminum EA9396 coupon, the crack is started and propagation continues wholly within the adhesive as seen in the 100x magnification orange box of Figure 4.68. The crack then propagates to the adhesive-to-aluminum interface and remains there until the loading is completed. This fracture propagation was consistent for all of the aluminum EA9396 coupons. The crack propagates to the aluminum interface due to the fracture wanting to move toward the surface because of the principal stress created by the mode II interlaminar shear load case.

Figure 4.69 displays the crack propagation within all variations of the unidirectional repaired configurations of the modified ENF coupons.

The fracture profile of the ENF-UNI-RPR in Figure 4.69A shows that the crack propagation continued into the adhesive layer at the beginning of the repaired region and in some minor areas the crack would move to the adhesive-to-laminate interface. Similarly the ENF-UNI-CL-HF and ENF-UNI-CL-LO samples sets (see Figure 4.69B and C) also both had crack propagation start entirely in the adhesive and then move to the adhesive-to-laminate interface. In the contaminated sample ENF-UNI-CONT-HF, as shown in Figure 4.69D, the fracture primarily stays within the repair resin layer. The fracture of the hydraulic fluid contaminated coupon, shows a non-uniform crack propagation, where rounded regions of fracture are observed possibly showing areas of porosity. For sample set, ENF-UNI-CONT-LO, the fracture propagates within the adhesive and moves to the adhesive-to-laminate interface and then further along the fracture (to the right in Figure 4.69E) there are circular features which is indicative of an area of porosity prior to the fracture staying within the adhesive. For all unidirectional samples, there was no visual indication of instances where the fracture migrated further into the laminate than the adhesive-to-laminate interface (i.e., interlaminarly into the 1^{st} ply).

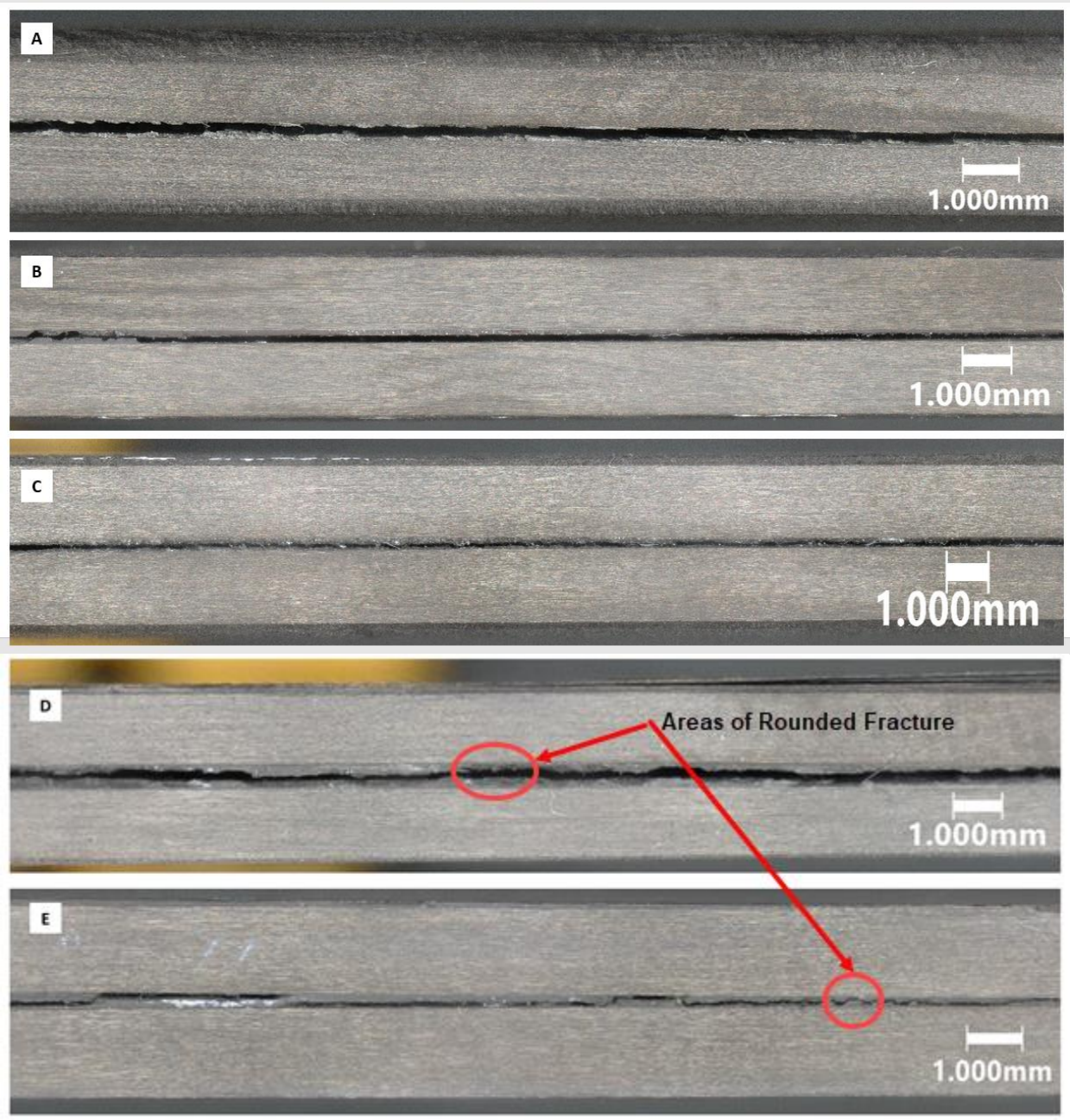

Figure 4.69. Profile view of unidirectional modified ENF repair fractures. A. ENF-UNI-RPR; B. ENF-UNI-CL-HF; C. ENF-UNI-CL-LO; D. ENF-UNI-CONT-HF; E. ENF-UNI-CONT-LO

The quasi-isotropic fracture profile for the repaired configuration (ENF-QUASI-RPR) is shown in Figure 4.70A, shows a fracture that starts in the adhesive-to-laminate interface then migrates transversely through the adhesive to the opposite laminate. The fracture then migrates

into the first ply of the laminate. In the ENF-QUASI-CL-HF coupon (shown in Figure 4.70B) the fracture starts in the adhesive then migrates to the first ply in the upper sub-laminate. The fracture then migrates back to the lower sub-laminate, which is an indication of where the ENF test was paused and the coupon was flipped and loaded for a second time; however the primary fracture is within the first ply. Similarly, the ENF-QUASI-CL-LO coupon had primarily first ply fracture in the lower sub-laminate as shown in Figure 4.70C and the fracture migrates transversely at the right end of the coupon, which is where the coupon was flipped and loaded for a second time. Both of the contaminated coupons, ENF-QUASI-CONT-HF and ENF-QUASI-CONT-LO, primarily had failures within the repair resin. The fracture shown in Figure 4.70D and E exhibit rounded fracture regions where the fracture was likely a result of propagation through porosity within the repair resin.

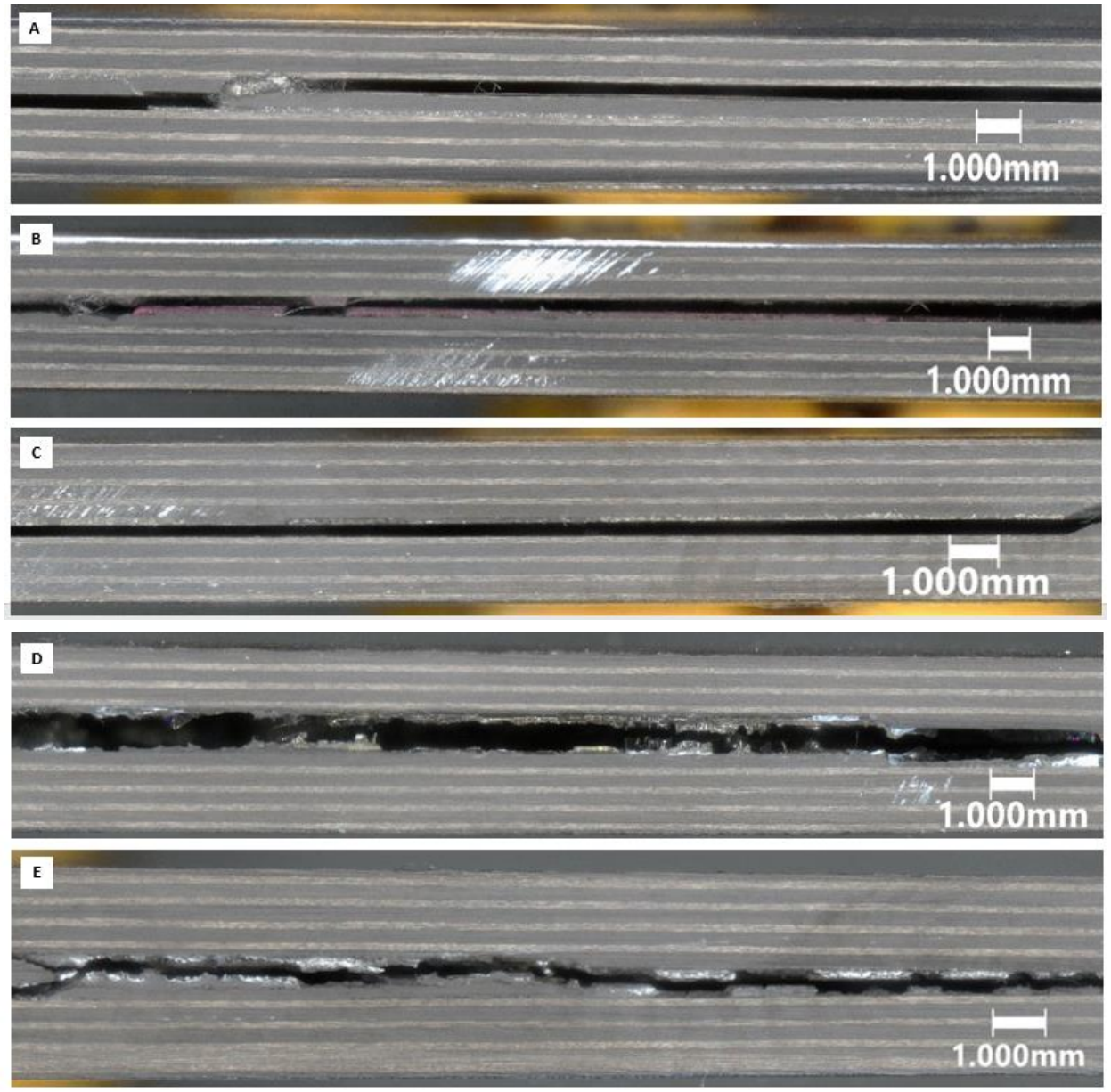

Figure 4.70. Profile view of quasi-isotropic modified ENF repair fractures. A. ENF-QUASI-RPR; B. ENF-QUASI-CL-HF; C. ENF-QUASI-CL-LO; D. ENF-QUASI-CONT-HF; E. ENF-QUASI-CONT-LO

Cross-ply modified ENF laminate fracture profiles are shown in Figure 4.71. The repaired configuration, ENF-CROSS-RPR, has a fracture that starts within the repair resin and immediately propagates to the first ply of the lower sub-laminate (see Figure 4.71). The fracture then propagates transversely upwards into the opposite sub-laminate first ply, which was due to the coupon being flipped after the first loading. The crack then propagates wholly within the first ply, creating a step-like profile from first ply within one sub-laminate into the opposite sub-laminate. Similar fractures are observed for the ENF-CROSS-CL-HF and ENF-CROSS-CL-LO fracture profiles (shown in Figure 4.71B and Figure 4.71C), where the fracture is within the first ply of one sub-laminate and propagates to the opposite sub-laminate after flipping the coupon in the test fixture and re-loading. At the transition region where the fracture propagates transversely, the region appears to have an interlaminar shear fracture at the step transition. The contaminated coupons ENF-CROSS-CONT-HF and ENF-CROSS-CONT-LO (shown in Figure 4.71D and Figure 4.71E) both have similar fracture within the repair resin. The fracture appears to have circular porosity regions and the fracture propagates fully within the repair resin, whereas in the non-contaminated or cleaned cross-ply repair coupons, the transverse propagation of the fracture is independent of the repair resin and correlated to where the initial fracture arrested and where the coupon was flipped and re-tested within the fixture. This indicates that the contaminated coupon repair resin layer was the path of least resistance for the fracture and the contaminant may have compromised the repair resin. In addition to the profile fracture photographic analysis, the average crack length for each loading of the modified ENF coupons was measured using a caliper and results are shown in Table 4.9.

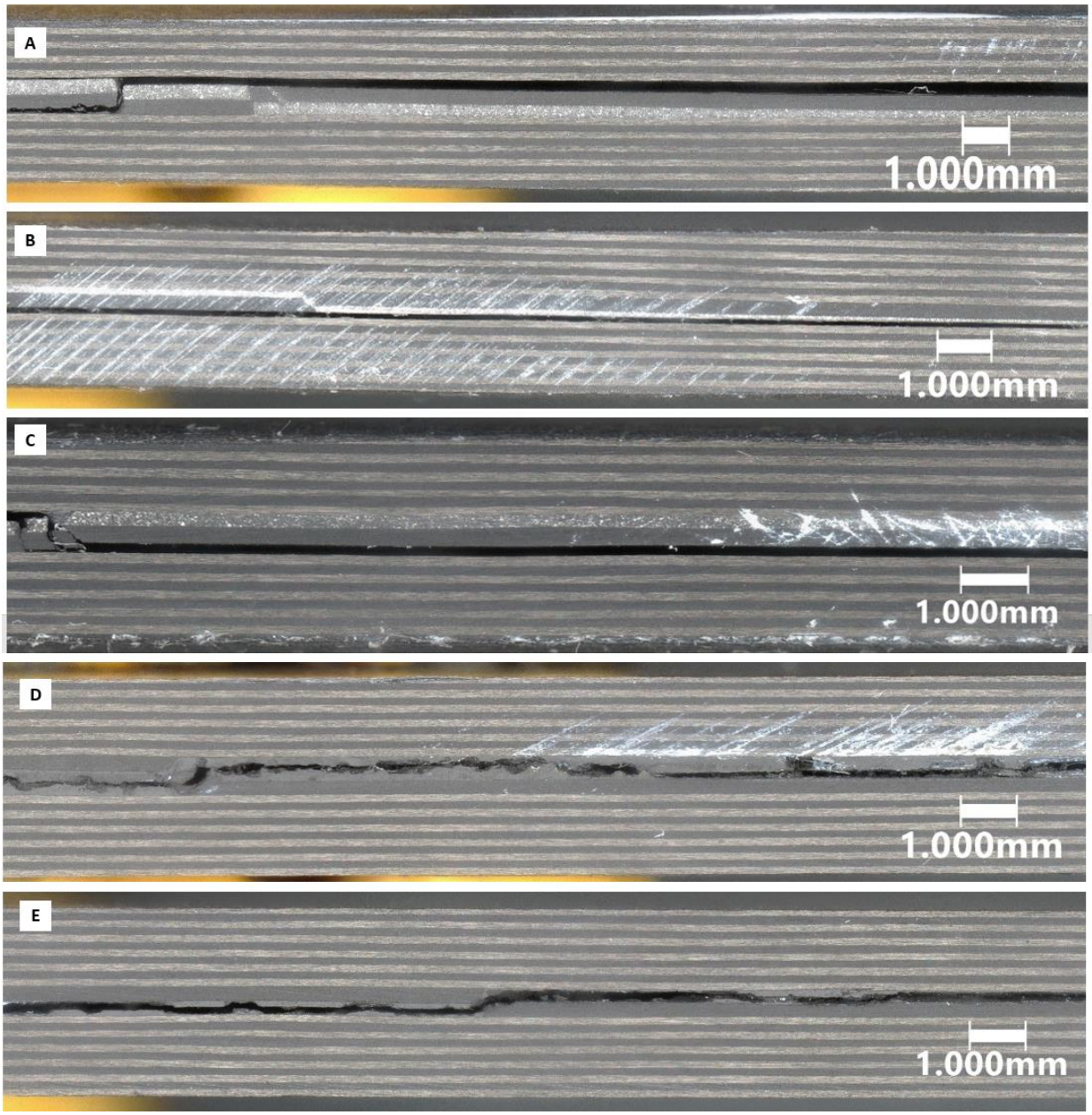

Figure 4.71. Profile view of cross-ply modified ENF repair fractures. A. ENF-QUASI-RPR; B. ENF-QUASI-CL-HF; C. ENF-QUASI-CL-LO; D. ENF-QUASI-CONT-HF; E. ENF-QUASI-CONT-LO

Table 4.9. Average fracture propagation after each ENF test

Sample Set	Avg. Fracture Propagation per ENF Test (mm)
ENF-UNI-BL	23.4
ENF-QUASI-BL	19.3
ENF-CROSS-BL	19.8
ENF-UNI-RPR	21.2
ENF-QUASI-RPR	22.0
ENF-CROSS-RPR	23.4
ENF-UNI-CL-LO	22.4
ENF-QUASI-CL-LO	19.3
ENF-CROSS-CL-LO	18.2
ENF-UNI-CL-HF	21.8
ENF-QUASI-CL-HF	22.2
ENF-CROSS-CL-HF	22.4

The average fracture propagation for the unidirectional sample set display that the crack propagation even with the injection repair are consistent with the baseline material. The quasi-isotropic laminates exhibit a slightly longer average crack propagation for the ENF-QUASI-RPR and ENF-QUASI-CL-HF sample sets when compared to the baseline set, however these values are only a 16% and 15% increase which is within the 3.1 mm standard deviation of the baseline sample set. Two of the cross-ply sample sets, ENF-CROSS-RPR and ENF-CROSS-CL-HF were also higher on average than the baseline sample set, however these values were also within the 3.9 mm standard deviation for the baseline sample set. Therefore the repaired configurations for all of the uncontaminated or cleaned and contaminated sample sets were consistent with their respective laminate configuration baseline sample sets. The average fracture propagation for the contaminated coupon sets is not shown because crack propagation was inconsistent due to lack of bonding and in some cases lack of bonding area, therefore consistent or accurate measurements could not be completed.

Microscopic Planar Fracture Analysis Results

Modified ENF coupons were inspected using the digital microscope to determine the failure modes of a representative coupon from each sample set. The macroscopic planar surface photographs of each test set are shown in Appendix C. Both sides of each fracture surface are presented in this section to ensure that the failure modes are accurately captured. For each representative coupon, in the upper left corner of each figure is the macro photograph of the fracture surface and selected sections that are color coded were analyzed under high magnification (300-2500x) to identify fractography and correlate to the failure modes. Fractography was completed utilizing methods, processes and reference fractographs from ASM Handbook Volume 12 [86]. First, the neat 10 percent acetone diluted EA9396 repair resin modified aluminum ENF sample set (AL-EA9396) fracture surfaces were analyzed to determine how the adhesive fails in transverse shear stress under mode II loading (see Figure 4.72).

The macro photographs of the fracture surfaces shown in Figure 4.72 indicated an interfacial failure between the adhesive (green) and the aluminum surface. However the high magnification (2500x) shown in the orange boxes show polymer on both surfaces. In Figure 4.72A, the rough surface can be identified as the grit blasted aluminum and the out of focus lighter areas are identified as fractured epoxy. On the opposite side of the coupon, in Figure 4.72B, the macro portion of the figure shows that the coupon appears to have green adhesive on the surface. The high magnification area of the fractured epoxy injection resin is shown with a lighter color for higher surface fractures and darker colored areas are lower fracture areas. These surfaces represent a cohesive failure mode with hackles and river patterns present in the repair epoxy adhesive supporting the conclusion of brittle fracture of the adhesive.

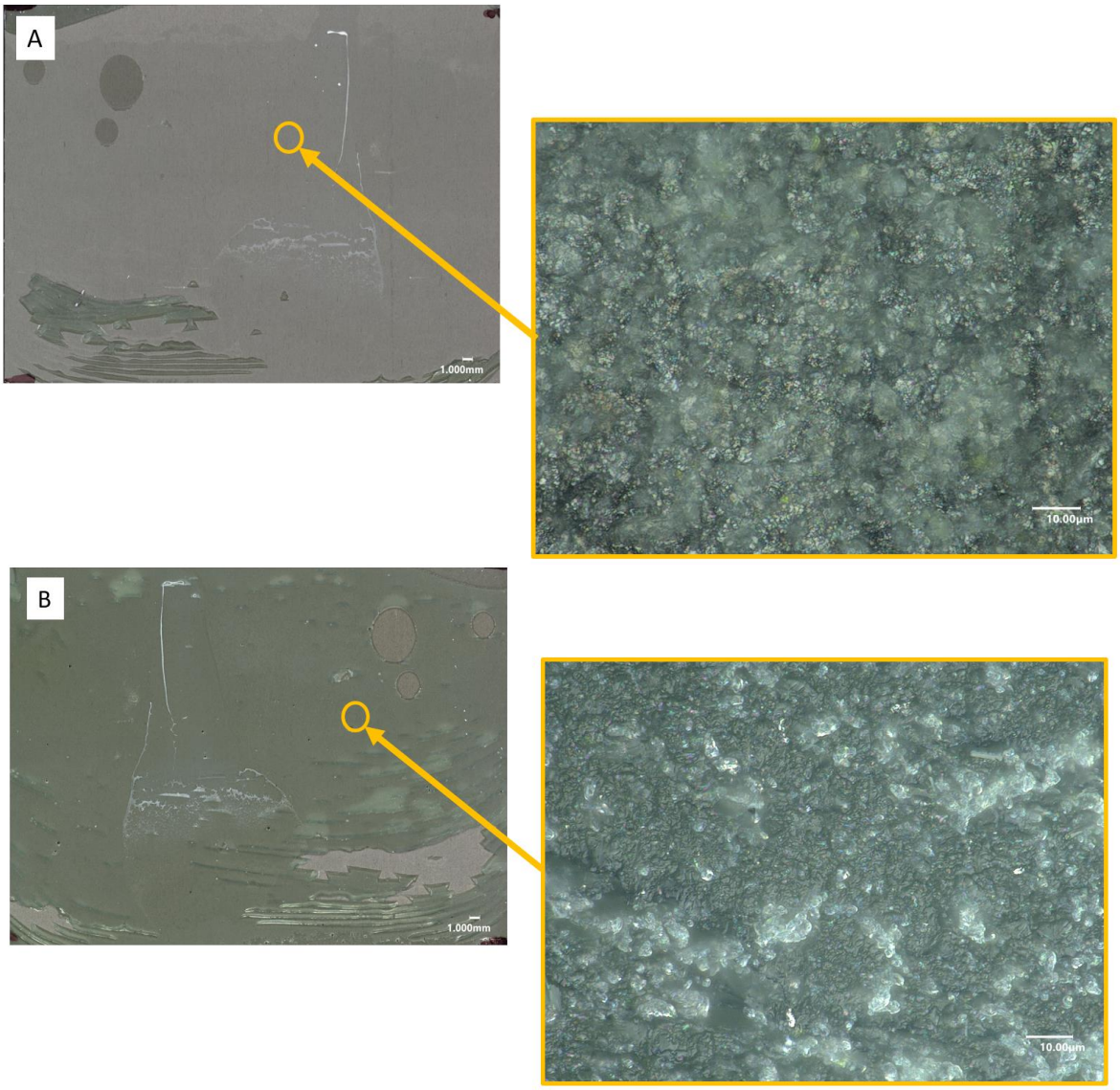

Figure 4.72. AL-EA9396 modified aluminum ENF coupon fracture surfaces. A. Top surface B. Bottom surface

Unidirectional Modified ENF Planar Fracture Analysis Results

Previously in section 4.2.4, the baseline laminate sample sets were analyzed to determine the native fracture surface of the parent composite material, however high magnification of the surface is shown in Figure 4.73.

The baseline unidirectional high magnification (2500x) fracture surface shown in Figure 4.73 exhibits brittle fracture between the carbon fibers. Yellow and orange boxed high magnification photograph were taken from separate areas of the same coupon. The darker area toward the top of the coupon was the first loading during ENF testing and the lighter area is the fracture propagation region once the coupon was flipped and loaded for a second time. The high magnification reveals that both areas exhibit interlaminar shear fracture within the laminate matrix areas. This is revealed by the hackles in between the fibers and the semi-transparent matrix material on the surface. The hackles are observed on both coupon surfaces which is not only indicative of the matrix shearing, but also the fiber shearing from the matrix due to the interlaminar shear experienced from mode II loading.

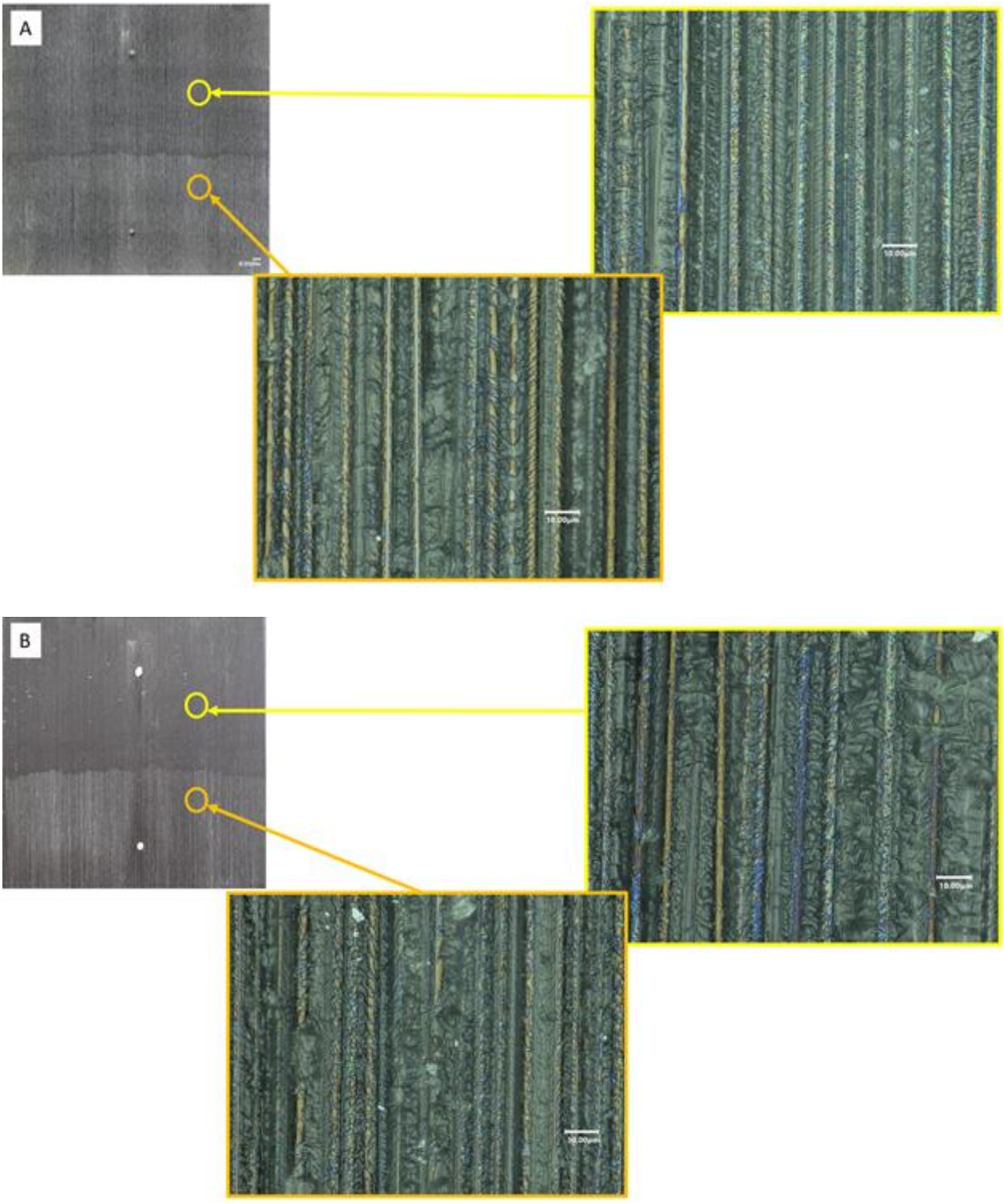

Figure 4.73. ENF-UNI-BL modified ENF coupon fracture surfaces. A. Bottom surface B. Top surface

The ENF-UNI-RPR sample fracture surfaces are shown in Figure 4.74. The macro photograph appears to have a primarily cohesive fracture surface. The orange boxed region in Figure 4.74A, exhibits river marks in the fracture of the green repair resin and hackles in between the fibers. In Figure 4.74B, the opposite side of the fracture exhibits similar fracture in the repair resin and mark-off of where the fibers fractured from the matrix epoxy. Although it is difficult to differentiate between the repair resin and the laminate matrix epoxy, these areas can be considered mixed cohesive fracture within the two polymers. Similar fracture is seen in the yellow boxed region where river patterns are present in the large regions of repair resin. The green boxed regions appear smooth and the shape is consistent for each side, indicating a void in the repair resin. In Figure 4.75, the white area around the edge of the "finger-like" region appears to be a cohesive fracture with lift off from the laminate. This type of fracture region is displayed around the specimen. This samples set had a higher G_{IIC} than the ENF-UNI-BL sample set and the cohesive fracture within the repair resin appears to be a primary contribution.

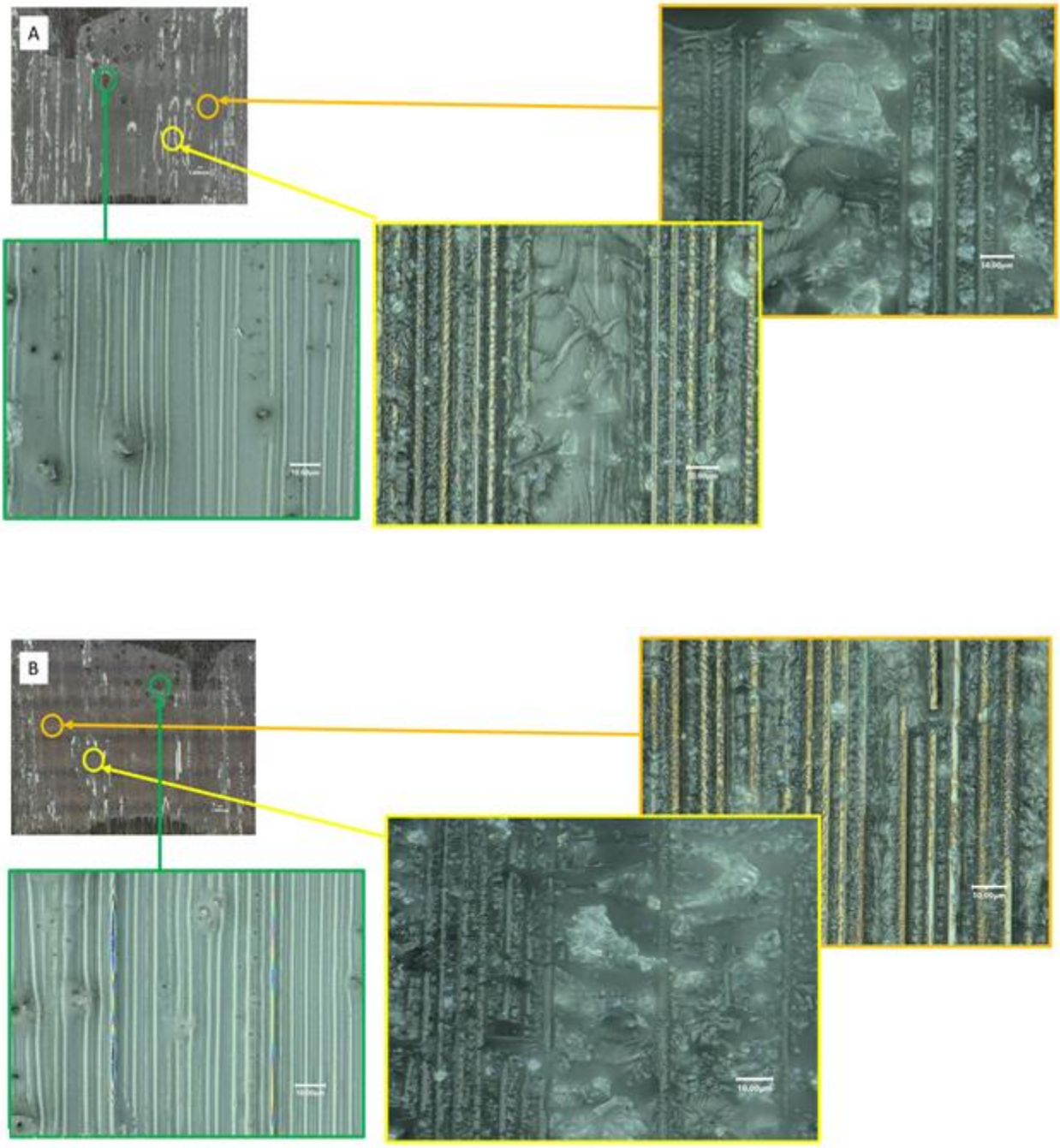

Figure 4.74. ENF-UNI-RPR modified ENF coupon fracture surfaces. A. Bottom surface B. Top surface

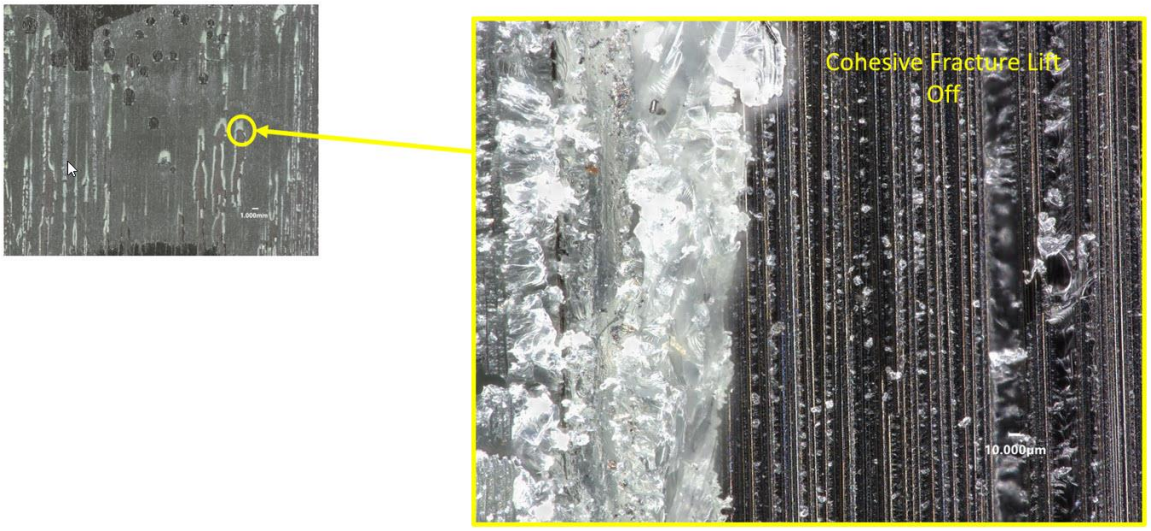

Figure 4.75. Cohesive fracture lift-off

The hydraulic fluid contaminated, cleaned and repaired representative specimen from the ENF-UNI-CL-HF sample set fracture surface is shown in Figure 4.76. The macro surface appears to also be a cohesive fracture within the repair resin or composite epoxy matrix. The green boxed region exhibits a brittle cohesive fracture on the bottom surface, but some porosity on the top surface. The yellow boxed region is similar to the brittle fracture of both the repair resin and epoxy matrix seen in the uncontaminated repair coupon (see Figure 4.73). The orange boxed area near the injection site appears to have micro-porosity and also exhibits fracture hackles in between the fibers. The similar increase in G_{IIC} when compared to the baseline laminate sample set, could also be attributed to the cohesive fracture within the polymers and potential toughness increase due to the micro-porosity or increased cohesive fracture within the repair resin.

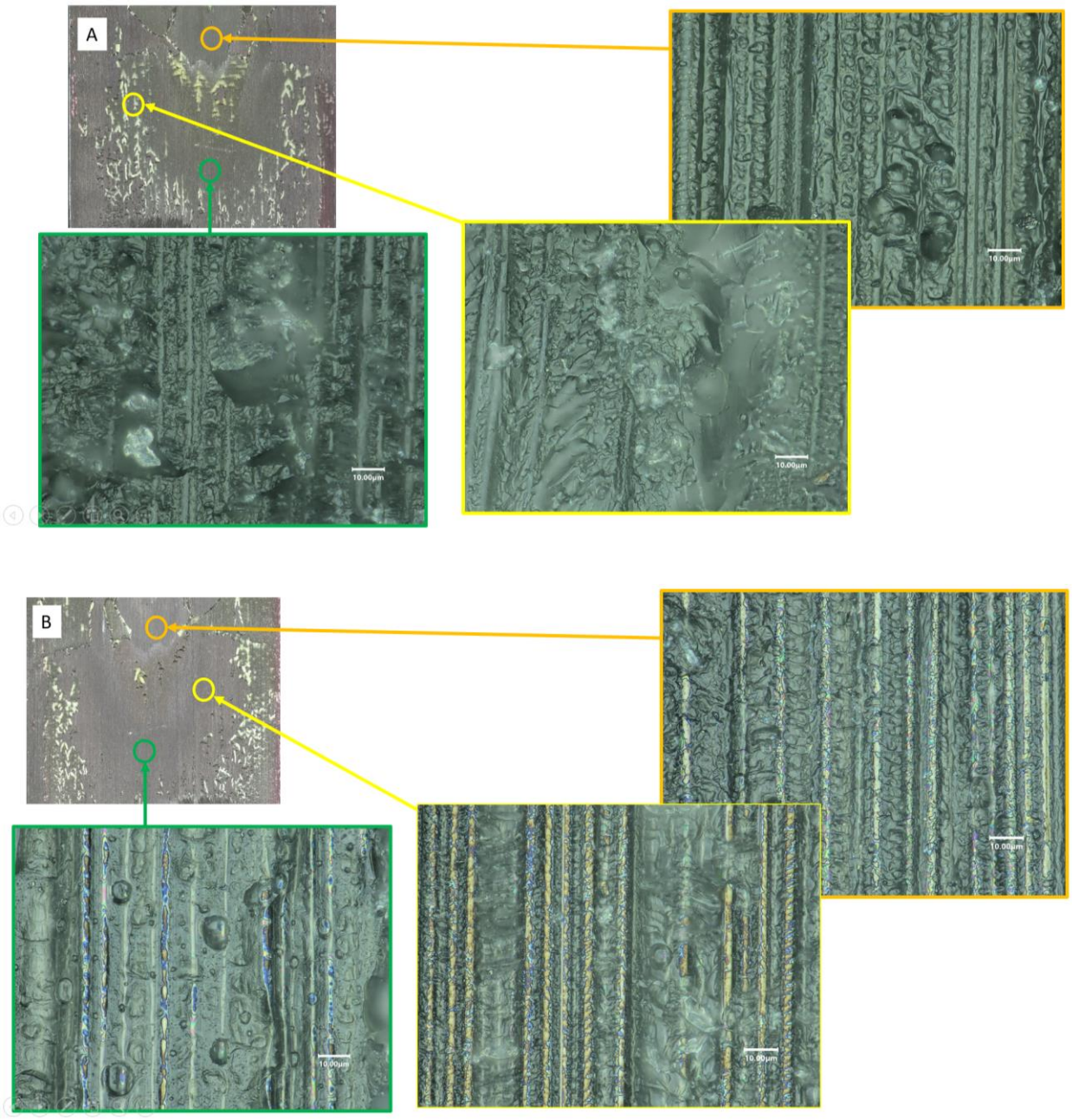

Figure 4.76. ENF-UNI-CL-HF modified ENF coupon fracture surfaces. A. Bottom surface B. Top surface

Shown in Figure 4.77 are the fracture surfaces of a coupon representing the ENF-UNI-CL-LO sample set. The macro view of the coupon also exhibits cohesive failure, with fractured adhesive shown on both sides of the coupon. The green boxed region exhibits an area of

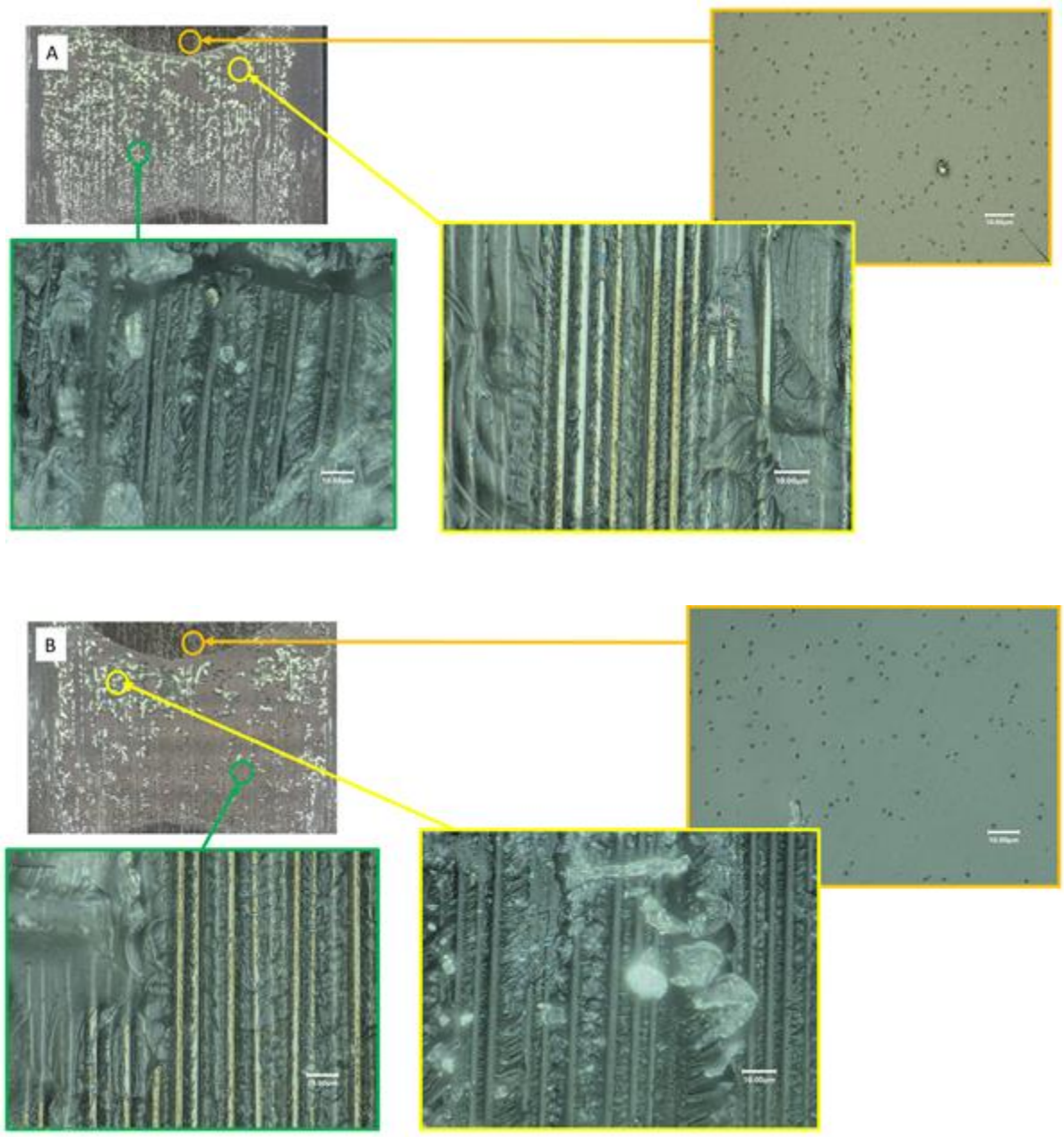

Figure 4.77. ENF-UNI-CL-LO modified ENF coupon fracture surfaces. A. Bottom surface B. Top surface

cohesive shear fracture hackles in both the laminate and the repair resin. There are also river patterns observed in between the fibers. Similar mixed cohesive fracture is found in the yellow boxed region. The orange boxed region has a smooth surface and a mirrored smooth surface is found on the bottom and top coupon surfaces. This sample set also had a significantly higher G_{IIC} when compared to the baseline set and the fracture surfaces are consistent with the ENF-UNI-RPR and ENF-UNI-CL-HF sample sets.

Fracture surfaces for the ENF-UNI-CONT-HF samples set are shown in Figure 4.78. This sample set was left contaminated with hydraulic fluid and macro visual indication is a mixed cohesive and interfacial failure in between the repaired delamination surface. The green boxed regions in Figure 4.78 show beach marks indicative of a brittle fractured cohesive failure surface and fiber imprint in the resin matrix. However, there are also regions of smooth surface that indicate an interfacial failure mode. The orange boxed region exhibits a fractured surface similar to the baseline coupons on the bottom surface and a smooth injection repair resin on the top surface infiltrating the fiber mark-off from the previously fractured surface. This is indicative of an interfacial failure between the two orange boxed region surfaces. The yellow boxed regions on the bottom and top surfaces are both smooth, indicating a micro-void in the fracture surface. Therefore a micrograph was taken at 100x and a large density of what appeared to be porosity was present. In order to verify that the anomaly was porosity, a 3-D scan was completed at 2500x. Shown in Figure 4.79 is the 3-D scan data verifying that the porosity was a micro-pocket void within the repair resin. This was primarily found in the contaminated coupons.

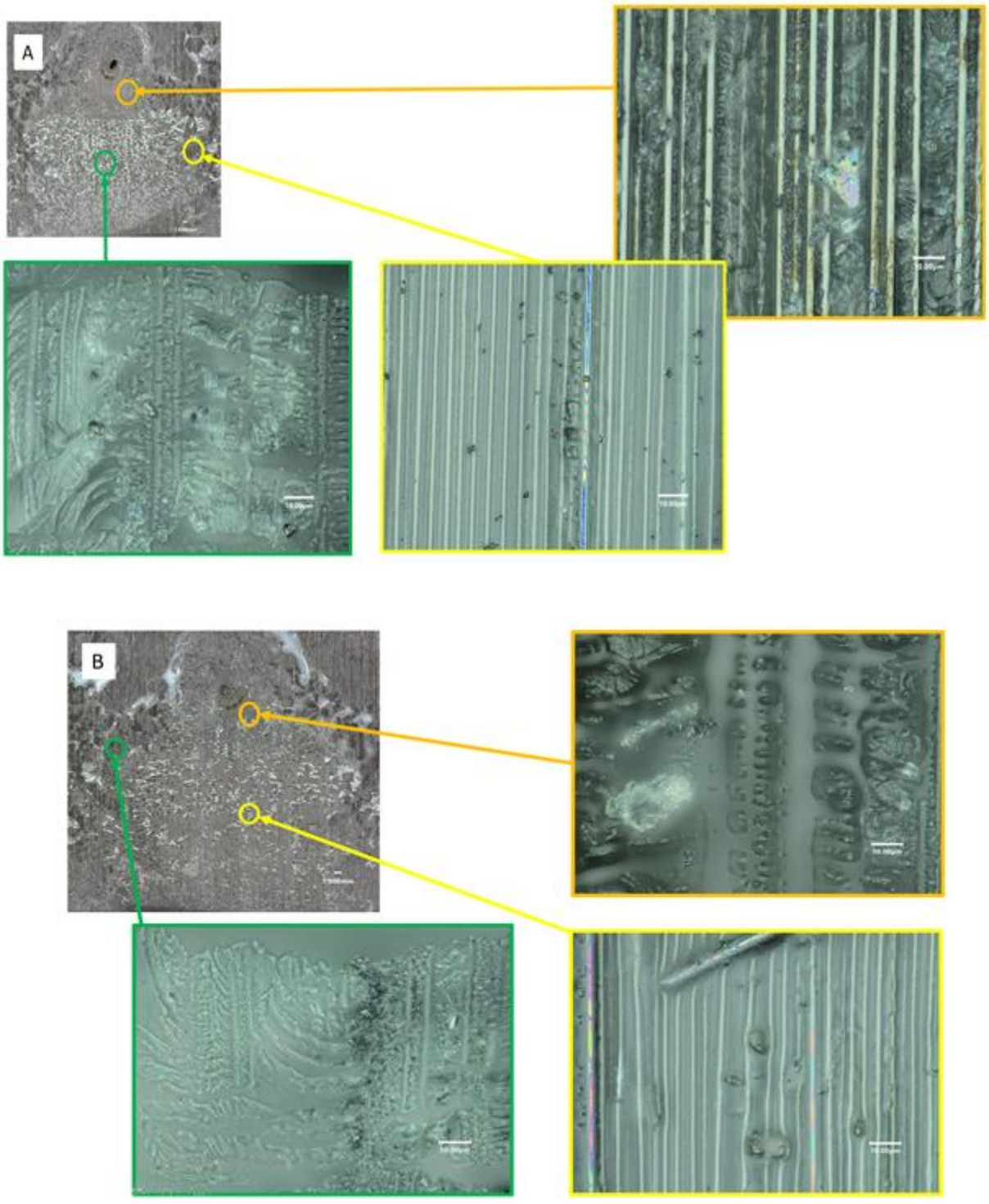

Figure 4.78. ENF-UNI-CONT-HF modified ENF coupon fracture surfaces. A. Bottom surface B. Top surface

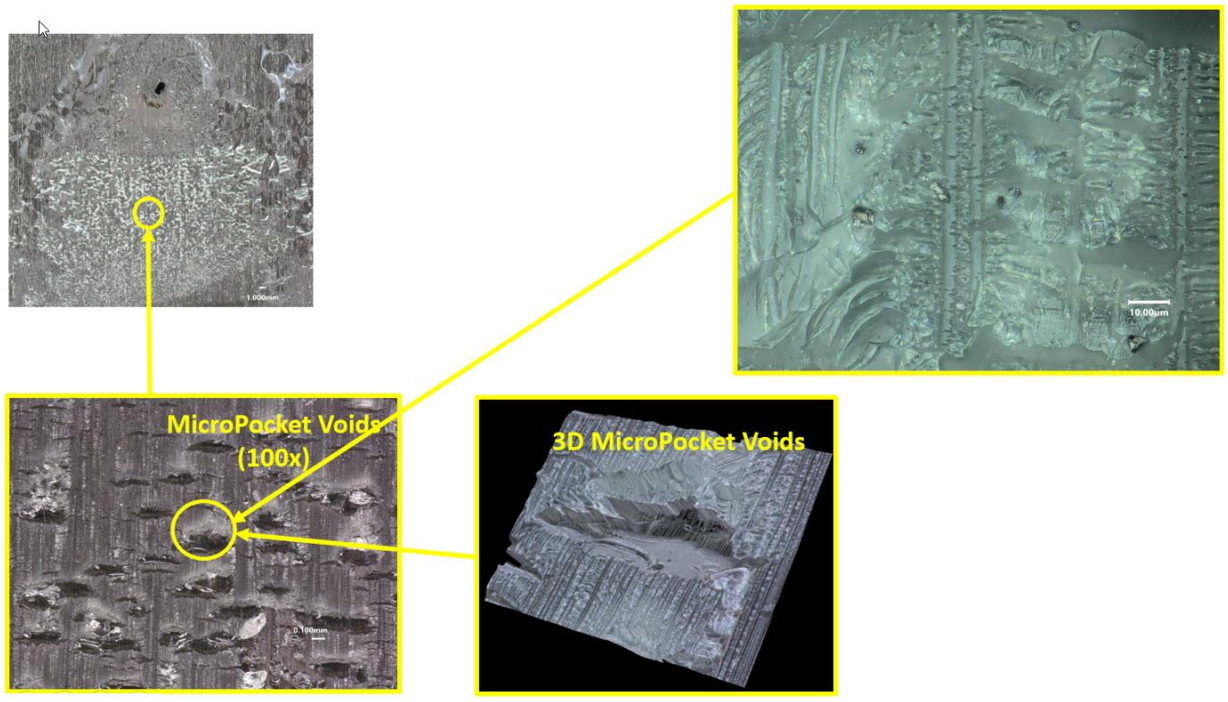

Figure 4.79. Surface micro-pocket voids

The unidirectional lubricating oil contaminated coupon, ENF-UNI-CONT-LO, fracture surfaces are shown in Figure 4.80. The macro photos of the fracture surfaces exhibit an interfacial failure at the top of the photo and cohesive failure closer to the bottom of the coupon. The green boxed high magnification region on the bottom surface exhibits a mixed-mode, cohesive fracture within the repair resin and smooth areas exhibiting surface voids. The lower region may be the area that was able to carry load during testing and as to why the values of G_{IIC} are not equal to 0. The yellow boxed region displays a fracture much like the baseline coupon where fiber impressions are left behind and smooth areas that are attributed to interfacial failure. The orange boxed region at the top of the coupon appears smooth on the bottom surface and the top surface has texture, but no indication of fracture. The orange boxed region represents the majority of the coupon, which is interfacial failure.

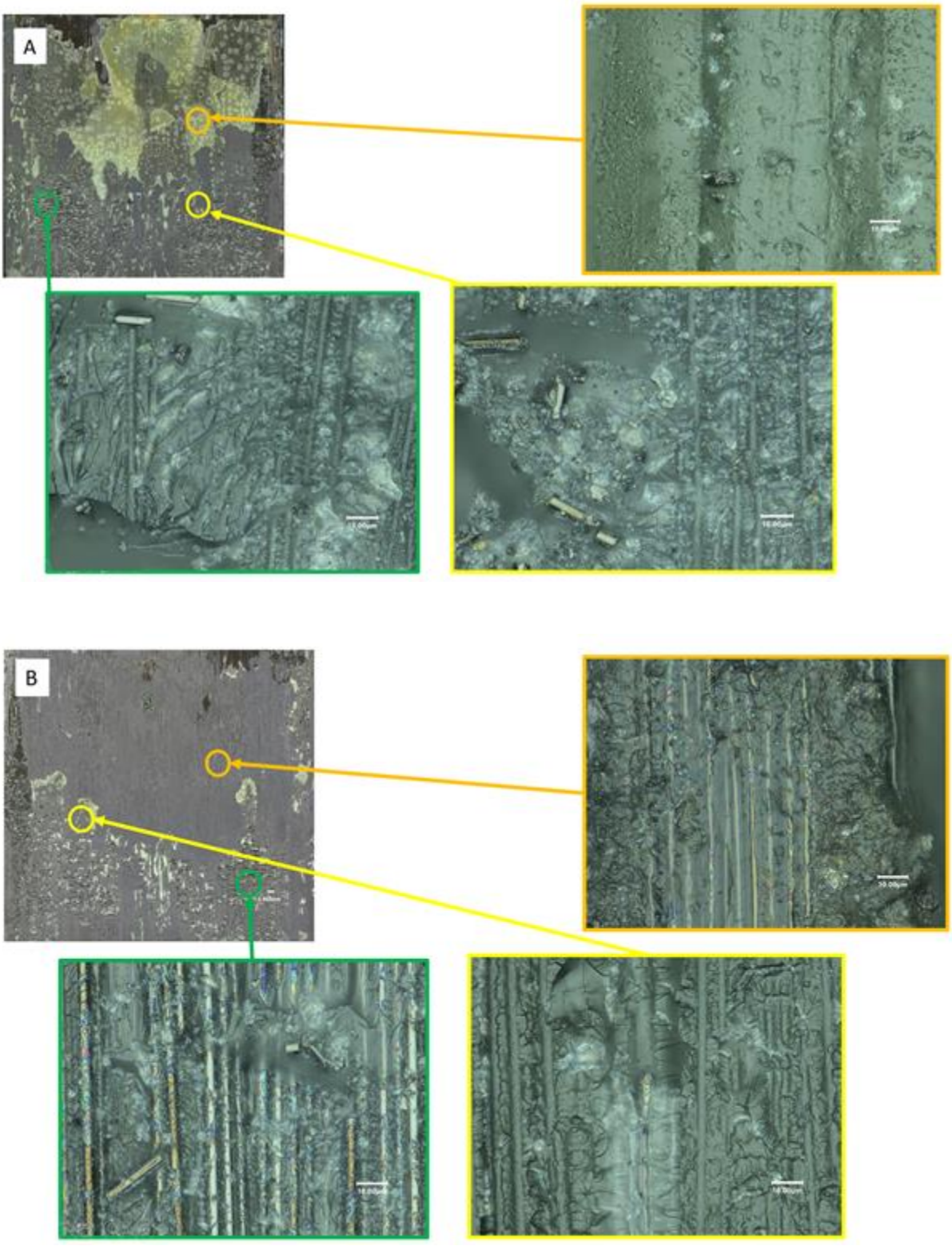

Figure 4.80. ENF-UNI-CONT-LO modified ENF coupon fracture surfaces. A. Bottom surface B. Top surface

In addition to the macro and high magnification micro digital photos taken of the unidirectional planar fracture surfaces, SEM photos were taken of the surface to verify the findings from the digital photomicrographs. For the baseline ENF-UNI-BL sample set, corresponding SEM images can be seen in Figure 4.81.

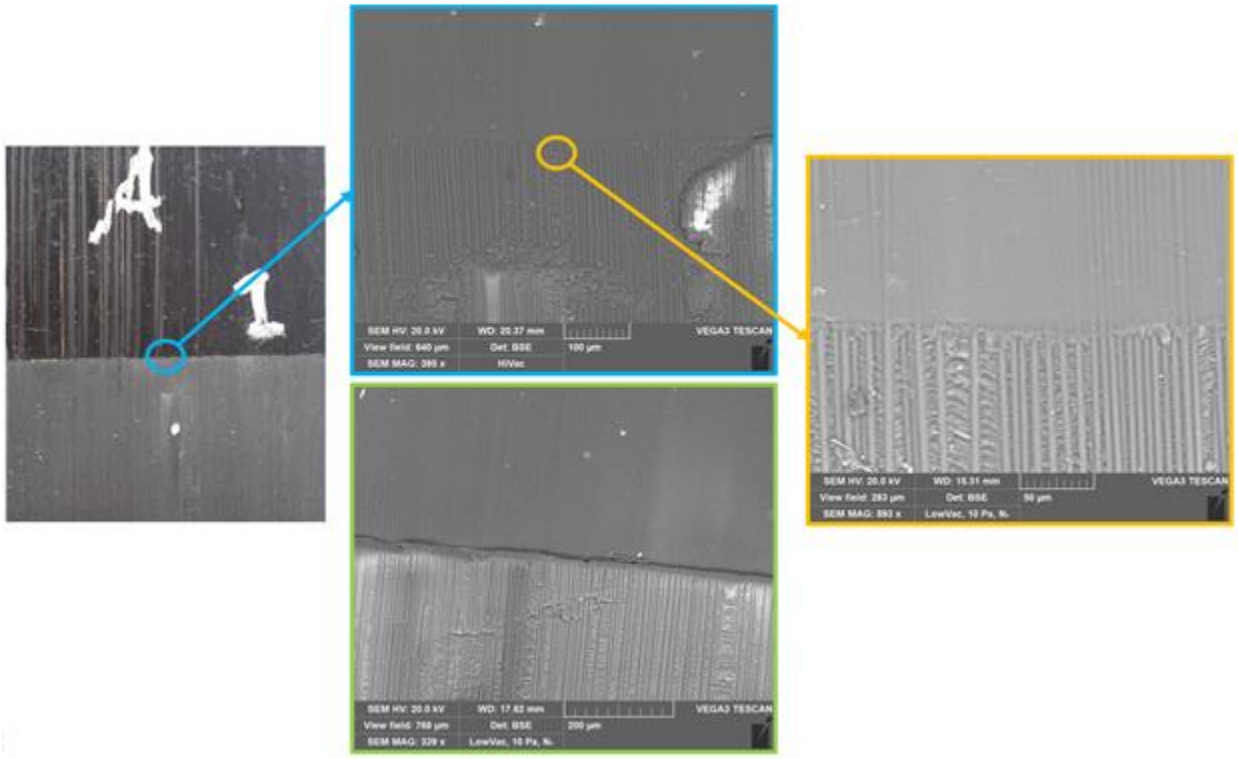

Figure 4.81. SEM Images of ENF-UNI-BL fracture surfaces. Green boxed region is taken from opposite coupon surface from blue boxed region

On the left side of Figure 4.81 is the macro photo of the baseline unidirectional fracture surface. The blue circled area corresponds to the blue boxed high magnification region shown at 395x zoom. This image displays a surface with carbon fibers exposed and hackles in the matrix between the fibers. This verifies the matrix fracture images taken from the digital microscope as

seen in Figure 4.73. Also pictured in Figure 4.81 is a zoomed green region (329x zoom) that was taken from the opposite surface as the blue boxed region. This green boxed region, shows the imprint from the unidirectional carbon fibers and corresponding hackles in the areas between the fiber locations. The SEM images verify that the baseline sample set primarily failed cohesively within the matrix from interlaminar shear forces. Both the green and blue zoomed in images had a smooth section at the top where the PTFE insert was located as a crack starter. Both sides are consistently smooth and do not show signs of fracture because they were not bonded. The orange boxed region on the right of the image is a high magnification zoomed region (893x) where the PTFE crack starter was located and where the interlaminar fracture occurred within the modified ENF coupon. This image clearly shows presence of hackles in between the fibers verifying the brittle fracture that occurs within the PMC laminate matrix.

In Figure 4.82, SEM images were collected on the surface of the ENF-UNI-RPR sample fracture surface. On the left had side of the image, a blue circle denotes where the SEM images were taken on the ENF-UNI-RPR coupon. This section was selected to image a void and different fracture surfaces observed to verify findings from the digital microscope. The blue boxed region (310x zoom) exhibits a smooth area on the left that is classified as a void, where no fracture is present but repair resin filled the surface topography from the initial fracture used to fabricate the coupon. In the middle of the blue region is a fractured surface with fracture tongues, hackles, and river patterns representative of a brittle fracture. This area is a combination of both the fractured repair resin and the fractured matrix from the PMC adherend. On the right side of the blue boxed region image is a transition from the mixed cohesive fracture of the bonded polymer to the primary fracture surface being within the matrix in the composite laminate. Two higher magnification regions in orange (799x zoom) and green (748x zoom) boxed regions were taken from the locations

circled in the blue region SEM image. The orange boxed region displays the larger brittle fracture from the repair resin on the left and the right of the image shows the adherend cohesive fracture within the matrix. The green boxed region further verifies the transition from void (smooth surface) to the cohesive fracture area (hackles and exposed fiber).

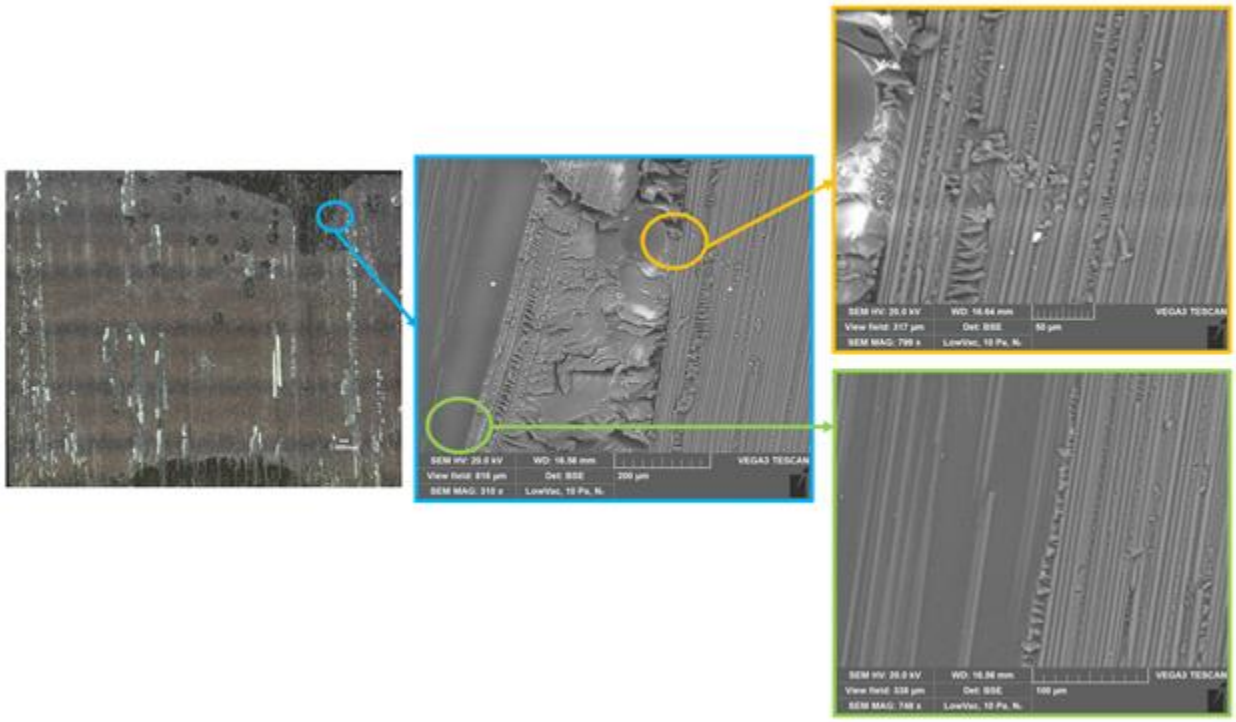

Figure 4.82. SEM images of ENF-UNI-RPR fracture surfaces

In Figure 4.83, the last set of SEM images were taken from a unidirectional lubricating oil contaminated coupon (ENF-UNI-CONT-LO), that previously exhibited areas of voids and interfacial failure modes.

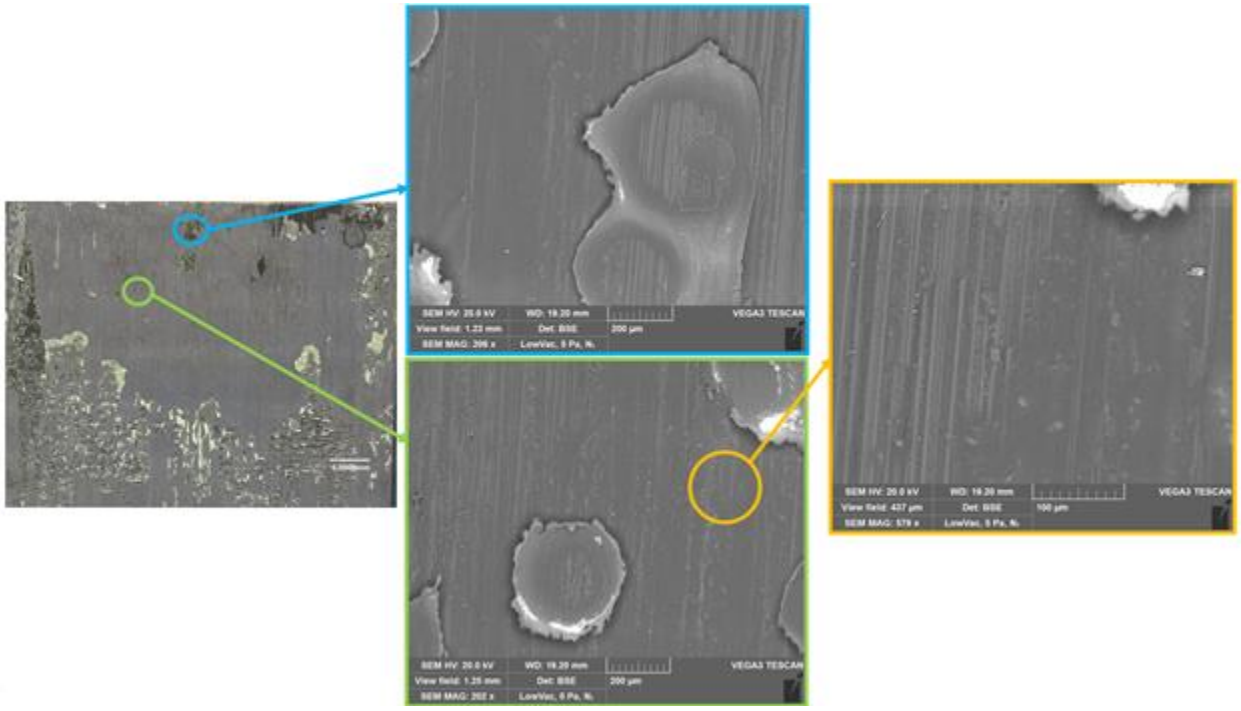

Figure 4.83. SEM Images of ENF-UNI-CONT-LO Fracture Surfaces

The macro image of the ENF-UNI-CONT-LO fracture surface reveals a surface that appears to have an area with little to no fracture at the top and middle. The bottom portion of the coupon appears to have fractured repair adhesive with porosity. The blue circled region is a zoomed (206x zoom) in portion of the coupon that appears to be a void. This blue boxed region is confirmed to have repair resin as evidence of circular micro-voids with brittle fracture around the edges. The rest of the region appears to have an interfacial failure surface with little to no fracture observed. The same type of surface was observed in the green circle region (202x zoom), however a region of the surface deemed to be interfacial failure was inspected in the orange boxed region at higher magnification (579x zoom). This region reveals a surface with little to no evidence of fracture, however there are microcracks within the resin. The microcracks could be the result of thermal

cycling the matrix or repair resin in that region. The SEM results confirm the majority of the contaminated coupon surface failure modes were interfacial or voids.

The correlation of fracture surfaces observed comparing SEM images to the high magnification images from the digital microscope verify that the digital microscope images are valid and that fracture surfaces and failure modes can be identified using this state-of-the-art technology for this study. Therefore digital microscope imaging was utilized for the remainder of the sample sets to verify fracture surface failure modes.

Quasi-Isotropic Modified ENF Planar Fracture Analysis Results

The quasi-isotropic baseline sample set, ENF-QUASI-BL, planar fracture surface macro and high magnification results are shown in Figure 4.84. The high magnification photos of the baseline quasi-isotropic fracture surfaces are similar to the baseline unidirectional surfaces. The green boxed region high magnification shows imprints from the fiber within the matrix on the bottom surface and the corresponding fibers exposed on the top surface. The bottom surface imprint also appears to be in between the 0° and 45° fibers because the 45° oriented fibers can be observed. There are areas of brittle fracture in between the fibers show by hackles. The orange boxed regions exhibit a similar fracture surface to the green boxed region, however there is a color change in the surface as shown by the macro photo. This change in color aligns with where the fracture regions are scribed on the side of the coupon. Therefore the lighter region is where the coupon was fractured for the second loading. The yellow boxed region at the top of the coupon exhibits similar fracture to the green and orange boxed regions, where there is evidence of brittle

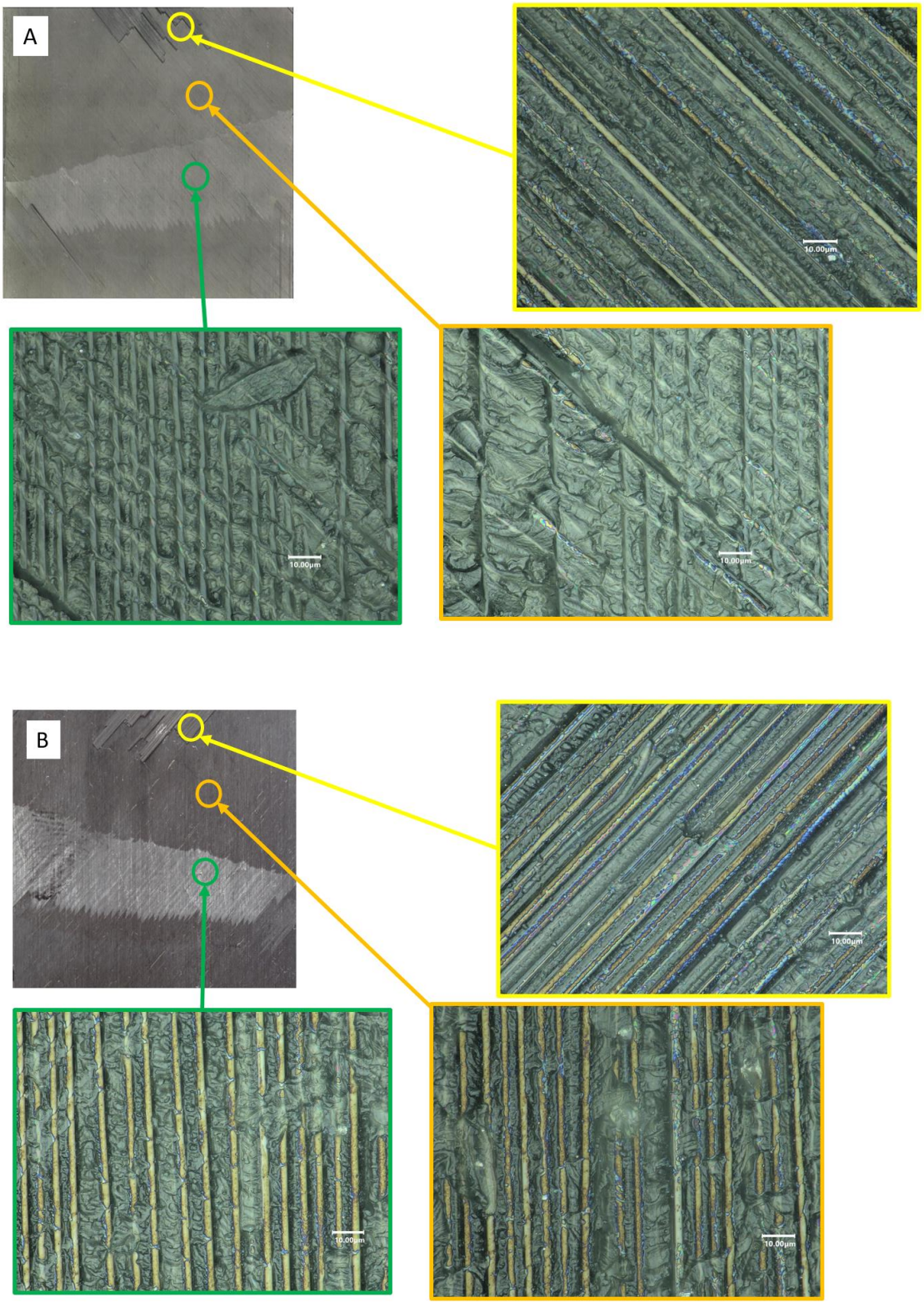

Figure 4.84. ENF-QUASI-BL modified ENF coupon fracture surfaces. A. Bottom surface B. Top surface

matrix fracture between fibers, however the fracture orientation is between two 45° plies. There is also a small area of fiber breakage observed in the middle of the photo micrograph.

The repaired quasi-isotropic coupon fracture surfaces can be seen in Figure 4.85. The macro photograph exhibits a primarily first-ply failure fracture surface. This is indicated by the primary exposed surface being the unidirectional PMC material. The bottom surface, green boxed region (see Figure 4.83A) microscopic photo displays a 0° orientation fiber and fractured repair resin. The top surface (Figure 4.83B) shows a fractured surface with 0° orientation fiber imprints, along with some fractured repair resin. Although fractured repair resin was observed in some areas, the primary fracture is within the 45° ply, indicating primarily adherend first ply fracture. The yellow boxed region exhibits a repair resin cohesive fracture. Both yellow boxed region surfaces exhibit brittle fracture within the repair resin, having hackles on the surface along with beach marks. The orange boxed regions are indicative of the same type of fracture surface seen at the top of the baseline coupon within the 45° plies, which indicates an adherend ply failure mode. The ENF-QUASI-RPR coupons exhibiting primarily adherend fracture supports the modified ENF test results where the sample set has G_{IIC} values within the range of the baseline laminate data (ENF-QUASI-BL). Both sample sets had fractures primarily within the parent laminate material.

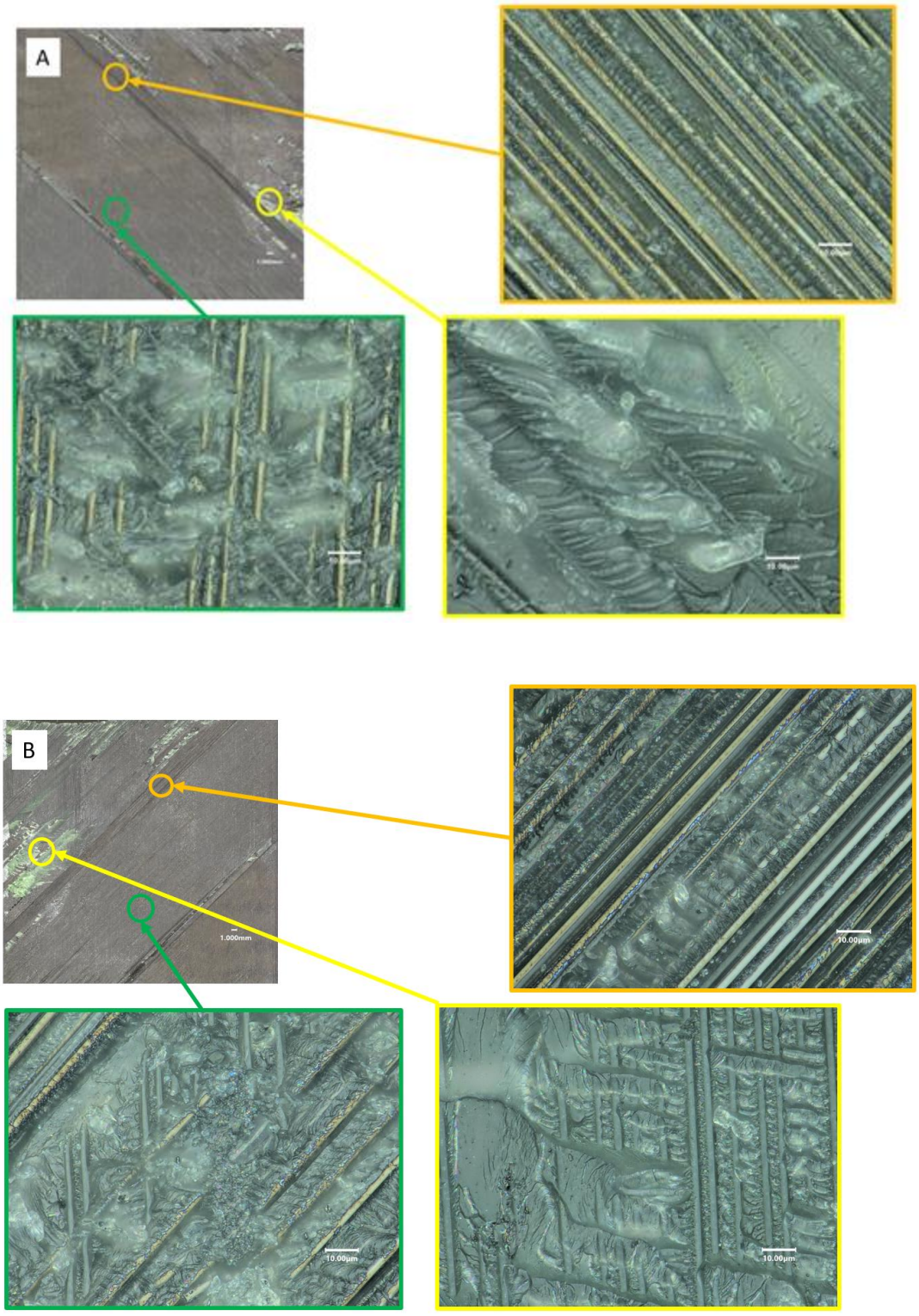

Figure 4.85. ENF-QUASI-RPR modified ENF coupon fracture surfaces. A. Bottom surface B. Top surface

Figure 4.86 shows the fracture surfaces of a representative coupon from the hydraulic fluid contaminated, cleaned, and repaired (ENF-QUASI-CL-HF) sample set. The macroscopic photos exhibit a cohesive fracture surface at the top with some porosity within the repair resin. The middle portion of the coupon appeared to have fracture within the adherend and the bottom portion of the coupon has a mixed cohesive fracture within the repair resin and adherend matrix. The high magnification orange boxed region confirms that the upper region of the coupon has fracture within the repair resin as indicated by imprint of the fibers on the bottom surface (Figure 4.84A) and brittle fracture between seen between he fibers on the top surface (Figure 4.84B). The orange boxed region exhibits micro-porosity in repair resin between the fibers. The yellow boxed high magnification region exhibits similar fracture to the ENF-QUASI-RPR coupon in the same area, where there is indication of fractured repair resin observed in some areas, however the primary fracture is within the 45° ply, indicating primarily adherend first ply fracture. The green boxed high magnification region exhibits a fracture surface with 0° fiber imprints in the repair resin on the bottom surface. The top surface of the green boxed region exhibits an exposed adherend surface that resembles the baseline laminate fracture surface along with small regions of brittle fracture within the repair resin. Much like the quasi-isotropic uncontaminated and repaired coupon configuration, the ENF-QUASI-CL-HF coupon had similar G_{IIC} results that were within range of the ENF-QUASI-BL sample set. This is supported by the primary failure mode of the fracture surface being within the adherend, therefore the interlaminar shear strength of the composite adherend was the limiting factor.

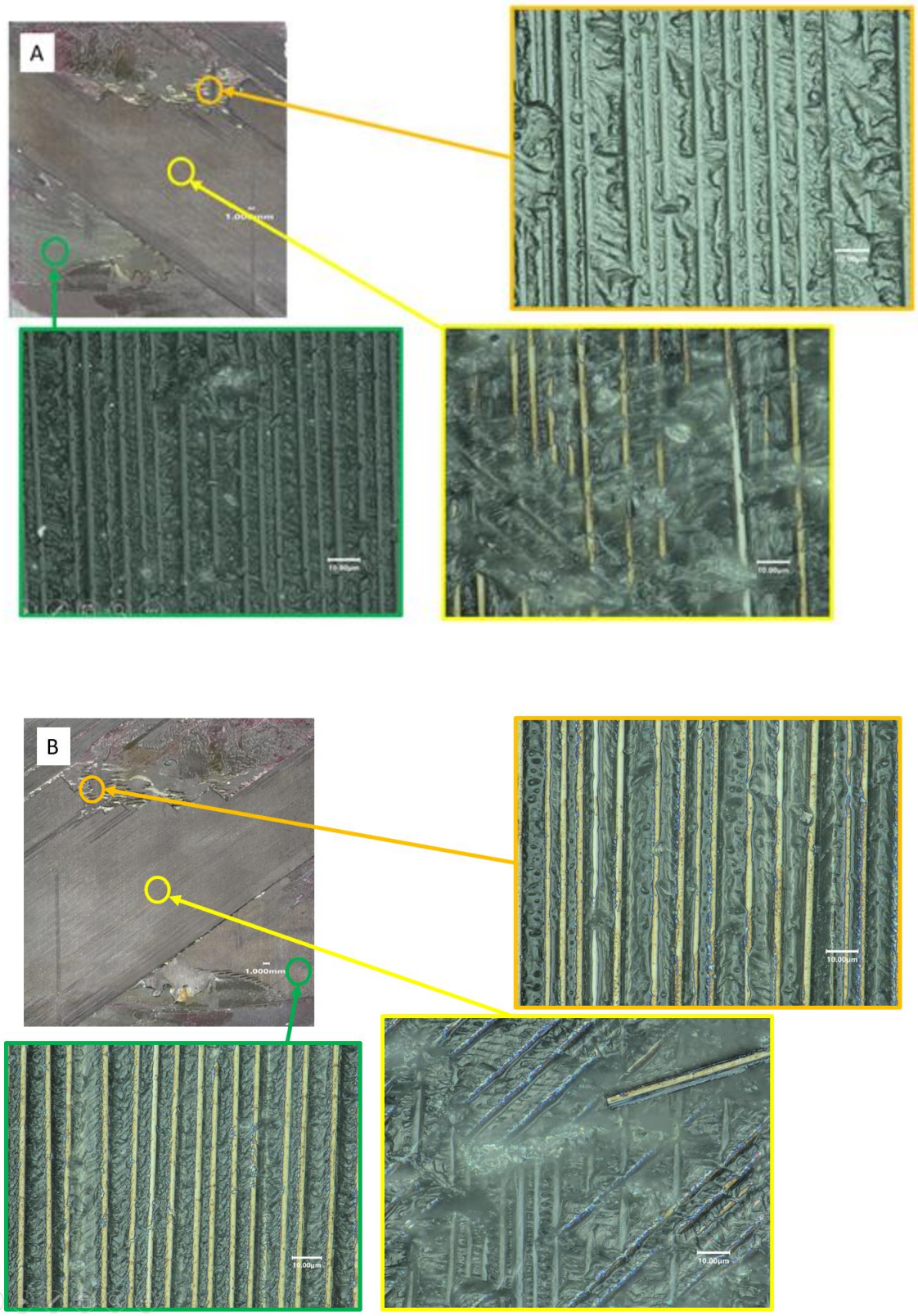

Figure 4.86. ENF-QUASI-CL-HF modified ENF coupon fracture surfaces. A. Bottom surface B. Top surface

Figure 4.87 shows the fracture surfaces from the lubricating oil contaminated, cleaned, and repaired representative coupon from the ENF-QUASI-CL-LO sample set. The macro shot shows a surface that exhibits both an adherend failure and cohesive failure within the repair resin. The high magnification (2500x) green boxed region exhibits a fracture in the 0° ply much like that seen in the ENF-QUASI-RPR coupon where on the bottom surface the repair resin rich surface exhibits brittle fracture with fiber imprints and the top surface has minor areas exhibit brittle fracture of the repair resin and adherend matrix in between fibers. The yellow high magnification boxed region exhibits a mixed cohesive fracture within the 45° ply where the bottom surface exhibits brittle fracture between the fibers as shown by the beach marks within the matrix resin. The yellow high magnification boxed region top surface displays a repair resin coated surface that has pronounced beach marks exhibiting fracture that correspond to the opposite surface. The orange high magnification boxed region in Figure 4.85 shows a surface that has the repair resin over a previously fractured surface, however it does not exhibit fracture within the repair resin itself. The top surface high magnification orange boxed region exhibits brittle fracture between the 0° fibers, however these fracture areas are the primarily within the adherend matrix. The high magnification of ENF-QUASI-CL-LO verifies that this coupon exhibits a mixed mode failure with primary failure within the PMC adherend and the repair resin. The failure within the adherend correlate to the G_{IIC} values for this sample set being within standard deviation of the baseline laminate sample set.

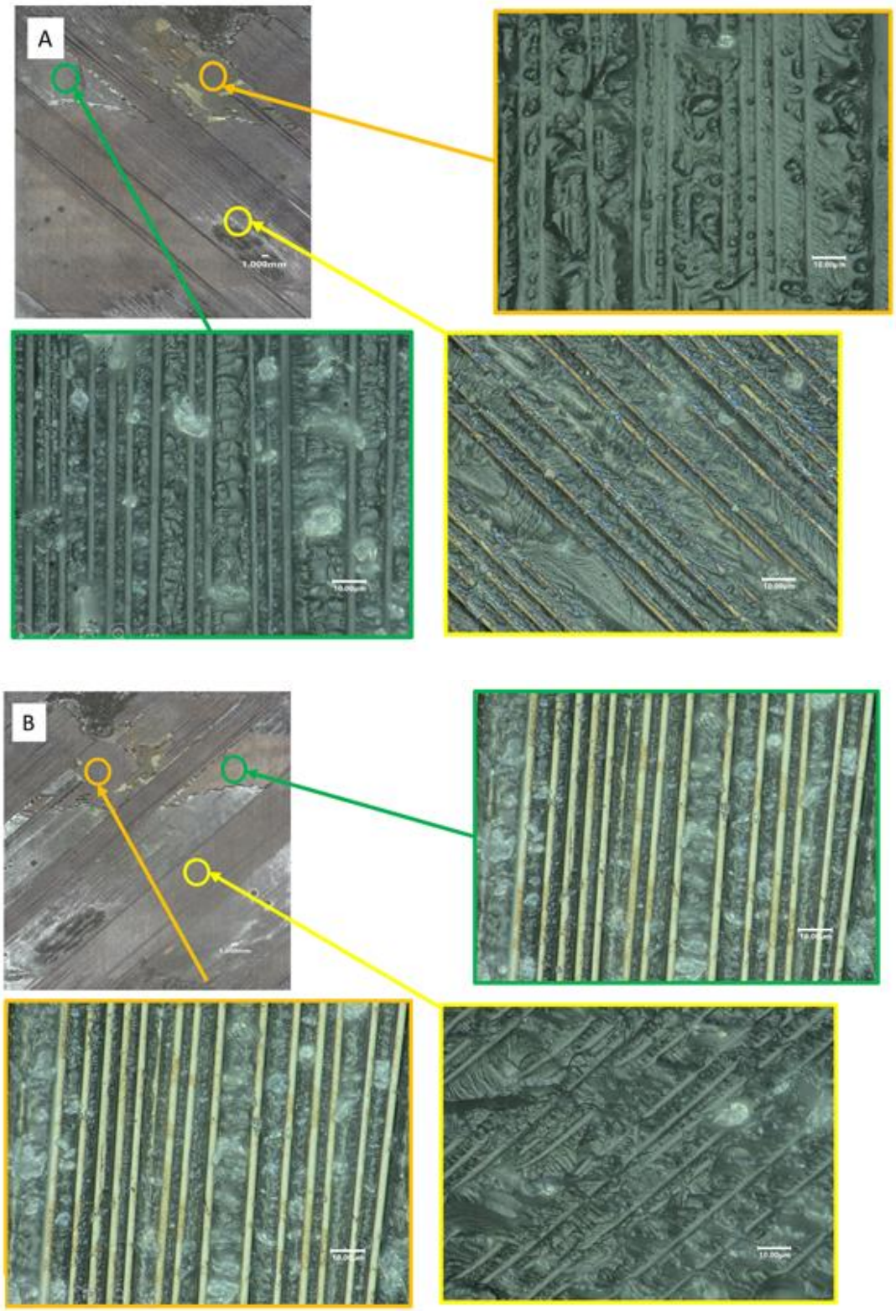

Figure 4.87. ENF-QUASI-CL-LO modified ENF coupon fracture surfaces. A. Bottom surface B. Top surface

Figure 4.88 displays the surfaces of a coupon representing the typical fractures found in the ENF-QUASI-CONT-HF sample set. This sample set was contaminated with hydraulic fluid and repaired without performing any cleaning operations. The macro images exhibit a surface that has interfacial failures between the repair resin and the PMC adherend. Other observations are that the resin appears to have major porosity compared to uncontaminated or cleaned samples sets. The high magnification green boxed regions in Figure 4.86A and B exhibit that both the bottom and top surfaces are coated in the repair resin, however either surface exhibits fracture within the repair resin and both have evidence of micro-porosity. The yellow high magnification boxed region on the bottom coupon surface shows the repair resin without fracture and the top surface to have the previously fractured surface without any evidence of fractured repair resin. The orange high magnification boxed region bottom surface has an exposed 45° ply with similar appearance to the baseline quasi-isotropic sample set. The top coupon surface orange boxed region has a repair resin with fiber imprints without evidence of brittle fracture, thus this region is evidently an interfacial failure between the repair resin and the PMC adherend. The high magnification of the ENF-QUASI-CONT-HF fracture surfaces verify that the majority of the coupon had interfacial failure between the repair resin and the PMC adherend and corresponds to the severely reduced G_{IIC}.

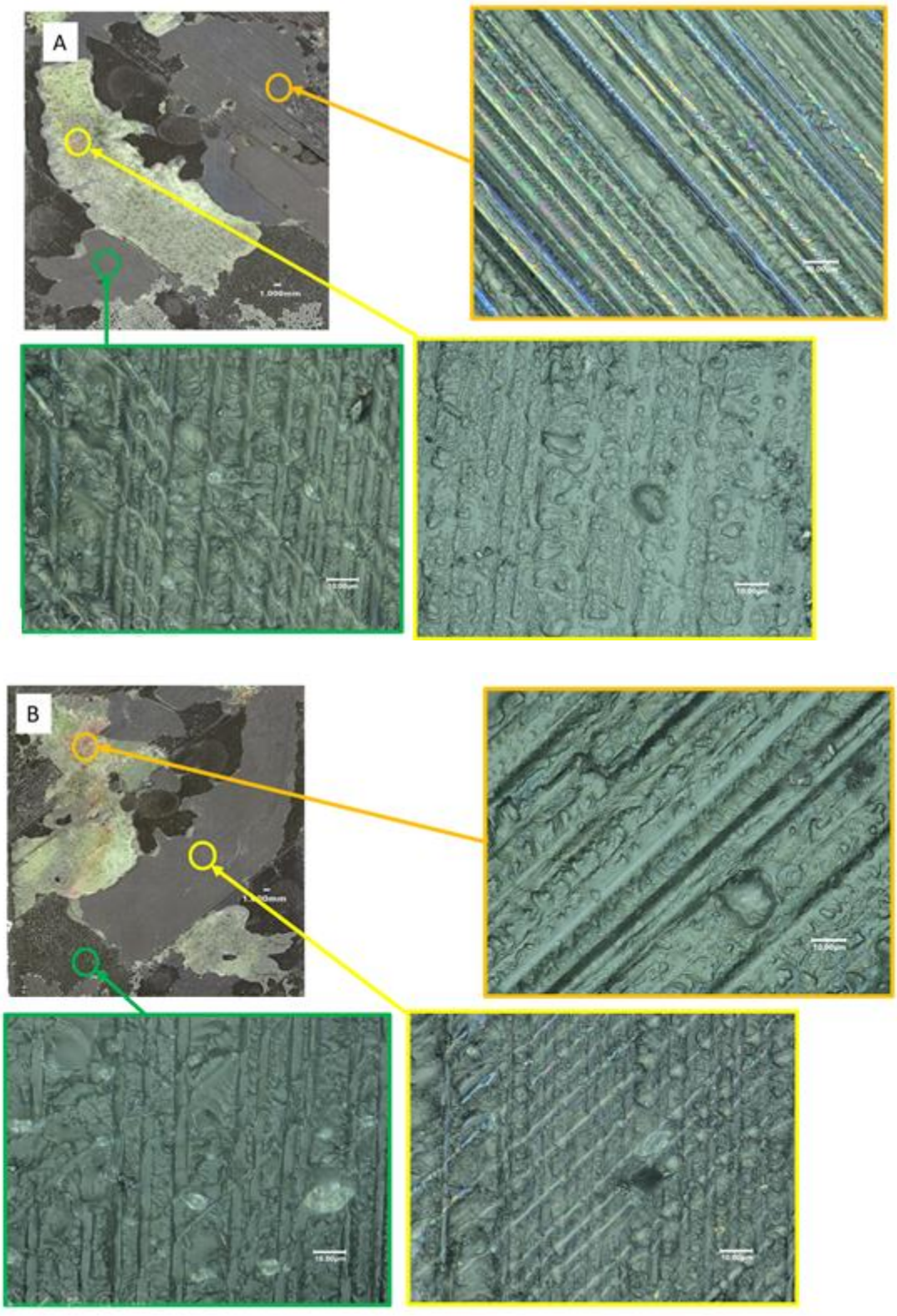

Figure 4.88. ENF-QUASI-CONT-HF modified ENF coupon fracture surfaces. A. Bottom surface B. Top surface

Pictured in Figure 4.89 are the macro and high magnification surfaces of a coupon representative of the ENF-QUASI-CONT-LO sample set. This sample set was contaminated with lubricating oil and repaired without any cleaning process. The macro photographs exhibit a surface that was hydrophobic and had poor wetting of the repair resin. The poor wetting resulted in large voids within the delamination. The green boxed high magnification areas photos were taken in areas that appeared to be voids. These areas both exhibit a smooth and resin coated surface. It appears that the original fracture was between a 0/45° interface and then coated with a thin layer of repair resin and show no evidence of fracture. The yellow boxed high magnification region from the bottom surface exhibits a fractured surface, with hackles residing between the 0° fibers which has a similar surface to the baseline sample set. The top surface yellow region is primarily repair resin with minor areas of hackles on the surface exhibiting approximately 50% percent fracture and 50% smooth un-fractured surface. The orange boxed high magnification region exhibits a cohesive fracture within the repair resin with noticeable beach marks on the top surface and hackles on the bottom surface. Although a small region of the coupon had preferable cohesive failure modes, the majority of the coupon was voids due to the hydrophobic surface or interfacial failure, which correlates with the G_{IIC} values being slightly higher than the hydraulic fluid contamination and approximately 50% the mode II fracture toughness of the baseline sample set.

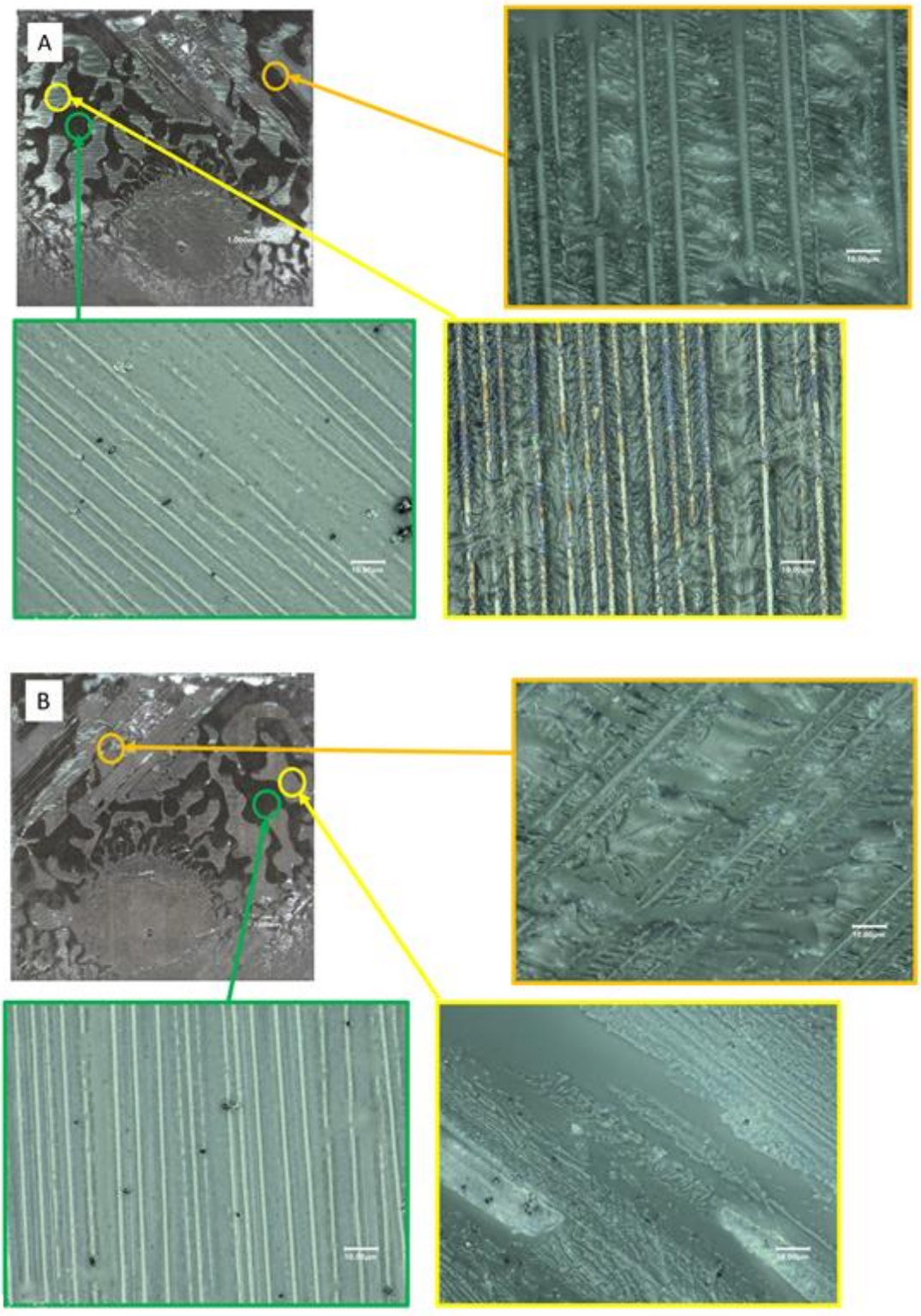

Figure 4.89. ENF-QUASI-CONT-LO modified ENF coupon fracture surfaces. A. Bottom surface B. Top surface

Cross-Ply Modified ENF Planar Fracture Analysis Results

Macro and high magnification microscopic pictures were taken of a representative coupon from the baseline sample set, ENF-CROSS-BL, and are show in Figure 4.90. Macro image visual inspection of the baseline fracture surface reveals the same type of fracture found in section 4.2.4 for the baseline cross-ply modified ENF coupon. The high magnification orange boxed regions on the coupon surface reveal a brittle fracture shown as hackles in between the fibers on the bottom surface. The top surface reveals a more matrix rich surface with fiber impressions and further brittle fracture on the matrix in between the fibers. The yellow boxed high magnification region also shares a similar fracture surface except the bottom surface is matrix rich, while the top had exposed fibers and fracture in between the fibers, this is due to the coupon being loaded, flipped, then tested again. The green boxed high magnification region also has similar fracture surfaces compared to the other laminate configurations; however horizontal cracks are observed. These cracks are unique to the cross-ply modified ENF coupons.

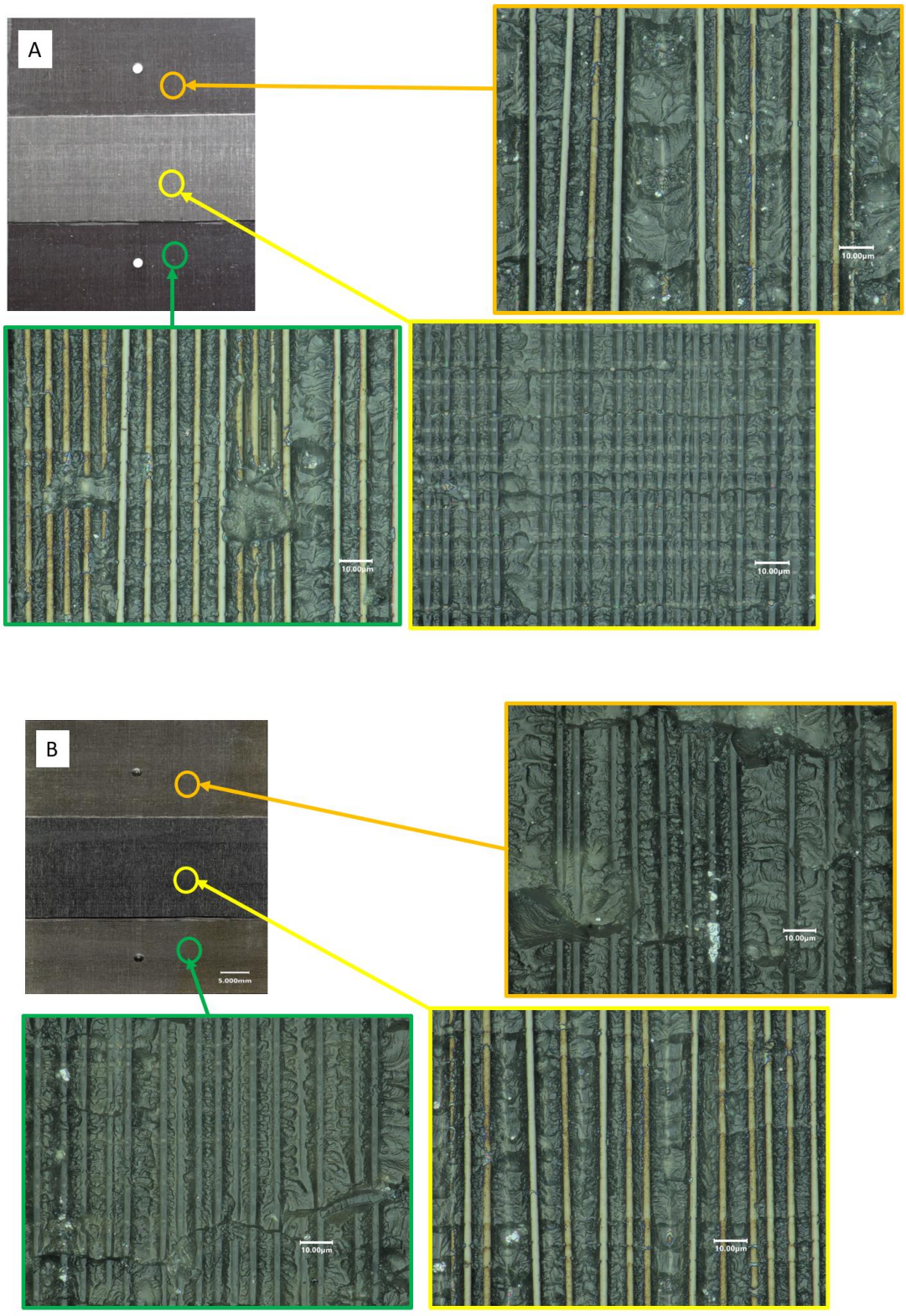

Figure 4.90. ENF-CROSS-BL modified ENF coupon fracture surfaces. A. Top surface B. Bottom surface

Shown in Figure 4.91 are the macro and high magnification fracture surfaces of a sample of the cross-ply repaired sample set, ENF-CROSS-RPR. The macro photos of the fracture surfaces exhibit a primarily adherend failure. There is an area near the middle of the coupon that appears to be exposed 90° fibers, whereas the rest of the coupons appears to be 0° oriented fibers. The high magnification orange boxed region exhibits a fracture surface that is similar to the matrix rich surface found in the baseline sample set. The orange boxed region top surface exhibits a surface with fracture hackles in between the exposed fibers. The yellow boxed high magnification region has 90° fibers and hackles in the matrix material in between the fibers. The green boxed region is similar to the orange boxed region however the matrix rich layer with fiber imprints is found on the top surface and the fibers exposed with hackles in between plies on the bottom surface. One unique feature is the horizontal cracks emanating through the matrix and fibers in all three high magnification regions. The ENF-CROSS-RPR set had a 162% higher average G_{IIC} than the baseline laminate, however the primary failure mode was within the adherend laminate. The adherends exhibited horizontal cracks in all surfaces and the profile shown in Figure 4.71 exhibit a compressive fracture at the stepped regions where the coupon previous fracture and repair moved transversely though the coupon. Previous work has concluded that the introduction of a step or increased profile topography can increase bond mechanical characteristics of a joint due to mechanical interlocking [87-90]. It is likely that the stepped region is providing a mechanical interlocking due to the geometry from the original fracture and this is contributing to the increase in G_{IIC}.

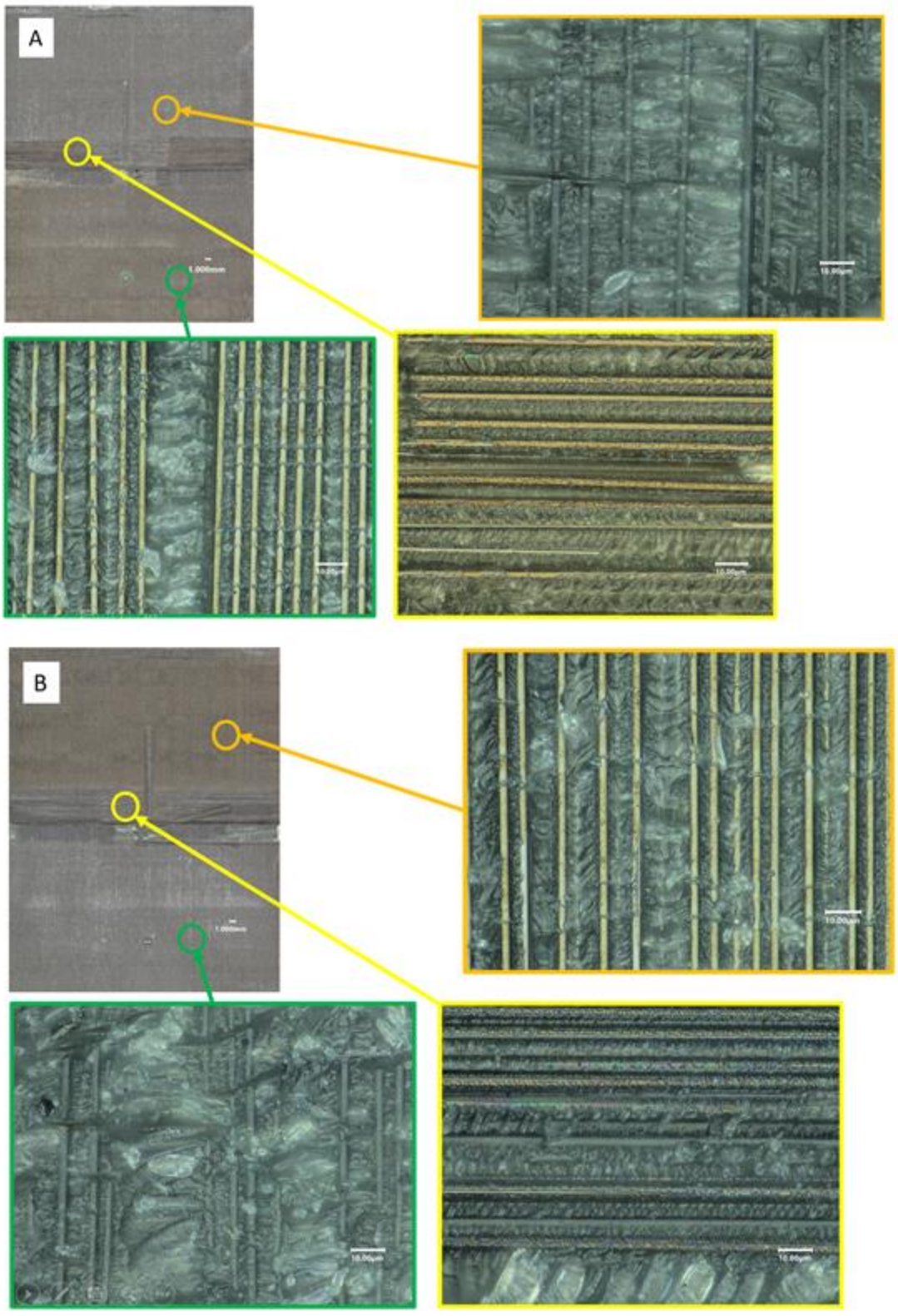

Figure 4.91. ENF-CROSS-RPR modified ENF coupon fracture surfaces. A. Bottom surface B. Top surface

Shown in Figure 4.92 is the planar fracture surfaces from a hydraulic fluid contaminated, cleaned and repaired (ENF-CROSS-CL-HF) coupon after ENF testing was completed. The macro fracture surface is very similar to the ENF-CROSS-RPR fracture surfaces. The primary failure mode appears to be within the adherend with some minor areas of cohesive failure within the repair resin or in the first ply matrix. The high magnification orange boxed region bottom surface has fiber imprints, brittle fracture as shown by hackles, and a horizontal crack through the coupon center. The orange boxed region bottom surface has a fiber exposed surface with hackles in between the fibers. This failure region appears to be wholly within the adherend 0° ply. The yellow boxed region bottom surface is within the 90° ply, at the coupon mid-plane, and also shows areas of brittle fracture between the fibers and on the top surface is a matrix layer with fiber imprints with fracture of the repair resin toward the bottom of the region. The green boxed region exhibits a surface with fiber exposed on the bottom surface with several horizontal cracks and hackles in between the fibers. At the center of the coupon appears a region where the repair resin has brittle fracture. The top surface green boxed region has more repair resin and matrix brittle fracture which can be seen by the beach marks on the surface. In addition to the fracture surface being similar to the ENF-CROSS-RPR coupon, the G_{IIC} values was similarly increased 182% from the baseline sample.

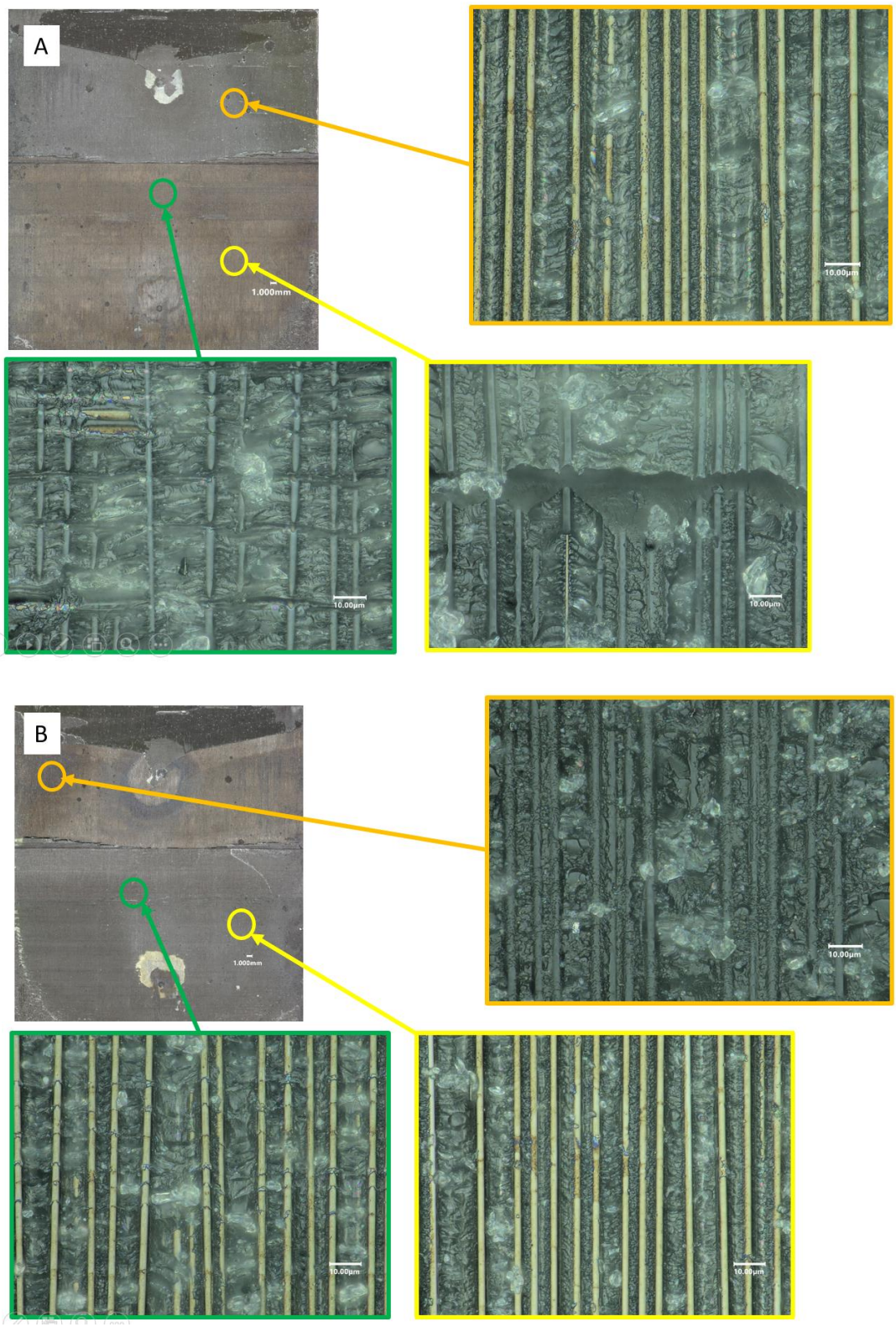

Figure 4.92. ENF-CROSS-CL-HF modified ENF coupon fracture surfaces. A. Bottom surface B. Top surface

In Figure 4.93 are the planar fracture surfaces of a representative coupon for the lubricating oil contaminated, cleaned, and repaired sample set (ENF-CROSS-CL-LO). The macro surface appears to be similar to the other un-contaminated or cleaned and repaired sample sets, except what appears to be a cohesive failure within the repair resin at the injection hole site. The majority of the coupon appears to have adherend failure with some regions of repair resin and adherend matrix cohesive failure. The high magnification orange boxed region exhibits a mixed cohesive failure within both the repair resin and the adherend matrix. This is displayed by the hackles found between the fibers and the imprints of the fibers on the top surface. The yellow boxed high magnification region reveals a cohesive failure primarily within the repair resin. On the bottom surface there is a repair resin layer with fiber imprints and evidence of fractured green resin. The top surface yellow boxed region has large chunks of fractured repair resin. In the green boxed region of the coupon, the bottom surface reveals a matrix rich surface with fractures including a tongue near the top of the micrograph. There is also noticeable horizontal cracking and imprints of fibers. The green boxed region top surface has exposed fibers and fracture hackles can be seen between the 0° orientation fibers, of which look to primarily be matrix material. The ENF-CROSS-CL-LO sample has similar high magnification fracture surfaces to the other cleaned or uncontaminated coupons and the G_{IIC} was similarly higher than the baseline sample set ENF-CROSS-BL, with an increase of 142%.

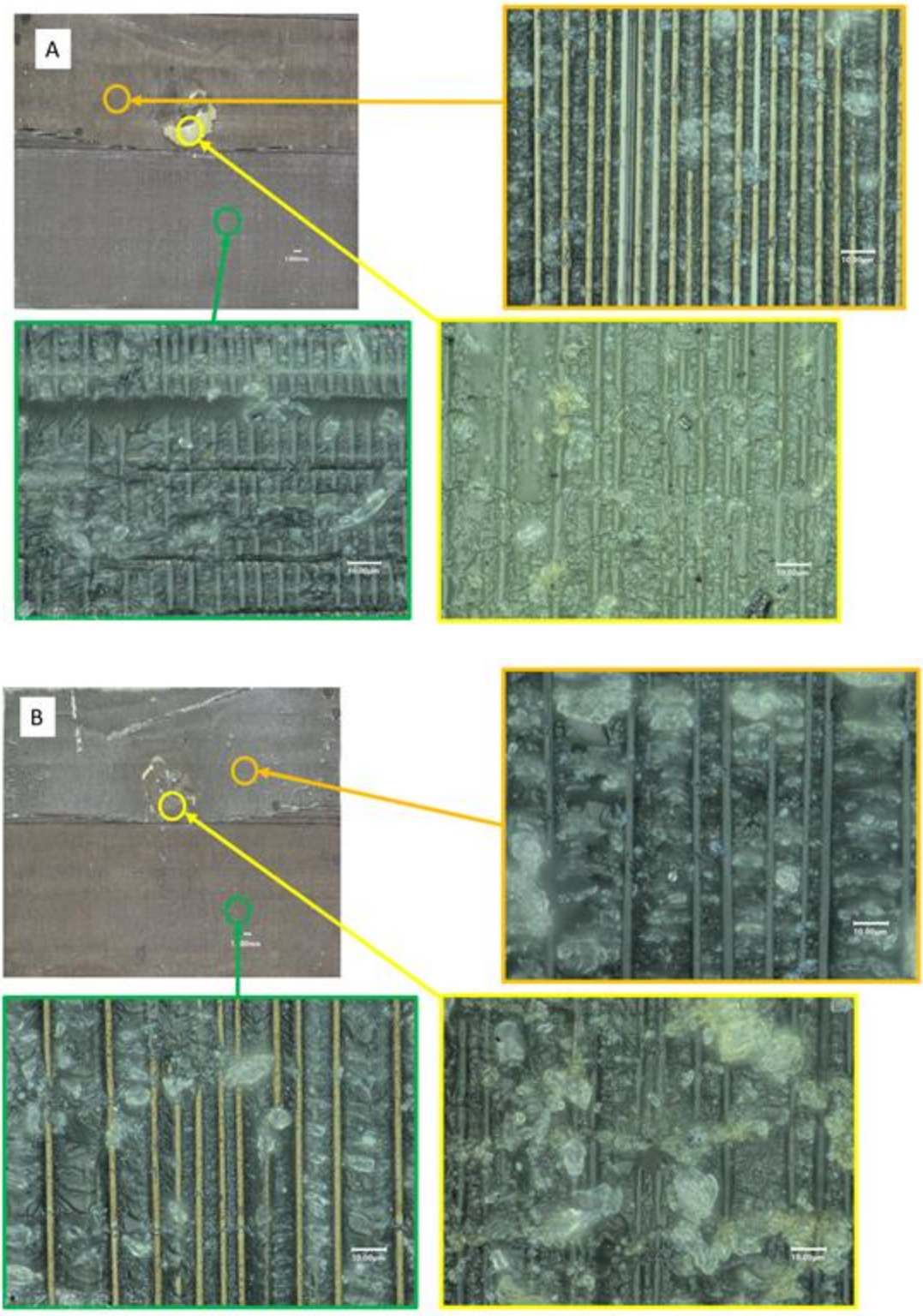

Figure 4.93. ENF-CROSS-CL-LO modified ENF coupon fracture surfaces. A. Bottom surface B. Top surface

In Figure 4.94 are the planar fracture surfaces of a cross-ply hydraulic fluid contaminated sample that was then repaired. The macro images reveal a surface that was largely hydrophobic due to the contaminant with major voids on the surface. However there are regions where repair resin is observed and possible interlaminar shear was carried by the coupon. The high magnification orange boxed region from both the top and the bottom of the coupon exhibit an area that had a coat of repair resin around the injection hole. This area shows minor signs of fracture within the resin where cracks forms however this in not indicative of a normal brittle fracture. The yellow boxed regions were taken in the void areas where a thin layer of repair resin coated the surface of the coupon and no evidence of fracture was present. The green boxed region exhibits a highly porous fracture surface. The lack of brittle fracture found in this coupon is likely why the G_{IIC} was reduced by 67% compared to the baseline sample set.

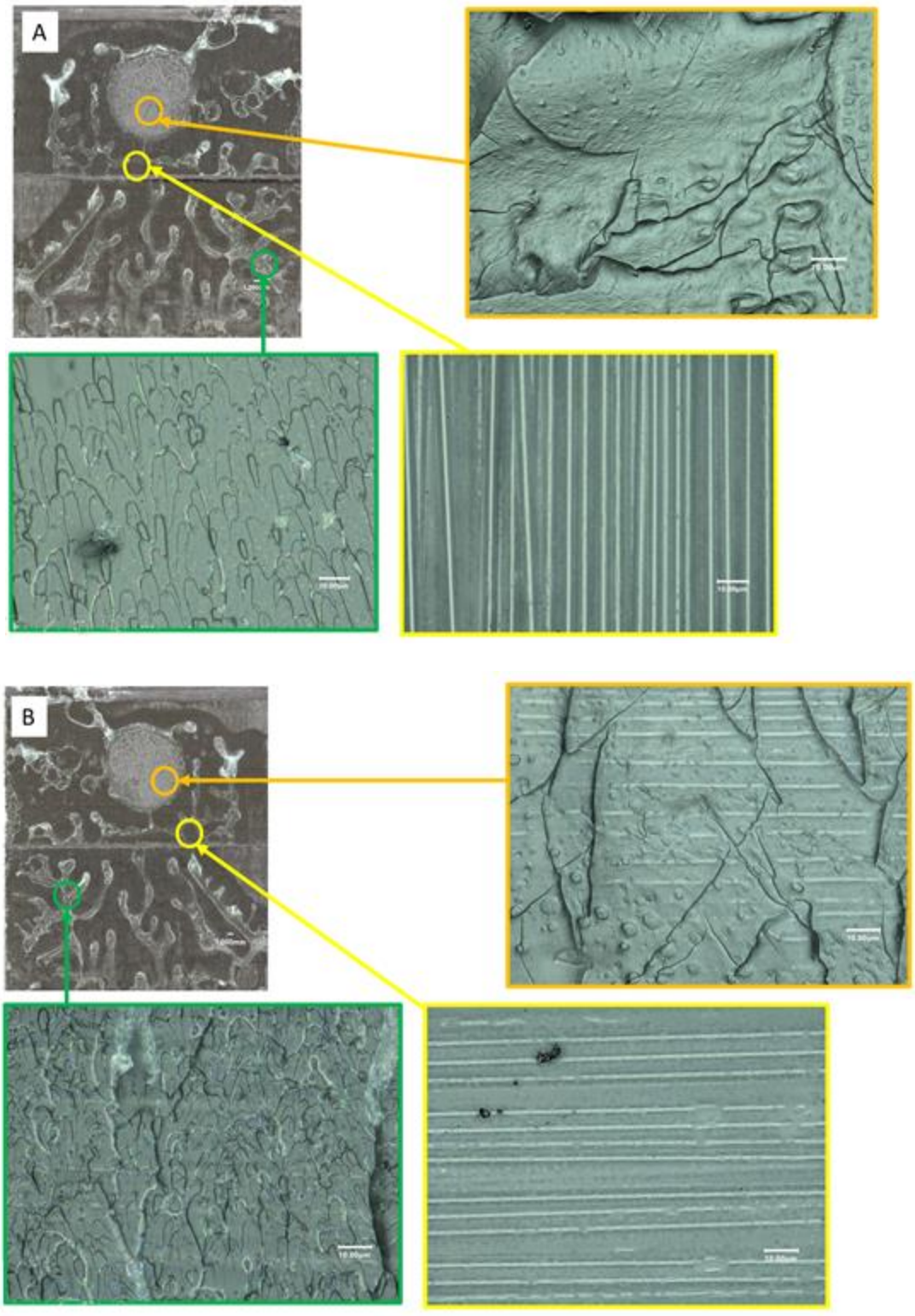

Figure 4.94. ENF-CROSS-CONT-HF modified ENF coupon fracture surfaces. A. Bottom surface B. Top surface

In Figure 4.95 are the macro and high magnification microscopic photos of a lubricating oil contaminated and repaired sample representing the ENF-CROSS-CONT-LO sample set. This sample set did not have any coupons that were bonded well enough to test, therefore the report value for G_{IIC} was 0. The macro surface of the coupon exhibits large areas that appear to be hydrophobic due to the lubricating oil contaminant and resulted in large void areas. These areas were shown under high magnification in the green boxed regions and display a surface with a thin coat of adhesive over the existing adherend fibers and no evidence of fracture. There are also areas of macro and micro porosity within the repair resin. The yellow boxed region was an area of macro porosity and high magnification verifies with presence of micro-porosity within the porous repair resin. The orange boxed region was visually determined to have micro-porosity from the macro photograph and was verified in the high magnification photos. There was no evidence of fracture from this coupon, therefore it is likely it was never fully bonded due to the presence of the lubricating oil contaminant.

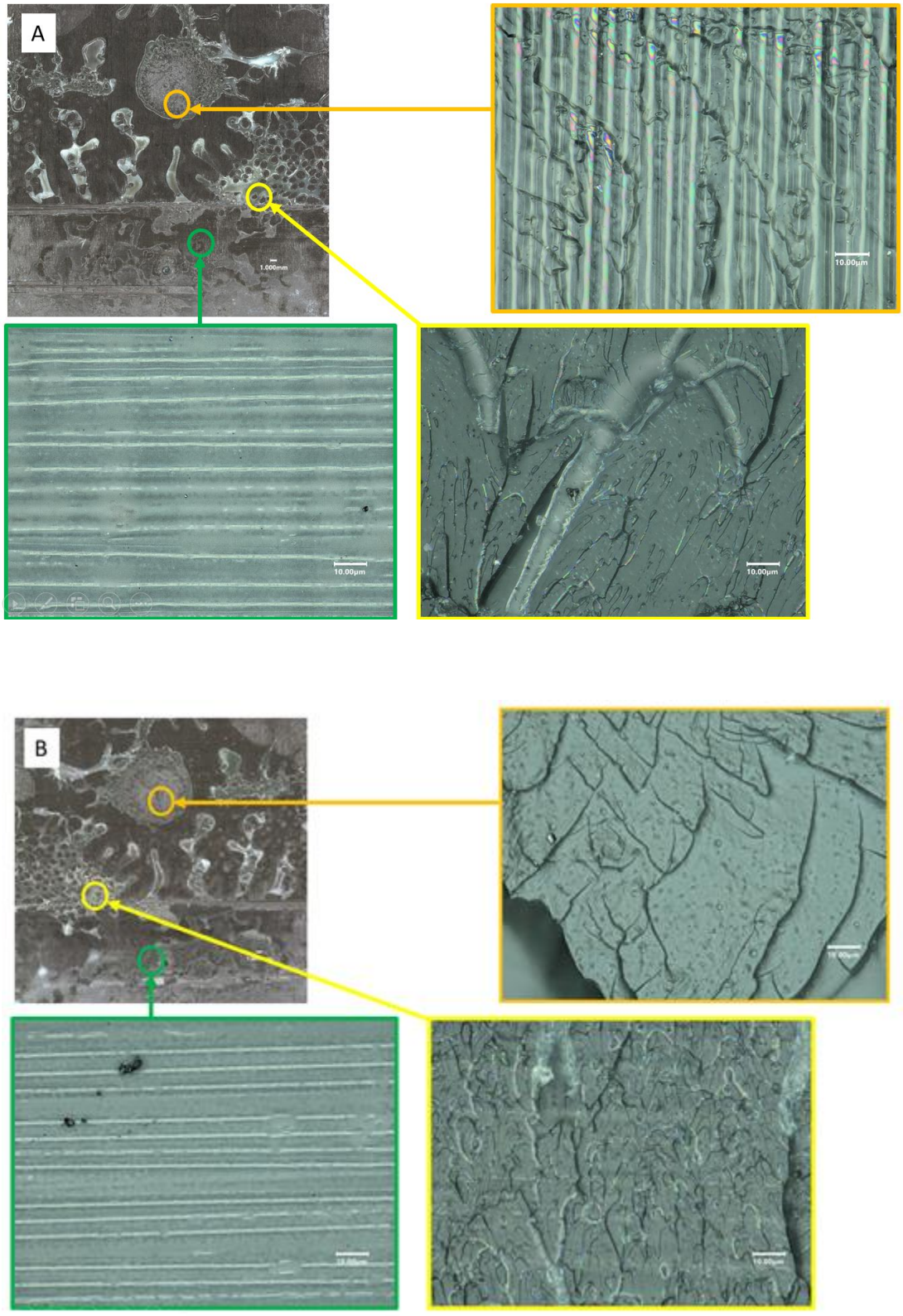

Figure 4.95. ENF-CROSS-CONT-LO modified ENF coupon fracture surfaces. A. Bottom surface B. Top surface

Summary of Fracture Observations and Correlation to Mode II Fracture Toughness

Modified ENF testing along with fractographic analysis has revealed a correlation between G_{IIC} values and the repair processing that was completed on each sample set. The G_{IIC} values collected in section 4.3.5 and primary observations for both, profile and planar microscopic fractography completed are summarized in Table 4.10. This table includes key primary fractographic observations, however further secondary or tertiary observations for fractography can be found within the description of the fracture surface for each representative sample discussed earlier in this section.

As previously discussed in section 4.2.2, baseline (ENF-UNI-BL, ENF-QUASI-BL, and ENF-CROSS-BL) sample sets had fracture within the PMC material, creating G_{IIC} values that would be used as the threshold value for comparing any sample set with a repaired configuration. In addition the Al-EA9396 sample set discussed in section 4.3.5 was used to determine the fracture toughness of the 10% acetone diluted EA9396 by itself. The modified repair resin had a much higher G_{IIC} value than the IM7/977-3 laminates and would affect the results of repaired modified PMC ENF configurations. ENF repaired samples sets with 20% acetone diluted EA9396 (ENF-UNI-RPR-20%, ENF-QUASI-RPR-20%, and ENF-CROSS-RPR-20%), did exhibit higher however investigation of fracture surfaces revealed major porosity within the repair resin. This porosity is of concern for repair scenarios that are subject to fatigue loading because the repair is likely to fail prematurely and could not be reliably inspected using traditional NDI techniques such as UT due to sound reflection from the volume of porosity.

Table 4.10. Summary of mode II fracture toughness and microscopic fracture observations

Sample Set	G_{IIC} (J/m^2)	Profile Fracture Observation	Primary Planar Fracture Observation
ENF-UNI-BL	857	At mid-plane within matrix	Adherend fracture at mid-plane
ENF-QUASI-BL	1302	1-2 transverse multi-ply	Adherend Failure 1-3 plies
ENF-CROSS-BL	831	1-3 transverse multi-ply	Adherend Failure 1-3 plies
AL-EA9396	3410	At mid-plane to repair resin-to-adherend interface	Cohesive fracture within repair resin
ENF-UNI-RPR-20%	2117	Mid-plane within repair resin	Major porosity in repair resin, cohesive repair resin failure.
ENF-QUASI-RPR-20%	3274	Mid-plane within repair resin	Major porosity in repair resin, cohesive repair resin failure.
ENF-CROSS-RPR-20%	2408	Mid-plane within repair resin	Major porosity in repair resin, cohesive repair resin failure.
ENF-UNI-RPR	3555	Mid-plane within repair resin	Mixed cohesive failure in repair resin and adherend matrix.
ENF-QUASI-RPR	1693	Mid-plane within repair resin and 1-2 ply into adherend	Adherend Failure 1-3 plies
ENF-CROSS-RPR	2178	Mid-plane within repair resin and 1-2 ply into adherend	Adherend Failure 1-3 plies with compressive fracture.
ENF-UNI-CONT-HF	100	Mid-plane within repair resin	Interfacial failure with micro-voids
ENF-QUASI-CONT-HF	449	Mid-plane within repair resin	Interfacial failure
ENF-CROSS-CONT-HF	274	Mid-plane within repair resin	Major voids and Interfacial failure
ENF-UNI-CL-HF	4059	Mid-plane within repair resin to interface with adherend	Mixed cohesive failure in repair resin and adherend matrix
ENF-QUASI-CL-HF	1776	1st ply in adherend and transverse migration through repair resin and 1-2 ply into other adherend	Adherend Failure 1-3 plies
ENF-CROSS-CL-HF	2346	1st ply in adherend and transverse migration through repair resin and 1-2 ply into other adherend	Adherend Failure 1-3 plies with compressive fracture.
ENF-UNI-CONT-LO	136	Mid-plane within repair resin	Interfacial failure
ENF-QUASI-CONT-LO	620	Mid-plane within repair resin	Major voids and Interfacial failure
ENF-CROSS-CONT-LO	0	Mid-plane within repair resin	Major voids and micro-porosity in repair resin
ENF-UNI-CL-LO	3771	Mid-plane within repair resin to interface with adherend	Mixed cohesive failure in repair resin and adherend matrix
ENF-QUASI-CL-LO	1509	1st ply in adherend and transverse migration through repair resin and 1-2 ply into other adherend	Adherend Failure 1-3 plies
ENF-CROSS-CL-LO	2011	1st ply in adherend and transverse migration through repair resin and 1-2 ply into other adherend	Adherend Failure 1-3 plies with compressive fracture.

Uncontaminated and repaired sample sets (ENF-UNI-RPR, ENF-QUASI-RPR, and ENF-CROSS-RPR) met the baseline threshold values for G_{IIC} of each respective laminate configuration, however there was a noticeable increase in G_{IIC} for the unidirectional sample set (ENF-UNI-RPR) where the primary fracture was within the repair resin. The quasi-isotropic sample set (ENF-QUASI-RPR) had approximately the same G_{IIC} values and similar fracture surfaces when compared to the baseline sample set (ENF-QUASI-BL). The cross ply sample set (ENF-CROSS-RPR) had slightly increased average G_{IIC} value when compared to the corresponding baseline sample set (ENF-CROSS-BL) and the primary difference in failure mode was the observed compression fractures in the repaired sample set that were due to mechanical interlocking of the previously fractured surface.

All contaminated (CONT) and repaired without cleaning sample sets, regardless of the contaminant, had lowered G_{IIC} values when compared to the baseline sample sets. The primary planar failure modes for all of the CONT sample sets were voids or interfacial between the repair resin and the adherend. This correlates to a poor bond and lack of repair resin in the delamination.

All contaminated and cleaned (CL) sample sets, regardless of the contaminant, had similar G_{IIC} values to the uncontaminated and repaired (RPR) sample sets of the same laminate configuration. In addition the CL sample sets had similar primary profile and planar failure modes to the RPR samples sets. This consistency of G_{IIC} values and fractography failure modes indicates that the cleaning process provides similar results to uncontaminated sample sets. In addition, the CL samples sets had higher G_{IIC} values than the threshold values of the baseline (BL) samples sets.

Based upon the fractography performed on both the profile and planar surfaces of the coupons it can be concluded that the novel injection repair process was able to restore the G_{IIC} of

the parent laminate equally for uncontaminated and contaminated and cleaned sample sets. The fractography of the post-tested surfaces were verified to have favorable brittle fracture within the repair resin and/or mixed fracture within the PMC laminate adherend matrix. This exhibits a strong bond of the repair resin to the parent laminate with the ability to carry interlaminar shear stress and provides mechanical property restoration of the fractured laminate. In addition to verification of the repair process within modified ENF simulated delaminations, it was also verified that if contamination was left inside and simply injected with the repair resin in an attempt to repair a dirty surface, the G_{IIC} was extremely low and would only fractionally restore mechanical properties to those of the baseline laminate, if at all. The analysis and conclusive results of the modified ENF surface fractures ensure that the novel injection repair process developed as part of this study is able to successfully repair single or simplified (1-3 ply deep) multi-level delaminations.

Chapter Acknowledgments

Chapter 4 included material as it appears in the Impact Damage and Injection Repair Strength Restoration, 2021, Massey, Justin, Romasko, Barrett, and Kim, Hyonny, Proceedings of the 36th Annual American Society for Composites Technical Conference and Novel Enclosed Delamination Injection Repair Process for Strength Restoration, 2022, Massey, Justin, Romasko, Barrett, and Kim, Hyonny, Proceedings of the 37th Annual American Society for Composites Technical Conference. Also material from Characterization of Transverse Impact Damage and Internal Contamination of In-Service Composite Aircraft Skins, Massey, Justin, Ellison, Andrew, and Kim, Hyonny, Proceedings of the 2023 Composites and Advanced Materials Expo. In addition material from Advanced Composite Novel Delamination Injection Repair Procedure for

Restoration of Laminate Mechanical Properties, Massey, Justin and Kim, Hyonny, in part is currently being prepared for submission for publication with the 2023 US-Japan Composite Symposium. Finally, unpublished material co-authored with Anagnostopoulos, Konstantinos and Kim, Hyonny for A Comparison of Carbon/Epoxy Composite Interlaminar Laboratory-Based Delamination Methods to In-service Aircraft Damage. The dissertation author was the primary investigator and author for all of these papers.

CHAPTER 5: CONCLUSIONS

A novel delamination injection repair procedure was developed and verified to restore mechanical properties to a previously delamination-fractured laminate. This was accomplished by first characterizing in-service delaminations damage to composite components. Microscopy, ultrasonic testing, X-ray CT imaging, and GC-MS spectrometry revealed multi-plane damage, with trace amounts of contamination. It was concluded that the ultrasonic testing correlated well to the X-ray CT results, defining damages in the same regions. However the X-ray CT post processing methods still required more development to increase definition in 3-D imaging of the delaminations. The in-service multi-plane delaminations were not as complex as previously characterized laboratory manufactured impact damages. Therefore laboratory-based delamination methods, including a new modified ENF coupon, impacted specimens, and PTFE insert specimens were compared to in-service delaminations. Results from microscopy (planar and through thickness profile) and digital surface metrology revealed that the in-service damage was best correlated with a modified ENF fracture coupon with a quasi-isotropic lay-up laminate. The metrology results quantitatively revealed a similar surface roughness and profile for both measurements along both the 90° and 0° directions. Microscopy revealed a similar result where the less complex quasi-isotropic modified ENF coupon had 1-3 planes that were fractured, which was the same as the excised in-service enclosed delaminations.

In addition to characterizing delamination damages, materials and process development were completed to perform cleaning and repair operations on the delamination damage. However there exists concerns that internal pressure within the delamination due the injection repair process could drive further growth of the delamination. Therefore a parametric FEA model utilizing VCCT, was completed for two different 25-ply, IM7/977-3 laminates, to determine at what internal

pressure the crack front would propagate. Results determined as the simulated delamination diameter was increased, the critical threshold internal pressure driving growth would decrease. For the 50mm diameter delamination size, a critical pressure of 0.26 MPa was found to be sufficient for growth of 1-ply sub-laminate (worst case scenario). This was higher than the maximum pressures estimated to be generated by both injection using an atmospheric plasma unit (0.07 MPa) or by hand injection of resin via a syringe (0.10 MPa).

For process development, a contamination procedure was successfully developed using a solvent-diluted hydraulic fluid or lubricating oil to reduce viscosity and ensure coverage of internal delamination fracture surfaces. Cleaning procedures were developed and verified using a solvent cleaning followed by an oxygen-helium atmospheric plasma application. Results from real-time mass spectrometry exhibits removal of hydrocarbon contaminants at 43, 44, 57, and 58 amu over 10 minutes of plasma treatment after an acetone rinse. In addition to real time mass spectrometry verification, WCA testing and FT-IR spectrometry revealed the removal of the contaminants. WCA had a reduction of approximately 60° after cleaning procedures were completed for a minimum of 20 minutes, which is a 37% increase in work of adhesion (W_{ls}) on the laminate surface (i.e. better bonding). The more sensitive FT-IR spectrometry results found that complete removal of contaminants, located between 2500-3900 cm^{-1}, was after 20 minutes of atmospheric plasma exposure.

Resin modification testing was investigated to ensure that the injection repair resin had a low enough viscosity to infiltrate the enclosed internal delamination damage while maintaining suitable mechanical properties. Single lap shear results show that 10% or 20% acetone dilution by weight-maintained shear strength properties within standard deviation of the undiluted EA9396 epoxy. Brookfield viscometer testing resulted in a viscosity of <100 cPs for 20% acetone dilution

and 540-697 cPs for 10% acetone dilution, both of which are a major reduction from the undiluted EA9396 viscosity of 3600 cPs. Cure parameter testing revealed that 20% acetone dilution of the EA9396 resin results in major porosity within the material and 10% acetone dilution had micro-porosity comparable to the undiluted EA9396 resin. Cure parameters testing also revealed that a five-day room temperature hold prior to cure would yield the most consistent results because the acetone would have enough time to off-gas prior to elevated temperature curing of the epoxy.

Modified ENF testing on three different laminate configurations was completed to verify that the novel delamination injection repair process would restore mechanical properties. Results for all three configurations show that the contaminated samples that were repaired with the contamination remaining in the delamination all had a reduced G_{IIC} when compared to the baseline laminate sample set. These results exhibit why contamination removal is imperative to execute a robust repair process. Results for repaired or cleaned and repaired sample sets of a laminate configuration yielded a return of G_{IIC} laminate properties to be in excess or within standard deviation of the baseline laminate properties.

Unidirectional samples set were repaired or cleaned and repaired showed an increase in mode II strain energy release rate when compared to the baseline values from fracture testing of the parent laminate. The increase in G_{IIC} for unidirectional modified ENF coupons was attributed to not only using a repair resin that had a higher resultant G_{IIC} compared to the parent laminate matrix, but also the bondline where the laminate was repaired resulted was thicker and produced a fracture process zone in front of the crack propagation that would increase the fracture toughness of the repaired laminate configuration. Failure analysis of the fracture surfaces using high magnification SEM and digital microscopy revealed a mixed cohesive fracture within the repair

resin and matrix failure for unidirectional sample sets that had higher G_{IIC} than the baseline laminate coupons.

For quasi-isotropic modified ENF laminates, repaired or cleaned and repaired samples display a G_{IIC} within standard deviation of the baseline laminate. These results were verified by planar fractographic analysis of the post-tested coupon surfaces. The repaired or contaminated, cleaned, and repaired samples fracture surfaces revealed a primarily first-ply adherend failure. The first ply failure and G_{IIC} values that are consistent with the baseline laminate are consistent, in that the quasi-isotropic adherend material itself (i.e., not the adhesive) was the limiting factor when placed into interlaminar shear.

The cross-ply modified ENF repaired or cleaned and repaired coupon configuration results showed a slight increase in G_{IIC} when compared to the baseline sample set. The fracture analysis of the profile and planar surfaces revealed a mechanical interlocking in a stepped region which caused compression in the laminate when placed under interlaminar shear. The primary failure mode was first ply adherend failure, however compression cracks were observed within the laminates, which was different from the quasi-isotropic laminate configuration.

The final results of the delamination characterization and materials and process development for a novel injection repair procedure yielded a new process that can be utilized to restore mechanical properties in PMC laminates. This study confirmed that the process could clean the internal surfaces of a multi-level PMC delamination and provide adequate fill using a modified injection repair resin to restore mechanical properties. However, further testing must be completed to verify that processing developed as part of this study can be applied to more complex impact damages and provide strength restoration.

CHAPTER 6: ADDITIONAL WORK AND MOVING FORWARD

In addition to the work completed for this study to verify mechanical property restoration of delaminations in mode II, preliminary work has been completed to verify the novel injection repair process on more complex impact damage coupons. This chapter will present preliminary work in testing compression after impact specimens and development testing for drill patterns into complex multi-level impact delaminations. Also a discussion of path forward for future testing will be included.

6.1. COMPRESSION AFTER IMPACT PRELIMINARY TESTING

Impact test coupons that were manufactured in section 3.1.2 were used to perform preliminary compression after impact (CAI) testing. Three panels were speckle painted with spray paint prior to testing. These coupons were tested in accordance with ASTM D7137 [91] using a CU-CI Wyoming test fixture and 222 kN load frame. Strain data was captured using a correlated solution 3-D digital image correlation (DIC) system and three bonded strain gauges were used to verify 3-D DIC data. The preliminary testing was conducted on impacted and unrepaired coupons only. The set was three samples impacted at 15J for panel type M as referenced in Table 4.3. Each coupon was tested to ultimate failure to determine the maximum failure load of the sample set. One concern was if the load frame and test fixture could withstand the high load associated with this test and coupon configuration. Figure 6.1 shows a representative coupon after impact testing, prior to CAI testing in the load frame and fixture, the strain field data collected by DIC during testing, and the coupon fractured after testing was completed.

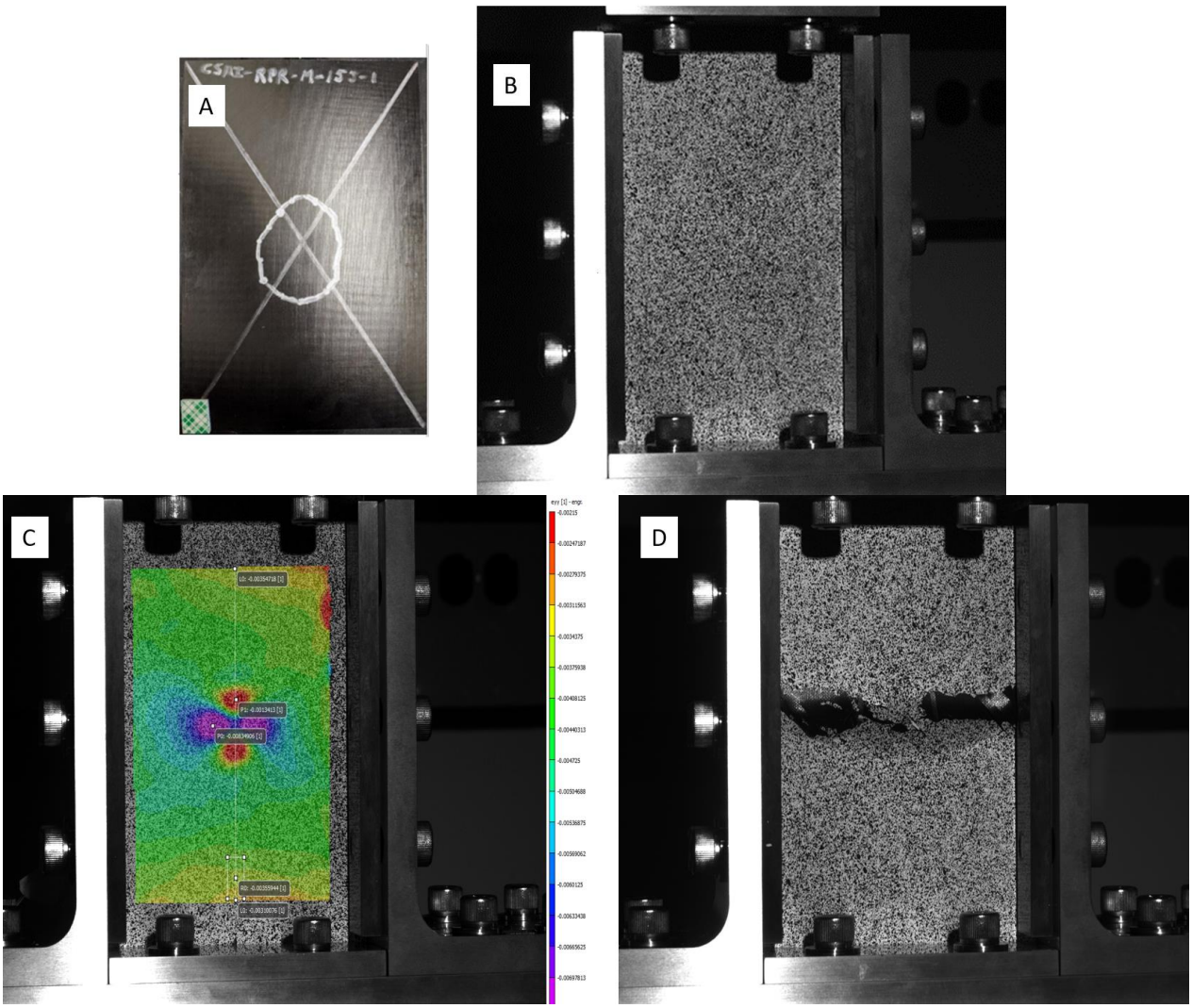

Figure 6.1. CAI testing of 15J impact tested coupon. A. Coupon with NDI indication, B. Coupon painted and in loading fixture, C. 3-D DIC strain field data while testing, D. Fractured coupon after testing completed

Results from the initial test set had an average ultimate compressive strength (F^{CAI}) of 262.75 MPa with a standard deviation of 16.18 MPa. The highest load experienced by the coupons was 21.11 kN. The average effective modulus calculated for the sample set was 6.7 GPa. A representative load versus displacement curve can be seen in Figure 6.2. Load versus displacement curve of delaminated CAI coupon.

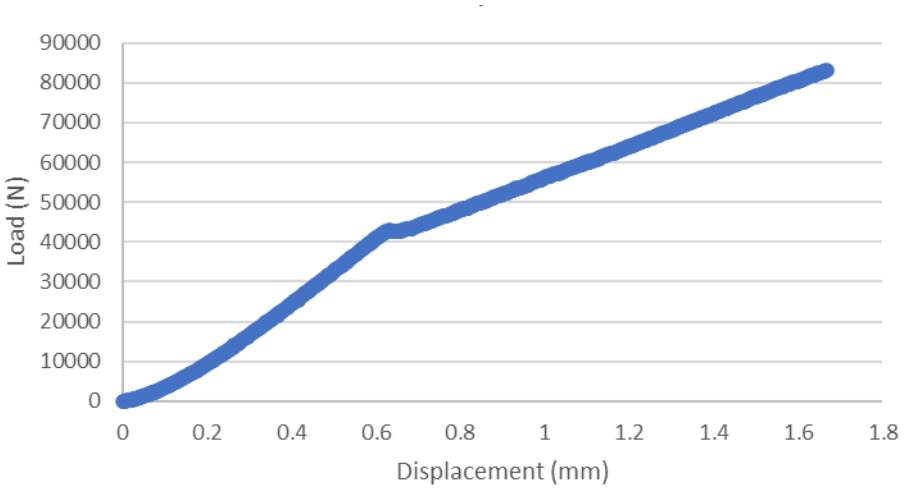

Figure 6.2. Load versus displacement curve of delaminated CAI coupon

Failure mode of the test coupons were all lateral through damage located at the middle of the specimens. The resultant values from this testing suggest that if the injection repair is as effective as it was for mode II fracture testing, the load frame and test fixture may require changing to higher strength materials and higher load frame capacity.

6.2. DELAMINATION DRILLING PROCESS DEVELOPMENT

Drill process testing was completed to determine if drilling process parameters could be established to optimized fluid flow of the repair resin into the complex multi-level impact damage. Drill depth and injection pressure testing was conducted on three type H, 10 J impacted panels. All three panels had approximately 44.45 mm diameter impact delaminations and named 1H-3H. A nine-hole drill pattern was tested on all three panels as shown in Figure 6.3. All holes were drilled to a 2.13 mm diameter using carbide twist drill bits.

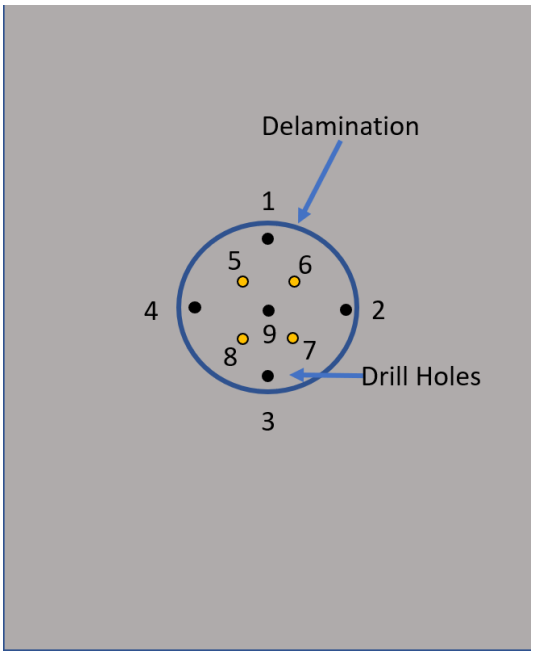

Figure 6.3. Nine-hole drill pattern for testing

For the drill depth study, a qualitative visual test was completed to determine to viability of a fluid to flow through a complex delamination when drilled at different depths. Panel 1H injection holes were drilled down to the damage depth reported by the ultrasonic A-scan as shown in Table 6.1. All panel 2H injection holes were drilled to within 2-plies of the back surface of the coupon which is a drill depth of 3.15 mm. This depth was chosen due to the results from the parametric injection pressure model study completed in section 4.3.1.

Table 6.1. Panel 1H injection hole drill depth information

Injection Hole Location	Drill Depth (mm)
1	2.57
2	2.57
3	2.57
4	2.84
5	2.84
6	2.84
7	2.74
8	2.74
9	2.84

Oatey's leak detector was spread over the holes to determine where air would come out of the delamination when it was injected in each hole with compressed air. Air injection was completed using a SEMCO sealant gun with 0.55 MPa compressed air (see Figure 6.4).

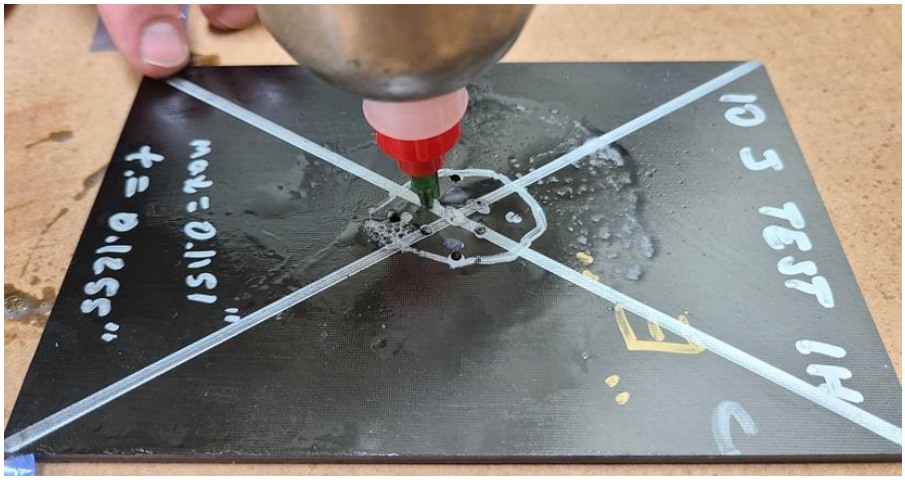

Figure 6.4. Drill depth injection testing

Results are reported in Table 6.2 where the injection site is the hole that was injected with air and holes where bubbles were observed are location where the air travelled out of the panel.

Table 6.2. Injection hole depth testing results

Injection Site	Panel 1H Holes Bubbles Observed	Panel 2H Holes Bubbles Observed
1	2,4,5,6,8,9	All Holes
2	1,4,5,6,8,9	All Holes
3	None	All Holes
4	1,2,4,5,6,8,9	1,2,4,5,6,7,8,9
5	1,2,4,5,6,8,9	All Holes
6	1,2,4,5,6,8,9	All Holes
7	None	All Holes
8	1,2,4,5,6,8,9	All Holes
9	1,2,4,5,6,8,9	1,2,4,5,6,7,8,9

Results indicate that drilling to within two plies of the backside skin provide better overall fluid flow within the delamination. On panel 2H, hole #3 was the most difficult to provide fluid flow. This may be a result of the drill bit used because no reaming of the injection holes was conducted and previous studies show that twist drills can potentially clog the delamination micro-fractures with debris [48].

Next, drill pressure testing was completed using panels 2H and 3H where all nine holes were drilled to within two plies of the back surface of the coupon. Since sample 2H was re-used for this study the injection holes remained the same from the drill depth testing, however for sample 3H the drill depth was to 2.91 mm based upon the thickness of the coupon. Leak detector was brushed over the holes and each hole was injected with variable pressure from 0-100 psi using compressed air and a regulator equipped with tubing and a 2.11 mm diameter needle (see Figure 6.5).

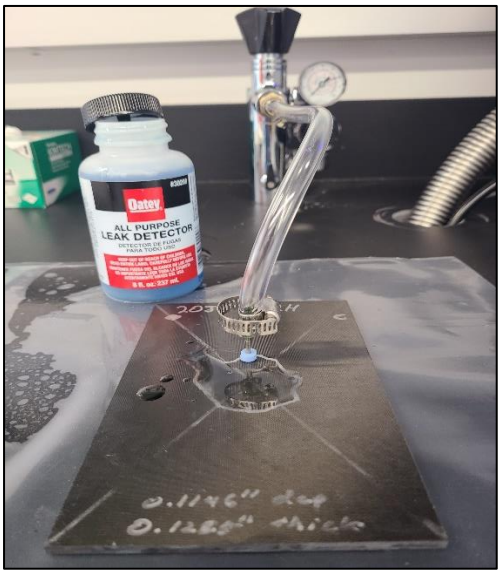

Figure 6.5. Mock-up of variable pressure testing for fluid flow in an impact delamination

Results of bubbles observed at different injection pressure at the other injection holes are shown in Table 6.3. “None” meant that the air did not travel to another hole. Results indicate that 0.55 MPa was the highest injection pressure for all holes that were able to transport fluid. The holes where fluid flow was not achieved was likely due to the hole not interconnecting with the multi-level delamination or the hole may have become plugged during the drilling process. Further drill process testing should be completed with reaming of the hole to prevent clogging.

Table 6.3. Injection pressure testing results

Injection Site	Panel 1H Pressure Bubbles Observed (MPa)	Panel 2H Pressure Bubbles Observed (MPa)
1	0.05	0.07
2	0.14	0.41
3	None	0.28
4	0.55	None
5	0.14	0.21
6	0.17	0.21
7	0.28	0.14
8	0.17	0.14
9	0.28	0.28

6.3. MOVING FORWARD

Although many novel contributions were completed as part of this study, including development of a new injection repair procedure, to fully transition this process to be an adopted method for aircraft repair, further testing must be considered. This testing includes determining the effects of injection repair on: compression after impact, fatigue (compression/tension or mode II), and environmental testing. In addition, further development of: drilling procedures using reamer bits to reduce drilling debris, testing of lower viscosity injection repair resins, and implementation of post repair quantification using advanced NDI techniques would also aid in this process becoming more robust.

CHAPTER 7: REFERENCES

1. Miracle, D.B., Donaldson, S.L. (2001). ASM Handbook: Composites, Vol. 21, pp. 245.

2. O'Brien, T.K. (1982). Characterization of Delamination Onset and Growth in a Composite Laminate. In Damage in Composite Materials, ASTM STP 775, pp. 140-167.

3. Davies, G.A.O., Robinson, P., Robson, J., Eady, D. (1997). Shear driven delamination propagation in two dimensions. Composites Part A: Applied Science and Manufacturing, 28(8), 757-765.

4. Rhodes, M.D., Williams, J.G., Starnes, J.H., Jr. (1981). Low-velocity impact damage in graphite-fiber reinforced epoxy laminates. Polym Compos, 2, 36-44.

5. Suemasu, H., Majima, O. (1996). Multiple Delaminations and their Severity in Circular Axisymmetric Plates Subjected to Transverse Loading. Journal of Composite Materials, 30(4), 441-453.

6. Richardson, M.O.W., Wisheart, M.J. (1996). Review of low-velocity impact properties of composite materials. Composites Part A: Applied Science and Manufacturing, 27(12), 1123–1131.

7. Liu, D., Malvern, L.E. (1987). Matrix cracking in impacted glass/epoxy plates. Journal of Composite Materials, 21(7), 594–609.

8. Ganesan, R. (2008). Experimental characterization of interlaminar shear strength. In Delamination Behaviour of Composites (pp. 117-137). Woodhead Publishing.

9. Jackson, W.C., Poe Jr, C.C. (1992, September). The use of impact force as a scale parameter for the impact response of composite laminates. In FAA, Ninth DOD (NASA) FAA Conference on Fibrous Composites in Structural Design, Volume 2.

10. Sjoblom, P.O., Hartness, J.T., Cordell, T.M. (1988). On low-velocity impact testing of composite materials. Journal of Composite Materials, 22(1), 30–52.

11. ASTM International. (2020). ASTM standard D7136/D7136M-20, Standard Test Method for Measuring the Damage Resistance of a Fiber-Reinforced Polymer Matrix Composite to a Drop-Weight Impact Event. West Conshohocken, PA.

12. Romasko,B. (2022). Flat Composite Panel Impact Testing and Characterization by Ultrasonic Non-Destructive Evaluation. Master's Thesis. University of California San Diego.

13. Sridharan, S. (2008). Delamination behaviour of composites. CRC press.

14. Kedward, K.T., Wilson, R.S., McLean, S.K. (1989). Flexure of simply curved composite shapes. Composites, 20, 527-536.

15. D'Amore, A., Grassia, L. (2019). Principal Features of Fatigue and Residual Strength of Composite Materials Subjected to Constant Amplitude (CA) Loading. Materials, 12(16), 2586.

16. Potter, K. D., Campbell, M. A., Langer, C. M., & Wisnom, M. R. (2005). The generation of geometrical deformations due to tool/part interaction in the manufacture of composite components. Composites Part A: Applied Science and Manufacturing, 36, 301-308.

17. Tříska, V., Jílek, A., Hnidka, J., Maňas, K., & Flášar, O. (2021). Infrared Nondestructive Inspection: Seeking a Suitable Insert to Simulate Delamination in a CFRP Laminate. 2021 International Conference on Military Technologies (ICMT), 1-5.

18. Krautkramer, J., & Krautkramer, H. (1990). Ultrasonic Testing of Materials (4th ed.). Springer-Verlag.

19. "Ultrasonic testing." Wikipedia, The Free Encyclopedia. Retrieved May 13, 2023, from https://en.wikipedia.org/wiki/Ultrasonic_testing

20. American Society for Nondestructive Testing. (1991). Ultrasonic Testing. In Nondestructive Testing Handbook (2nd ed.).

21. Heindel, T. (2011). A Review of X-Ray Flow Visualization with Applications to Multiphase Flows. Journal of Fluids Engineering. 133.

22. Friddell, K. D., Lowrey, A. R., & Lemprier, B. M. (1985). Application of Medical Computed Tomography (CT) Scanners to Advance Aerospace Composites. In D. O. Thompson & D. E. Chimenti (Eds.), Review of Progress in Quantitative Nondestructive Evaluation, Vol 4 (pp. 2207-2214). Plenum Press.

23. Bossi, R. H., & Friddell, K. D. (1990). Non-Destructive Testing of Fiber-Reinforced Plastic Composites. Computed Tomography. Elsevier Science Publishers.

24. Youngberg, J. E. (1995). Three Dimensional Computed Tomography for Rocket Motor Inspection. In Nondestructive Evaluation of Aging Aircraft, Aerospace Hardware and Materials.

25. Bossi, R., & Cooprider, K. K. (1990). X-ray Computed Tomography of Composites. WRDC-TR-90-4014, Wright Research Development Center.

26. Bull, D. J., Spearing, S. M., Sinclair, I., & Helfen, L. (2013). Three-dimensional assessment of low velocity impact damage in particle toughened composite laminates using micro-focus X-ray computed tomography and synchrotron radiation laminography. Composites Part A: Applied Science and Manufacturing, 52, 62-69.

27. Ellison, A., & Kim, H. (2018). Computed tomography informed composite damage state model generation. Journal of Composite Materials, 52(25), 3523-3538.

28. Benzeggagh, M.L., & Kenane, M. (1996). Measurement of Mixed-Mode Delamination Fracture Toughness of Unidirectional Glass/Epoxy Composites with Mixed-Mode Bending Apparatus. Composite Science and Technology, 56(4), 439-449.

29. Reeder, J. R. (2006). 3D mixed-mode delamination fracture criteria - An experimentalist's perspective. Damage Composites, 1.

30. ASTM International. (2021). ASTM standard D5528/D5528M-21, Standard Test Method for Mode I Interlaminar Fracture Toughness of Unidirectional Fiber-Reinforced Polymer Matrix Composites. West Conshohocken, PA.

31. ASTM International. (2019). ASTM standard D7905/D7905M-19e1, Standard Test Method for Determination of the Mode II Interlaminar Fracture Toughness of Unidirectional Fiber-Reinforced Polymer Matrix Composites. West Conshohocken, PA.

32. ASTM International. (2013). Standard Test Method for Mixed Mode I Mode II Interlaminar Fracture Toughness of Unidirectional Fiber Reinforced Polymer Matrix Composites (ASTM standard D6671/D6671M-13e1). West Conshohocken, PA.

33. Pereira, A.B., & de Morais, A.B. (2008). Mixed mode I+II interlaminar fracture of carbon/epoxy laminates. Composites Part A: Applied Science and Manufacturing, 39(2), 322-333.

34. Krueger, R. (2015). Numerical Modelling of Failure in Advanced Composite Materials.

35. Dry, C. (2008). Proc. Of SPIE, ISOE.

36. Wilkins, D.J., et al. (1982). Characterizing Delamination Growth in Graphite-Epoxy. In Damage in Composite Materials (ASTM STP 775).

37. O'Brien, T.K. (1985). Analysis of Local Delaminations and Their Influence on Composite Laminate Behavior. In Delamination and Debonding of Materials (ASTM STP 876).

38. Bhatia, N.M., & Labor, J.D. (1985). Depot Level Repairs for Composite Structures, Development and Validation, Vol 1. Naval Air Development Center Contractors Report 79172–60.

39. Myhre, S.H., & Labor, J.D. (1980). Repair of Advanced Composite Structures. Journal of Aircraft, 18, 546-552.

40. Miracle, D.B., & Donaldson, S.L. (2001). ASM Handbook: Composites, Vol. 21. ASM International.

41. Ahn, S.H., & Springer, G.S. (2000). Repair of Composite Laminates. FAA Report No. DOT/FAA/AR-00/46.

42. Hall, Z.E.C., Liu, J., Brooks, R.A., Liu, H., Crocker, J.W.M., Joesbury, A.M., Harper, L.T., Blackman, B.R.K., Kinloch, A.J., Dear, J.P. (2022). The effectiveness of patch repairs to restore the impact properties of carbon-fibre reinforced-plastic composites. Engineering Fracture Mechanics, 270.

43. Russell, A.J. (1991). Resin Requirements for Successful Repair of Delaminations. In 36th International SAMPE Symposium.

44. Russell, A.J. (1996). Delamination Repair Demonstration. Esquimalt Defence Research Detachment Presentation.

45. Hautier, M. (2010). Investigation of a Composite Repair Method by Liquid Resin Infusion. In International Conference on Composite Materials, Journal of Plastics, Rubber, and Composites, 39.

46. Hayes, B.S. (2016). Structural Injection Repair Resin and Process for Composite Materials. Journal of Advanced Materials, 3, 1-14.

47. Wu, K.-W., Lee, C.-L., Chang, Y.-C., & Ong, C.-L. (1996). Compressive strength of delaminated and repaired composite plates. Materials Chemistry and Physics, 43(2), 173-177.

48. Seneviratne, W.P., Saathoff, B.L., Palliyaguru, U.R., Hayes, B.S., & Dixon, D.G. (2019). Injection repair for restoration of composite properties. SAMPE Journal, 55(2), 16-25.

49. Musaramthota, V., Huang, J., Guo, Q., & Li, W. (2012). Effect of surface contamination on composite bond integrity and durability. In JAMS 2012 Proceedings (pp. 1-8). University of Washington.

50. Oakley, B., Dillingham, R. G., & St.Clair, T. L. (2015). TRUST- A Novel Approach to Determining Effects of Archtype Contaminant Compounds on Adhesion of Structural Composites. In 2015 SAMPE Conference Proceedings (pp. 1-13). Society for the Advancement of Material and Process Engineering.

51. Hart-Smith, L. J. (2002). Adhesive bonding of composite structures – Progress to date and some remaining challenges. Journal of Composites Technology & Research, 24(3), 133-153.

52. SAE International. (2002). SAE standard AMS 7201, Standard Contaminant for Testing Aerospace Cleaners. Warrendale, PA.

53. Wingfield, J. R. J. (1993). Treatment of composite surfaces for adhesive bonding. International Journal of Adhesion and Adhesives, 13(3), 151-156.

54. Fang, X., Guo, Q., Li, W., & Musaramthota, V. (2018). Effectiveness of surface treatment techniques for composite bonding with different contamination levels. In 2018 SAMPE Conference Proceedings (pp. 1-14). Society for the Advancement of Material and Process Engineering.

55. Hernandez, B., Broussard, J., Oakley, B., & Dillingham, R. G. (2019). Effect of surface contamination with mitigation methods on adhesive composite bond integrity and durability. In 2019 SAMPE Conference Proceedings (pp. 1-14). Society for the Advancement of Material and Process Engineering.

56. Encinas, N., & Belcher, M. A. (2014). Surface Modification of Aircraft Composites for Adhesive Bonding. International Journal of Adhesion and Adhesives, 50, 157-163.

57. Gude, M. R., Prolongo, S. G., & Urena, A. (2012). Adhesive Bonding of Carbon Fibre/Epoxy Laminates: Correlation Between Surface and Mechanical Properties. Surface & Coatings Technology, 207, 602-607.

58. Baldan, A. (2004). Adhesively-bonded Joints and Repairs in Metallic Alloys, Polymers and Composite Materials: Adhesives, Adhesion Theories and Surface Pretreatment. Journal of Materials Science, 39, 1-49.

59. Zaldivar, R. J. (2010). Effect of Processing Parameter Changes on the Adhesion of Plasma-Treated Carbon Fiber Reinforced Epoxy Composites. Journal of Composite Materials, 44(12).

60. Dillingham, R. G., & Oakley, B. R. (2014). Effect of Atmospheric Plasma Treatment on the Surface Properties and Adhesive Bonding of Graphite/Epoxy Composites. SAMPE 2014 Proceedings.

61. Dighton, C., Rezai, A., Ogin, S. L., & Watts, J. F. (2019). Atmospheric Plasma Treatment of CFRP Composites to Enhance Structural Bonding Investigated Using Surface Analytical Techniques. International Journal of Adhesion and Adhesives, 91, 142-149.

62. Harris, E., & Massey, J. (2014). Atmospheric Plasma for Hydraulic Fluid Contamination Removal in Composite Surfaces. CAMX 2014 Proceedings.

63. Roberts, R., Orme, M., Keene, T., & Przekop, K. (2022). Plasma Treatment Efficacy on Unclean Surfaces for Bonding Processes. CAMX 2022 Proceedings.

64. Akiyama, H., Hasegawa, K., Sekigawa, T., & Yamazaki, N. (2018). Atmospheric Plasma Treatment for Composite Bonding. Mitsubishi Heavy Industries Technical Review, 55(2).

65. Tran, N.T., Boyer, A.J., & Knorr, D.B. (2022). Multiple local hydroxyl groups as a way to improve bond strength and durability in structural adhesives. The Journal of Adhesion, 98(12), 1834-1854.

66. Mohamed, M.A., Jaafar, J., Ismail, A.F., Othman, M.H.D., & Rahman, M.A. (2017). Fourier Transform Infrared (FTIR) Spectrometry. In N. Hilal, A.F. Ismail, T. Matsuura, & D. Oatley-Radcliffe (Eds.), Membrane Characterization (pp. 3-29). Elsevier. ISBN 9780444637765.

67. Volland, W. (1999). Organic Compound Identification Using Infrared Spectrometry. Bellevue Community College, Washington.

68. Seelenbinder, J. (2012). Measurement of composite surface contamination using the Agilent 4100 ExoScan FTIR with diffuse reflectance sampling interface. Agilent Technologies Inc.

69. Zaera, F. (2014). New advances in the use of infrared absorption spectrometry for the characterization of heterogeneous catalytic reactions. Chem. Soc. Rev., 43, 7624.

70. Hamming, M.C., & Foster, N.G. (1972). Interpretation of mass spectra of organic compounds. Academic Press.

71. McLafferty, F.W. (1980). Interpretation of Mass Spectra (3rd ed.). University Science Books.

72. National Institute of Standards and Technology. (2020). Chemistry WebBook.

73. Kolapkar, S. (2018). Pyrolysis of Fiber-Plastic Waste Blends. Master's Thesis, Michigan Technical University.

74. Hiden Analytical Inc. (2017). Quantitative Gas Analyser Brochure (TDS 191/3). Warrington, England.

75. Robinson, P., & Song, D.Q. (1992). A Modified DCB Specimen for Mode I Testing of Multidirectional Laminates. Journal of Composite Materials, 26(11), 1554-1577.

76. Harvard Apparatus. (2019). Syringe Selection Guide. Holliston, MA.

77. International Organization for Standardization. (2017). Sterile hypodermic syringes for single use- Part 1: Syringes for manual use. ISO 7886-1:2017.

78. Hayward, W. A., Jr., Hill, L. R., Williams, J. L., & Walker, J. B. (1989). Pressure generated by syringes: Implications for hydrodissection and injection of dense connective tissue lesions. Scandinavian Journal of Rheumatology, 18(4), 221-224.

79. Ranatunga, V. P. (2011). Structural Technology Evaluation and Analysis Program: Delivery Order 0045: Progressive Failure Analysis of Translaminar Reinforced Composite Structures (Report No. AFRL-RB-WP-TR-2011-311). Air Force Research Laboratory.

80. Dean, S., Davidson, B., & Teller, S. (2010). Recommendations for an ASTM Standardized Test for Determining G_{IIc} of Unidirectional Laminated Polymeric Matrix Composites. Journal of ASTM International, 7(10), 1-11.

81. ASTM International. (2019). ASTM Standard D1002-10(2019), Standard Test Method for Apparent Shear Strength of Single-Lap-Joint Adhesively Bonded Metal Specimens by Tension Loading (Metal-to-Metal). West Conshohocken, PA.

82. Askins, R. (1991). Report No. WL-TR-92-4060, Accession No. ADA271931, Characterization of EA9396 Epoxy Resin for Composite Repair Applications. USAF Wright Laboratory.

83. ASTM International. (2007). ASTM Standard D2583-13a (2007), Standard Test Method for Indentation Hardness of Rigid Plastics by Means of a Barcol Impressor. West Conshohocken, PA.

84. American Society of Mechanical Engineers. (2019). ASME Standard B46.1-2019, Surface Texture (Surface Roughness, Waviness, and Lay). New York, NY.

85. Urness, K. N., Gough, R. V., Widegren, J. A., & Bruno, T. J. (2016). Thermal Decomposition Kinetics of Polyol Ester Lubricants. Applied Chemicals and Materials Division, National Institute of Standards and Technology, 325 Broadway, Boulder, CO 80305.

86. ASM Handbook: Fractography. Volume 12. (1987). United States: ASM International.

87. Mittal, K. L. (Ed.). (2009). Adhesive bonding: science, technology and applications. Wiley-VCH.

88. Kinloch, A. J. (1982). Adhesion and adhesives: science and technology. Chapman and Hall.

89. Abadie, M. J., & Kinloch, A. J. (1990). Surface topography and the strength of adhesive bonds. International Journal of Adhesion and Adhesives, 10(4), 215-222.

90. Guo, J., & Kinloch, A. J. (1999). The strength of adhesively-bonded stepped lap joints. Journal of Adhesion Science and Technology, 13(5), 539-561.

91. ASTM International. (2021). ASTM D7137-21. Standard Test Method for Compressive Residual Strength Properties of Damaged Polymer Matrix Composite Plates.

APPENDIX A: GC-MS CHROMATOGRAM

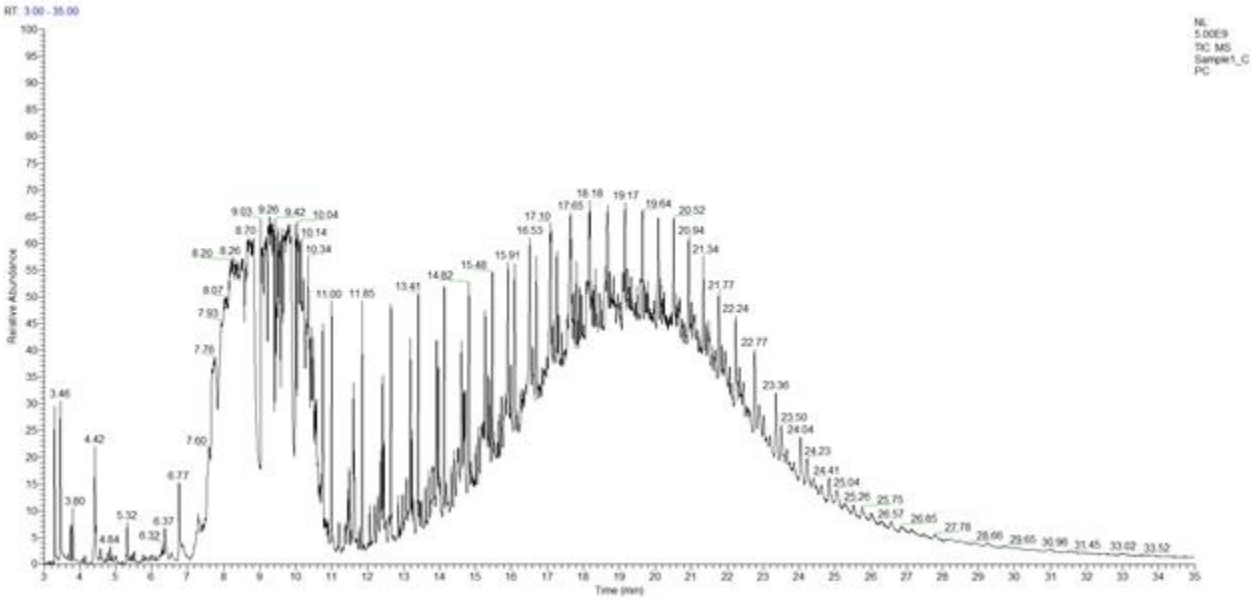

Figure A.1. Corrosion preventative compound gas chromatogram

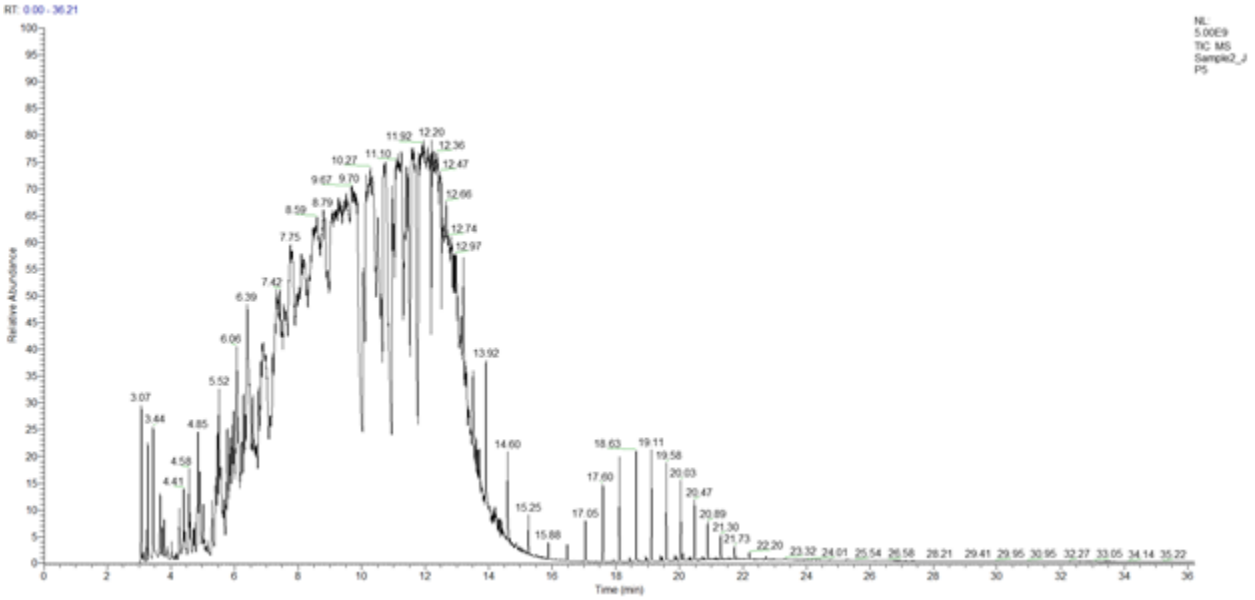

Figure A.2. Jet fuel gas chromatogram

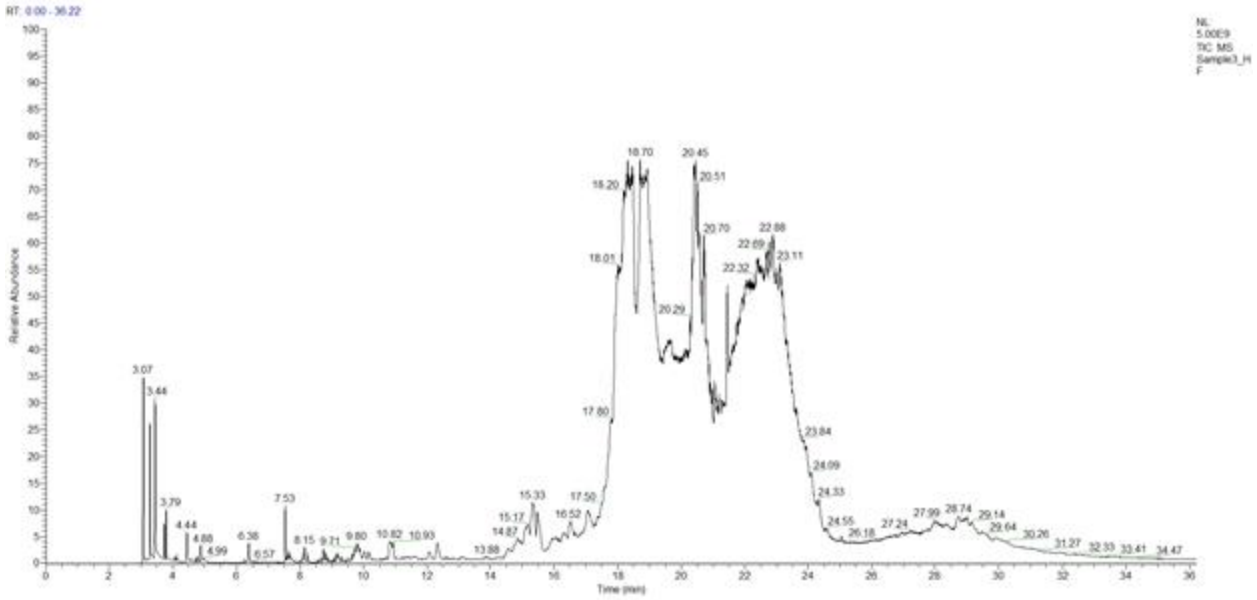

Figure A.3. Hydraulic fluid gas chromatogram

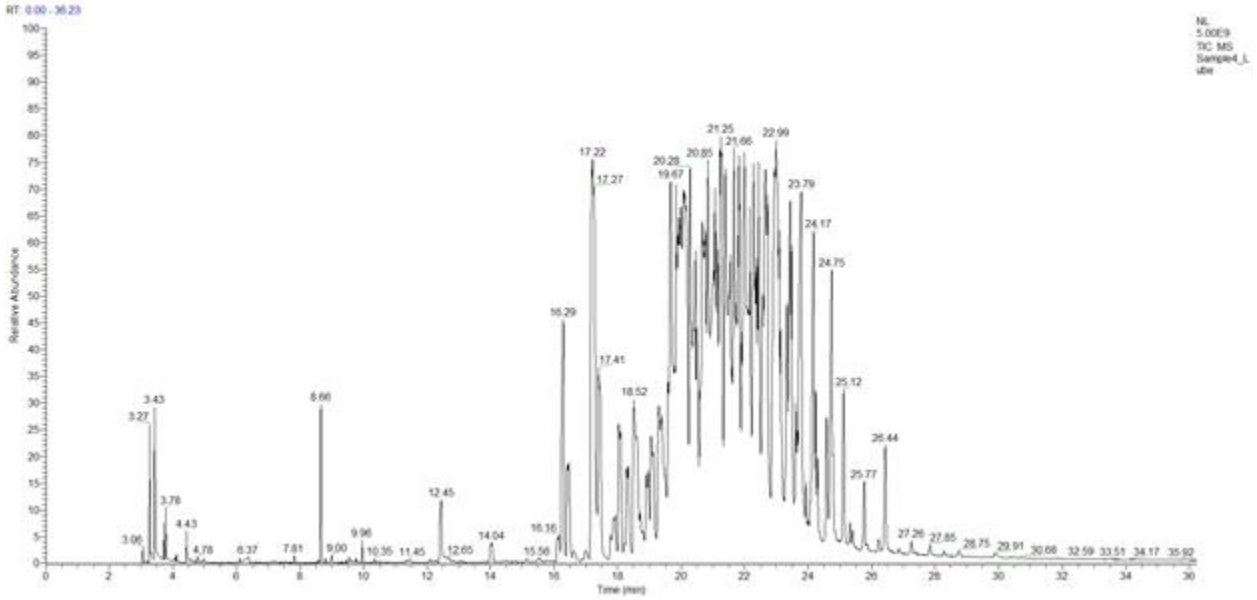

Figure A.4. Lubricating oil gas chromatogram

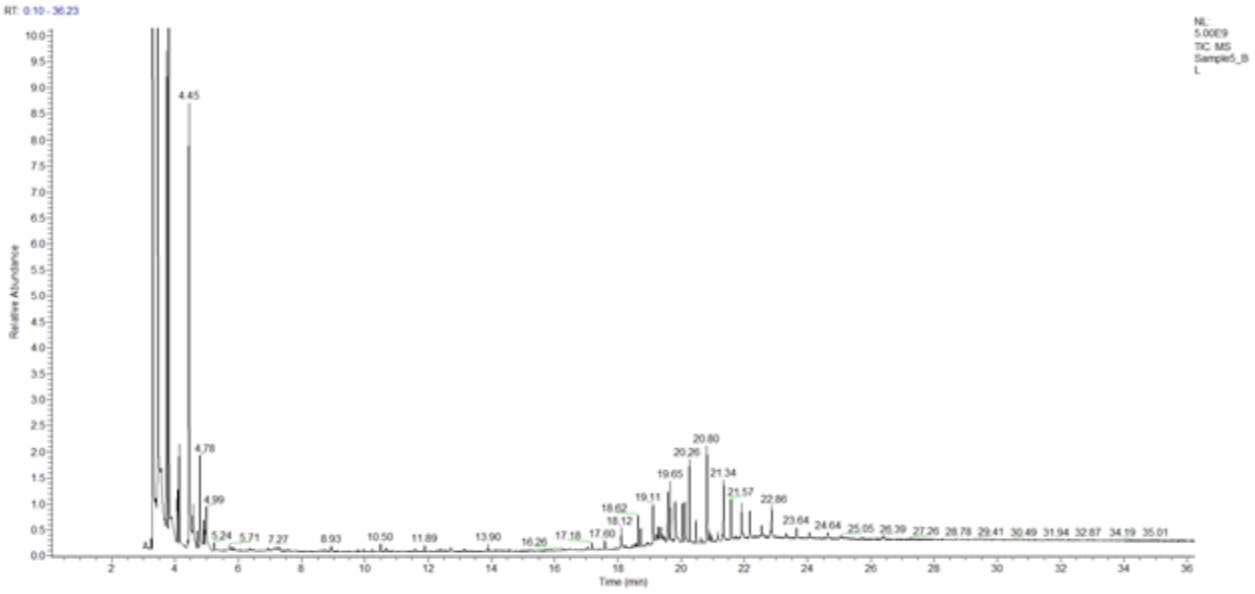

Figure A.5. Baseline IM7/977-3 composite laminate gas chromatogram

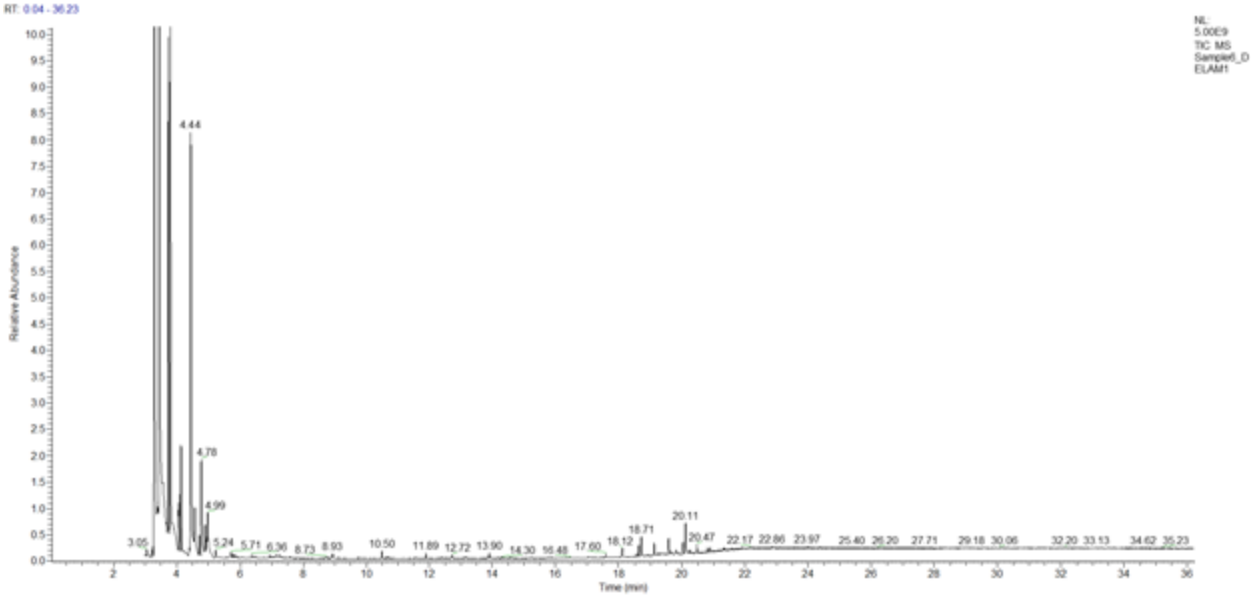

Figure A.6. Delamination IS-1 surface gas chromatogram

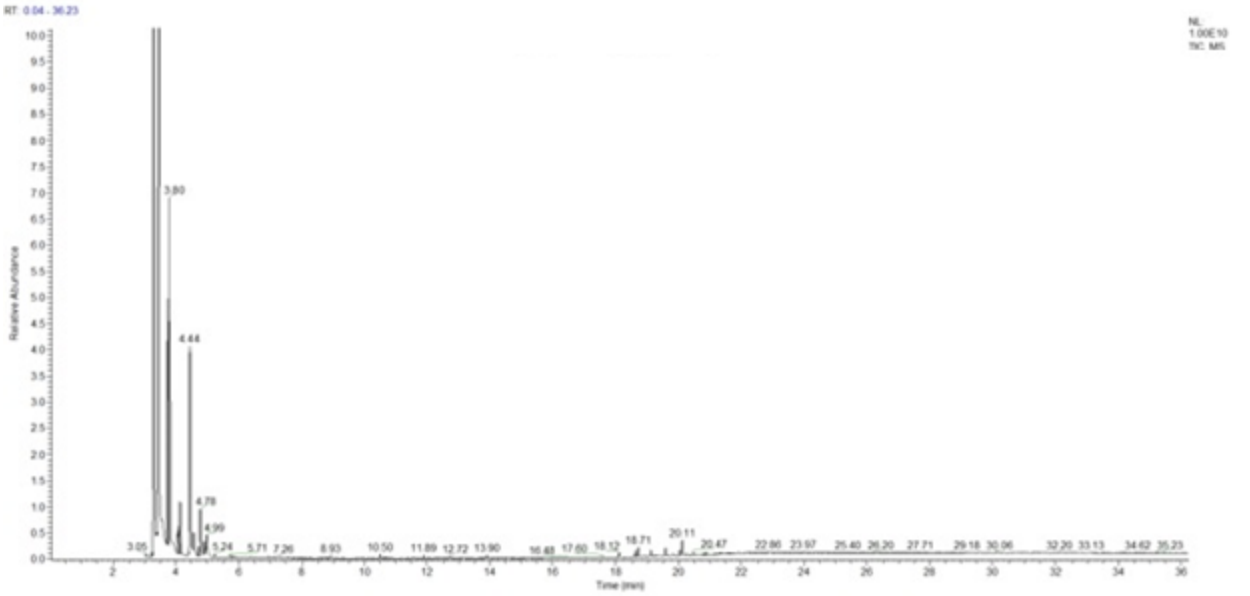

Figure A.7. Delamination IS-3 surface gas chromatogram

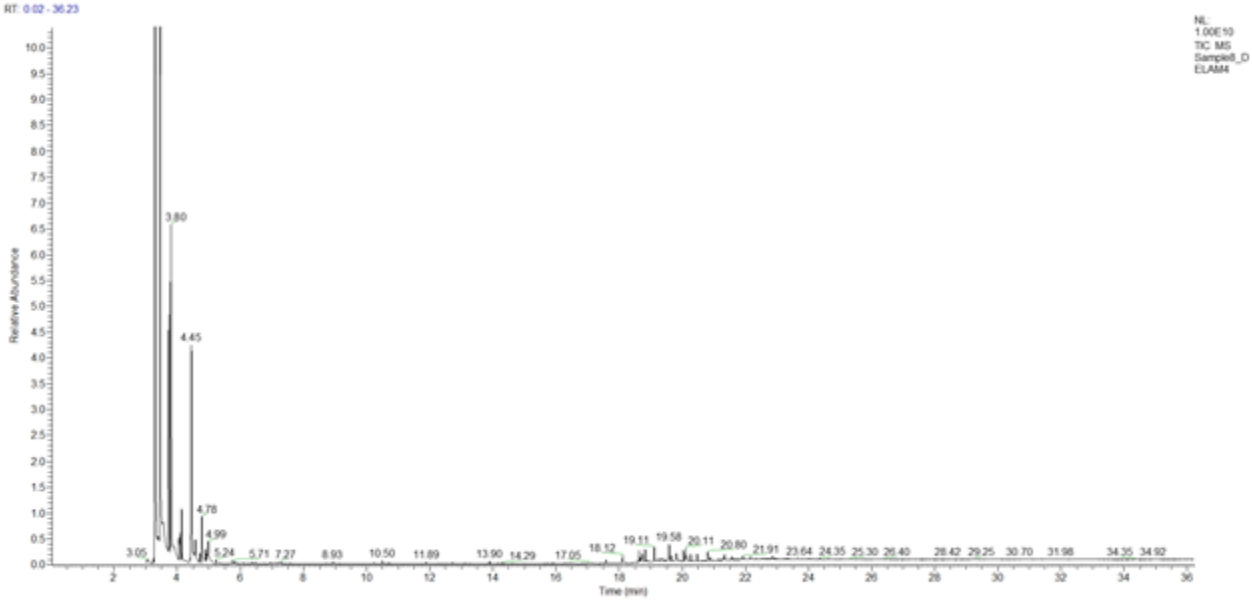

Figure A.8. Delamination IS-4 surface gas chromatogram

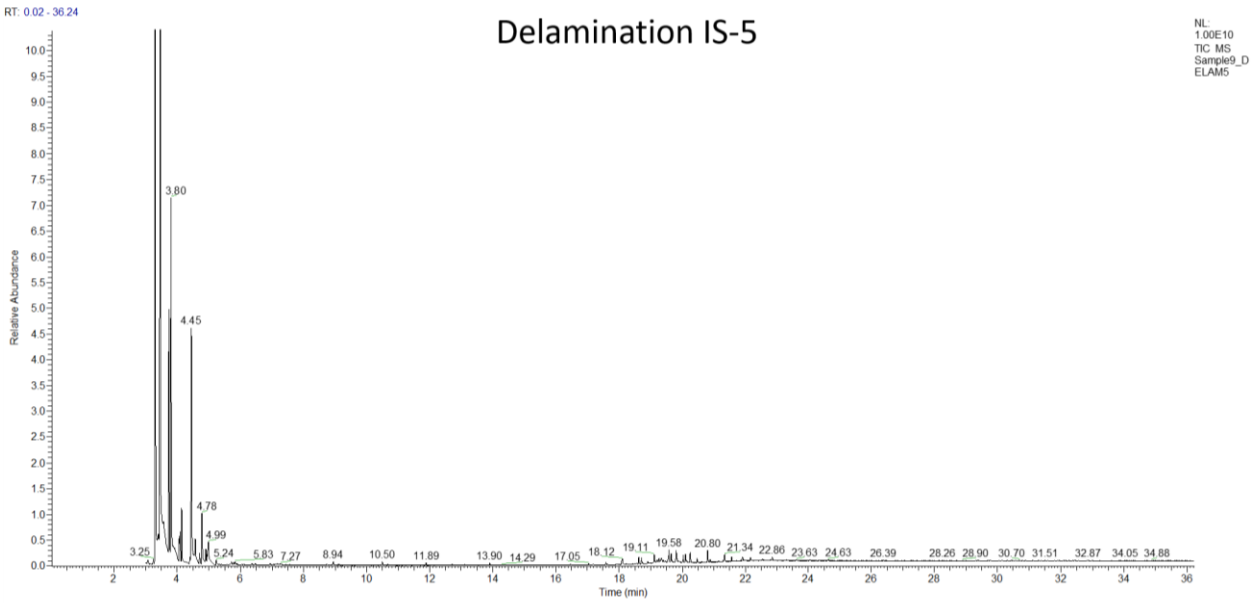

Figure A.9. Delamination IS-5 surface gas chromatogram

APPENDIX B: SINGLE LAP SHEAR FAILURE SURFACES

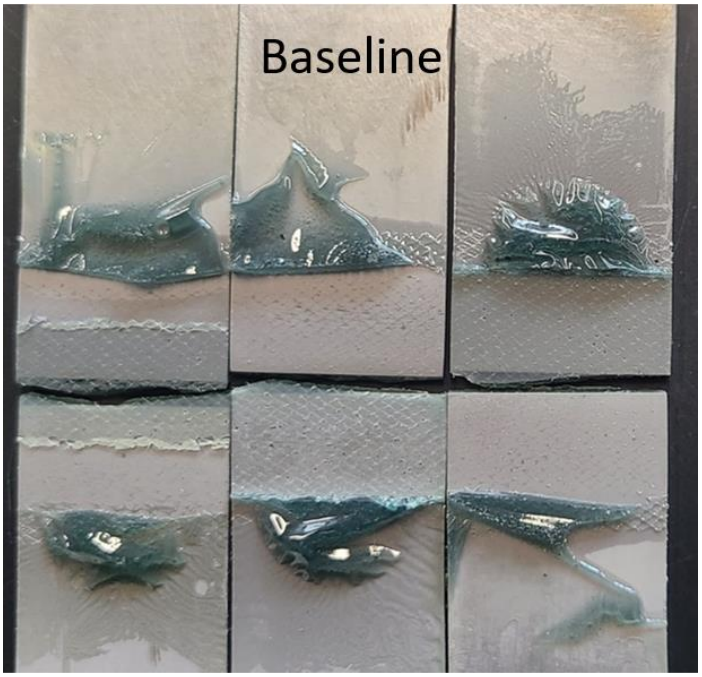

Figure B.1. LS-BL coupon failure surfaces

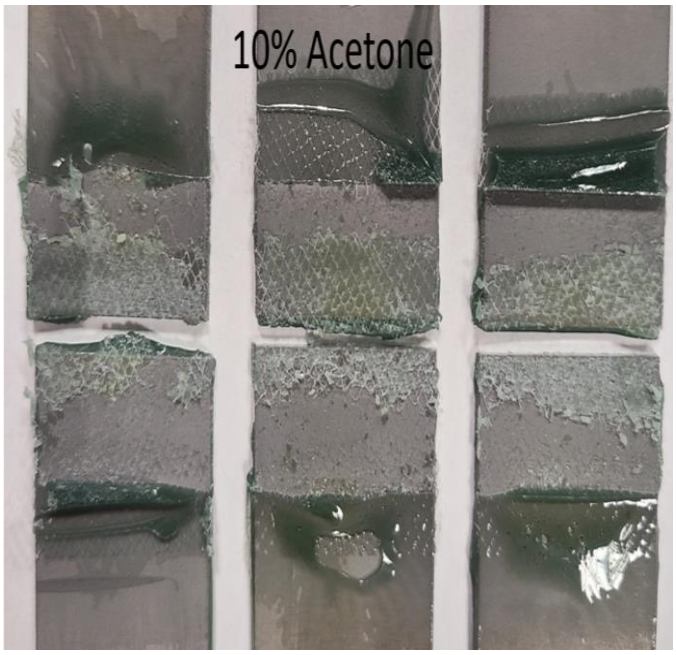

Figure B.2. LS-ACE-10 coupon failure surfaces

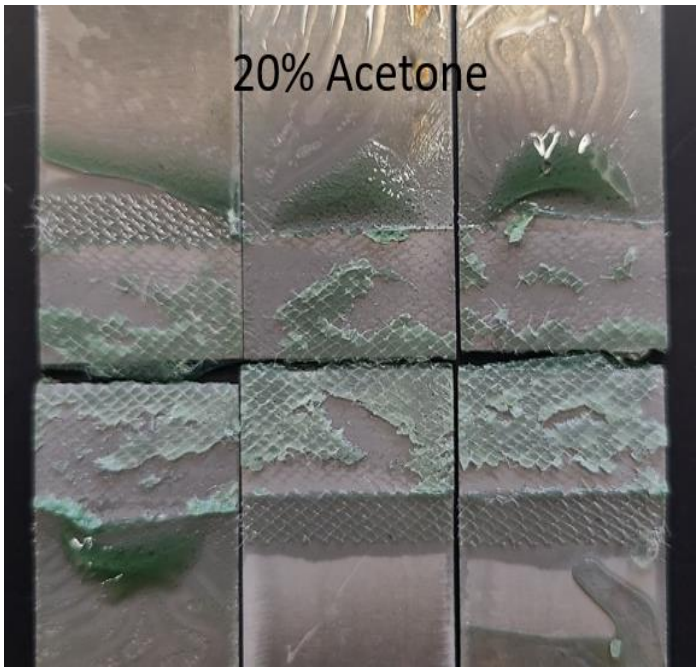

Figure B.3. LS-ACE-20 coupon failure surfaces

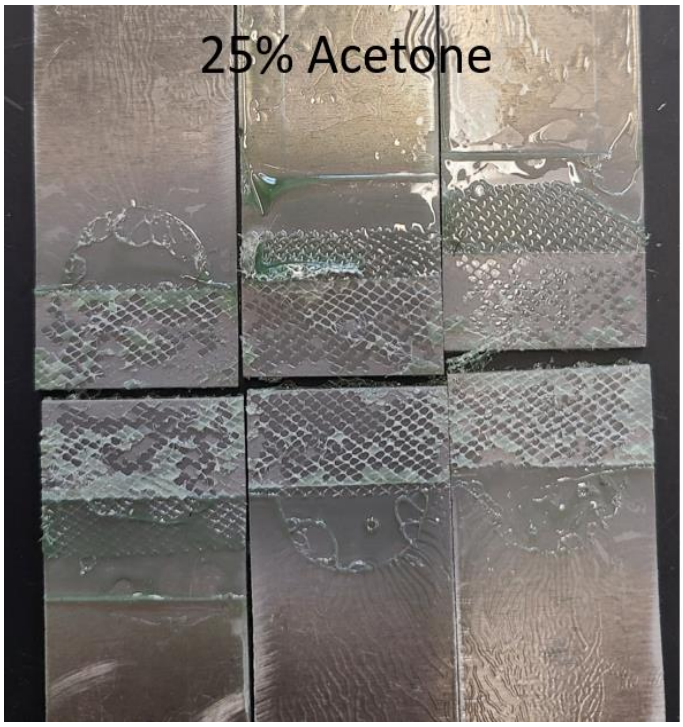

Figure B.4. LS-ACE-25 coupon failure surfaces

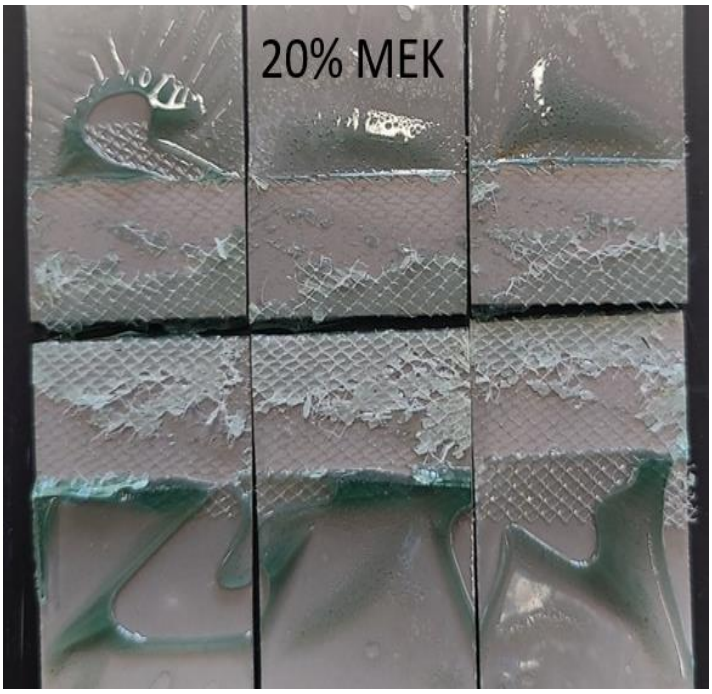

Figure B.5. LS-MEK-20 coupon failure surfaces

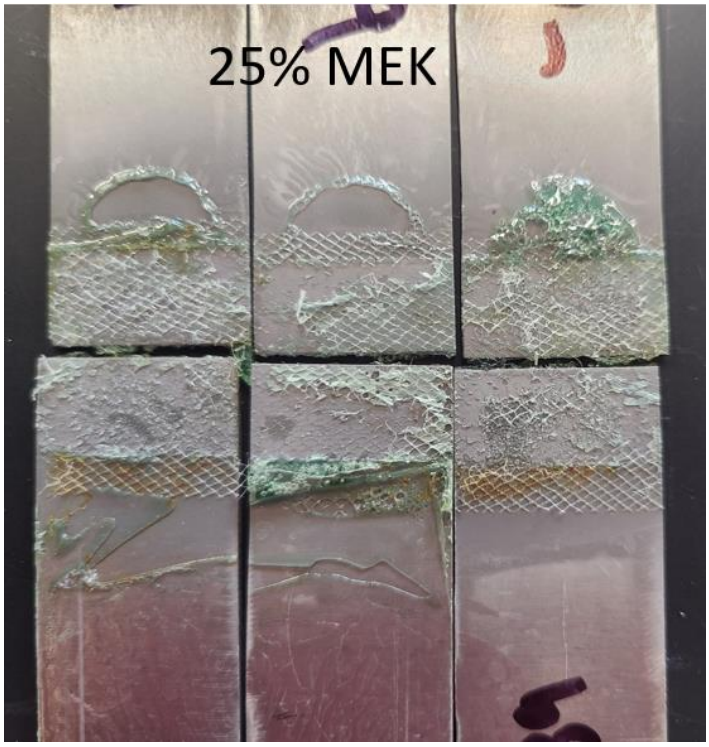

Figure B.6. LS-MEK-25 coupon failure surfaces

APPENDIX C: MODIFIED ENF MACRO FAILURE SURFACES

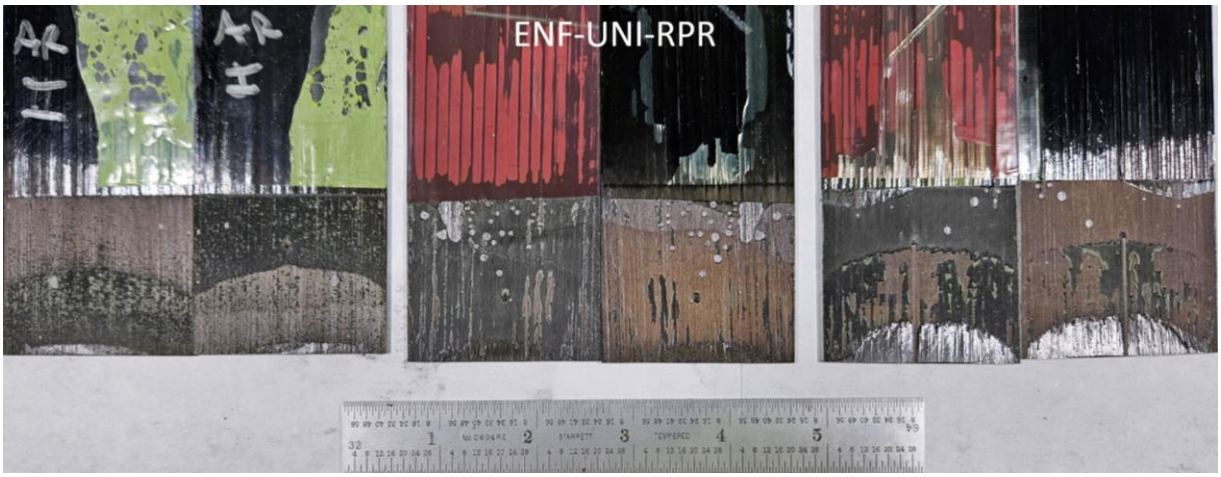

Figure C.1. ENF-UNI-RPR failure surfaces

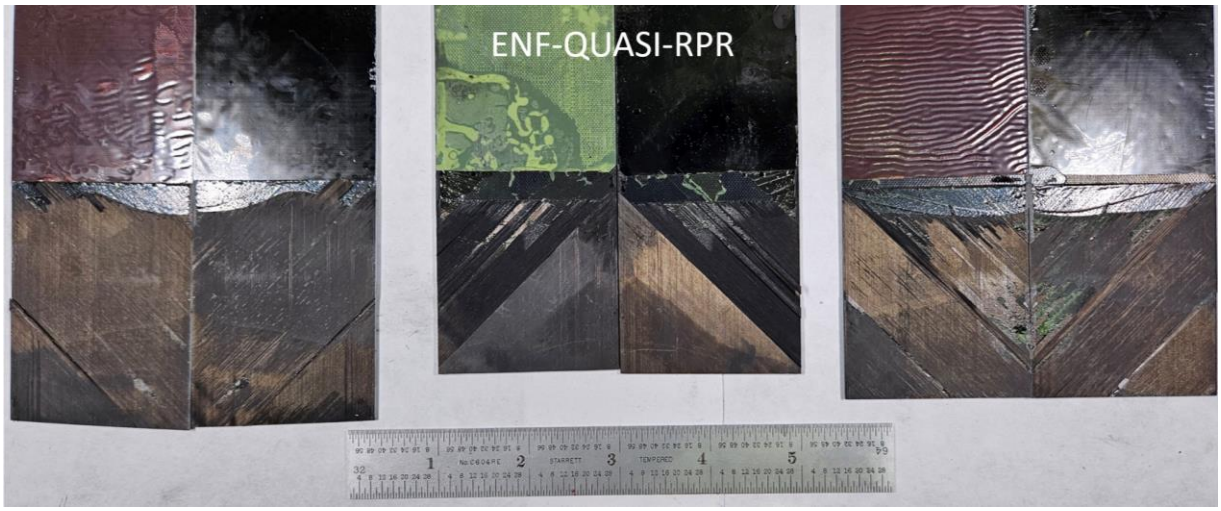

Figure C.2. ENF-QUASI-RPR failure surfaces

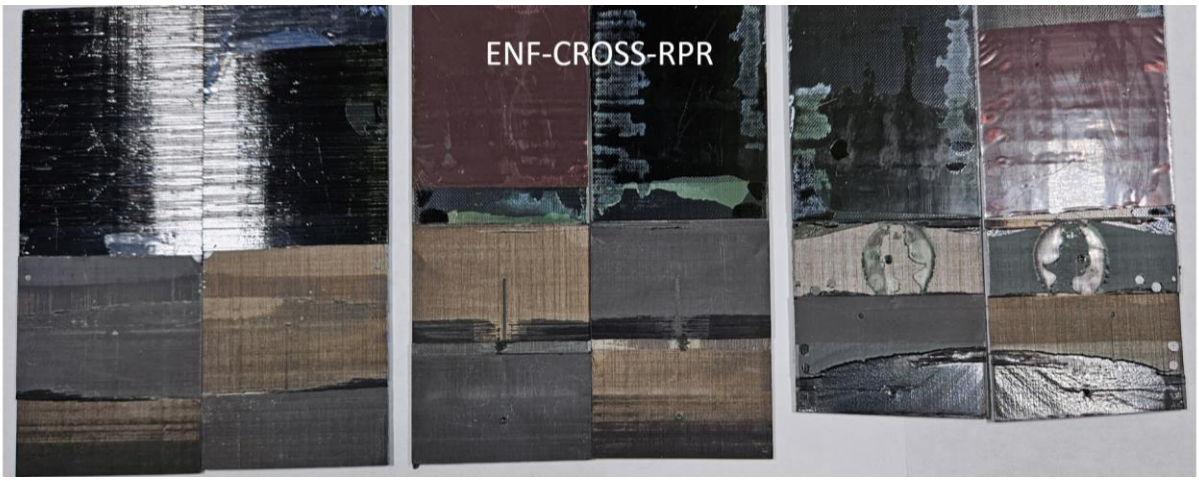

Figure C.3. ENF-CROSS-RPR failure surfaces

Figure C.4. ENF-UNI-CONT-HF failure surfaces

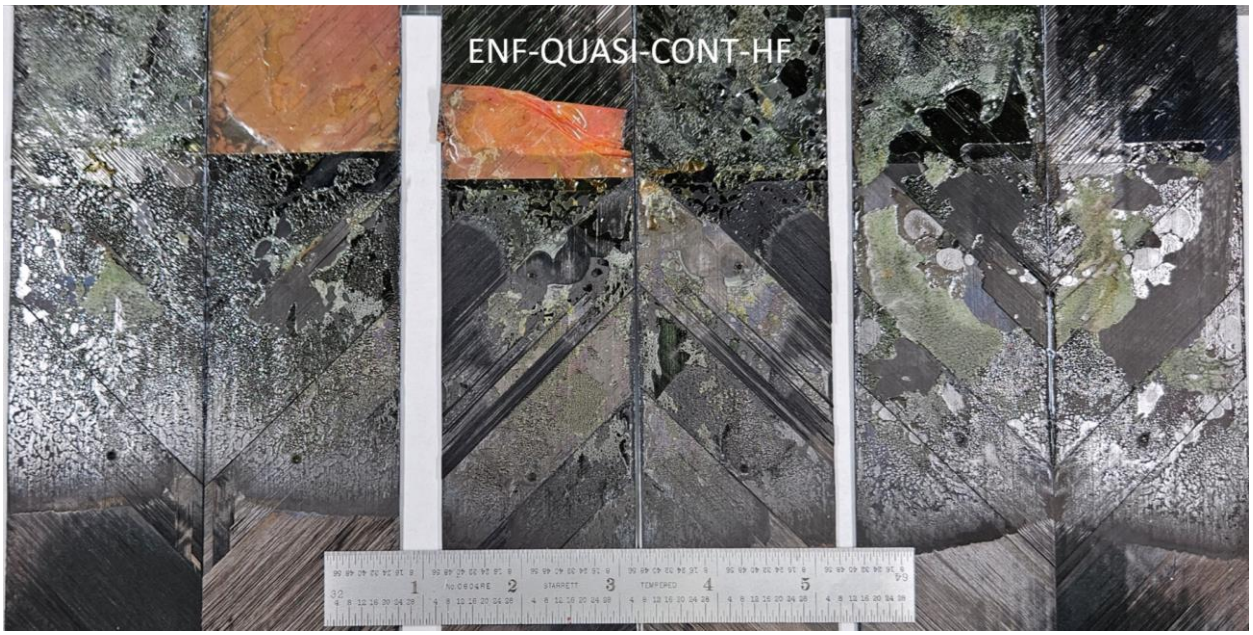

Figure C.5. ENF-QUASI-CONT-HF failure surfaces

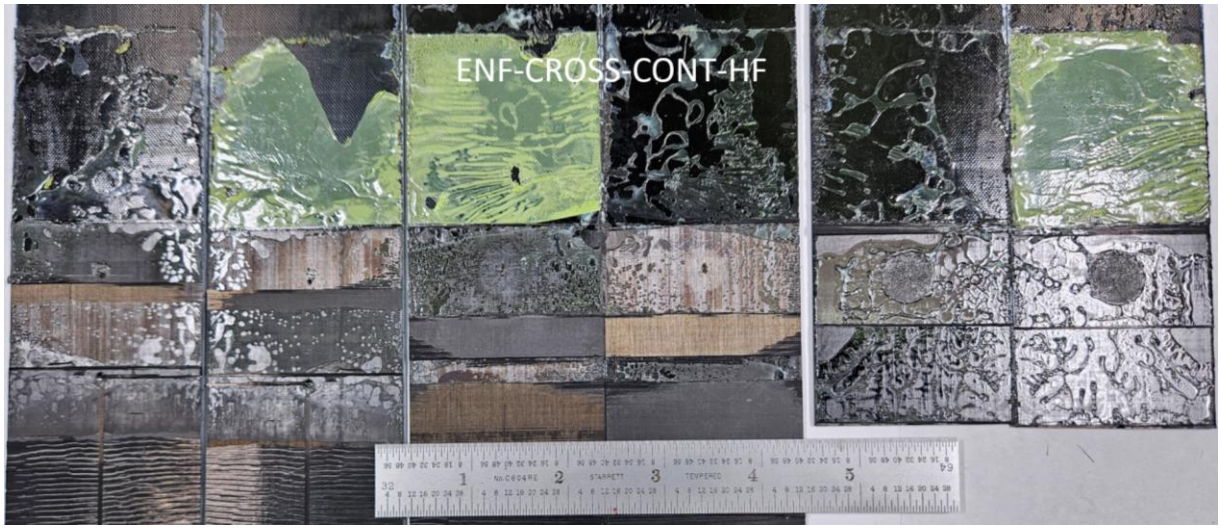

Figure C.6. ENF-CROSS-CONT-HF failure surfaces

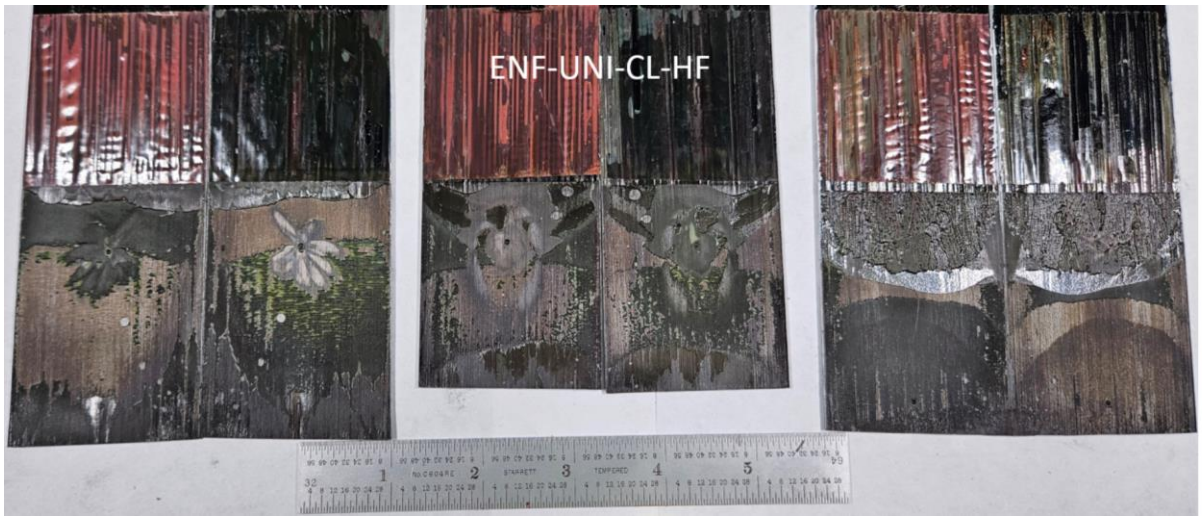

Figure C.7. ENF-UNI-CL-HF failure surfaces

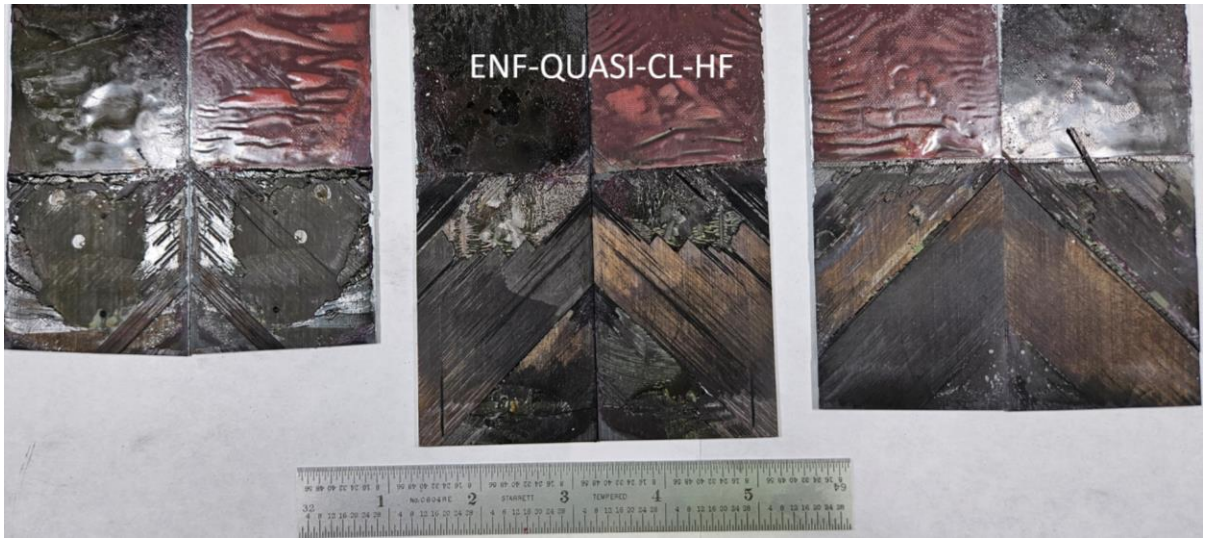

Figure C.8. ENF-QUASI-CL-HF failure surfaces

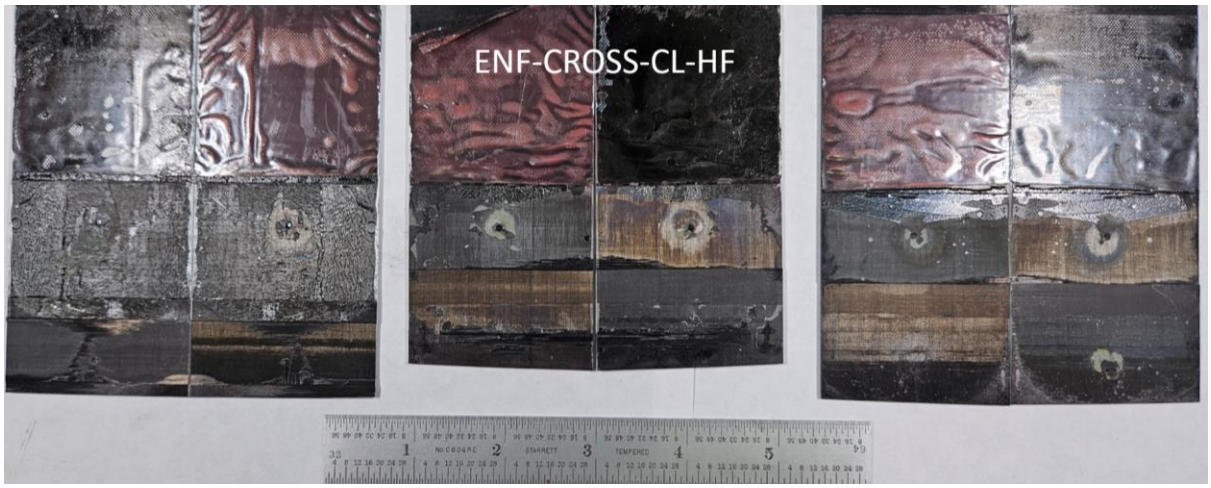

Figure C.9. ENF-CROSS-CL-HF failure surfaces

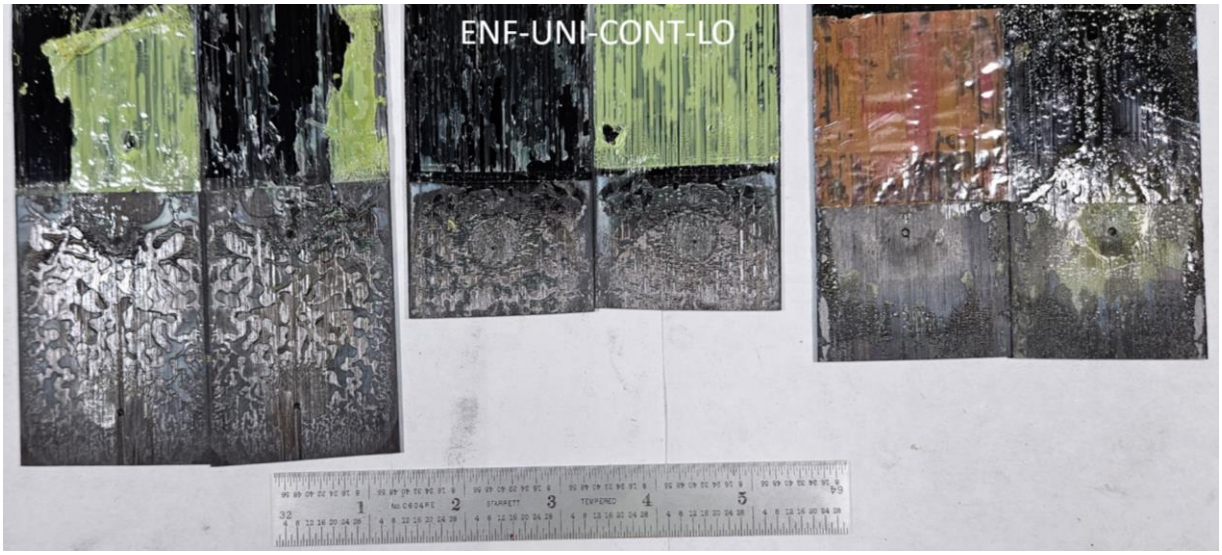

Figure C.10. ENF-UNI-CONT-LO failure surfaces

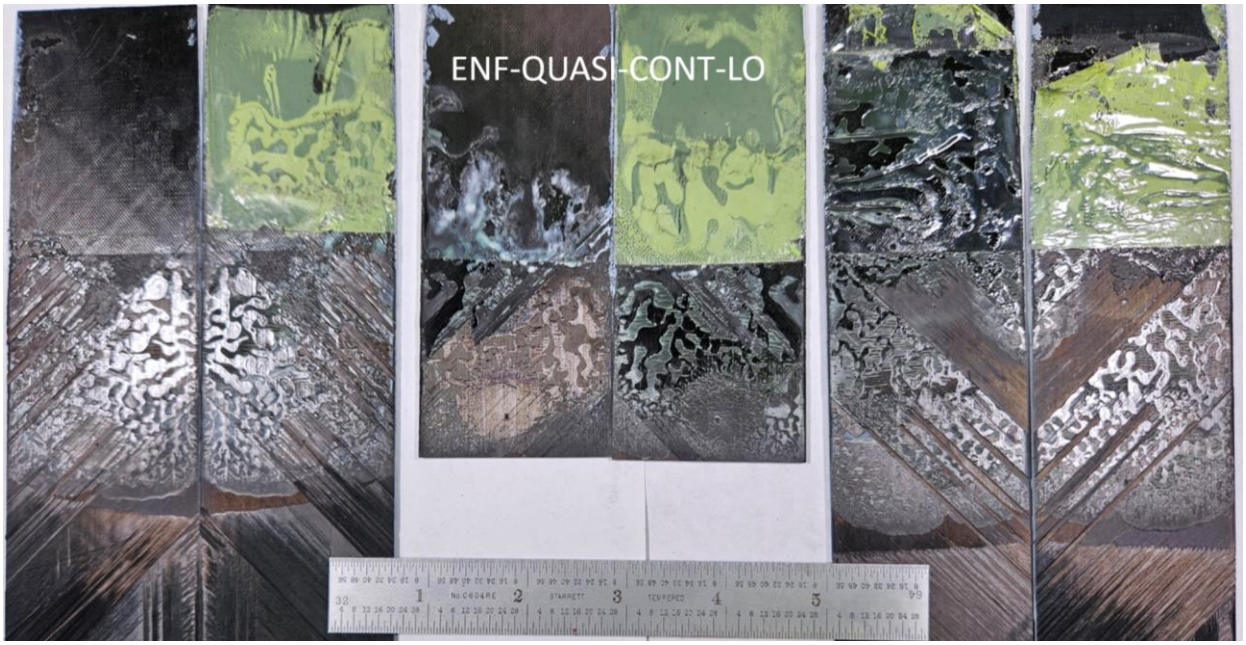

Figure C.11. ENF-QUASI-CONT-LO failure surfaces

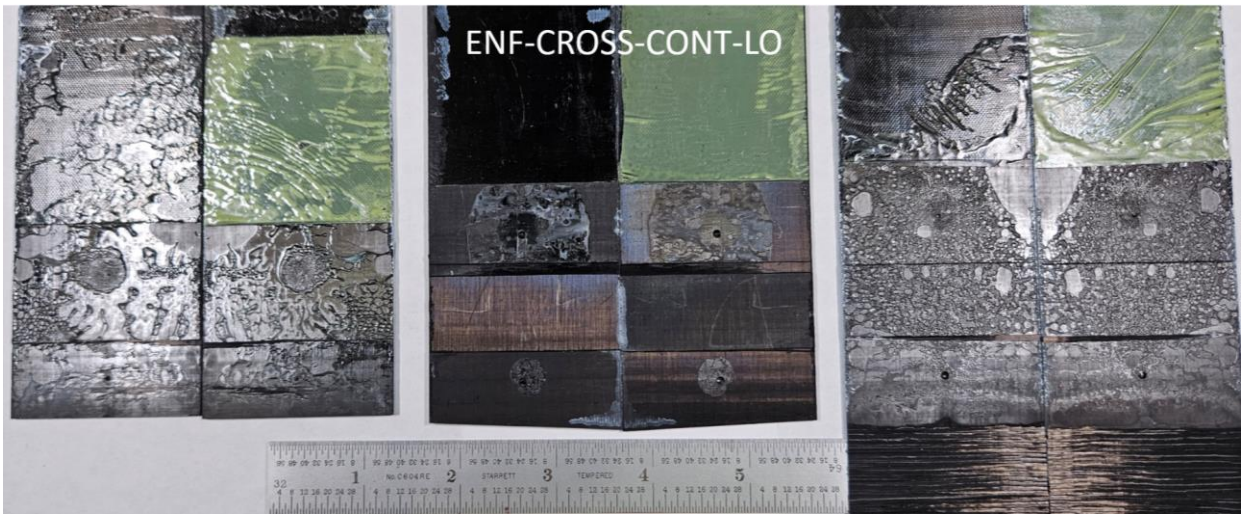

Figure C.12. ENF-CROSS-CONT-LO failure surfaces

Figure C.13. ENF-UNI-CL-LO failure surfaces

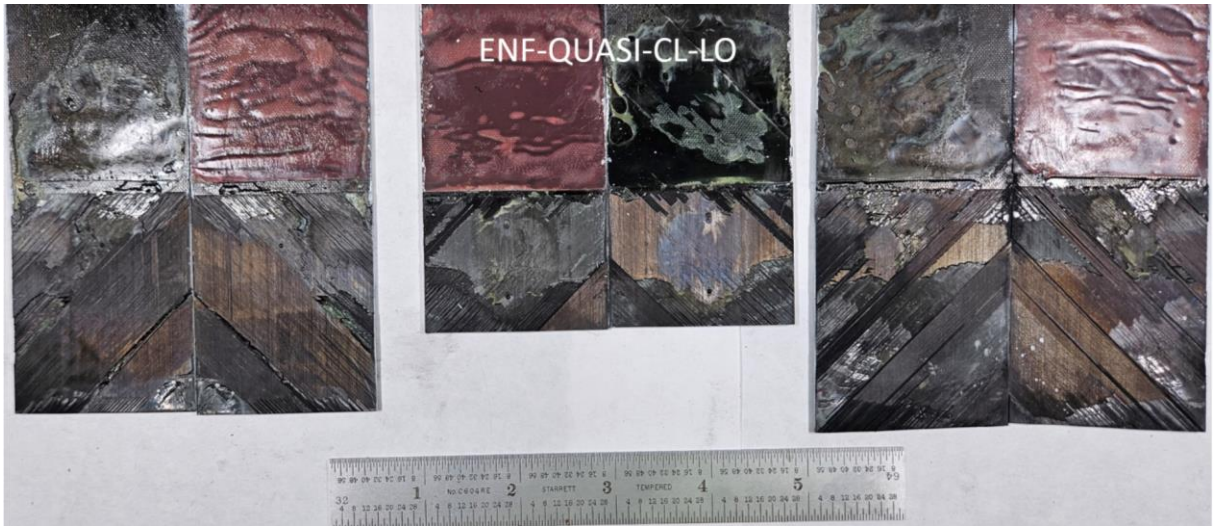

Figure C.14. ENF-QUASI-CL-LO failures surfaces

Figure C.15. ENF-CROSS-CL-LO failure surfaces

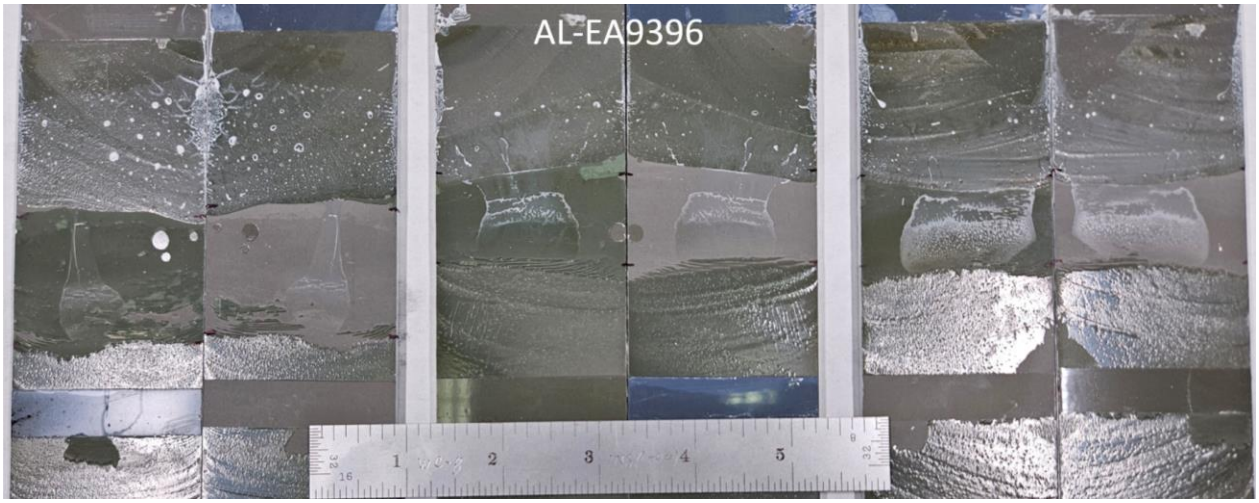

Figure C.16. AL-EA9396 failure surfaces